University of Birmingham

Biosynthesised nanoparticles as Polymer Electrolyte Membrane Fuel Cell (PEMFC) catalysts

By
Alan. J. Stephen
A thesis submitted to the University of Birmingham for the degree of
DOCTOR OF PHILOSOPHY

Lead supervisor: Professor Lynne Macaskie
Secondary supervisor: Dr. Neil Rees
Tertiary supervisor: Dr. Sophie Archer

CDT in Fuel cells and their fuels
School of Chemical Engineering
University of Birmingham
July 2020

Abstract

Polymer Electrolyte Membrane Fuel Cells (PEFMCs) currently utilise platinum group metal (PGM) nanoparticles (NPs) as a catalyst for their hydrogen oxidation reaction (HOR) and the oxygen reduction reaction (ORR). Platinum (Pt) and Palladium (Pd) are the most efficient catalysts for these reactions with platinum nanoparticles on carbon (Pt/C) being used commercially. Biosynthesised nanoparticles have recently emerged as a green alternative to conventional chemical synthesis; *Escherichia coli* has been shown to synthesise nanoparticles of Pt (*E. coli*-Pt) and Pd (*E. coli*-Pd). The HOR and ORR activities of these *E. coli*-NPs were previously confirmed. This study investigates these *E. coli*-NPs and their bimetallics (*E. coli*-Pt:Pd* and *E. coli*-Pd:Pt*) for direct use as ORR catalysts.

Initially *E. coli*-Pd, *E. coli*-Pt, *E. coli*-Pt:Pd* and *E. coli*-Pd:Pt* were all synthesised and characterised. *E. coli*-Pd showed ubiquitous NP synthesis (intracellular NPs and surface bound clusters) whereas *E. coli*-Pt showed Pt-NPs primarily associated to the surface of the cell. It was shown that this patterning influenced the synthesis of bimetallic *E. coli*-NPs. *E. coli*-Pt:Pd* was synthesised by reducing Pt (IV) ions onto *E. coli*-Pd and *E. coli*-Pt:Pd* showed similar NP localisation across the cell as *E. coli*-Pd. Similarly, *E. coli*-Pd:Pt* was synthesised by reducing Pd (II) ions onto *E. coli*-Pt and *E. coli*-Pd:Pt* showed similar NP localisation in surface bound clusters. Unlike *E. coli*-Pt, however, some intracellular NPs were seen. All *E. coli*-NPs showed promise for ORR activity with the crystal face (111) being detected via X-ray diffraction (XRD) and selected area electron diffraction (SAED). Both bimetallics are thought to be alloys of Pt and Pd as scanning transmission electron

microscopy – energy dispersive X-ray (STEM-EDX) maps showed co-localisation of both metals. This was further evidenced by X-ray photoelectron spectroscopy (XPS) and XRD data. Furthermore, *E. coli*-Pt:Pd* showed evidence of a "Pt-rich" skin around clusters whereas this was not seen for *E. coli*-Pd:Pt*.

All *E. coli*-NPs were tested ex-situ electrochemically for ORR activity. *E. coli*-Pd:Pt* did not show any discernible electrochemical activity while *E. coli*-Pt:Pd* (10%:10%) showed better activities than single metal versions with a mass activity (MA) of 2.8 mA mg^{-1}_{PGM} relative to a MA of 1.7 mA mg^{-1}_{PGM} for *E. coli*-Pt and *E. coli*-Pd at 0.3 mA mg^{-1}_{PGM}. This increase in activity is attributed to the increased conductivities afforded by Pt:Pd* NP dispersion. However, these results are significantly lower than MA values for commercial Pt/C catalyst at ~ 250 mA mg^{-1}_{PGM}. To increase conductivities, and thus MA, multiwalled carbon nanotubes (MWCNTs) were mixed with *E. coli*-Pt:Pd*. This showed an increase in MA to 8.6 mA mg^{-1}_{PGM} relative to 2.8 mA mg^{-1}_{PGM} for untreated *E. coli*-Pt:Pd*. However, this activity still falls significantly short of commercial Pt/C activities (~250 mA mg^{-1}_{PGM}).

A screening life cycle analysis (LCA) was conducted to establish the environmental benefits in biosynthesis of NPs, over using conventional Pt/C, as PEMFC catalysts. However, it showed that relative to *E. coli*-NPs, commercial Pt/C only had ~2% of the environmental impacts when used as PEMFC catalysts, i.e., using Pt/C was more environmentally friendly than *E. coli*-NPs. This was attributed to the low MA of *E. coli*-NPs relative to Pt/C. In using catalysts with low MAs, a greater mass of catalyst had to be used to generate the same power (157.1 mg for *E. coli*-Pt:Pd*

relative to 1.8 mg for Pt/C) resulting in more environmental impacts by their use. An alternative LCA using a hypothetical *E. coli*-Pt:Pd* catalyst with an MA of ~250 mA mg^{-1}_{PGM} (similar to Pt/C) showed fewer environmental impacts. This catalyst only required 1.8 mg to generate the same power and thus, relative to commercial catalyst (Pt/C) it only had ~50% of the environmental impacts.

Thus, this body of work investigated the potential of *E. coli*-NPs as direct use ORR catalysts. It was concluded that *E. coli*-NPs showed environmental advantages over commercial catalysts only if their mass activities can be significantly improved.

Acknowledgments

Throughout writing this thesis and my entire PhD journey, I have been blessed with the support of so many people. It is therefore important that I acknowledge their effort.

I would firstly like to thank my lead supervisor Professor Lynne Macaskie for her invaluable experience and consistent support. Through our many discussions, you helped me develop into a fully realised scientist and for that, I am grateful. I would also like to thank my secondary supervisor Dr Neil V. Rees; your guidance, through my many electrochemistry woes, was vital to finishing this thesis. I would also like to specifically thank Dr Sophie Archer for teaching and assisting me with my Life Cycle Analysis.

I would like to thank the rest of the Fuel Cell group and the Macaskie group for all that you have done for me. Specifically, Dr. Iryna Mikheenko, Dr Ahmad El-Kharouf, Mr. John Hooper and Dr Rafael Orozco-Pulido. It is through your assistance and guidance that I developed the necessary skills for my PhD.

I would like to thank my collaborators Professor Mohamed Merroun, Dr Jaime Gomez-Bolivar and Dr María del Mar Abad Ortega from the University of Granada and Dr Mark Isaacs at HarwellXPS. Thank you for hosting me during my visit and your assistance was crucial to my work. I would also like to thank the EPSRC, NERC and Blue Sky Bio Ltd for their roles in funding my PhD.

I would also like to thank my friends from the fuel cell group. Aimee, Hal, Lois, Bea, Satish, Oujen, Kun and all the others in the fuel cell group; thank you for making this PhD a memorable experience. I would like to thank Pete, Abby, Ollie, Liam, Mel, Laura, and Rich. Through various cribbage games, living together and pub nights, you have become a second family to me. I would like to specifically thank Pete for introducing me to Jitsu; who knew that throwing people would be an efficient way to destress. I would also like to thank Szi Kay, Graham and Sahana, for being the people I called (numerous times) to vent. Finally, I would like to thank my family. Any success I may have is down to your consistent support.

Contents

List of Figures and Tables

The figures tables used in this thesis are listed below

Glossary

Abbreviation	Full Name
ADF	Annular dark field
AFC	Alkaline fuel cell
AFM	Atomic force microscopy
BF	Bright field
bio-NPs	Bio-synthesised nanoparticles
BSE	Back-scattered electrons
CCD	Charge-coupled device
CE	Counter electrode
CL	Catalyst layer
CML	Not an abbreviation; Type of LCA methodology
CNT	Carbon nanotubes
CV	Cyclic voltammetry
D.O.E.	Department of Energy (United States of America)
DALY	Disability adjusted life years
Dark field	DF
DFT	Density-functional Theory
E. coli-Pd:Pt*	E. coli synthesised bimetallic platinum/palladium nanoparticles with platinum seeds
E. coli-Pt:Pd*	E. coli synthesised bimetallic platinum/palladium nanoparticles with palladium seeds
E. coli-Pd	E. coli synthesised palladium
E. coli-Pt	E. coli synthesised platinum
ECSA	Electrochemically active surface area
EDX	Electron-disruptive X-ray spectroscopy
EIS	Electrochemical impedance spectroscopy
EM	Electron microscopy

EPR	Electron paramagnetic resonance
EU	European union
EXAFS	Extended x ray absorption fine structure
FCEV	Fuel cell electric vehicles
GCE	Glassy carbon electrode
GDL	Gas diffusion layer
GG	Greenhouse gas
GO	Graphene oxide
HAADF	High angle annular dark field
HOR	Hydrogen oxidation reaction
HRTEM	High resolution transmission electron microscopy
ICEV	Internal combustion engine vehicles
ICP-MS	Inductively coupled plasmon mass spectrometry
IPCC	Intergovernmental Panel on Climate Change
ISO	International standards organisation
KL	Koutecky-Levich
LCA	Life cycle analysis
LCIA	Life cycle impact assessment
LSV	Linear sweep voltammetry
MA	Mass activity
MEA	Membrane electrode assembly
ML	*Micrococcus luteus*
MS	Mass spectrometry
MWCNT	Multiwalled carbon nanotubes
NB 2	Nutrient broth No. 2
NP	Nanoparticle
OCV	Open circuit voltage
OFN	Oxygen free nitrogen

ORR	Oxygen reduction reaction
PEMFC	Polymer electrolyte membrane fuel cell
PGM	Platinum group metals
PPX	Polymer (p-xylylene)
PPY	Polypyrrole
Pt/C	Platinum on Carbon Black
PVA	Poly(vinyl-alcohol)
RDE	Rotating disk experiments
RE	Reference electrode
ReCiPe	Not an abbreviation; Type of LCA methodology
rGO	Reduced graphene oxide
RHE	Reversible hydrogen electrode
SA	Specific activity
SAED	Selected area electron diffraction
SCE	Saturated calomel electrode
SE	Secondary electrons
SEM	Scanning electron microscopy
SHINERS	Shell Isolated Nanoparticles for Enhanced Raman Spectroscopy
SOFC	Solid oxide fuel cell
SRB	Sulfate-reducing bacteria
TEM	Transmission electron microscopy
TKK	Tanaka Kikinzoku Kogyo (Pt/C catalyst)
TPB	Triple phase boundary
WE	Working electrode
wt	Weight
XANES	X-ray absorption near edge structure
XPS	X-ray photoelectron spectroscopy
XRD	X-ray diffraction

Chapter 1: Introduction

Climate change and greenhouse gas (GG) emissions continue to be a major global concern with various research groups warning of their long-term effects[1] including natural disasters[2] effects on agriculture[3] and even the economy.[4] As such, research focus has shifted to non-carbon energy systems such as a "Hydrogen Economy".[5] Within this emerging concept, H_2, as opposed to fossil fuels, would act as the global energy carrier (figure 1.1).[6] H_2 can be produced from the electrolysis of water driven by solar[7] or wind[8] energy or through algal[9] and bacterial[10] photosynthesis. It would act as the energy carrier and it can be converted into other forms via combustion,[11] used in nuclear fusion (as deuterium)[12] or used to generate electricity via fuel cells.[13] Comparable to batteries, fuel cells are electrochemical cells that convert chemical energy into electricity but are distinct from batteries by requiring a continuous supply of fuel to sustain the chemical reaction.[14]

Fuel cells have been an established area of research since the mid-20th century and as such a range of types have been developed.[15] These operate at various temperature ranges and are often classified by the materials used.[15] For example, a major class is the Solid Oxide Fuel Cell (SOFCs) that work at the range of 600–1000 °C and are often used in power generation applications.[16] SOFCs can use a variety of fuels including methane[16] which they convert to H_2 and CO_2 using an internal reformer.[16] Another type, Alkaline Fuel Cells (AFCs), work at a range of 50 °C – 200 °C and were previously used in the space

program.[17] Finally, a commonly investigated type for automotive applications is the Polymer Electrolyte Fuel Cell (PEMFC).[18]

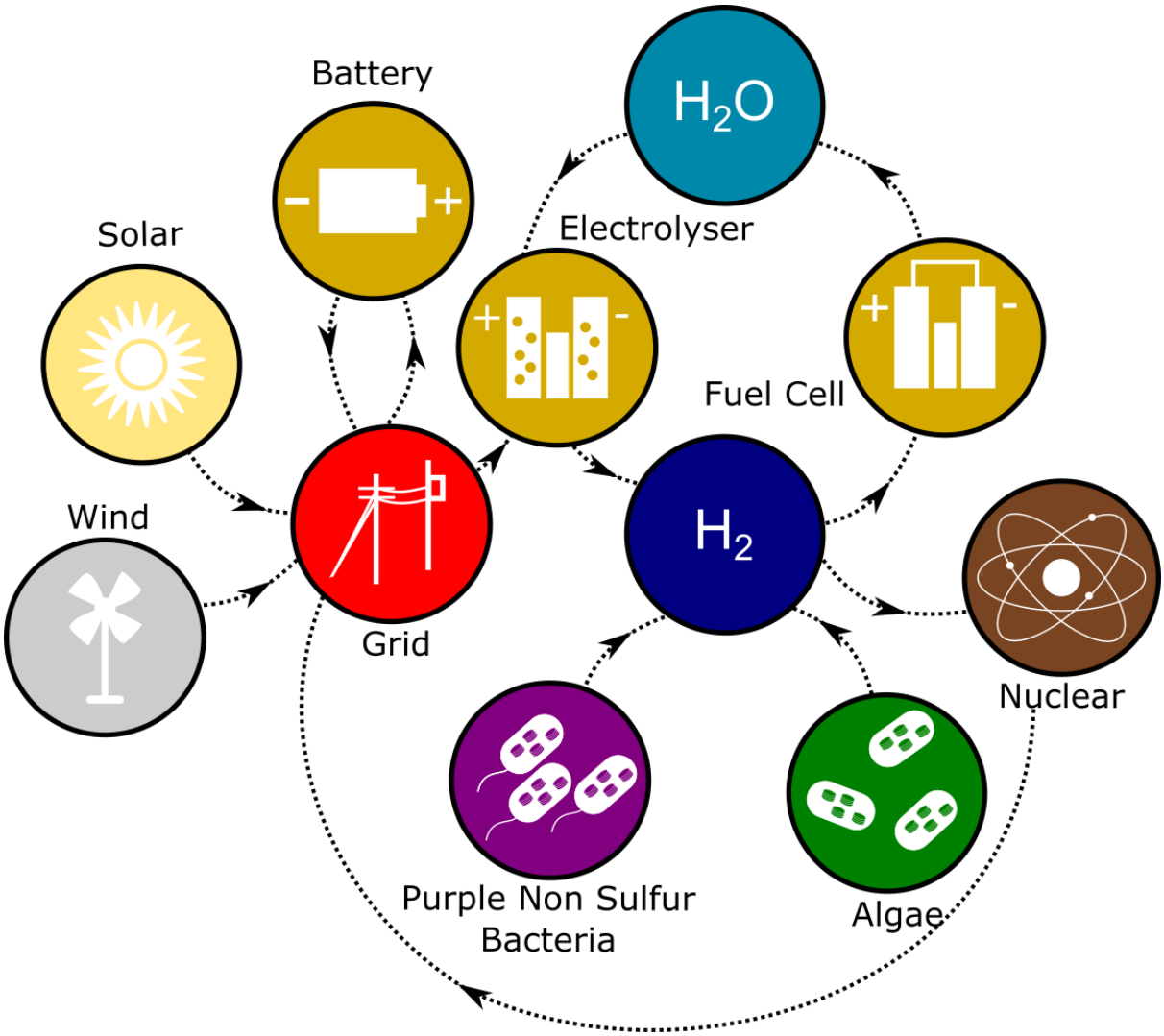

Figure 1.1 This shows a simplified version of the proposed hydrogen economy using clean, non-fossil fuel, sources. Here hydrogen is produced by either water electrolysis through solar or wind power or directly by biological means. The produced hydrogen is then utilised for power generation via fuel cells or (in the future) through nuclear fusion (deuterium). The resultant waste product of fuel cells is water which can be recycled back into electrolysers for further H_2 production. H_2 here acts as an energy carrier / storage molecule.

1.1 PEMFCs and their catalysts

PEMFCs operate at a temperature of 80 °C and require ultra-pure H_2 as fuel.[19] Figure 1.2 shows a general scheme for PEMFC operation. Here, the H_2 is converted into electricity in an electrochemical reaction between H_2 and O_2 by separating the hydrogen oxidation reaction (HOR) and the oxygen reduction reactions (ORR) via use of the anodic and cathodic chambers.[19] As shown in figure 1.2, H_2 is supplied to the anode where it dissociates into protons and electrons via a catalyst (see section 1.1.1). The electrons travel through the circuit to the cathode, while the protons travel through the polymer electrolyte (often Nafion®) and meet the electrons to reduce oxygen to water at the cathode via a catalyst.[19] Both electrodes contain a gas diffusion layer (GDL), which is a conductive surface that also mediates uniform distribution of gas across the entire electrode, and a catalyst layer (CL), which is the catalyst and its conductive support. The CL is often either coated onto the GDL or the membrane itself.[19] The entire setup which includes the anode, the electrolyte, and the cathode, is known as the membrane electrode assembly (MEA).[19] The overall reactions for this process are as follows:

$$\textbf{Anode: } H_2 \leftrightarrow 2H^+ + 2e^- \qquad \textbf{(Eq 1.1)},$$

$$\textbf{Cathode: } O_2 + 4H^+ + 4e^- \leftrightarrow 2H_2O \qquad \textbf{(Eq 1.2)},$$

$$\textbf{Overall: } H_2 + \frac{1}{2}O_2 \leftrightarrow H_2O \qquad \textbf{(Eq 1.3)},$$

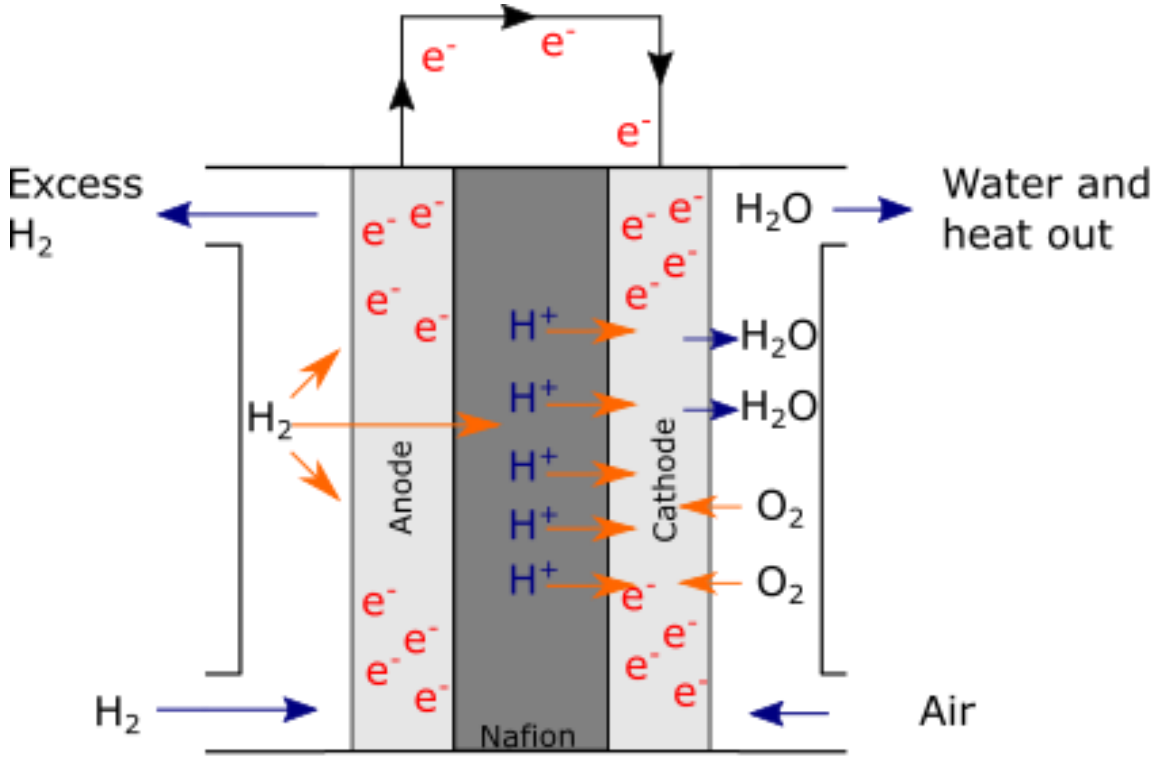

Figure 1.2: A general schematic for PEMFC. Here the H_2 molecules enter the anodic chamber and dissociate into electrons and protons at the anodic CL. The electrons travel through the circuit while the protons travel through an ion conducting polymer membrane (often Nafion®). They meet O_2 at the cathodic CL and reduce it to form water.

The potential energy of this redox reaction is characterised by the open circuit voltage (OCV) of the cell containing this redox pair, which is the given by the Nernst equation:

$$E_{OCV} = E^{\theta} - \frac{RT}{nF} ln \frac{[Red]}{[Ox]} \qquad \textbf{(Eq 1.4)},$$

where E_{OCV} is the voltage of the cell for an incomplete circuit, E^{θ} is the Nernst voltage, R is the molar gas constant, T is the temperature, n is the number of electrons transferred and F is the Faraday constant in the relevant S.I. units. The Nernst voltage is the potential difference for this redox pair at standard

temperature and pressure conditions; for this redox reaction (Eq 1.3) it is 1.23 V. However, during operation, this voltage is subject to losses as shown in the polarisation curve (figure 1.3). These losses are the kinetic losses, the ohmic losses and the concentration losses[20] and they can be modelled using the equation[20] shown below:

$$E_{Cell} = E_{OCV} - \eta_{activation} - \eta_{ohmic} - \eta_{concentration} \qquad \textbf{(Eq 1.5)},$$

where E_{Cell} is the actual voltage of the cell and overpotential (η) signifies the various voltage losses. $\eta_{activation}$ is the voltage loss due to the energy required to overcome the activation barrier (kinetic losses) for the reaction. η_{ohmic} is the voltage loss due to ionic and electronic resistance from the various components of the cell and $\eta_{concentration}$ is the voltage loss due to poor mass transport of reactants at high current densities. This is characterised in fuel cells through a polarisation curve as shown in figure 1.3. As shown the area under the polarisation curve (purple) indicates the power generated by the fuel cell whereas the area between the polarisation curve and the Nernst voltage (dotted black line) is the energy lost in a fuel cell through heat. Thus, fuel cell research focuses on improving performance by limiting these voltage losses. These include research into materials to improve conductivities throughout the cell[21,22] and thus lower ohmic losses, into water management to decrease mass transport losses[23,24] and catalyst research to minimise activation (kinetic) losses.[25]

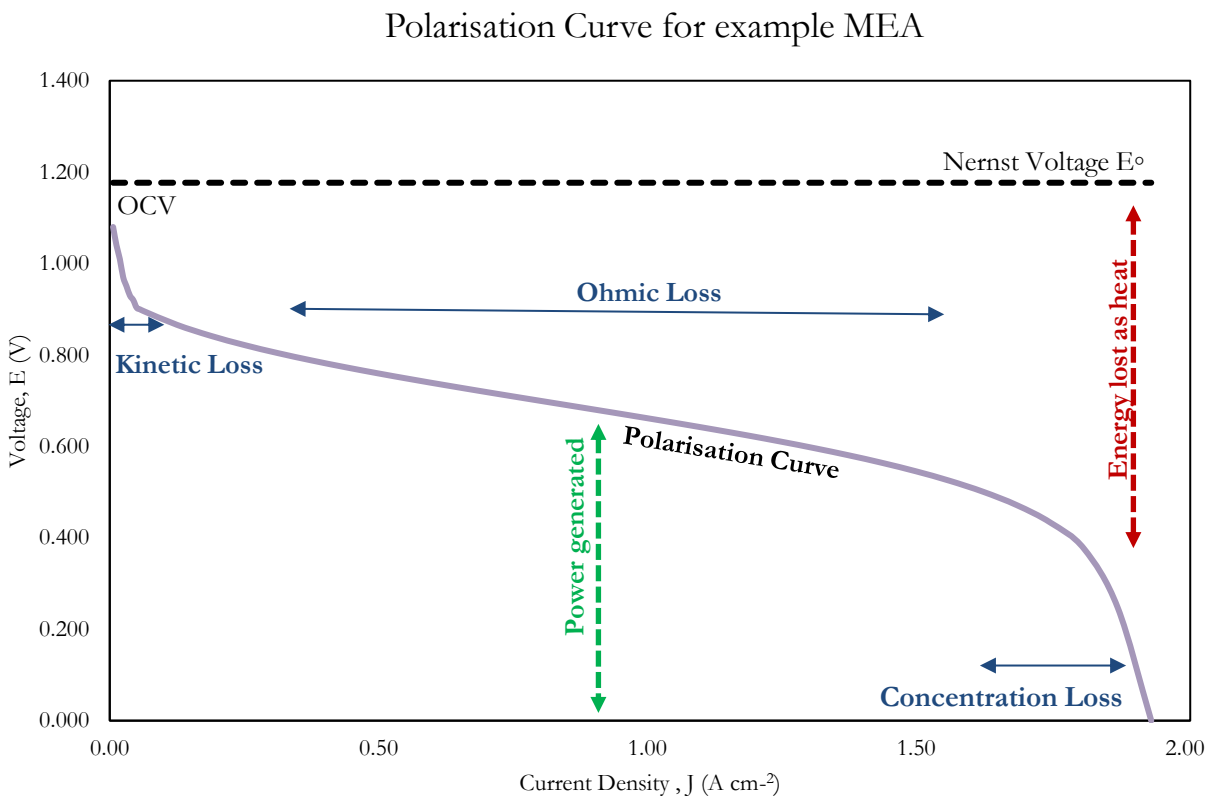

Figure 1.3 shows a characteristic polarisation curve for this PEMFC. The polarisation curve (purple) shows the current density drawn at various voltages. The voltage losses are shown in blue, the energy lost in red, and the power generated in green.

1.1.1 Role of catalysts in PEMFC operation

To decrease kinetic losses, both, the HOR and the ORR require a catalyst within the anode and cathode as shown in figure 1.2. The Sabatier principle, which describes the ideal interaction between a substrate and a catalyst, was used to identify the most efficient catalyst for both using volcano plots[26] (figure 1.4). It plots the ORR activity (y-axis) of a metal against its oxygen binding energy (x-axis) and from this it was identified that Pt, followed by Pd, were the most efficient of all bulk metals[27] for both reactions. The mechanism of action for HOR and ORR using Pt (and Pd) are as follows:

HOR

$$Pt + H_2 \leftrightarrow Pt - H_2 \quad \textbf{(Eq 1.6)},$$

$$Pt - H_2 + Pt \leftrightarrow 2Pt - H \quad \textbf{(Eq 1.7)},$$

$$2Pt - H \leftrightarrow 2\,Pt + 2H^+ + 2e^- \quad \textbf{(Eq 1.8)}.$$

ORR

$$Pt + O_2 \leftrightarrow Pt - O_{2(ads)} \quad \textbf{(Eq 1.9)},$$

$$Pt - O_{2(ads)} + H^+ + e^- \leftrightarrow Pt - O_2H_{(ads)}\ (\textbf{\textit{Rate determining step}}) \quad \textbf{(Eq 1.10)},$$

$$Pt - O_2H_{(ads)} + 3H^+ + 3e^- \leftrightarrow Pt + 2H_2O \quad \textbf{(Eq 1.11)}.$$

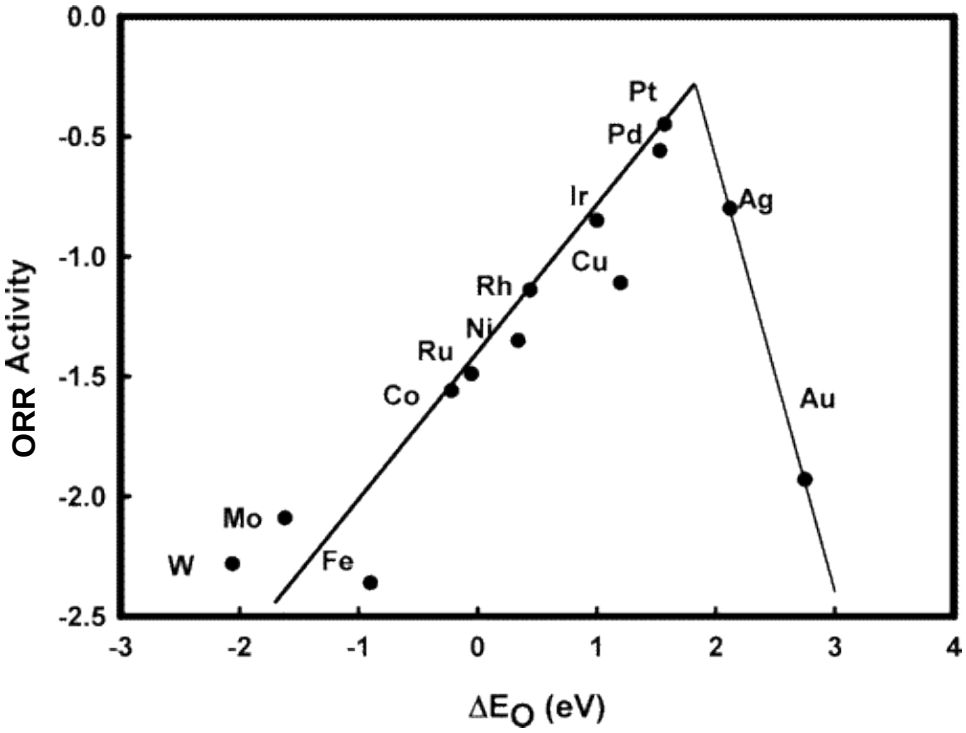

Figure 1.4: Volcano plot showing the trends in ORR activity across various transition metals. The y axis shows ORR activity while the x axis shows the strength of oxygen binding. As seen from the plot, the optimal catalyst will sit at the top of the volcano; Pt and Pd are the two transition metals closest to this ideal catalyst. Image adapted with permission from Norskøv *et al.*[26]

The high prices of platinum group metals (PGM) combined with a major competing global demand for use in automotive catalysts[28] has driven research into decreasing the amount of Pt (loading) whilst maintaining its performance.

The United States Department of Energy (D.O.E.) has identified catalyst benchmarks to be achieved before commercialisation becomes economically feasible (modified version shown in Table 1, D.O.E.).[29,30] The major factors in consideration are the total PGM content used (A,B), the catalytic activity of the catalyst for ORR (C) and the durability of the catalyst (D).

Table 1.1 PEMFC targets adapted from the DOE website. A and B relate to the amount of platinum used in an individual fuel cell. C is a measure of the efficacy of the catalyst while D is a measure of the durability of the total fuel cell (135)

	Characteristic	Units	2015 Status	2020 Targets
A	Platinum group metal total content (both electrodes)	g/kW @ 150 kPa (abs)	0.16	0.125
B	Platinum group metal (PGM) total loading (both electrodes)	mg PGM/cm^2 electrode area	0.13	0.125
C	Mass activity	A/mg PGM @ 900 $mV_{IR\text{-}free}$	>0.5	0.44
D	Loss in initial catalytic activity	% mass activity loss (cycling voltage over 30,000 scans)	66	<40

The PGM content (A,B) used is invariably dependent on the activity (C) and durability (D) of the catalyst.[31] As shown in table 1.1, the PGM loadings (A,B) achieved (for both electrodes) in 2015 were nearing 2020 targets and the activities achieved in 2015 (C) surpassed the 2020 targets. However, at these low loadings of PGM content, durabilities (D) of the catalyst pose a serious problem. Thus, further work on catalysts is required. As shown in the above mechanism (Eq 1.10), the ORR was identified to be the rate determining step of the overall reaction and, as such, research has been focused on improving the kinetics of this reaction.[32] When a novel ORR catalyst is designed and synthesised, its activity is evaluated, prior to testing in a fuel cell, by conducting

ex-situ electrochemical tests. The scientific principles behind these are described in section 2.3 (Chapter 2).

When improving ORR activity of a catalyst, the major *ex-situ* metrics to consider are the electrochemically active surface area (ECSA), the specific activity (SA), the mass activity (MA)[33] and durability.[34] ECSA refers to the surface area of catalyst available for electrochemical activity, SA refers to turnover frequency (i.e., measure of reactions per area of catalyst) and MA is a measure of reactions per mass of catalyst used. These are discussed in depth in section 2.3 and 4.1.

1.1.2 Current standards for PEMFC catalysts

Initially, Pt black was utilised as PEMFC catalysts; these are a fine powder of Pt metal which is mixed with carbon and directly applied as catalysts onto either the GDL or the membranes of PEMFC MEAs.[35] As shown by the SEM image of Pt Black (figure 1.5 A), they tend to be clusters of Pt metal with an average cluster size in the 1 μm range.[140] Since the 2000's however, Pt nanoparticles (NP) seeded on a carbon support (Pt/C) have emerged as the preferred alternative.[36] Nanoparticles provide advantages over bulk materials through improved mass transport, high catalytic surface area, and control over their microenvironment.[37] Figure 1.5B and C show a diagrammatic representation and a TEM image of Pt/C, respectively. As seen here, Pt nanoparticles are embedded into a conductive carbon scaffold.[42]

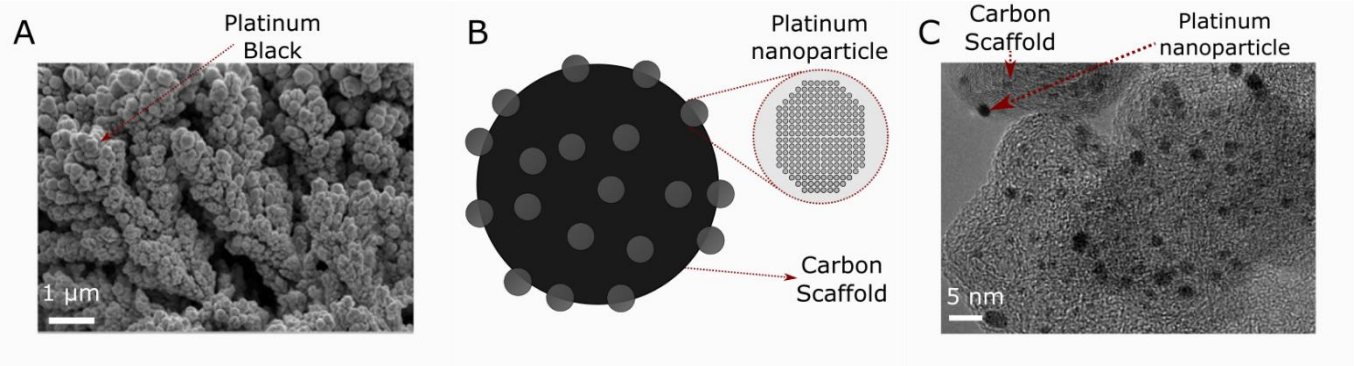

Figure 1.5 (A) Shows an SEM image of platinum black adapted with permission from Stanca *et al.*[140] (B) shows Pt/C drawn schematically. Here the Pt nanoparticles are embedded on a carbon scaffold. This is shown in (C) with a TEM image adapted with permission from Shao *et al.*[42]

These have been traditionally synthesised using a variety of methods including (1) impregnation reduction methods,[38,39] (2) colloidal methods[40] or by (3) physical deposition of metallic platinum directly on the carbon support[41] (discussed further in chapter 5). Their synthesis follows a general schematic where Pt ions, from a precursor, are mixed with a carbon support and a reducing agent at high temperatures; this promotes nanoparticle synthesis onto the conductive supports.[38]

Immediately these catalysts were shown to have much higher activities than Pt black due to increased surface areas (ECSAs), specific activities and consequently mass activities relative to Pt black. Various studies have investigated ORR activity of low index Pt surfaces and showed a preference for ORR activity as (100) << (111) ≤ (110).[25] Furthermore, it has been shown that the mass activity for Pt nanoparticles, between the ranges of 5nm – 1 nm, increases as size decreases till 2.2 nm after which it falls. The specific activity, however, stays relatively the same, from sizes of 5 nm – 3 nm after which the

value decreases sharply; this particle size effect is not fully understood within the field.[42] These catalysts are currently the most mature technology available in market offering significant advantages over platinum black.[43] Variations of (Pt/C) have reported mass activities of around[44–46] 0.2 A mg^{-1}_{PGM} which is less than half of the required D.O.E. target[29] (at 0.44 A mg^{-1}_{PGM}, table 1.1). Further optimisation is also limited due to the inability to further tailor activity or durability.[25] Durabilities are often increased by manipulating catalyst-scaffold interactions as opposed to modifying the catalyst itself.[30]

As such, this catalyst is not commercially viable in the long-term as Pt prices are expected to increase alongside demand.[43] Thus, further research has investigated other Pt based nanostructures with improved activities while lowering the total amount of Pt used.[32] These include nanoalloys[47], core-shells[48] and shape-controlled nanostructures.[49] Some of these have even reached commercialisation such as the Pt/Co nanoalloys used as a catalyst in Toyota's fuel cell car the Mirai.[50] Such metal 'thrifting' is often used in automotive catalysts[51] as the PGM are often substitutable, but the degree of success may be application specific. Many groups have researched non-PGM ORR catalysts with reasonable success,[52,53] although none have become economically viable.[43]

Thus, using (Pt/C) as a benchmark, further research has focused on other Pt based nanomaterials.[51] While these are reported to show higher activities relative to Pt/C, thereby decreasing the Pt amounts required, these improvements often come at the expense of catalyst durabilities.[43]

1.1.3 PEMFC Catalysts in Development

PEMFC nano-catalysts in development mainly take advantage of the variety of nanotechnologies available. These have resulted in nanostructures of all dimensionalities i.e., zero dimensions (0D), one dimension (1D) and two dimensions (2D).[54] These are classified based on the number of dimensions that measure in the nanometre range. As noted earlier, non-precious metal catalysts for ORR have not achieved comparable activities and durabilities to Pt/C and as such will not be discussed here.[55, 43]

1.1.3.1 PEMFC Nanoalloys

Pt/C are 0D nanostructures and in these, all dimensions measure in the nanometre range. As noted earlier, standard Pt/C nanoparticles do not reach the required benchmarks set by the D.O.E.[30] As such, immediate research focused on alloying Pt/C with other metals to increase activities. These studies have included alloying with a variety of metals including Co,[56] Ni,[57] Fe,[58] Cu,[59] Pd,[60] and Ag[61] and these structures have, overall, shown better mass activities and similar or better durabilities than Pt/C. The transition metal used makes a significant difference with Co, Ni and Fe showing superior activities.[47] Furthermore, transition metal composition relative to Pt can affect the activity enhancement; for example, PtCo/C has an optimal activity at metal atomic ratio of 3:1 (Pt:Co) whereas for PtNi/C it was 1:1.[62] Research into ternary[63] quaternary[64] and even quinary[65] alloys (that utilised Pt, Ru, Cu, Os and Ir) have been studied in recent years, giving increased mass activities relative to Pt/C.[51]

This improved catalytic activity is often credited to weakened adsorption of O species to the catalyst.[25] The surface layer of such alloys is often composed of nearly pure Pt[25] and this can be achieved through various pre and post-treatment methods such as acid-leaching,[66] thermal treatment,[67] and UHV annealing.[68] Figure 1.6 shows schematically the formation of a "Pt-rich skin" (adapted from Wang *et al.*).[142] Here Pt (grey) is alloyed with Ni (pink) as seen in figure 1.6A (3D view) and B (cross section). On acid leaching the Pt and Ni atoms rearrange to a higher proportion of Pt atoms on the surface (figure 1.6 C,D). After a final heat treatment, the outer surface of the nanoparticle is composed entirely of a thin platinum rich skin indicated by black arrows (figure 1.6 E,F).

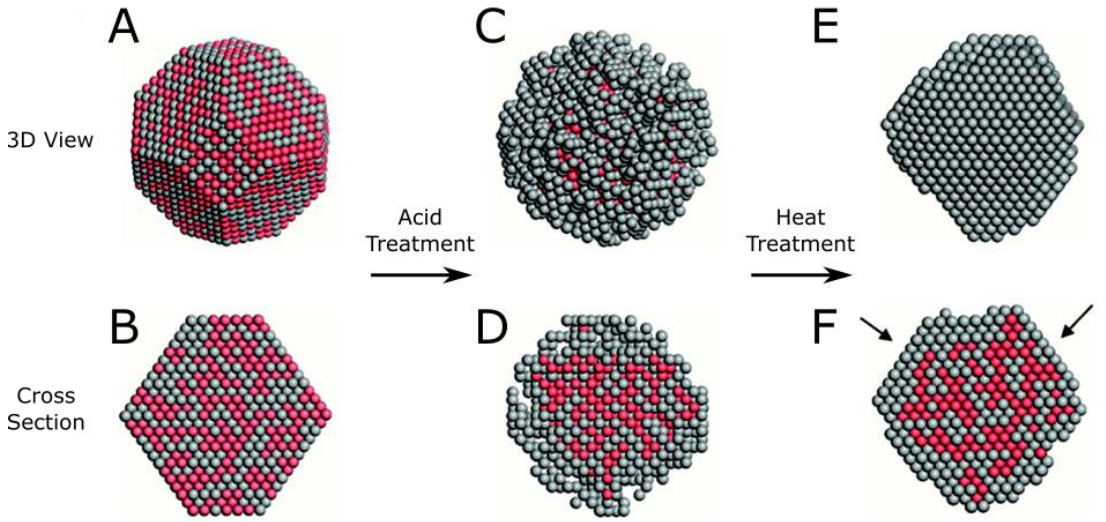

Figure 1.6 (A, B) shows a nanoalloy with Pt atoms(grey) and Ni atoms (pink) with A showing a 3D view of the nanoparticle and B showing a cross-section. (C,D) shows the same nanoparticle after acid leaching with C showing a 3D view of the nanoparticle and D showing a cross-section. (E,F) show the nanoparticle after high temperature annealing with E showing a 3D view of the nanoparticle and F showing a cross-section. This image shows the formation of the Pt-rich skin with the black arrows indicating this on F. This image was adapted with permission from Wang *et al.* (142)

The structural and electronic effects of the secondary metals affect the Pt surface layer through either ligand or strain effects.[69] Ligand effects are brought about by subsurface alloying (i.e. secondary metal atoms in the second atomic layer), which modifies the electronic structure of surface Pt atoms and thus weakens binding of oxygen containing intermediates.[69] Strain effects occur when the Pt surface layer is compressed laterally which brings about a downshift in the d-band centre away from the fermi level[70] and this effect is observed when the Pt surface layer is placed over a core with lattice parameters smaller than Pt.[69] In practice, deconvoluting the ligand and strain effects is difficult and often the enhanced activity is due to an interplay of the two effects.[69] Density function theory (DFT)[70] and experimental[71] studies have confirmed the enhanced catalytic activity due to this Pt-rich skin. Furthermore, it also increases durability of the catalyst,[72] and this effect has been tested *in-situ.*[73] The technology has reached relative maturity with PtCo/C catalysts being used in the Toyota Mirai.[74]

1.1.3.2 Core-shell structures

Pt core shell structures have been heavily researched recently with multiple studies showing excellent mass activities and durabilities.[75–77] The primary concept of core-shell structures is an extension of the Pt-rich skin of Pt nano-alloys. Here the ORR active Pt is only located on the surface[76] with a less expensive core. The nanoparticle core is often a less expensive metal including Pd,[77] Ru[78] and Re.[79] These can be synthesised through a variety of methods including chemical reduction methods,[80] electrochemical methods[81] and dealloying methods,[82] among others.

Figure 1.7 (adapted from Taufany *et al.*)[143] shows the synthesis of a core shell nanoparticle with a Pt skin and a Pd core.[143] First, Pd NPs are synthesised after which a Cu monolayer is reduced onto them (using H_2 and $CuCl_2$). The Cu monolayer is then replaced by Pt to finally form a Pt shell on a Pd core. This is shown in the adjoining TEM image on figure 1.7.[143]

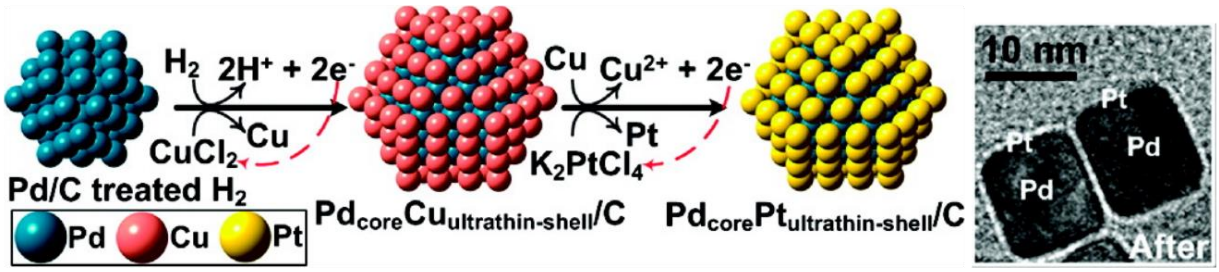

Figure 1.7 shows schematically the synthesis of a Pt shell on a Pd core. The Pd NPs are synthesised first after which a Cu monolayer is reduced onto it. The Cu is then replaced with a Pt to form a Pt shell on a Pd core. This image was adapted with permission from Taufany *et al.*[143]

In doing so, Pt utilisation (i.e., amount of Pt directly involved in ORR activity relative to total amount of Pt) is maximised and, thus, this improves ECSAs and mass activities.[43] Furthermore, they have been shown to have better durabilities for a variety of different reasons. Some have shown to have inherent "self-healing" abilities, whereby the inner core metal dissolution during potential cycling (where applied voltage is cycled through a pre-set range) induces a contraction in the Pt shell.[83] This contraction affords the catalyst a higher specific activity and further stabilises the catalyst.[83] Work has been done with a variety of core metals, but a majority have focused on using a Pd or Au core. The choice of core does afford a level of tunability on the ORR activity of the shell and this has been shown *ex-situ*.[84] However, it is important to note that these catalysts have not been tested extensively *in-situ*.

1.1.3.3 Shape controlled nanoparticles (Polyhedrons, Nanowires and Nanoframes)

While core-shell structures increase mass activities by increasing both ECSAs and Pt utilisation, shape-controlled nanoparticles aim to increase specific activities to achieve higher mass activities.[49] This is achieved by attempting to recreate the ideal crystal structure features identified by single crystal studies and have resulted in a variety of different nanostructures. These can be broadly classified into polyhedrons[49] nanowires[86] and nanoframes[85] and these have shown good activities relative to 0.2 A mg^{-1}_{PGM} for Pt/C (see above).

PtNi alloys of all three have shown extremely high mass activities. A 9 nm $Pt_{2.5}Ni$ octahedron (figure 1.8 A) showed a mass activity of 3.3 A mg^{-1}_{PGM} with the high activity attributed to the clean and preserved (111) surfaces resulting in a high specific activity.[141] Similarly, high mass activities of 5.7 A mg^{-1}_{PGM} were seen with the Pt_3Ni nanoframes (figure 1.8B)[144] while nanowires of Pt with NiO core (figure 1.8C)[86] have shown the best mass activities at 13.6 A mg^{-1}_{PGM}. Development of shape-controlled nanoparticles is still in its infancy and while *ex-situ* tests are promising, *in-situ* tests are still being conducted.

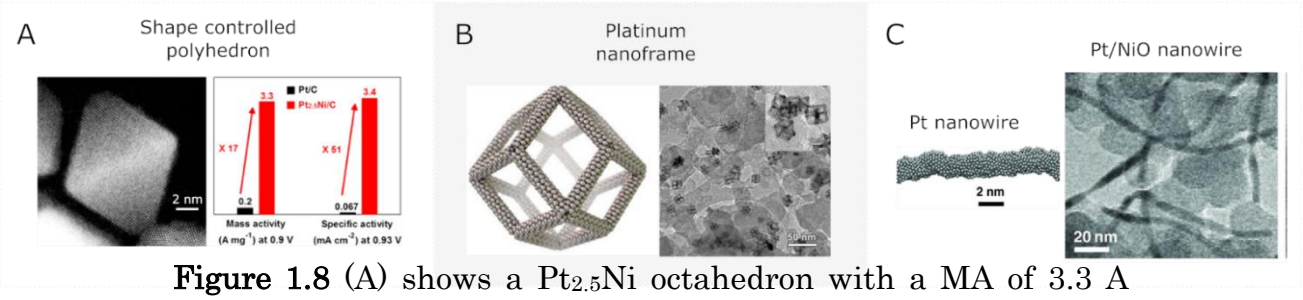

Figure 1.8 (A) shows a $Pt_{2.5}Ni$ octahedron with a MA of 3.3 A mg^{-1}_{PGM}. This image was adapted from Choi *et al.*[141] (B) shows a Pt_3Ni nanoframe with a MA of 5.7 A mg^{-1}_{PGM}. This image was adapted from Chen *et al.*[144] (C) shows a Pt nanowire (left) and Pt nanowire with a NiO core (right) with a MA of 13.6 A mg^{-1}_{PGM}. This image was adapted with permission from Li *et al.*[86]

1.2 Biosynthesised nanoparticles

All previously described nanostructures utilise high temperatures and toxic chemicals for synthesis. Recently biosynthesis of nanoparticles (bio-NPs) has emerged as an attractive and 'eco-friendly' alternative to conventional chemical synthesis.[88,89] This approach entails the use of biological materials to promote nanoparticle synthesis from aqueous solutions of metal salts. The biomaterials used range from plants,[90] fungi,[91] yeasts,[92] bacteria[93] and also biomolecules[94] obtained from these. Using various bio-scaffolds, a variety of nanostructures have been produced including shape-controlled polyhedrons,[87] core-shells[95] and nanowires.[96] Nanoparticles produced in this manner have proven applications as energy catalysts[97] including for use in fuel cells.[98–100] The majority of work in this field has focused on palladium,[97,103,104] gold[101] and silver[102] nanoparticles with size and shape control. However, biosynthesis of Pt–NPs (and bi-metallic NPs) has been achieved using a variety of bacteria (*E. coli* and *D. desulfuricans*).[97] This was achieved by reducing metal salts of platinum to metal NPs by using a variety of electron donors (H_2, Formate etc.).[125]

1.2.1 Bio-NPs synthesised by bacteria.

Bacteria are considered an ideal route for biosynthesis of nanoparticles due to their ease of handling, high growth rates and ease of genetic manipulation.[105] Furthermore, 'second life' bacteria (produced as wastes from other primary processes) have previously been used in bio-NP synthesis; *E. coli* used in biohydrogen production have been used for Pd-NP synthesis.[131] Finally, the NP synthesis conditions use environmentally friendly chemicals in ambient physiochemical conditions that allow for easy scaling up to an industrial level.[106]

Bacteria can be found in extreme environments[107] including those with heavy metal ion concentrations.[108] Some have consequently evolved natural defences against these stress conditions through metal efflux pumps and systems,[109] inactivation and complexation of metals[110] and, crucially, intracellular sequestration[111] and extracellular precipitation[112] of metals. While most of these are assumed to have been evolved as defence mechanisms, certain strains have utilised metal sequestration to their advantage. Magnetotactic bacteria can synthesise magnetic particles to orient themselves along the earth's magnetic field lines and it is hypothesised that they use these particles for navigation.[113] These mechanisms can be exploited for eco-friendly nanoparticle synthesis; they are either classified into extracellular and intracellular mechanisms.[105] Regardless of localisation, the bacterial matrix is thought to act as a scaffold for metal ion adsorption, promoting nanoparticle reduction and capping through bio-catalysis following formation of 'seeds' at the biomatrix nucleation sites.[114]

A wide variety of bacterial strains has been used to synthesise nanoparticles. Beveridge and Murray were one of the first to show metal deposition in bacteria using, a Gram-positive strain, *B. subtilis* and gold.[115] Since then, a wide variety of Gram-positive and Gram-negative bacterial strains have shown to synthesise NPs[93] of various metals. The Gram stain is a useful classification of bacteria that is based around the structure of the cell envelope. As shown in figure 1.9 both have a peptidoglycan cell wall and a cellular membrane composed of phospholipids. Gram-positive bacteria have a relatively thick cell wall (20-80nm) surrounding the cellular membrane while Gram-negative bacteria have a relatively thin one <10nm. [286] Gram-negative bacteria, however, also possess

a secondary cellular membrane surrounding the cell wall. The space between the two membranes is known as the periplasmic space.[286]

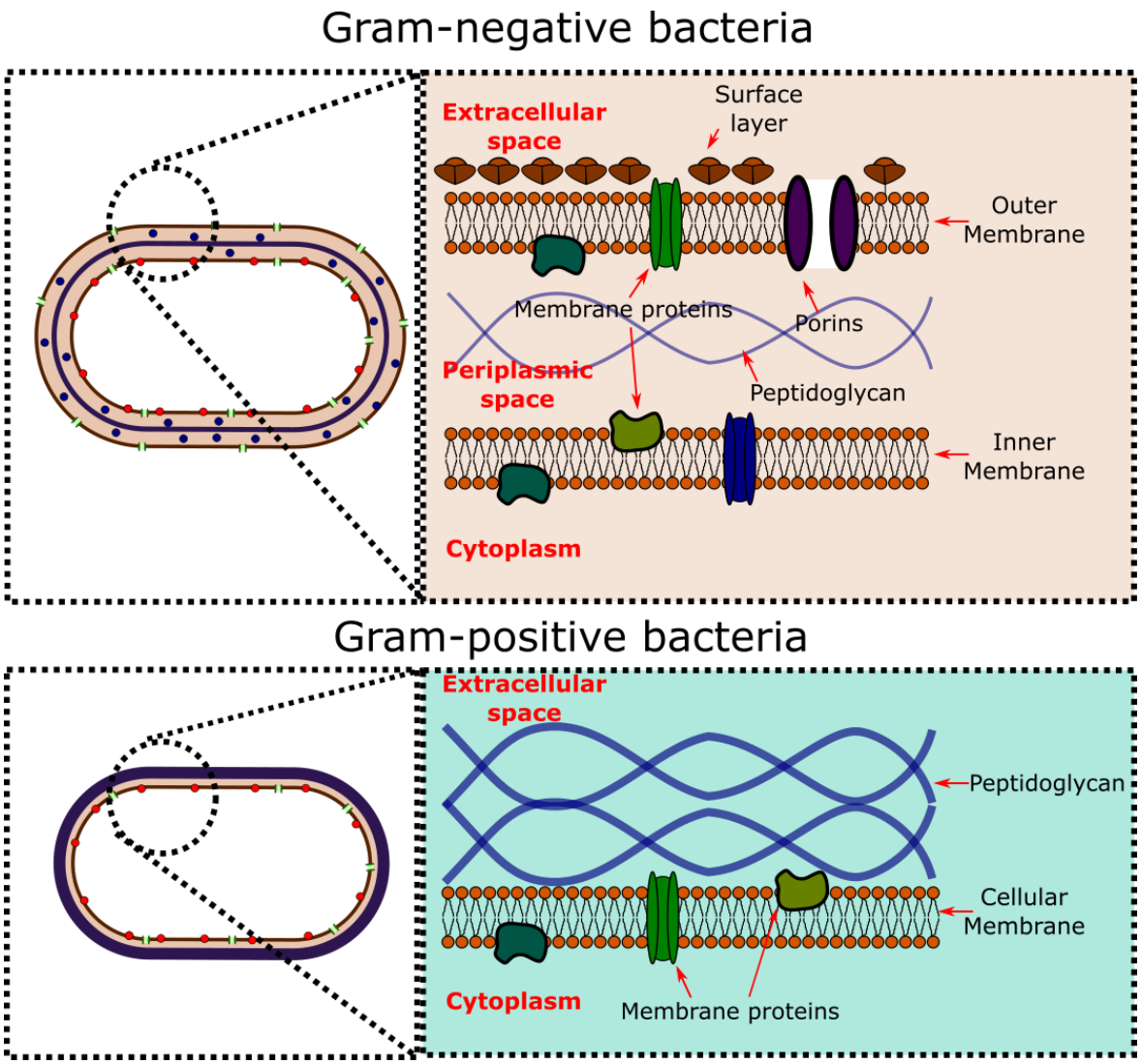

Figure 1.9: This shows the difference in the cellular envelope between Gram-negative and Gram-positive bacteria. As seen Gram-negative bacteria have two cellular membranes (an inner one and an outer one) with a periplasmic space in between. There also exists a relatively thin cell well made of peptidoglycans in the cell wall. Gram-positive bacteria, however, have only one cellular membrane with a thick peptidoglycan cell wall surrounding it.

The choice of bacteria can affect nanoparticle synthesis. Not only can broad classifications such as Gram-positive or negative bacteria affect nanoparticle synthesis, differences between specific strains within a species can impact the

resultant nanoparticles. Cell free supernatants of various *Pseudomonas* species (*P. antarctica, P. proteolytica and P. meridiana*) all showed extracellular synthesis of Ag NPs but *P. antarctica* supernatant synthesised larger NPs on average with an average size of 12 nm relative to the 6.9 nm and 6.2 nm of the other strains.[116] Mutants of the same strain can have an effect too; when Deplanche *et al.*, researched Pd-NP synthesis by bacterial *E. coli.* hydrogenase mutants, it was shown that Pd-NP synthesis occurred, but with differing intracellular localisations and was mediated by the hydrogenase expressed (further expanded in section 1.2.2, see below); while native cells showed periplasmic Pd-NPs, deletion of the periplasmic hydrogenase showed Pd-NPs were synthesised bound to the cytoplasmic side of the inner membrane.[117]

A wide variety of metals have been investigated for biosynthesis of nanoparticles. These include metal salts that are reduced to zero valent metal nanoparticles such as Au,[118] Ag,[119] Cu,[120] Pt,[122] Pd,[123] and metal salts reduced to oxides and sulfides of metals such as Fe reduced to Fe_2O_3 and Fe_3S_4.[121] It was shown that this reduction was primarily biologically mediated, and that the choice of metal had an impact on nanoparticle synthesis. When a novel strain of *Stenotrophomonas* was used to synthesise Au and Ag nanoparticles, AgNPs sized at a higher range (40–60nm) relative to AuNPs (10–50nm).[124]

1.2.2 BioNPs as FC catalysts.

Various strains have been shown to synthesise Pt and Pd NPs including *Shewanella*,[99] *Desulfovibrio*,[98] and *E. coli*.[125] Their catalytic efficacy can be application specific; for example, *D. desulfuricans*-Pd[128] had comparable activity

to commercial catalysts for the Heck reaction while it performed poorly in fuel cells.[98] Nevertheless, various studies have attempted the use of bio-Pt and bio-Pd as FC catalysts and shown reasonable success as anodic catalysts in fuel cells when *in situ*.[97, 99, 100] Yong *et al.*, originated this research in 2007 by synthesizing Pt and Pd nanoparticles using *D. desulfuricans*; *in-situ* fuel cell testing showed proof of concept but the FC had poor performance.[98] In a more recent attempt, Xiong *et al.*, produced Pd nanoparticles supported on *Shewanella* cells as ORR catalysts. The *Shewanella*-Pd was subjected to alkaline "activation" before sintering at 420 °C after which it showed moderate to low ORR activity.[99] Arguably the most successful attempt was by Liu. *et al.*, in 2016, where *Shewanella* cells were used to manufacture a highly dispersed PdAu nanoalloy. The resultant catalyst was then mixed with graphene oxide (GO) sheets before the entire system was hydrothermally treated. This treatment resulted in reduction of GO to rGO, carbonisation of the entire bacterial mass and conversion of the separate Pd and Au nanoparticles into a PdAu nanoalloy. This catalyst proved to be highly effective for ethanol and methanol electrooxidation but was not tested for ORR catalysis.[100] Williams showed the most promise for ORR activity with *E. coli*-Pt that had been extensively cleaned using NaOH; the catalyst showed cathodic electrochemical activity *ex-situ* comparable to commercial Pt/C.[125]

In engineering bio-NPs as FC catalysts, a key factor to consider is the microenvironment in which the NP sits. As shown (figure 1.10), the ORR occurs at sites where the electrolyte, the gaseous oxidant and the catalyst supported on a conductive material interact, known as the triple phase boundary (TPB).[129]

Here, the oxygen molecules (shown in blue) meet the electrons from the conductive support and H^+ ions from the electrolyte to form water. Thus, it is essential to recreate the TPB using bio-NPs and this can prove challenging. Bacteria are inherently non-conductive, and the nanoparticles synthesised are often localised both on the cell surface and intracellularly[127] and thus, many NPs are in poor contact with both electrolyte and conductive support. The various strategies previously used (high temperature sintering, NaOH cleaning etc.) to alleviate these problems[99, 100, 126] did not result in materials that are directly applicable as catalysts. Furthermore, these methods utilised destructive high temperatures (sintering) /aggressive chemical treatments that offset the advantages offered by the biosynthetic process.

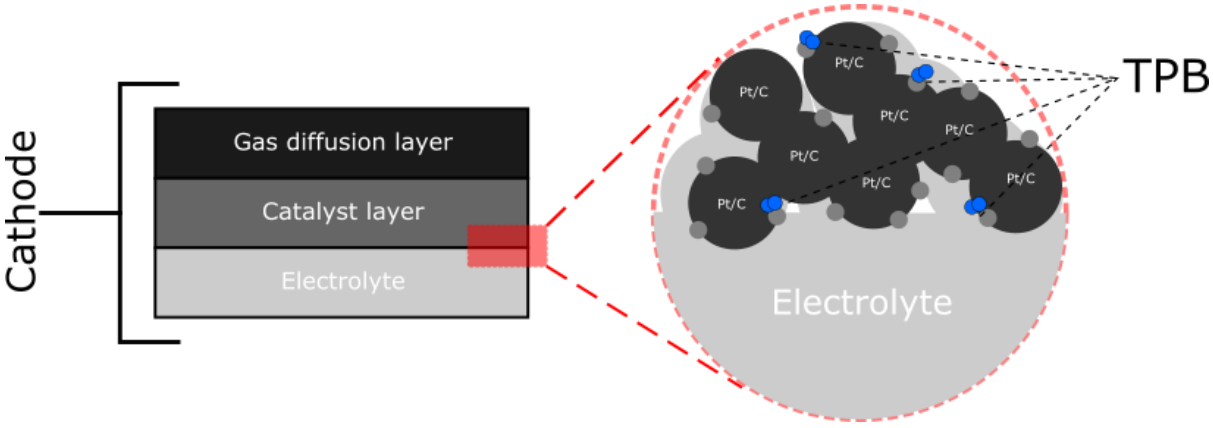

Figure 1.10: This shows the Triple Phase Boundary (TPB) where the catalytic reactions occur in a fuel cell. On the left is a cross section of the Membrane Electrode Assembly (MEA) that includes the gas diffusion layer (GDL), the Catalyst Layer (CL) and the electrolyte. The right shows a microscopic depiction of the CL and electrolyte interface. Catalytic reactions take place where the electrolyte, the Pt, and conductive support all meet the reactant (shown in blue).

1.2.3 *E. coli* synthesised NPs.

An alternative strategy towards sustainable development would use waste *E. coli* bacteria left over from other primary industrial processes, valorising waste into high value material while mitigating waste disposal costs[97] and potentially offsetting the environmental impacts in processing the catalyst. Such 'second life' use of *E. coli* bacteria to make bio-NP catalyst was shown in chemical catalysis[130] while Orozco *et al.*, (2010)[131] showed use of *E. coli* left over from a biohydrogen process to make a fuel cell catalyst to convert the biogenic H_2 (which is free of the catalyst poisons that require extensive purification of petrochemically-derived H_2) into power.

Indeed, *E. coli* is widely used industrially (for e.g., pharmaceuticals production) and hence is potentially available as a low-cost resource.[132] Furthermore, it is easily manipulated genetically, and this route might limit the need for further processing (see above) of *E. coli*-NP catalyst. Finally, *E. coli* was shown to synthesise various metal nanoparticles including platinum and palladium from solutions of metal salts of the same (*E. coli*-Pt and *E. coli*-Pd respectively).[125,126] Thus, it is timely and necessary to research *E. coli* synthesised NPs as PEMFC catalysts.

While the exact mechanism of *E. coli*-Pt and *E. coli*-Pd synthesis remains elusive, various studies using multiple strains have helped build a hypothesis. *E. coli*-Pt and *E. coli*-Pd synthesis seem to have similar mechanisms of reduction. They are synthesised when anaerobically pre-grown *E. coli* is challenged with metal salt solutions (here K_2PtCl_6 and Na_2PdCl_4 are used and the metal atoms are

complexed with Cl atoms as $[PtCl6]^{2-}$ and $[PdCl_4]^{2-}$) at low pH (~pH 2.0) and reduced using an electron donor (like H_2). Their syntheses seem to follow a similar three step process with (1) an initial influx and sorption, (2) enzyme-dependent metal reduction and (3) an autocatalytic reduction stage[133] (see below).

The initial sorption of metal ions onto the cell surface is thought to occur via physicochemical mechanisms.[125] These include electrostatic interactions between metal ions and functional groups on the cell surface, ion exchange, chelation and passive diffusion through the cell membranes. As the cellular surface and the extracellular polymeric substances of *E. coli* are polyanionic, a low pH is required to protonate these anions and thus, allow approach of complexed metal anions for sorption. The influx of $[PtCl6]^{2-}$ and $[PdCl_4]^{2-}$ (hereafter referred to as Pt (IV) and Pd (II) respectively) are thought to occur differently. It is important to note that this entire process places significant stress on the cells. Low levels of pH (~4–5)[146] and high toxic metal concentrations[145] were both shown to upregulate and express various genes to combat these stresses. However, given the lower pH and higher metal ion concentration for metal reduction it is unlikely that *E. coli* can initiate a meaningful response to these stressors before cell death. Further studies are required to test this hypothesis.

Once sorption is complete both metals undergo enzyme dependent metal reduction, but the mechanism of this process differs for each. Once the metal is

reduced to nanoparticle seeds, they can autocatalyze further metal reduction. The hypothetical mechanisms for both are described below.

1.2.3.1 *E. coli*-Pd

Figure 1.11A and B shows TEM images of an empty *E. coli* cell(A) and *E. coli*-Pd cell (B), with a majority of Pd nanoparticles seen in the periplasmic space and cell surface (figure 1.11B).[117] Various studies taken together can hypothesise a mechanism for this *E. coli*-Pd reduction.

Firstly, it is expected that the negatively charged Pd (II) ions will interact with protonated groups (due to low pH) on the biomass.[134] Deplanche *et al.*, hypothesised that post-biosorption, the Pd ions are internalised through Ni transporter proteins, where the Pd (II) ions are mistaken for Ni(II) ions by the cellular machinery.[147] There is precedence for the erroneous internalisation of transition metals by bacterial cells.[148] A variety of strains have developed resistances to toxic heavy metals using efflux ion pumps after these metals have been internalised.[148] The preference for such a mechanism, as opposed to a more specific metal ion uptake pump, could be attributed to the lower metabolic costs in activating efflux pumps only when necessary.[148]

Pd (II) ions are hypothesised to be internalised via Ni (II) ion channels, in large part due to the localisation of the Pd nanoparticles post reduction.[126,147] Pd-NP synthesis by *D. desulfuricans* was shown to be enzymatically mediated by Lloyd *et al.* with the enzyme hydrogenase implicated as a major contributor; [148] when cells were treated with Cu^{2+} (an inhibitor of periplasmic hydrogenase), Pd-NP reduction ceased.[148] Hydrogenases are a class of metalloenzymes that catalyse

the oxidation of hydrogen to protons and electrons or the reverse reaction. They are divided into subclasses ([NiFe], [FeFe] and [Fe]) based on the metals found in their active sites.[149] Various studies since, have dissected the roles of these hydrogenases in Pd NP reduction.[117, 135]

Mikheenko *et al.*, first studied the role of hydrogenases in *Desulfovibrio. Fructosivorans*.[135] This strain contains membrane bound hydrogenases facing both the periplasm and the cytoplasm. Figure 1.11D, E and F shows *D. fructosivorans*-Pd wild type, *D. fructosivorans*-Pd lacking the cytoplasmic facing hydrogenase and *D. fructosivorans*-Pd lacking the periplasmic facing hydrogenase, respectively. As seen, the mutant lacking the cytoplasmic periplasmic facing hydrogenases showed Pd synthesis within the periplasmic space (figure 1.11E) while the mutant lacking the periplasmic facing hydrogenase synthesised NP primarily on the cytoplasmic side of the membrane. Deplanche *et al.*, expanded on this and investigated the role of 3 membrane bound [NiFe] hydrogenases (two periplasmic facing, one cytoplasm facing) in *E. coli*-Pd synthesis.[117] Mutants of the various hydrogenases showed a similar Pd patterning on the periplasm and/or the cytoplasm dependent on the expressed hydrogenase.[117] Furthermore, a mutant that deprived the cell of all hydrogenase activity (figure 1.11C) showed a linear rate of Pd (II) reduction similar to chemically reduced Pd (II), thus, further confirming the role of hydrogenases.[117] It is suggested that the Ni (II) transport is heavily linked with the hydrogenase system.[150] HypAB, the complex that mediates Ni insertion to hydrogenases[151] has been suggested to control Ni trafficking.[152] Thus, given the importance of hydrogenases in Pd-NP patterning, it could be hypothesised that

Pd ion internalisation is mediated via the Ni transport system where the transport proteins mistakenly intakes Pd ions and traffic them towards hydrogenase enzymes but are unable to substitute functionally for Ni. Thus, the cell would perceive Ni(II)-starvation under excess Pd (II) and maintain an upregulated Ni(II) accumulation system alongside metal efflux to avoid toxicity. It is also likely that Pd(II) ion internalisation could occur via porins. These allow slow passive uptake of hydrophilic molecules[287] and could allow internalisation of Pd(II) ions.

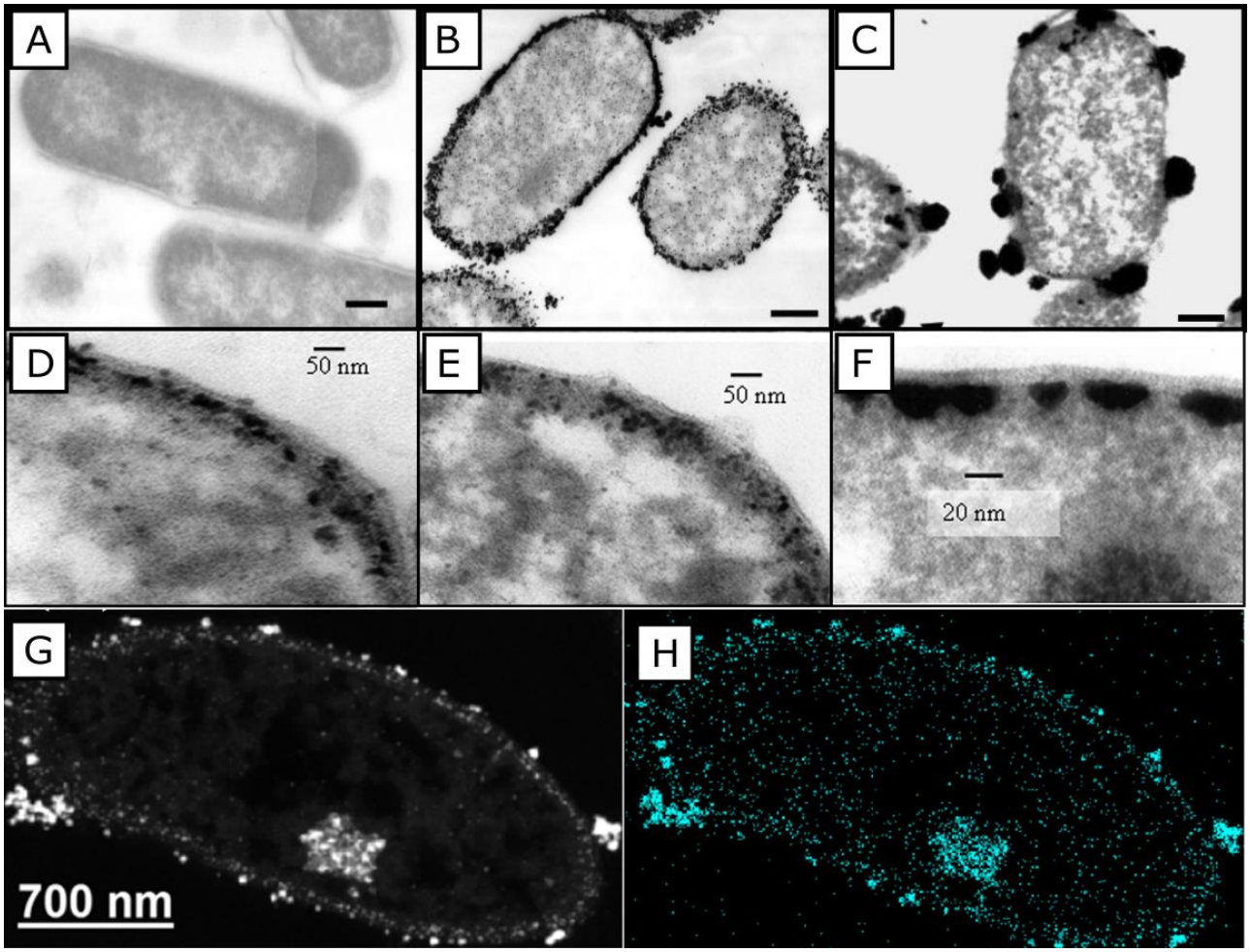

Figure 1.11: (A,B,C) are TEM images where (A) shows an empty *E. coli* cell, (B) shows *E. coli*-Pd wild type and (C) shows *E. coli*-Pd synthesised using mutant strain FTD 150 (lacking all hydrogenases). Scale bars shown in black is 200 nm. These images are adapted with permission from Deplanche *et al.*[117] (D,E,F) are TEM images where (D) shows a *D. fructosivorans*-Pd wild type cell, (E) shows a *D. fructosivorans*-Pd cell lacking the cytoplasmic hydrogenase and (F) shows a *D. fructosivorans*-Pd cell lacking the periplasmic hydrogenase. Scale bars are shown in black. These images are adapted with permission from Mikheenko *et al.*[135](G,H) are images taken using a STEM where (G) is a STEM-HAADF image of *D. desulfuricans*-Pd and (H) is an elemental map of Pd for the same image. Here the Pd is also seen strongly associated with the nuclear mass of the cell. Scale bar is shown in white. These images are adapted with permission from Omajali *et al.*[126]

Once Pd ions have been trafficked towards hydrogenases, it is hypothesised that the hydrogenases enzymatically reduce Pd (II) ions to form Pd (0) "seeds" by oxidising reducing agents and transferring electrons to Pd (II) ions.[117,135] Different reducing agents can be utilised by hydrogenase enzymes; *D. desulfuricans* was shown to synthesise Pd nanoparticles using formate and H_2.[136] It is also expected that the enzymes might channel endogenous electrons from the biomass to Pd (II) ions; it is likely that a mixture of the two mechanisms occur. Once a pattern of seeds is synthesised, they then auto-catalyse further reduction of Pd (II) ions onto their surface under the presence of a reducing agent.[136] Thus, live cells are required only for patterning and nucleation.

Recently, a study by Torgeman disputed this hypothesis.[156] When a novel screening assay that dissected the roles of various transporter genes in Pd (II) uptake was conducted, the genes associated with Cu, Fe, Mo, Co and Mg efflux played a significant role while the Ni transport system did not.[156] Furthermore, the study could not demonstrate a hydrogenase-driven mechanism for Pd-NP synthesis when an *E. coli* mutant deleting all hydrogenases was used. However, this was conducted at a low Pd:biomass (w/w) dry wt ratio (3–7%);[156] as such, it could be argued that this hypothesised mechanism is relevant for the higher metal loadings used in previous studies[117,135] (>10% w/w). Furthermore, previous work by Omajali *et al.*, confirmed the presence of Pd-NPs within the cellular cytoplasm of *D. desulfuricans* and *B. benzeovorans,* implying a non-hydrogenase mediated Pd synthesis. Figure 1.11G and 1.11F show a HAADF STEM image of *D. desulfuricans*-Pd (20%) and the Pd elemental mapping,

respectively.[126] Here Pd nanoparticles are seen both in the periplasmic space and intracellularly.

Taken together, these results suggest that, at higher loadings the hydrogenase enzymes have a degree of control over Pd-NP synthesis, but this does not preclude Pd-NP synthesis through other mechanisms whose effects are still significant.[156] For example, Foulkes *et al.*, showed that *E. coli*-Pd could be synthesised under aerobic conditions through the action of a molybdoprotein-mediated mechanism. [154] Furthermore, at low loadings of metal (<10% w/w), porins could allow easy internalisation of $[PdCl_4]^{2-}$ ions as they allow slow passive uptake of hydrophilic molecules.[287] It is likely that at higher loadings the hydrogenase mechanism works in conjunction with porins to internalise Pd.

A simplified version of the hydrogenase mechanism is shown diagrammatically in figure 1.12. Here, the low pH of the solution allows polyanionic $[PdCl_4]^{2-}$ ions to adsorb onto the protonated surface layer of the bacterial cell. The Pd(II) ions are transferred into the bacterial cell passively through porins or through a Ni (or other metal) transport system. Then, they are trafficked to membrane bound hydrogenase enzymes (or other metalloenzymes like cytochromes) in the periplasm (light green) and the cytoplasm (blue). Here they undergo enzyme mediated reduction to form seeds (black) where (in this example) their patterning is dependent on hydrogenase expression. This provides a point of genetic control for engineering Pd-NP synthesis. Finally, these Pd (0) seeds auto catalyse reduction of more Pd (II) to form larger Pd-NPs.

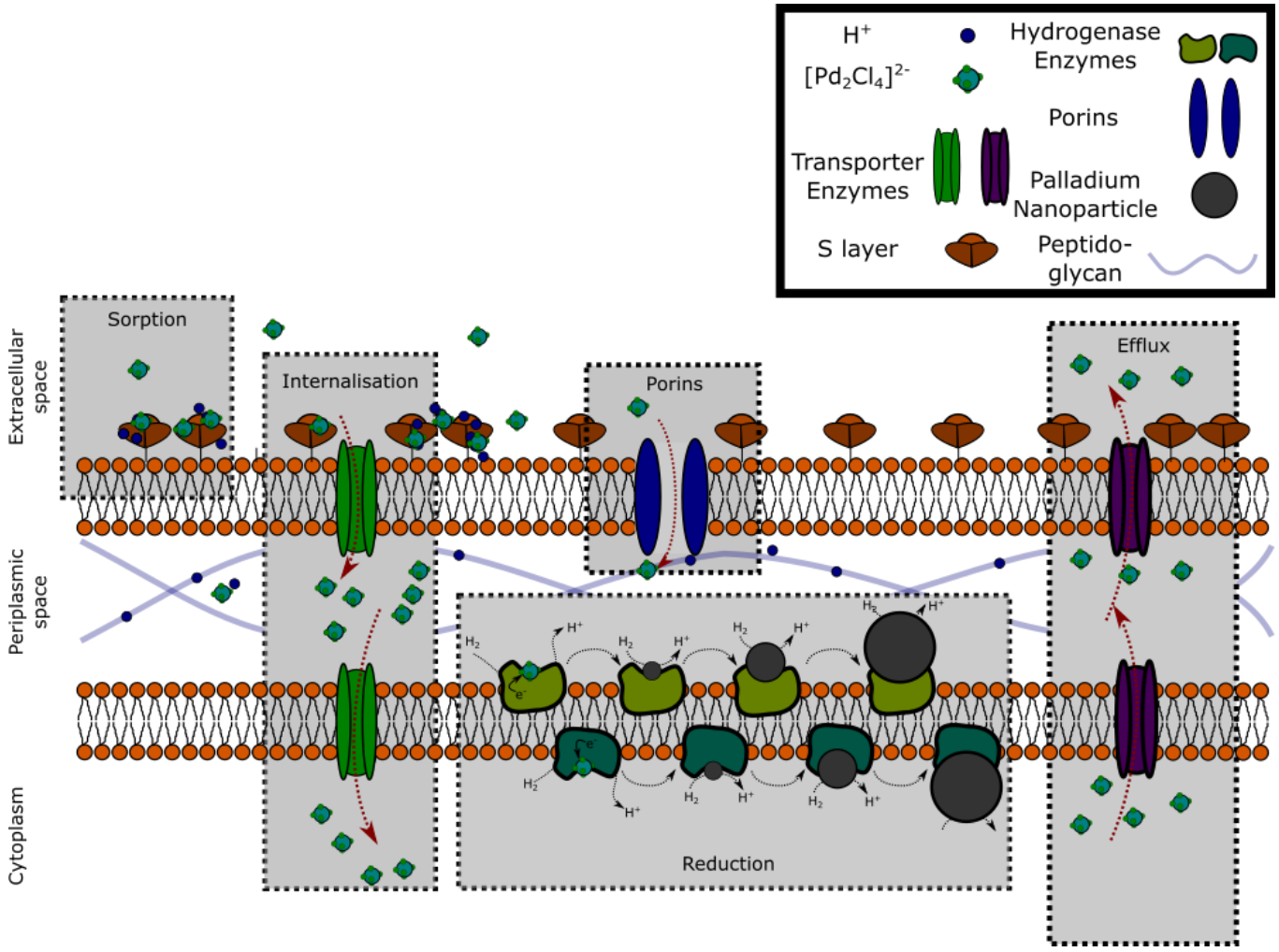

Figure 1.12: A hypothesised mechanism for *E. coli* mediated Pd-NP synthesis. $[PdCl_4]^{2-}$ or Pd (II) ions are shown on the left, where sorption takes place on protonated (blue dots) cell surface. It is hypothesised that they enter the cell through a Ni transporter (green). Once inside they interact with the hydrogenases in the periplasm (light green) and cytoplasm (blue). Pd (II) gets reduced to Pd (0) through the enzymatic action of the hydrogenase enzymes under H_2. These initial Pd (0) seeds are then auto-catalysed under H_2 to form bigger Pd nanoparticles. This occurs in the cytoplasm and periplasm. It is further expected that the cell attempts to efflux Pd (II) ions through transporter proteins (possibly Ni ion transporters) (seen in purple). An alternative internalisation mechanism would involve the passive uptake of Pd (II) ions using porins (seen in blue).

1.2.3.2 *E. coli*-Pt

Relative to Pd synthesis, the mechanism for Pt-NP synthesis is less studied with fewer studies conducted overall with bio-Pt. Various strains have been studied for bio-Pt synthesis including sulphate-reducing bacteria[137] (SRB), *E. coli*,[125] *Shewanella*[155] and halophilic bacteria.[157] However, not many studies have fully explored the mechanisms behind bio-Pt synthesis.

Pt is more commonly found in salts as Pt (IV), and while this can be utilised to form Pt nanoparticles, current evidence indicates an intermediary Pt (II) step.[137] The initial sorption and internalisation of Pt (IV) are expected to be different from Pd (II). Pt (IV), being toxic, has previously been shown to increase membrane permeability; this was shown with SRB where, when challenged with Pt (IV) ions, membrane permeability was increased, indicating a mechanism for internalisation.[138] Furthermore, although the cell surface is usually polyanionic, it is expected that a low pH will protonate the surface and allow the negatively charged $[PtCl_6]^{2-}$ ions (Pt(IV)) to adsorb and permeate the cell surface. It is also likely that porins also play a role in the slow and passive internalisation of Pt(IV) ions here.[287]

When SRB synthesised Pt-NPs from Pt (IV) ions, Pt (II) ions were detected in the reduction, indicating an intermediary step.[137] This effect was not observed in heat killed cells which led Riddin *et al.*, to propose a two-step enzymatic mechanism for Pt reduction.[137] When SRB cells (grown anaerobically) were challenged with metal in the presence of O_2, Pt (IV) to Pt (II) reduction was shown to be minimal relative to when challenged in an anaerobic environment.

Whereas Pt (II) to Pt (0) reduction was not affected by an aerobic environment;[137] this suggested that the O_2-tolerant periplasmic hydrogenase and the O_2-sensitive cytoplasmic hydrogenases were both involved. To investigate the role of specific hydrogenases, Cu(II) mediated inhibition was used as pre-treating cells with Cu(II) inhibits periplasmic hydrogenases. On doing so, it was shown that Pt (IV) reduction continued, whereas Pt (II) reduction was limited. Heat-treating the cells, confirmed the requirement for enzymatic activity; here, all reduction was diminished.[137] When the periplasmic hydrogenase of *D. desulfuricans* was expressed in yeast cells,[158] the resultant strain could effectively reduce Pt (II) to Pt (0) further confirming the role of periplasmic hydrogenases in Pt (II) reduction.

It is likely that the hydrogenase enzyme mechanism is not the only possible route for *E. coli*-Pt synthesis. Indeed, anaerobically pre-grown *Shewanella algae* synthesised Pt at a pH of 7.0 in the presence of lactate, thus indicating an alternative mechanism (figure 1.13 B).[155] As such, reaction conditions can clearly have an effect on bio-Pt synthesis. When Williams compared *E. coli*-Pt with H_2 (figure 1.13 C) and formate (figure 1.13D) as a reducing agent, *E. coli*-Pt synthesis was primarily confined to the periplasmic space for the former and was seen throughout the cytoplasm for the latter.[125] Furthermore, Gaidhani *et al.*, synthesised Pt using a strict aerobe *Acinetobacter calcoaceticus* with four distinct enzymes implicated in this process; while their identities were not elucidated,[159] it is unlikely that the proposed hydrogenase mechanism is used as this utilises oxygen sensitive hydrogenases. Thus, it is likely that *E. coli*-Pt

could also be synthesised through multiple routes and the role that hydrogenase plays may be condition-specific.

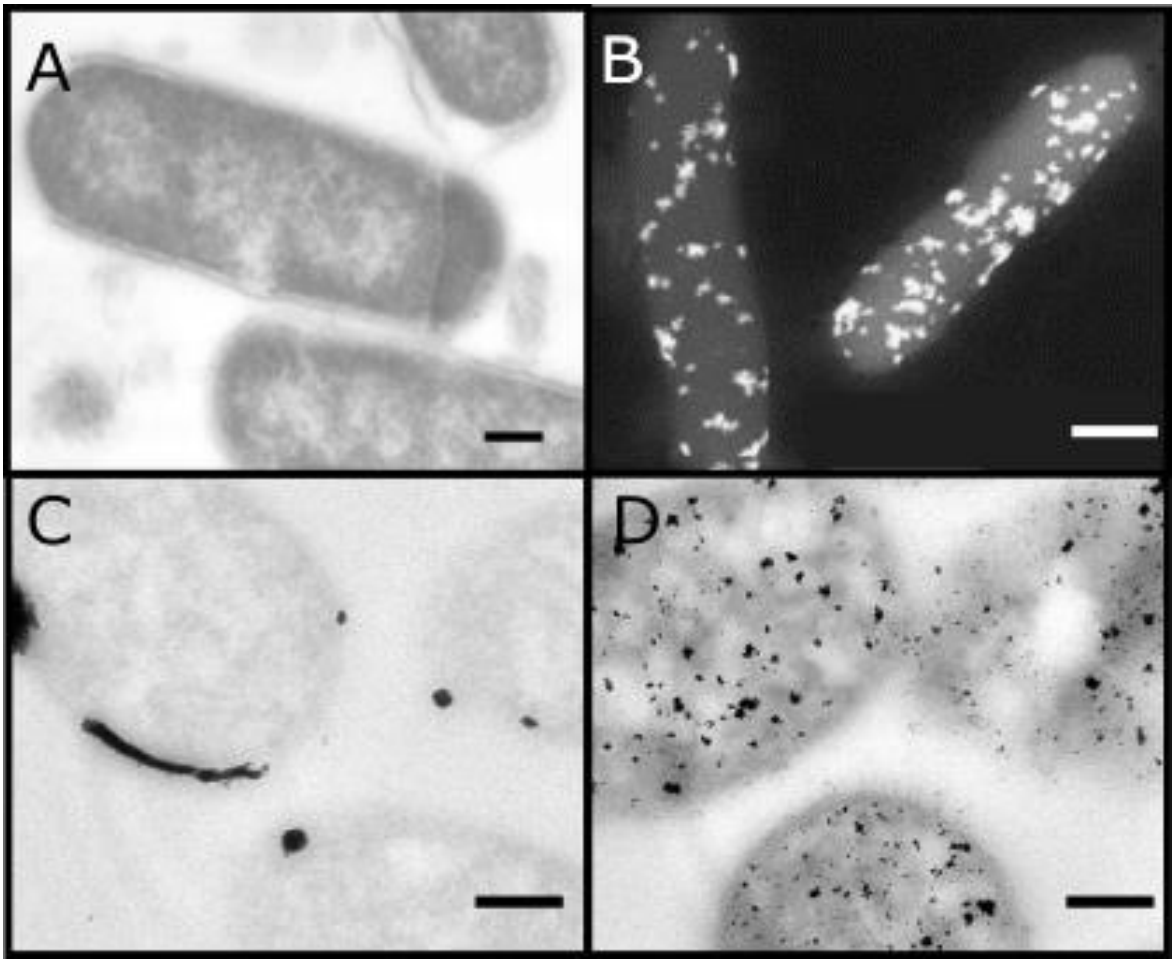

Figure 1.13: A,B,C and D shown TEM images each with a scale bar (shown in black or white) of 200 nm. (A) shows an empty *E. coli* cell, (B) shows a DF TEM image of *S. algae*-Pt with periplasmic Pt-NPs. This image was adapted with permission from Konishi *et al.*[155] (C and D) are TEM images where (C) shows *E. coli*-Pt produced using H_2 as the reducing agent and (D) shows *E. coli*-Pt produced using formate as the reducing agent. As seen the former shows periplasmic Pt whereas the latter shows Pt synthesis throughout the cell. This image was adapted from Williams.[125]

Figure 1.14 shows diagrammatically a hypothetical mechanism by which Pt ions are reduced to Pt (0) under H_2. As seen, $[PtCl_6]^{2-}$ or Pt (IV) is thought to permeate the membrane into the cytoplasm. The low pH of the reaction mixture is thought to allow internalisation of polyanionic Pt(IV) ($[PtCl_6]^{2-}$) into the cell where it is reduced to Pt (II) (red) via the action of the oxygen-sensitive cytoplasmic facing hydrogenase (blue).[138] Pt (II) then travels to the periplasm where Pt (II) is further reduced by an oxygen-tolerant periplasmic facing hydrogenase (light green) to Pt (0). Once this enzymatic-dependent reduction is complete, Pt (0) seed can auto-catalyse further reduction. Alternatively, as shown in the figure, Pt(IV) ions may be internalised passively through the action of porins.[287]

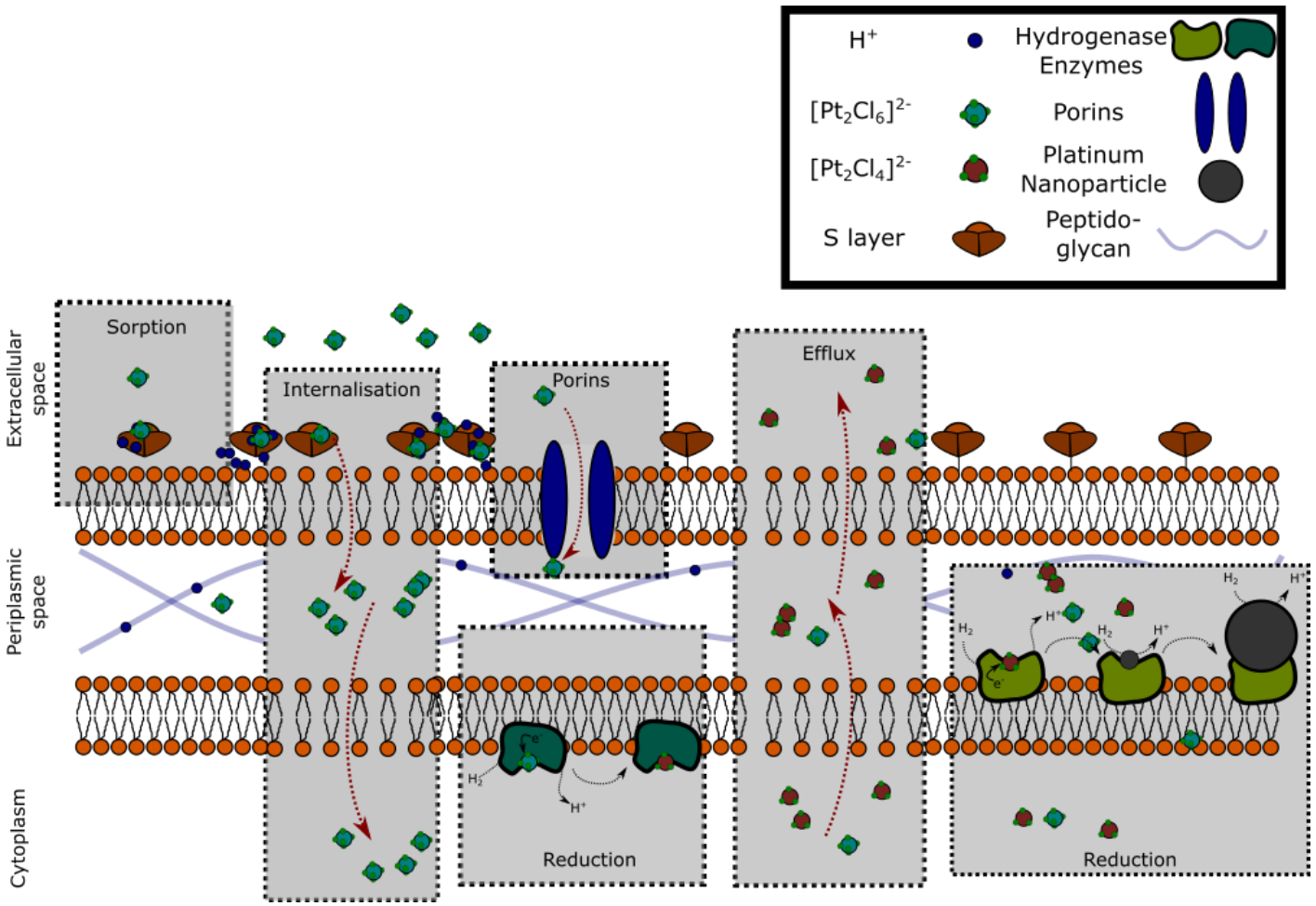

Figure 1.14: A hypothesised mechanism for *E. coli* mediated Pt nanoparticle synthesis. $[PtCl_6]^{2-}$ or Pt (IV) ions are shown on the left (light blue), where the toxic Pt (IV) permeabilizes the cell. The ions then travel through the membranes to the cytoplasm. Once inside they interact with the cytoplasmic facing hydrogenases (light blue) where they get reduced to Pt (II) (red). The Pt (II) undergoes efflux (unknown mechanism) into the periplasm where it gets reduced to Pt (0) through the periplasmic hydrogenase enzymes (light green) under H_2. These initial Pt (0) seeds then auto-catalyse under H_2 to form bigger Pt nanoparticles. This appears to occur primarily in the periplasmic space under H_2. An alternative mechanism would include the passive internalisation of Pt(IV) ions via the action of porins found in the outer membrane.

1.2.4 Bimetallic nanoparticles synthesised by *E. coli*

At least two studies have previously synthesised bimetallic nanoparticles using *E. coli*.[192,284] In both cases, cells were pre-seeded with Pd (0) and, instead of reducing additional Pd (II) autocatalytically, the Pd (0) seeds were utilised for the reduction of a secondary metal. In this manner Au(III) and Ru(IV) were reduced onto *E. coli*-Pd seeds to synthesise *E. coli*-Pd/Au[284] and *E. coli*-Pd/Ru[192] NPs, respectively. Both catalysts were shown to perform as well as or better than commercial catalysts in specific chemical reactions. *E. coli*-Pd/Au (2.5 wt% Au, 2.5% wt% Pd) metal showed comparable catalytic activity to commercial catalyst in the oxidation of benzyl alcohol[284] and *E. coli*-Pd/Ru (5 wt% Pd 5 wt% Ru) showed better catalytic activity when upgrading 5-hydroxymethyl furfural to 2,5 dimethylfuran than commercial catalyst. Furthermore, bacteria synthesised bimetallics have been used for FC catalyst development previously by Liu *et al.*, *Shewanella* synthesised PdAu nanoalloy showed better catalytic activities for methanol oxidation (anode) in direct liquid fuel cells.[100] Thus, mirroring these developments, the biosynthetic approach to bimetallic catalysts was deemed to have potential in impacting FC catalyst development.

1.2.5 Optimisation of Bio-Nanoparticles for FC activity

By understanding the mechanism of NP synthesis and the chemical parameters involved, on can optimise NPs for specific applications. Manipulating chemical parameters can affect the size, shape and localisation of the produced particles. The chemical parameters at play include pH,[118] reducing agent,[139] metal loading[140] and use of bimetallics in various formats as described earlier.

For example, *Rhodobacter capsulata* can biosynthesise gold nanoparticles of different shapes based on pH.[118] At a pH of 7, it produces spherical nanoparticles with sizes of 10–20 nm, and gold triangular nanoplates at pH 4, with sizes of 50–400 nm.[118] When Courtney *et al.*, synthesised *E. coli*-Pd nanoparticles using different reducing agents, H_2 or formate (at high metal loadings (w/w)), highly agglomerated Pd nanoparticles were shown on the cell surface with H_2 and smaller and more evenly dispersed nanoparticles were seen with formate.[139] In another example, when Attard *et al.*, synthesised *E. coli*-Pt at different metal loadings (i.e. wt metal : dry wt bacteria) and further processed them, the Pt nanoparticle sizes for the *E. coli*-Pt (1% w/w) were in the range of 1.5–3 nm whereas *E. coli*-Pt (20% w/w) showed nanoparticles in the range of 2.5–6 nm.[140] Furthermore, pre-treating the cells can induce an effect on NPs synthesised. Gomez-Bolivar *et al.*, used microwave injury to predispose *D. desulfuricans* and *E. coli* cells to making altered NPs of Pd. In doing so, the polydispersity index (measure of heterogeneity within NPs) of bioPd synthesised reduced to 39% and 32% relative to uninjured cells for *D. desulfuricans* and *E. coli* respectively.[285] Thus, these established chemical parameters could afford a level of control in optimisation of *E. coli*-Pt and *E. coli*-Pd for FC applications.

1.2.6 Engineering *E. coli*-NPs as FC catalysts

As stated previously Pt and Pd are the most efficient of bulk transition metals for ORR catalytic activity[26] and *E. coli* was shown to synthesise both *E. coli*-Pt[125] and *E. coli*-Pd.[117] Recently, Williams[126] and Courtney *et al.*,[139] investigated *E. coli*-Pt and *E. coli*-Pd as potential FC catalysts. Both syntheses used a low pH (~2.0), high metal loading (>10 wt% for Pd) and H_2 (amongst others) as the

reducing agent. Under these conditions, it is likely that the described mechanisms play a role, but this has not been confirmed.

Williams[125] showed *E. coli*-Pt NPs, under these conditions, were primarily confined to cell surface clusters of some (but not all) cells. These NPs showed promise as ORR catalysts but required energy intensive processing methods; the most promising result required the catalyst to be cleaned using NaOH for 6 weeks. When Courtney *et al.*, synthesised *E. coli*-Pd under similar conditions, they saw cell surface clustered Pd alongside intracellular Pd nanoparticles. Furthermore, untreated *E. coli*-Pd showed electrochemical activity (although its ORR activity was not checked).[139] It is expected that *E. coli*-Pd may have lower resistances due to their high cellular dispersion. While both were characterised, high resolution imaging was not done for either and as such this warrants further characterisation.

An optimised *E. coli*-NP FC catalyst would produce low environmental impacts and engineer an ideal microenvironment to form TPBs (see section 1.2.2). To minimise environmental impacts, *E. coli* used in other industrial processes, such as biohydrogen production, could be used for NP synthesis. Within this concept, *E. coli* is used to produce 'clean' biohydrogen as a part of a two-stage process (Appendix A6). Waste *E. coli,* from this process, has been shown to synthesise Pd-NPs.[131] This strategy uses clean H_2 (not sourced from fossil fuels) and the waste *E. coli* for bio-NP synthesis; thus, it would significantly minimise overall environmental impacts. The microenvironment produced by both Pt and Pd nanoparticles, however, is not ideal for PEMFC catalysis. *E. coli*-Pt clusters will

limit the amount of Pt accessible for catalysis and have high resistances (due to unmetallised native biomass) and a significant portion of *E. coli*-Pd is expected to be inaccessible internally.

It was hypothesised that a bimetallic version of the two could alleviate the problems faced by single metal versions. As noted in section 1.1.3, Pt nanoalloys tend to have better activities than single Pt nanoparticles. Furthermore, the localisations of individual metals can be utilised to engineer an ideal microenvironment. *E. coli*-Pd is found across the entire cell. The intracellular NPs could act as a conductive environment thus offsetting the biogenic resistances seen in *E. coli*-Pt. Additionally, the Pd clusters seen on the cell surface could be used as a seed to reduce Pt autocatalytically, thus forming a bimetallic mix of the two. Platinum synthesis usually requires enzymatic action, but bacteria are dead post-palladium synthesis. This alternate route might divert Pt synthesis onto Pd seeds and result in a more evenly spaced nanoparticle shell as required from an engineered solution. Finally, in engineering such a solution, the resultant catalyst might not require substantial further processing, providing significant environmental advantages.

1.3 Aims and Objectives

This thesis aims to address the issues identified above by investigating an environmentally friendly alternative to Pt and Pd nanoparticle production by using *E. coli*-Pt and *E. coli*-Pd (singly and in combination) as fuel cell catalysts. Chapter 2, by way of further introduction, will delve into the scientific principles

behind various techniques utilised and instrumentation used. The aims and objectives of the individual chapters are listed below.

Chapter 3:

- Aim: Synthesise and characterise single metal and bimetallic *E. coli*-NPs.
- Objectives: Synthesise *E. coli*-Pt and *E. coli*-Pd and two bimetallic versions of the two *E. coli*-Pt:Pd* and *E. coli*Pd:Pt*. Identify the resultant nanoparticle size, shape, and localisation within the cells.
- Results: *E. coli*-Pt, *E. coli*-Pd, *E. coli*-Pt:Pd* and *E. coli*-Pd:Pt* were synthesised and characterised using STEM, SAED, XRD, ICP-MS and XPS. *E. coli*-Pt:Pd* used *E. coli*-Pd as a seed to autocatalyze Pt-NPs and *E. coli*-Pd:Pt* used *E. coli*-Pt as a seed to auto-catalyse Pd-NPs onto it. The characterisation identified nanoparticle size, shape, and localisation within the cells.

Chapter 4:

- Aim: Characterise the catalytic activity of synthesised *E. coli*-NPs and improve performance.
- Objectives: Evaluate the catalytic activity of *E. coli*-NPs using *ex-situ* electrochemical tests. Identify methods to improve performance of biosynthesised catalysts.
- Results: The catalyst performance was evaluated using cyclic voltammetry, linear sweep voltammetry, durability tests and impedances. All biosynthesised catalysts performed poorly relative to commercial catalysts, but this established a baseline performance. Their

performance was then improved using carbon nanotubes, but this improvement was not competitive against commercial.

Chapter 5:

- Aim: Compare biosynthesised nanoparticles to commercial catalysts for their relative environmental impacts.
- Objectives: Perform a comparative life cycle analysis (LCA) on biosynthesised nanoparticles and commercial Pt/C as PEMFC catalysts.
- Results: A comparative LCA showed that biosynthesised nanoparticles had far greater environmental impacts than conventional Pt/C when used as PEMFC catalysts. A hypothetical biosynthesised catalyst with comparable activity (to Pt/C) showed fewer environmental impacts than Pt/C. This was a preliminary study as any meaningful analysis will require an entire supply chain to be established.

Chapter 6 highlights the key findings of each chapter and presents a wider discussion of the field. It compares *E. coli*-NPs against commercial catalysts and identifies methods to improve their catalytic activities alongside approaches to further lower environmental impacts.

Chapter 2: Scientific principles behind techniques used to characterise biosynthesised nanoparticles

2.1 Introduction

The various scientific principles behind the techniques and instrumentation used in this thesis are discussed here. This chapter is divided into two sections materials characterisation (results discussed in chapter 3) and electrochemical characterisation (results discussed in chapter 4).

2.2 Materials characterisation

Typically, NP characterisation includes elucidating their size, shape, alloying,[160] and (as they are biosynthesised) localisation within the bacterial cell.[127] Electron microscopy (EM) can be utilised to identify size, shape and localisation of nanoparticles.[161] X-ray diffraction (XRD) is often used to further elucidate the crystallite component of the nanoparticle and can also be used to check for alloying.[162] X-ray Photoelectron Spectroscopy (XPS) and Inductively Coupled Plasma Mass Spectrometry (ICP-MS) is used to identify elemental composition[163,164]; XPS has the further advantage of identifying electronic and oxidation states of the elements and can be used to check for alloying.[165] As such these tests were utilised to characterise the catalysts. Further characterisation methods such as extended X-ray absorption fine structure (EXAFS), X-ray absorption near edge structure (XANES), Electron paramagnetic resonance (EPR), atomic force microscopy (AFM) and shell-isolated nanoparticle-enhanced Raman spectroscopy (SHINERS) etc. can also be used but as they were not utilised here, they are not described.

2.2.1 Electron Microscopy

Electron microscopy is a technique that, unlike light microscopy, uses accelerated electrons to obtain high resolution images.[166] The Rayleigh criterion, used for diffraction patterns, states that patterns are distinguishable when the minimum of one pattern falls on the central maximum of the other.[167] From this Abbe's resolution limit[168] was derived as given below:

$$\boldsymbol{R = \frac{0.61\lambda}{NA}} \qquad \textbf{(Eq 2.1),}$$

where $\boldsymbol{R}$ is the resolution, $\boldsymbol{\lambda}$ is the wavelength of the radiation, $\boldsymbol{NA}$ is the numerical aperture of the magnifying lens. From this, we can show that conventional light microscopy has a resolution limit of around 200 nm for light at a wavelength of 500 nm.[169] This resolution is obviously insufficient for evaluating nanoparticles (range of 0.5–100nm) and as such, electron microscopy is used. Unlike photons used for light microscopy, here electrons are utilised to form an image. Electrons are scattered by atoms as a result of the electrostatic interactions between the positively charged nuclei and the negatively charged electron cloud of the atoms.[170] The wave-particle duality of the electrons, as described by the de Broglie equation, (Eq 2.2) allows them to be utilised to image objects at a higher resolution than visible light.[170]

$$\boldsymbol{\lambda = \frac{h}{p}} \qquad \textbf{(Eq 2.2),}$$

where $\boldsymbol{\lambda}$ is the wavelength, $\boldsymbol{h}$ is Planck's constant and $\boldsymbol{p}$ is the momentum of the particle. For higher resolutions, electrons require a wavelength smaller than visible light. As shown in equation 2.2, wavelength is indirectly proportional to

the momentum and thus, to achieve high momentums, electrons are accelerated by applying a voltage.[170] The electrons are generated and accelerated using an electron gun at voltage ranges of 200–400 kV;[170] this results in speeds greater than half the speed of light. As such, when considering the momentum of electrons, the relativistic effects must be considered[170] and this results in the following equation

$$\lambda = \frac{h}{[2m_0eV\left(1+\frac{eV}{2m_0c^2}\right)]^{0.5}} \quad \textbf{(Eq 2.3),}$$

where m_0 is the electron rest mass, e is the charge on the electron, V is the accelerating voltage and c is the speed of light in a vacuum.[170] Once these high-speed electrons are generated, they are focused through a series of anodes, condenser lenses and apertures.[171] The electron beam is then focused onto the sample; the electrons can then interact with the sample in a variety of ways. In a magnetic environment, the electrons are subject to Lorentz forces[172] and this can be a limiting factor with certain samples. However, most electrons are either transmitted through without interacting or scattered due to electrostatic interactions with either nuclei or electron clouds of the sample; the force of this interaction is given by coulomb's law (Eq 2.4) and this coulombic scattering of electrons will generate a wide variety of signals as shown in figure 2.1.[173]

$$F = \frac{1}{4\pi\epsilon_0}\frac{q_1q_2}{r^2} \quad \textbf{(Eq 2.4),}$$

where F is the force, ϵ_0 is the permittivity constant, q_1 and q_2 are the charges on the two bodies and r is the distance between the two charged bodies.

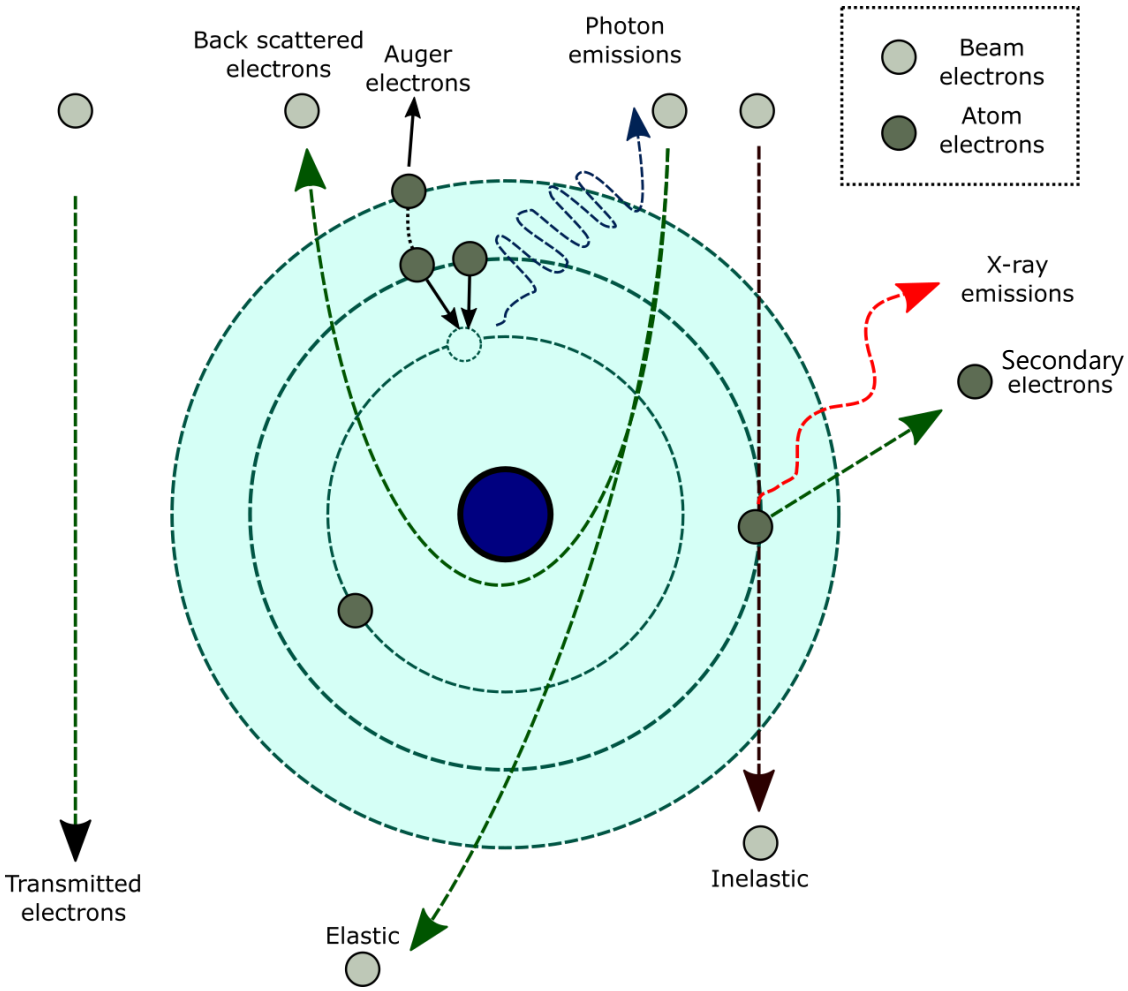

Figure 2.1 Interactions of high-speed electrons and atoms are depicted here. As shown the electrons can either be transmitted through or interact with the atom in an elastic or inelastic manner.

Generally, the electrons can interact with the sample elastically or inelastically. Inelastic interaction occurs between beam electrons and the electric field of the atom electron. Here transfer of energy from beam to the atom takes place and results in the ejection of the atom electron resulting in a secondary electron (SE).[173] The vacancy created by this electron is filled by an electron from a higher orbit with either an accompanied emission of characteristic X-rays or

through the transfer of energy to outer shell electron resulting in its emission form the atom. These electrons are known as the Auger electrons.[173]

Elastic interactions occur between the transmitted electron and the electric field of the nucleus of an atom. This results in the scattering of electrons and if the electron is deflected back out of the specimen, it is characterised as a back scattered electron (BSE).[173] Once the electrons have passed through the sample, the resulting electrons and photons have to be put through a further series of apertures and lenses before they can be utilised to study the samples.[174] Different apertures and lenses are used for different modes of electron microscopy that are disccused below. Furthermore, these modes have different applications and sample requirements and these are also discussed below.

2.2.1.1 Scanning electron microscopy (SEM)

SEM is a type of electron microscopy that scans the surface of samples using a focused beam of electrons. The produced images can be used to identify surface morphology, crystalline structure, elemental composition, and electrical behaviour of the top 1 μm of the specimen.[175] As shown in figure 2.2, an SEM requires an electron source, an anode to converge the electron beam, and a couple of condenser lenses, an objective aperture and lens to focus the electron beam. The objective lens also has X-Y scan coils; these are used to scan horizontally across the specimen in both axis through a process known as raster scanning.[176] The electron beam is then focused onto a sample and SE, BSE and X-ray detectors are utilised to characterise the sample.

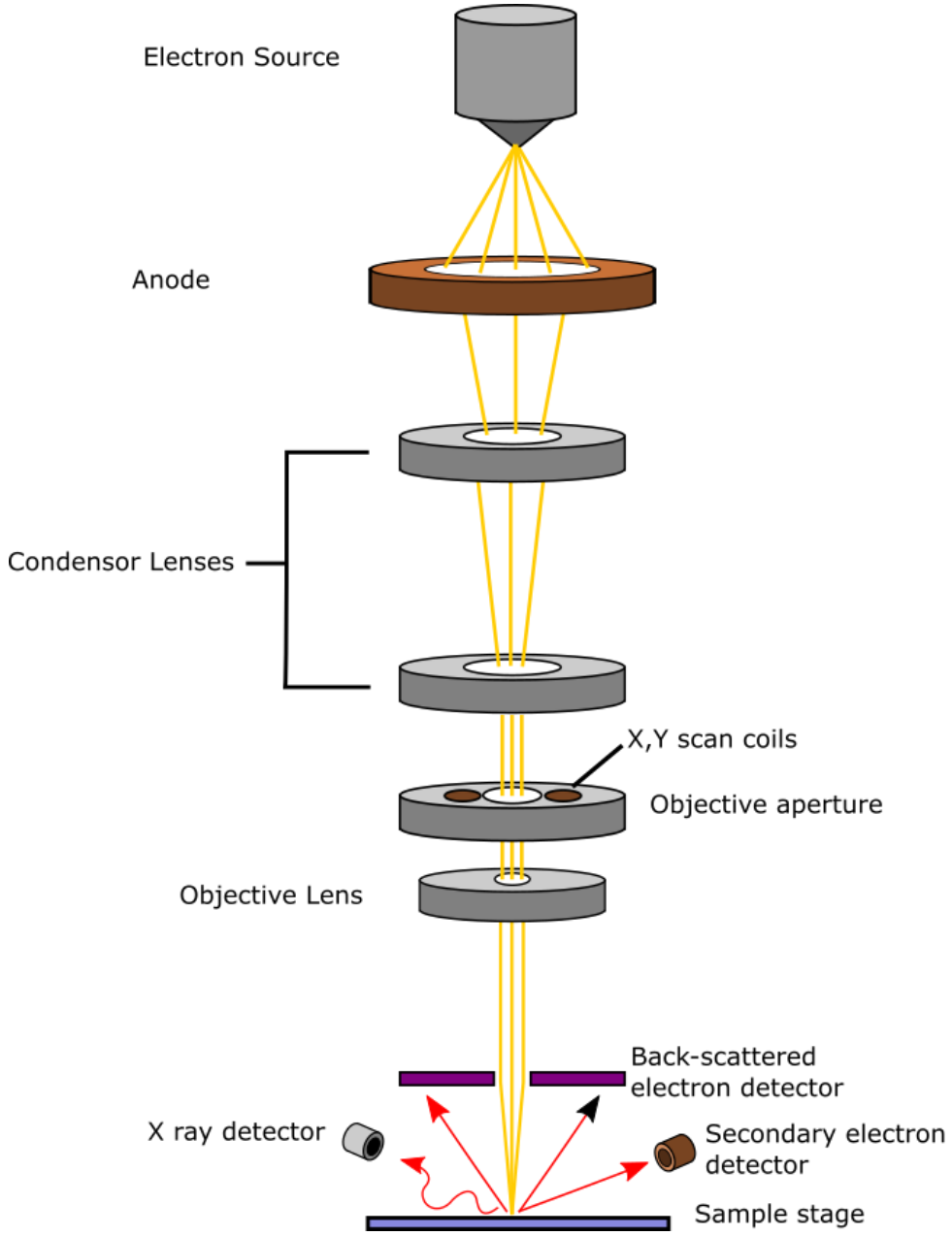

Figure 2.2 General schematic of a scanning electron microscope (SEM). The electrons are generated by an electron source and focused onto the sample via a series of condenser lenses. The focused beam is then scanned horizontally across a sample to generated BSE and SEs which are then detected by separate detectors.

SEM utilises secondary (SE) or backscattered (BSE) electrons to generate images. As shown in figure 2.3, the electron beam can penetrate the sample to various depths from which different electrons are projected. The microscope can switch between using SE or BSE to form an image or combine the two. SE

electrons originate from the surface regions and have low energies.[175] This can be exploited to generate a topographical image of the sample. For example, if a sample has peaks and troughs, SEs generated from the troughs will find it harder to reach the detector relative to those generated from the peaks.[125] This will create a disparity in their relative intensities thus creating contrast and a sharper image.[177] BSE are higher energy electrons that originate from a broad region of the sample volume.[175] As shown in figure 2.1, they are a result of elastic interactions of beam electrons and nuclei. Larger atoms are stronger scatterers of electrons and thus BSE show greater sensitivities to differences in atomic numbers.[178] This mode of imaging can be used to differentiate phases and elements within a sample. Furthermore, the emitted X-rays from a specific region on the sample can be collected using an electron-dispersive X-ray spectroscopy detector (EDX) to identify the elements at that region.[190]

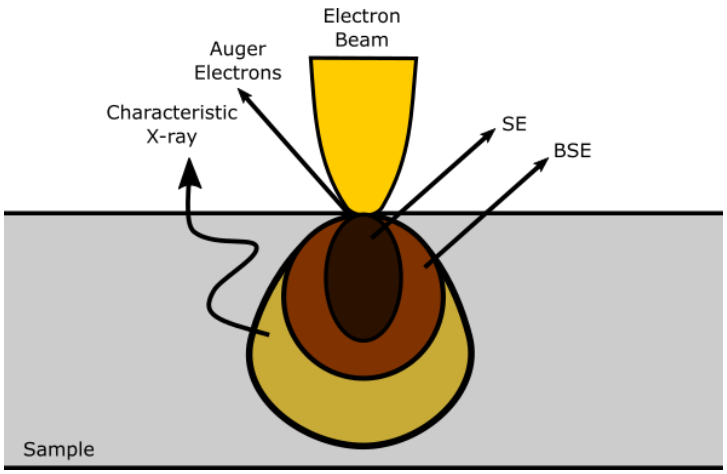

Figure 2.3 A simplified diagram of the interaction between an electron beam and the sample. The beam produces auger electrons, SEs and BSEs at increasing depths, respectively. These can be utilised to image the sample. The X-rays produced can be used for elemental analysis of the sample.

SEM is often used to image surface morphologies of biological samples. However, to achieve this the samples must be sputter-coated with a thin film layer of conductive material (Pt, Au etc). The electron beams from SEM microscopes are highly energetic and can damage biological materials. Furthermore, biological materials (due to their non-conductive nature) can act as an electron trap. This results in surface accumulation of electrons in a process known as "charging" which creates white patches on the image. Both effects are prevented by sputter coating the material.[179]

For example, these various modes of SEM were used to characterise AuNPs synthesised using a bacteria-polymer composite mesofibers.[191] *Micrococcus luteus* (ML) and poly(vinyl-alcohol) (PVA) were electrospun on to a sterile steel mesh. The resultant composite was then encapsulated in polymer (p-xylylene) (PPX) using chemical vapour deposition to form a nonwoven composite.[191] SEM images using SE detectors were used to study the morphology of the resultant composite (figure 2.4A). These composite nonwovens were used to synthesise AuNPs on the ML. The synthesised AuNPs were identified using SEM imaging using a BSE detector as seen in figure 2.4B.[191] Here the AuNPs, having a greater atomic number relative to surrounding elements, show up as bright spots on the images as indicated by the white arrows.[191] The presence of Au was confirmed using the x-rays emitted from those regions and an EDX detector. As seen in figure 2.4C, the detector identifies the energy of the emitted X-rays and can correlate these to individual elements, as shown by the Au peak.[191]

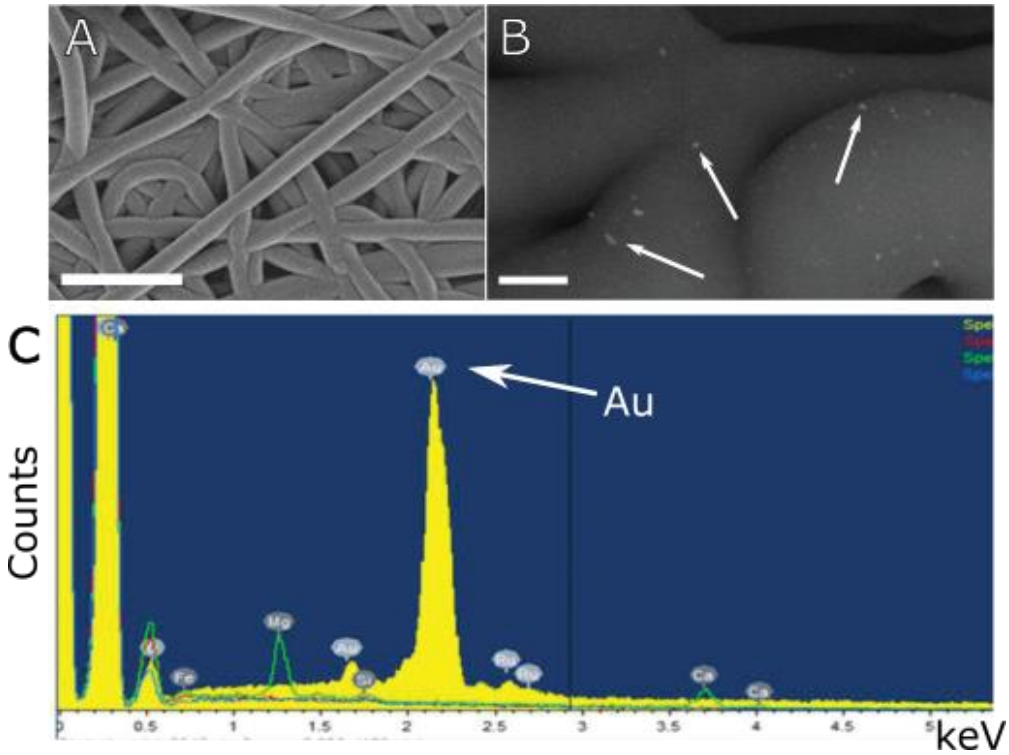

Figure 2.4 (A) shows an SEM image generated using SE of a polymer/bacteria composite. This shows the surface morphologies of the fibres. Scale shown by white bar 10 μm. (B) shows an SEM (BSE) image of the composite after AuNP synthesis by the bacteria. The white arrows indicate AuNPs and the scale shown by white bar (1 μm). (C) shows the elements detected by EDX at a specific region. A peak is shown for Au indicating its presence. X axis shows energy of emitted x rays (keV) and y axis are arbitrary counts. Images were adapted with permission from Reich *et al.*[191]

2.2.1.2 Transmission electron microscopy (TEM)

Unlike SEM, transmission electron microscopy utilises the transmitted electrons to form an image, thus this mode of microscopy requires sufficiently thin samples for effective imaging.[180] As shown in figure 2.5, like an SEM, TEM microscopes utilise an electron gun, condenser lenses and apertures to focus an electron beam.[181] The beam is then transmitted through the sample and magnified using a projector lens.[182]

Transmitted electrons can be selected with the objective aperture (figure 2.5) to form a brightfield image (BF).[183] Here the scattered electrons are blocked and in the resultant image, areas of the sample with high crystallinity and mass will appear dark, whereas areas with less mass will appear bright[184] (figure 2.6A). Dark field (DF) imaging is the opposite of this; here the aperture is used to block out unscattered electrons and scattered electrons are selected for imaging[184] (figure 2.6B).

TEM imaging for biological samples require significant sample preparation as biological materials are usually too thick. Sample preparation requires chemical fixation to stabilise the speciman; proteins are stabilised by glutaraldehyde while osmium tetroxide fixes lipids and provides a 'stain'.[185] Fixation is followed by dehydration using organic solvents (usually an ethanol series) and embedding in a resin before sectioning the sample into thin samples (50–100nm) for TEM imaging.[169] TEM images can be used to identify nanoparticle size, size distribution (with suitable data processing programs), shape, aggregation, morphology and localisation. High-resolution TEM (HR-TEM) images can also be used to identify the crystal structure of single particles. As well as being used to distinguish monocrystalline, polycrystalline and amorphous nanoparticles,[186] HR-TEM can be used to measure lattice fringe spacings and hence identify the crystal faces presented which has implications for catalysis.[186]

2.2.1.3 Selected area electron diffraction (SAED)

Within TEM microscopes, selected area electron diffraction (SAED) can be utilised for crystal structure determination.[186] The crystal structure of

crystalline regions in a sample acts as a natural grating for electron diffraction.[187] To take the image, as shown in figure 2.5 and figure 2.6H, the selected area aperture is used. The image is taken at the back focal plane rather than the image plane normally used for TEM. This provides a diffraction pattern with regularly spaced maxima where each maximum corresponds to a Miller index. With nanoparticles, the maxima will appear in a pattern of concentric circles as there are a multitude of orientations.[188] Unlike X-ray diffraction (XRD), a bulk method, SAED examines single NPs or clusters, which can be used to distinguish between crystalline structures present in various NP subpopulations within the bacterial cell.[125]

2.2.1.4 Scanning transmission electron micrography (STEM)

STEM is a combination of both TEM and SEM. As shown in figure 2.5, STEM is essentially a TEM that like an SEM focuses the electron beam to a fine spot and utilises the raster scanning aspect of an SEM.[189] In a TEM, an aperture is used to collect scattered electrons for dark field imaging; in STEM, scattered electrons are not collected but detected using an annular dark field (ADF) detector (figure 2.5). This allows far more scattered electrons to be sampled relative to conventional DF. Furthermore, this technique can be used in conjunction with BF and EDX (for elemental mapping).[189]

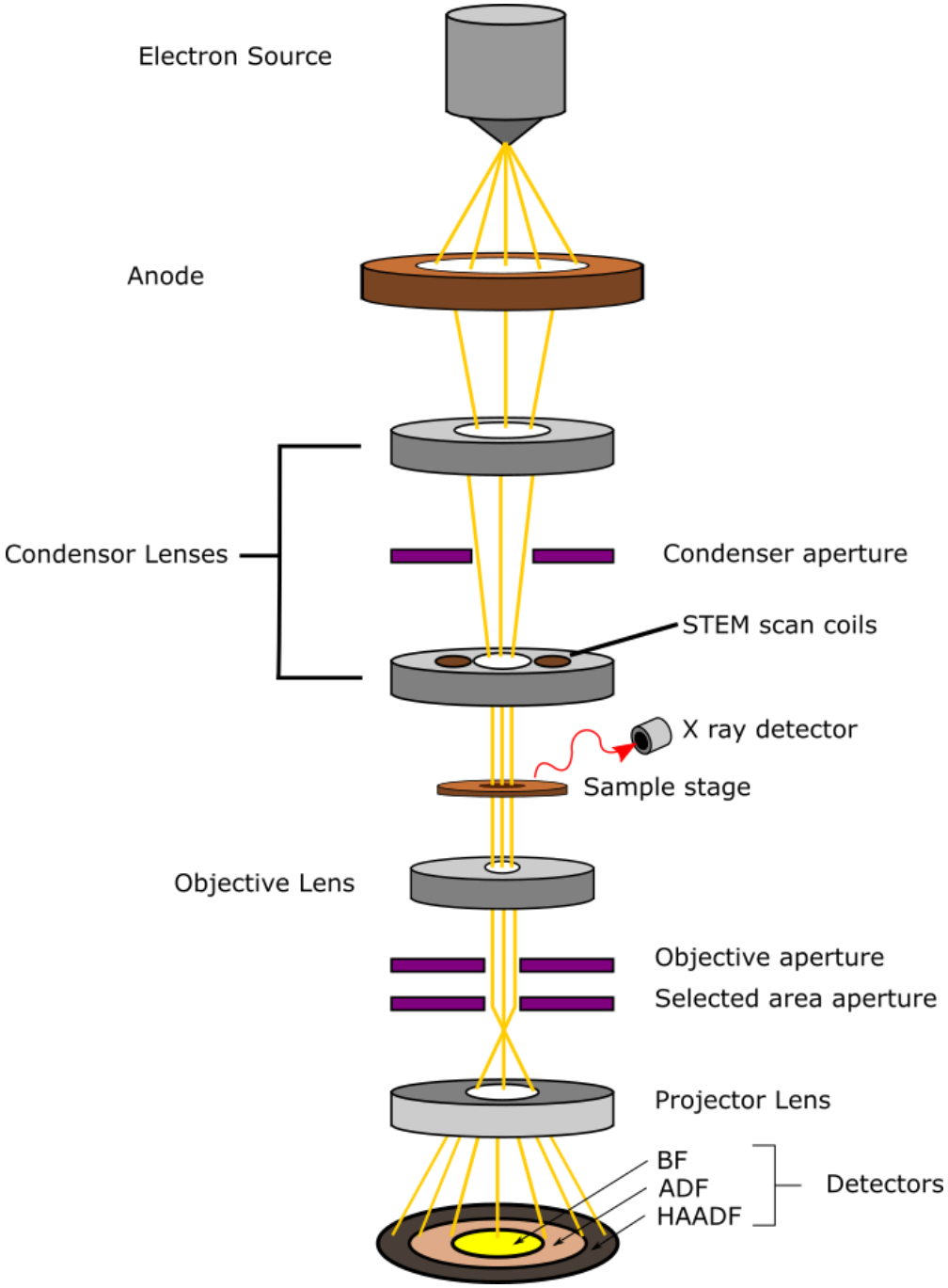

Figure 2.5 General schematic of a Transmission electron microscope (TEM) and a scanning transmission electron microscope (STEM). The electrons are generated by an electron source and focused onto the sample via a series of condenser lenses. The focused beam is transmitted through the sample to generated scattered electrons and transmitted electrons which are then detected by separate detectors (see text). When in STEM mode, the scan coils are used and the ADF and HAADF detectors can be utilised

DF uses conventional Bragg scattered electrons (i.e., electrons scattered by interactions with sample electrons). High angle annular dark field (HAADF) detectors can be used to detect electrons scattered at a very high angle (due to interactions with the sample nuclei) (figure 2.5 and figure 2.6C). This technique is highly sensitive to the atomic number of the sample, with a greater signal coming from atoms with a higher atomic number. These will appear brighter in the HAADF images relative to their surroundings and as such can be used to study nanoparticles embedded in a bio-scaffold identify.[190] These images can be used to size individual nanoparticles using appropriate imaging software such as ImageJ. Here, the individual nanoparticles can be measured using a set scale manually or via specific program functions such as the "analyse particles" function on ImageJ.[213,214]

Gomez-Bolivar *et al.*, used these techniques with great effect when investigating bimetallic *E. coli*-Pd/Ru nanoparticles. In figure 2.6A and figure 2.6B, BF and HAADF images of *E. coli*-Ru 2.6 wt.% are seen respectively. Ru nanoparticles are clearly visible on the cell surface as dark (in BF mode, figure 2.6A) or bright (in DF mode figure 2.6B) spots. Figure 2.6C,D,E and F focus on one *E. coli* cell loaded with both Pd and Ru.[192] Figure 2.6C shows an HAADF image of the cell with the nanoparticles clearly visible as bright spots embedded in the darker cell matrix.[192] Figure 2.6 E and F are elemental maps of Pd, and Ru respectively done simultaneously using EDX on the same cell with D showing an overlay of the two.[192] Figure 2.6G shows a HRTEM image of two individual nanoparticles and was used to identify lattice spacing and thus identify the crystal face of the nanoparticle.[192] Finally figure 2.6H was taken (with permission) from a

published study on Ag nanoparticles synthesised by fungi. The Ag nanoparticles were observed under a TEM microscope and SAED was used to further elucidate crystal structure. As shown here, the diffraction pattern (for NPs) is seen as concentric circles.[193]

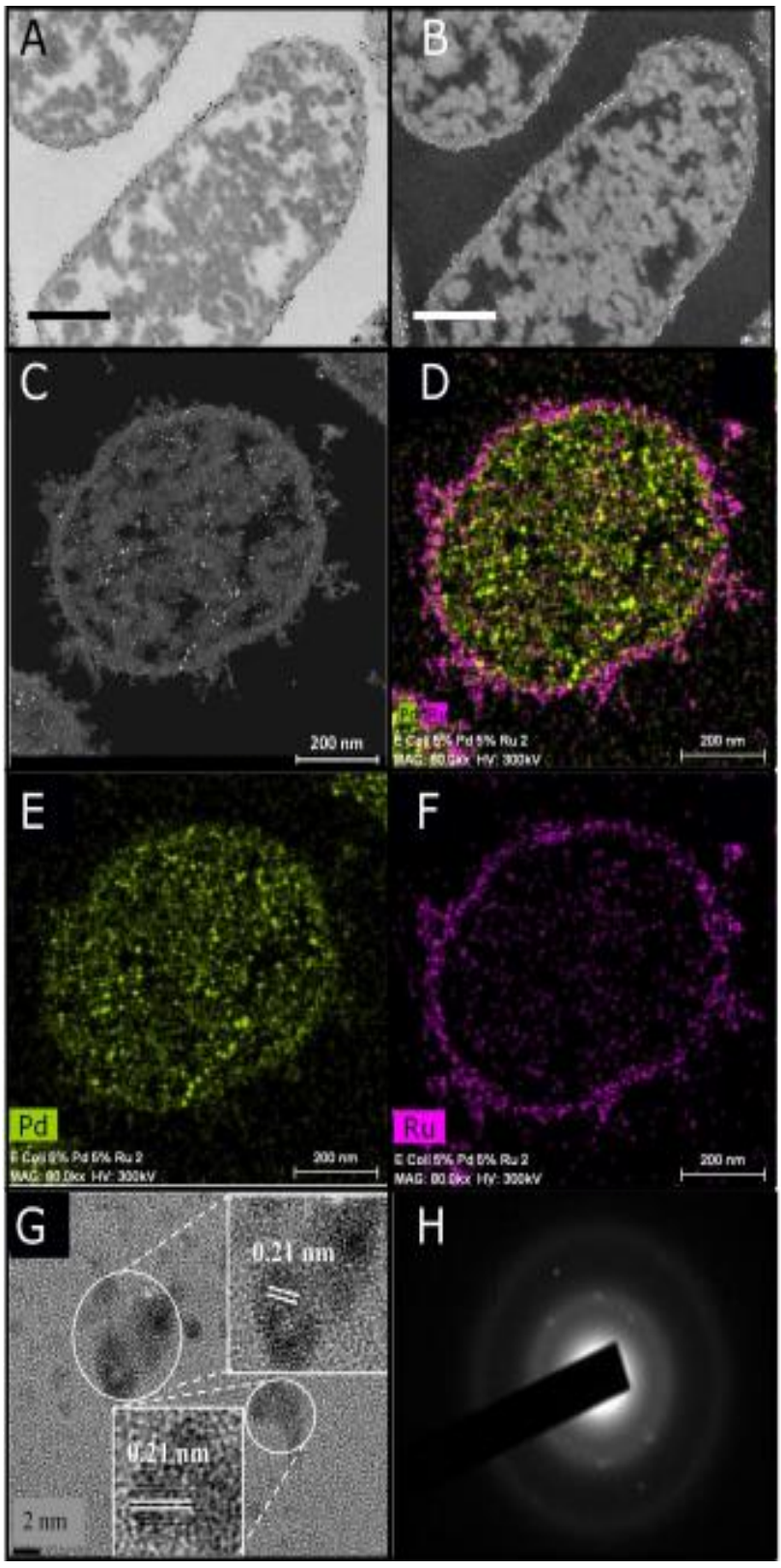

Figure 2.6 Examples of image and data acquisition using electron microscopy methods. (A,B) shows the BF and DF STEM images of a representative *E. coli*-Ru cell (scale bare shown is 200nm). (C, D, E and F) show the same cell loaded with both Pd and Ru nanoparticles. C is an HAADF image of the cell with nanoparticles clearly visible as bright spots. D, E, F are EDX maps conducted in on the same cell with E showing Pd localisation, F showing Ru localisation and D showing an overlay of both. (G) shows a HRTEM image of two representative nanoparticles and the identifies the lattice spacing for both. (H) shows an SAED pattern taken under TEM for Ag nanoparticles synthesised by fungi. All images were adapted with permission from Gomez-Bolivar *et al.,* (Fig A–G)[192] and Devi and Joshi (Fig H).[193]

2.2.2 X-ray Powder Diffraction (XRD)

XRD is a commonly used technique to determine nanoparticle shape, structure, and size although since it records only crystalline components of a sample, its application requires validation by other techniques.[194] This technique works on the principle that X-rays will undergo elastic scattering when passing through a crystal structure. At the right angle of incidence, this scattering can provide a diffraction pattern through the constructive interference of the light.[195] This diffraction will follow Bragg's law shown below:

$$\lambda = 2d_{hkl} \sin\theta \qquad \textbf{(Eq 2.5)},$$

where λ is the wavelength, d_{hkl} is the spacing of crystal planes, and θ is half of the diffraction angle.[196] Thus, by illuminating monochromatic X-rays through a sample at a range of wavelengths, nanoparticle structures can be probed.

A typical experimental setup comprises an X-ray source, a rotating sample holder and a charge-coupled device (CCD) detector. The X-rays are produced through striking a metal (e.g., Cu) with accelerated electrons. These are then passed through the sample at a range of different angles and the diffracted rays are collected using a detector which will detect intensities at angles that obey Bragg's law.[197] The angle at which these peaks occurs can be used to identify d-spacing for the peak, which in turn, can be used to determine crystalline orientations of the element.[197]

Nanoparticles, and other crystals, show multiple peaks on an XRD pattern and these peaks relate to various crystal faces and crystallographic orientations within the substance.[198] Specific elements will have peaks at characteristic angles for different orientations. Crystallographs of a wide range of materials

in different structures have been determined and as such, these can be used as database to identify elements and structures in unknown samples.[198]

XRD powder patterns can also be used to identify degree of alloying within nanoparticles. For example, diffraction patterns for a mixture of Cu and Ni will show an XRD pattern with peaks corresponding to both Cu and Ni (figure 2.7B) whereas an XRD pattern for the Ni_3Cu alloy (figure 2.7A) will show new peaks corresponding specifically to the alloy.[199] Bimetallic alloy peaks lie between the peaks for single metal crystals. As seen in figure 2.7C, Pt, Pd and Pt/Pd (alloy) XRD patterns are shown. The peaks for the alloy lay in between the corresponding peaks for the single metals.[201]

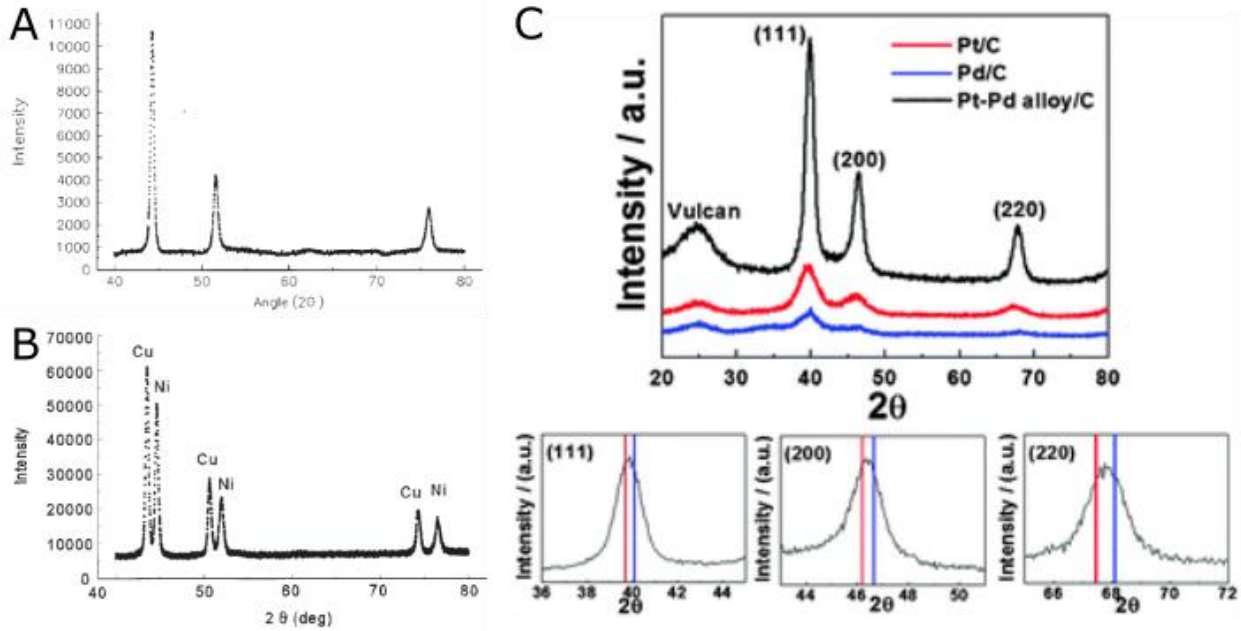

Figure 2.7 (A) shows an XRD pattern of Ni_3Cu alloy. (B) shows an XRD pattern of a mixture Ni and Cu crystals. Adapted with permission from Butera and Waldeck.[199] (C) shows the XRD patterns for Pt/C (red), Pd/C(blue) and Pt-Pd alloy/C (black). The peaks for Pt-Pd alloy lie in between the corresponding peaks for Pt/C and Pd/C. Adapted with permission from Lee *et al.*[201]

2.2.3 X-ray Photoelectron Spectroscopy (XPS)

XPS is a surface chemistry technique that utilises the photoelectric effect to analyse the elemental composition on the outermost surface of a material.[202] The photoelectric effect is the emission of electrons from a material when electromagnetic radiation hits the material. This is given by the equation:

$$h\nu = E_{kinetic} + \phi \qquad \textbf{(Eq 2.6),}$$

where h is Planck's constant, ν is the frequency of the light, and ϕ is the work function of the material and $E_{kinetic}$ is the kinetic energy of the photoelectron. The work function here corresponds to the strength of binding between the emitted electron and its nucleus. This can be rewritten to represent the binding energy of the element and its electrons by the following equation:

$$E_{binding} = E_{photon} - (E_{kinetic} + \phi) \qquad \textbf{(Eq 2.7),}$$

where E_{photon} is the energy of the photon and $E_{binding}$ refers to the binding energy between the electron emitted and its nucleus; this value is characteristic of the nuclei it is bound to, its electronic state (i.e., shells and orbitals (2p, 3s, 3d etc.,)) and the chemical environment it is in (oxidation state of the atom). Thus, by utilising this phenomenon, an XPS survey can act as a fingerprint to identify the elemental composition of the surface layer of the material. XPS achieves this by bombarding the sample with high energy X-rays in ultra-high vacuum. This is necessary to prevent collisions of the electrons with any other atoms in a gaseous phase which would dampen the signal. The X-rays induce the emission of photoelectrons that can be detected by a highly sensitive electron detector, which is often a hemispherical analyser.[203] This detector will identify the kinetic

energy of the detected electrons and deduce the binding energy using eq 2.7. XPS scans are often represented in terms of binding energy to allow for easier comparison.[203]

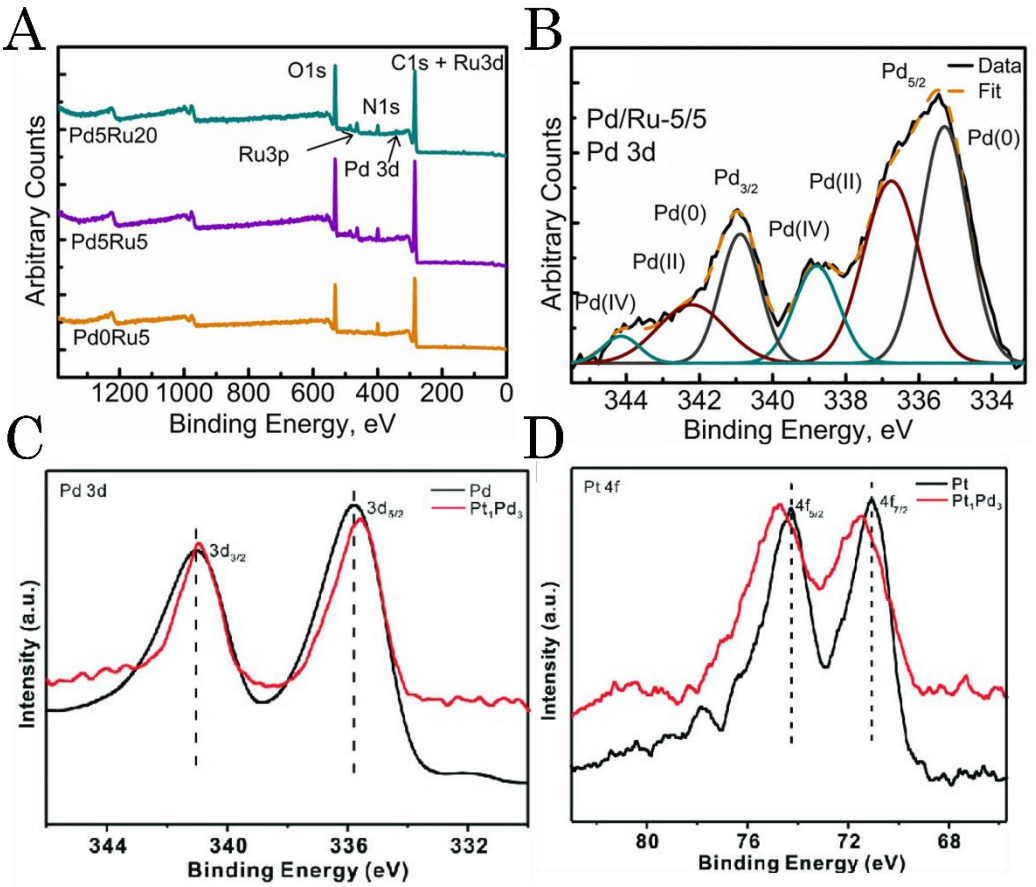

Figure 2.8 (A) An XPS survey scan of *E. coli*-Pd/Ru with different molar ratios of Pd and Ru. As seen the Pd_5Ru_{20} scan (blue) identifies the elemental composition of this catalyst. (B) High resolution Pd3d scan of *E. coli*-Pd/Ru with Pd/Ru-5/5. The data is shown in black and the fit is shown overlaid in yellow (Dashed line). This doublet is deconvoluted into the Pd (0) (black), Pd (II) (red) and Pd (IV) (blue) peaks. Image adapted with permission from Gomez-Bolivar *et al.*[192](C) and (D) show high resolution Pd3d and Pt4f scans done for nanoalloy Pd_1Pd_3 (in red) respectively overlaid against high resolution Pd3d and Pt4f scans done for nanometals Pt and Pd (in black) respectively. The scans show a shift in peaks with the nanoalloy. Image adapted with permission form Liu *et al.*[274]

XPS scans detect electrons emitted from the surface of the sample. While the X-rays penetrate the entire sample, only the electrons in the outermost layers can escape the sample to be detected; the electrons from the inner layers will get trapped and blocked within the sample. Furthermore, XPS scans cannot detect electrons with binding energies greater than X-ray energies as these are not emitted. As such, the inner shell electrons of heavier elements are not emitted. It can, however, detect auger electrons (section 2.2.1 and shown in figure 2.1). These are denoted here in shell terminology, for example, KLM auger electrons are M electrons emitted when a K shell hole is filled by an L shell electron.

Figure 2.8A shows a typical XPS survey scan conducted on *E. coli*-Pd/Ru nanoparticles.[192] As seen by the arrows (blue line), the peaks relating to O, C, N Pd and Ru were all identified.[192] Once a survey scan is conducted, high resolution scans can be performed on peaks of interest. Figure 2.8B shows a high-resolution scan conducted on the 3d peaks of Pd atoms in *E. coli*-Pd/Ru.[192] As seen (black line (data) with yellow dashed line (fit) overlaid, Pd 3d electrons emit two separate peaks (a doublet). This effect arises due to the spin-orbit coupling of the electrons emitted and is present in electrons from any orbital apart from the s orbital. Spin orbital coupling describes interaction of the electron (with spin 's') with its electronic orbital (with orbital angular momentum l). The total angular momentum of an electron j is given by the following equation:

$$\boldsymbol{j = |\, l \pm s|} \qquad \textbf{(Eq 2.8),}$$

Electrons with different j values will result in different peaks. This is shown in figure 2.8B where the two Pd peaks are assigned as $Pd_{3/2}$ and $Pd_{5/2}$. These values indicate their j value as the l value for orbital d is 2 and the s value can be either ½ or -½. Each of these peaks can be deconvoluted further to identify the different atomic environments form which these electrons are emitted. Here, Pd3d electrons are emitted from Pd atoms with oxidation states Pd (0) (black line), Pd (II) (red line) and Pd (IV) (blue line) peaks (figure 2.8B). XPS has been utilised to identify oxidation states of Pt nanoparticles as this can have a direct impact on electrocatalytic activity.[204,205]

XPS is often used for catalyst characterisation as it provides detail of the local binding environment.[204] High resolution scans can identify changes in electron binding energies due to different interatomic interactions. Figure 2.8C and 2.8D show the high resolution Pd3d and Pt4f scans(in red) respectively for a Pt_1Pd_3 nanoalloy. When compared to Pd3d and Pt4f scans of pure Pd (2.8C) and Pt (2.8D) nanometals (in black) respectively, the peaks for both elements had shifted in the nanoalloy. This arises because of the effect of interatomic interactions on electron binding energies.[274]

2.2.4 Inductively Coupled Plasma Mass Spectrometry (ICP-MS)

MS is a widely used analytical technique that measures that measures the mass of chemicals.[206] ICP-MS is a type of mass spectrometry that uses inductively coupled plasma to ionise the sample.[207] MS works by ionising the sample, separating the various elements or compounds by their charge to mass ratio and finally achieves their detection by their respective m/z ratio and abundance. Figure 2.9 shows the general scheme of a mass spectrometer; The sample flows through an inlet chamber which follows onto an ion source. The ion source ionises the sample which then flows into the mass analyser. Here the ions are sorted by mass/charge ratio as the heavier ions will travel through the analyser more slowly than smaller ones. They are finally detected by an ion detector. The detected data is analysed by the data system.[206] ICP-MS uses an inductively coupled plasma to ionise the sample. This powerful technique has good precision, and low detection limits to analyse elements in a wide variety of samples.[207]

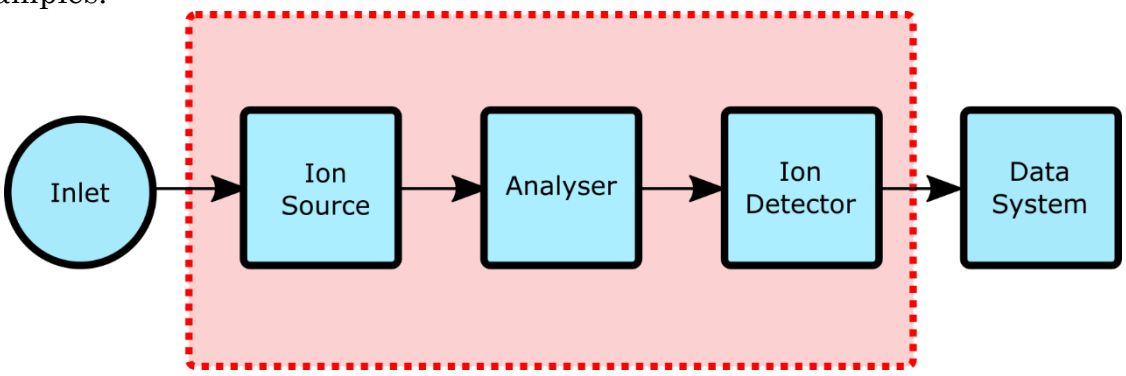

Figure 2.9 Schematic diagram of a mass spectrometer. The sample flows through the inlet into the source chamber. Here it is ionised by the ion source and the products flow into the analyser chamber. Here charged sample molecules are sorted by mass/charge ratio and flow onto an ion detector where they are detected, to be analysed by the data system.

2.3 Electrochemical Characterisation

The biosynthesised nanoparticles are tested for ORR activity as discussed in chapter 1 and chapter 4. As the ORR is an electrochemical reaction, the catalysts are evaluated via *ex-situ* electrochemical tests to test their catalytic activity. This is done *ex-situ* in a three-electrode half-cell. This section will cover the instrumentation used and the techniques used to characterise the catalysts electrochemically. For a basic introduction of electrochemistry please see Appendix A1.

2.3.1 Experimental set-up.

All *ex-situ* electrochemical tests were conducted in a three-neck half-cell. A general schematic is shown in figure 2.10. As shown, the half-cell has three openings to allow insertion of the counter electrode (CE), the reference electrode (RE), the working electrode (WE) and a gas inlet. The half-cell is surrounded by a glass jacket that allows circulation of water; this is used to control the temperature by using water of a set temperature.

Here, the WE used, was a glassy carbon electrode (GCE), the RE used was a reversible hydrogen electrode (RHE) (made in-house) and the CE used was a platinum wire mesh. The RE is used to set a potential difference across the RE and the WE. The CE is used as a separate electron sink in order to prevent any voltage losses at the RE by passing a current through it. The GCE was washed and polished using a series of alumnia slurries (1.0 μm, 0.3 μm and 0.05 μm) before a thin film of the catalyst was applied onto the top.

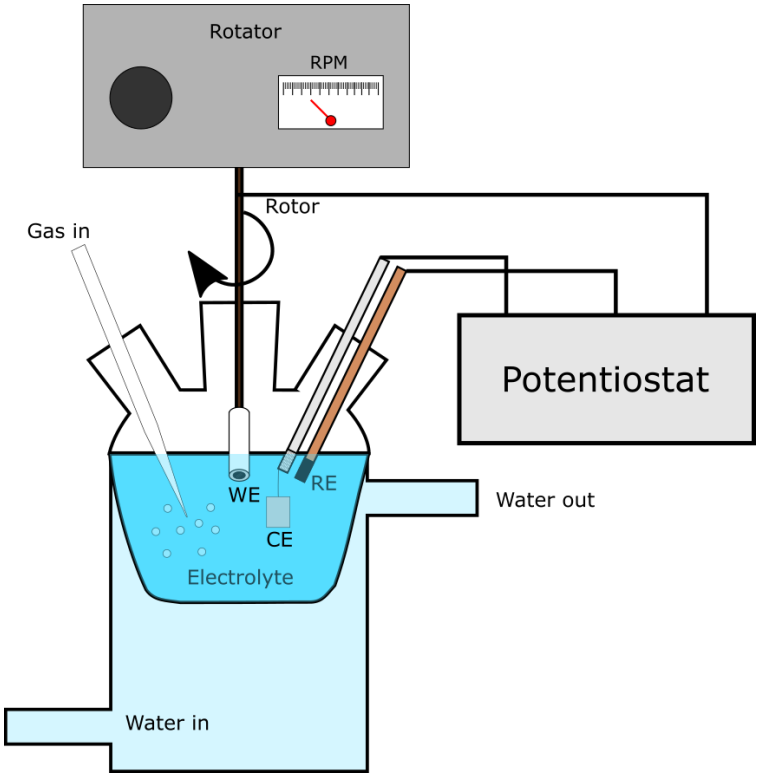

Figure 2.10 *Ex-situ* electrochemistry test setup with a three-neck half-cell. The cell is filled with 0.1M $HCl0_4$ electrolyte with a platinum mesh CE, GCE WE and an RHE RE. The electrodes are connected to a potentiostat that can apply a voltage and measure a current. The GCE is connected to a rotor whose rotation rates are controlled by a rotator. A gas inlet is used to saturate the electrolyte with N_2 or O_2.

The half-cell is filled with an electrolyte. In this work, 0.1 M $HClO_4$ was used as it is the standard electrolyte for ORR tests for a PEMFC catalyst. This is used for *ex-situ* tests as it mimics a perfluoro-sulfonic acid ionomer (such as Nafion®) and is provided at a suitable concentration to show excellent activity in Pt catalysts.[33] The gas inlet is used to switch between inert N_2 saturated atmosphere and an O_2 saturated environment depending on the experiment. The GCE (containing catalyst), RE and CE are all inserted into the three-electrode cell containing the electrolyte. The three electrodes are attached to a potentiostat. This used to control the potential difference across the RE and GCE and the current at each set voltage is recorded.

2.3.2 **Scientific basis of experiments conducted.**

The scientific basis for these experiments is described here; the information presented here (unless stated otherwise) is adapted from Bard and Faulkner[207] and the lecture notes on Introduction to Electrochemistry kindly provided by Dr. Neil V. Rees and Dr. Sarah Horswell, University of Birmingham.[275]

The potential energy of an electrochemical reaction, like the rection between oxygen and hydrogen in a fuel cell, can be characterised by the Nernst equation (Appendix A1) given below:

$$E = E^{\theta\prime} + \frac{RT}{nF} ln \frac{C_o^*}{C_R^*} \qquad \textbf{(Eq 2.9),}$$

where E is the potential difference, $E^{\theta\prime}$ is the conditional cell potential and C_o^* and C_R^* are the concentrations of the oxidised and reduced species respectively on the electrode surface. The current density drawn from the reaction can be related to the potential applied by the Butler Volmer equation (Appendix A1):

$$j = j_o \left(\frac{C_o^*}{C_o^B} e^{\left(\frac{\beta nF\eta}{RT}\right)} - \frac{C_R^*}{C_R^B} e^{\left(\frac{(-\alpha)nF\eta}{RT}\right)} \right) \qquad \textbf{(Eq 2.10),}$$

where j is the current density drawn, j_o is the exchange current density, and C_o^B and C_R^B are the bulk concentrations of the oxidised and reduced species respectively, η is the overpotential where $\eta = E - E^0$, n is the number of electrons transferred and α and β are the transfer coefficients which are a measure of the symmetry of the intermediate. j_o is specific to the catalyst material used and is a measure of how readily the reaction will occur. The higher the exchange current density the better the catalyst and as such is an important parameter to consider.

However, since the catalysts being examined are either Pt, Pd or a bimetallic of the two, the j_o is not expected to be substantially different from commercial Pt/C or Pd/C catalysts of the same. Furthermore, calculating this parameter is time-intensive and does not accurately represent the entire catalyst (metal and scaffold). As such the alternative parameters are considered, namely the electrochemically active surface area (ECSA), specific activity (SA) or the mass activity (MA).[33] These can be evaluated *ex-situ* using a three-electrode setup as described above.

2.3.2.1 Cyclic voltammetries (CV) for to evaluate ECSA

A CV scan is used in a three-electrode setup to identify the individual electron transfer events taking place in a reaction. CVs are performed by cycling the potential (E) of the WE against the RE in a stepwise manner (voltage scan rate (v)) and measuring the resultant current. Figure 2.11A shows a representative CV[208] taken of the redox couple $Fe(III)(CN)_6^{3-}$/ $Fe(II)(CN)_6^{4-}$ whose reaction is shown below:

$$\boldsymbol{Fe^{III}(CN)_6^{3-} + e \rightarrow Fe^{II}(CN)_6^{4-}} \qquad \textbf{(Eq 2.11),}$$

The representative CV is taken for the above reaction with 6.0 mM $K_3Fe(CN)_6$ in 1.0 M KNO_3 in water as the supporting electrolyte with a saturated calomel electrode (SCE). As seen (figure 2.11A), a potential of 0.8V vs SCE is set and decreased slowly (indicated by the right indicating arrow) to a potential of -0.2V vs SCE at which point, the potential is then scanned back to 0.8V vs SCE (left-indicating arrow). When the potential is sufficiently negative to reduce Fe(III), a cathodic current is generated and increases rapidly as indicated by the cathodic peak $E_{pc.}$ This current increases until the concentration of Fe(III)

immediately surrounding the electrode starts to diminish and the current decreases as the reaction rate is mediated by the diffusion (see appendix A1) of [Fe(III)] from the bulk solution to the electrode. When the scan is reversed, there is still a cathodic current as the electrode is still sufficiently negative to continue reduction of Fe(III). When the electrode becomes sufficiently oxidising, the Fe(II) ions that have been accumulating can now be oxidised by the electrode and an anodic current is seen. This reaches a peak at E_{pa} and diminishes as [Fe(II)] decreases. The two peaks seen are the reversible peaks for the above Fe(III)/Fe(II) redox couple. The formal reduction potential, $E^{o\prime}$ for this reversible couple can be identified by the following equation.

$$E^{o\prime} = \frac{E_{pa} + E_{pc}}{2} \qquad \textbf{(Eq 2.12)}$$

and peak current is given by the Randles-Sevick equation which for a reversible couple is the following:

$$I_p = \left(2.69 \times 10^5\right) n^{\frac{3}{2}} A C_{bulk} \left(vD\right)^{0.5} \qquad \textbf{(Eq 2.13)}$$

where Ip is the peak current, n is the number of electrons. A is the area of the electrode, C is the bulk concentration of the electroactive species, v is the voltage scan rate (Vs^{-1}) and D is the diffusion constant.

CVs can be used to characterise electrocatalysts as the peaks represent individual electron transfer events. As seen in figure 2.11B a CV is taken for Pt/C, in 0.1 m$HClO_4$ under inert N_2, to characterise it. The inert environment ensures no O_2 from the atmosphere will interact with the Pt/C catalyst. The H^+ and H_2O in the electrolyte will get reduced and oxidised by the Pt/C at various potentials and this is seen as peaks on the CV. As seen, the O_2 oxidation and

reduction peaks are seen at higher potentials (0.6–1.03V vs RHE) and the H_2 oxidation and reduction peaks are seen at lower potentials (0.05–0.4V vs RHE).

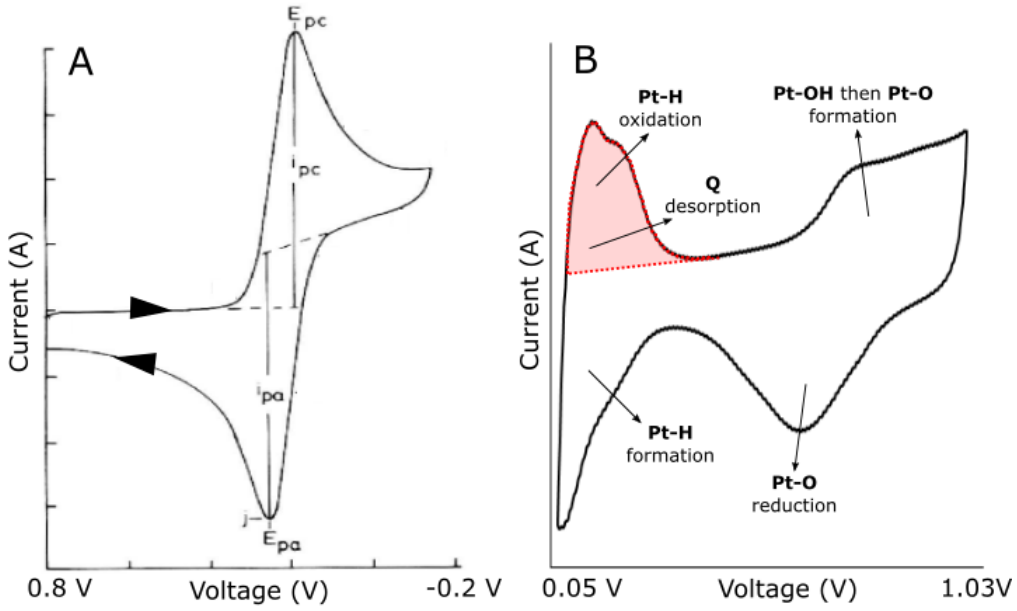

Figure 2.11 (A) Representative CVs of $Fe(III)(CN)_6^{3-}$/ $Fe(II)(CN)_6^{4-}$ redox couple using 6.0 mM $K_3Fe(CN)_6$ in 1.0 M KNO_3 in water as the supporting electrolyte with a SCE. Adapted with permission from Kissinger and Heineman.[208] (B) Pt/C in 0.1M $HClO_4$ under an inert atmosphere (N_2) with an RHE (this work).

These peaks can be used to calculate the ECSA of the catalyst, i.e., a measure of the total surface area of the catalyst available for catalysis. As shown in figure 2.11B the hydrogen peaks can be used to quantify ECSA. The area under the peak can be used to measure the amount of charges adsorbed onto the catalyst. The ECSA can then be calculated using the equation below.[33]

$$ECSA_{PGM}\left(m^2 g_{PGM}^{-1}\right) = \left[\frac{Q_{H\ adsoroption}}{210\ \mu C\ cm_{PGM}^{-2}\ L_{Pt}(mg_{Pt}cm^{-2})A_g(cm^{-2})}\right] 10^5 \quad \textbf{(Eq 2.14)},$$

where Q_H refers to the amount of charges adsorbed, $\mathbf{210\ \mu C}$ is a conversion factor, L_{Pt} is the loading of platinum on the electrode surface and A_g is the area of the working electrode.

Thus, CVs can be used to discern the electron transfer processes of an electrochemical reaction and to identify the ECSA of a catalyst. It cannot, however, be used to identify the kinetic activity of a catalyst. This is because the current measured under CVs is mediated by both the kinetics of the reaction and the mass transfer of electroactive species to the electrode. To combat this, rotating disk electrode experiments are used (RDE).

2.3.2.2 Linear sweep voltammetries (LSVs) conducted using RDEs

The mass transfer of electroactive species in the CVs discussed above are governed by diffusion and migration (Appendix A1). These mass transfer regimes can be hard to control and model. Alternatively applying a forced convection (Appendix A1) to the electrolyte via mechanical agitation results in a well-defined and easily interpretable mass transfer effect. The GCE shown in figure 2.10 is attached to a control system that allows the GCE to be rotated at set speeds (usually at speeds between 0–5000 RPM). This rotation of the GCE results in a constant and defined flow of the electroactive species from the bulk to the surface of the electrode. Thus, unlike a conventional CV (figure 2.11A) where after a specific potential (E_{pc}), the current decreases due to the rapid depletion of electroactive species, with an RDE, the current will not decrease. Instead, as there is a constant flow of reactants to the electrode, a limiting current will be achieved. This is given by the Levich equation below:

$$I_L = 0.62nFAD_0^{\frac{2}{3}}\omega^{\frac{1}{2}}v^{-\frac{1}{6}}C_0^* \quad \textbf{(Eq 2.15),}$$

Where I_L is the limiting current, A is the area of the electrode, D is the diffusion constant, ω is the rotation speed, v is the voltage scan rate, and C_0^* is the electrode surface concentration of the electroactive species. This can be simplified into the following equation:

$$I_l = B_L\omega^{\frac{1}{2}} \quad \textbf{(Eq 2.16),}$$

where B_L is the Levich constant. As seen from the equation, the limiting current is a dependent on the rotation rate. This can be seen when LSVs were taken for an electrochemical reaction at varying rotation rates (figure 2.12 A). An LSV scan, like a CV, measures the current produced when the potential difference applied is changed in a stepwise manner across a pre-set range. Unlike a CV, an LSV only scans in one direction. As seen, I_L , which was achieved at 350 mV in each case, progressively increased at higher rotation rates (figure 2.12A). Using Eq 2.16 and the Koutecky-Levich (KL) equation given below, one can identify the value of kinetic current I_k at any given potential.

The KL equation is shown below:

$$\frac{1}{I_{measured}} = \frac{1}{I_k} + \frac{1}{I_L} \quad \textbf{(Eq 2.17),}$$

can be rewritten as

$$\frac{1}{I_{measured}} = \frac{1}{I_k} + \frac{1}{B_L\omega^{\frac{1}{2}}} \quad \textbf{(Eq 2.18),}$$

This equation is used to plot a KL plot (figure 2.12B) whose intercept gives the value for I_k. As seen in figure 2.12B, the value for I_k can be determined for various potentials. For ORR catalysts, this value can then be used to identify the SA and MA of the catalyst as shown below.

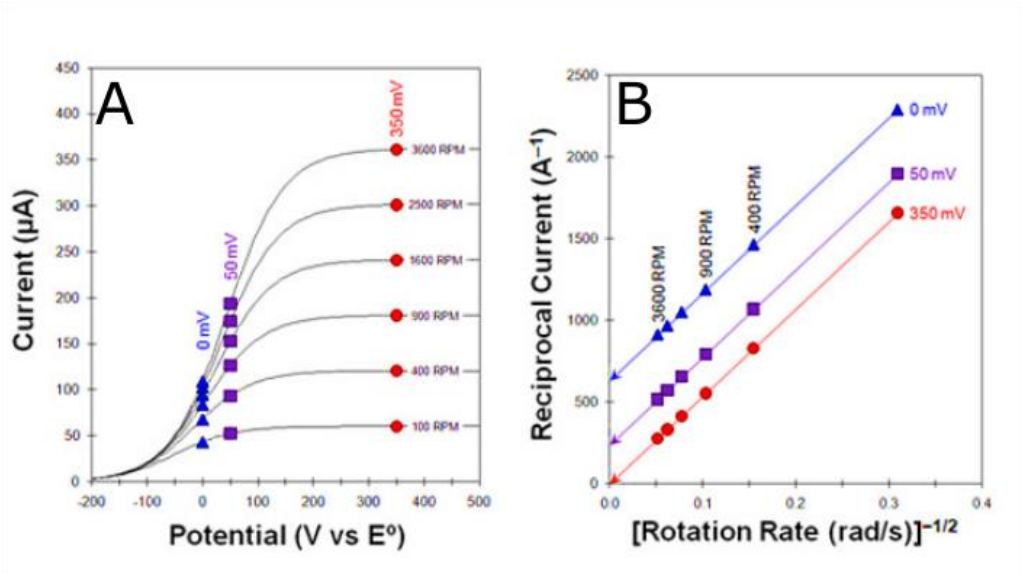

Figure 2.12 (A) LSVs for a representative electron transfer reaction at varying rotation rates. (B) shows the KL plot for the same set of LSVs shown in A. The currents identified at potentials 0 mV, 50 mV and 350 mV were used to produce KL plots. Adapted from Pine Research [277]

2.3.2.2.1 Specific Activity (SA) and Mass activity (MA)

SA is a measure of the turnover frequency of the catalyst, i.e., the amount of reactions occurring per second.[141] The I_k is then used to identify the specific activity of the catalyst using the following equation:[137]

$$Specific\ Activity\ (Ag^{-1}_{PGM}) = \left[\frac{I_K\ 210\ \mu C\ cm^{-2}_{PGM}}{Q_{H\ adsoroption}}\right] \qquad \textbf{(Eq 2.19)},$$

Where, I_k is the kinetic current, Q_H refers to the amount of charges adsorbed and **210 μC** is the conversion factor.

2.3.2.2.2 Mass activity (MA)

The mass activity relates to the activity of the catalyst per mass of PGM used. From this we can identify the mass activity using the following equation:[137]

$$\boldsymbol{Mass\ Activity}\left(\boldsymbol{Ag^{-1}_{PGM}}\right) = \left[\frac{\boldsymbol{I_K}}{\boldsymbol{L_{Pt}(mg_{Pt}cm^{-2})A_g(cm^{-2})}}\right] \qquad \textbf{(Eq 2.20),}$$

where, $\boldsymbol{I_k}$is the kinetic current, $\boldsymbol{L_{Pt}}$ is the loading of platinum on the electrode surface and $\boldsymbol{A_g}$ is the area of the working electrode.

2.3.2.3 Electrochemical impedance spectroscopy

A further experiment conducted to characterise the *E. coli*-NPs as ORR catalysts is electrochemical impedance spectroscopy. A proper introduction to electrochemical impedance is beyond the scope of this thesis but it has been introduced properly elsewhere.[276] In essence, it is a measure of the opposition to current, that the circuit presents, when a voltage is applied. In DC circuits, this impedance is commonly referred to as the resistance of the circuit and resistance '$\boldsymbol{R}$' is given by Ohms law:

$$\boldsymbol{R = \frac{V}{I}} \qquad \textbf{(Eq 2.21),}$$

In AC circuits, both voltage and current are sinusoidal and will thus, have a magnitude and phase angle. Impedance is thus, given by the ratio of the complex number representations of voltage and current, which is given below:

$$\boldsymbol{Z = \frac{V}{I}} \qquad \textbf{(Eq 2.22),}$$

and will also be a complex number with real and imaginary parts. Electrochemical impedance spectroscopy (EIS) is a method of applying a sinusoidal perturbation to the AC (either at the potential or the current) over a

wide range of frequencies. In the experiments described here, we used EIS by perturbing the applied voltage over a range of frequencies and measuring the current seen. In doing so, a true measure of the catalyst impedance is obtained. The catalyst on the WE within the electrolyte can be modelled using a simplified Randles cell, shown in figure 2.13A. As seen there is a resistance due to the electrolyte and a charge transfer resistance at the catalyst. Furthermore, the charged species in the electrolyte will form a double layer on the catalyst surface and confer a capacitance to the entire system. On applying a voltage on this circuit and perturbing it through a range of frequencies, the resultant current and thus the impedance can be measured. From this the real and imaginary components of the calculated impedance can be identified and plotted against each other in a Nyquist plot (figure 2.13B). The real impedance of this circuit is given by the equation:

$$\boldsymbol{Z_{Re} = R_e + \frac{R_{c,t}}{1+\omega^2 R_{c,t}^2 C_{dl}^2}} \qquad \textbf{(Eq 2.23),}$$

where $\boldsymbol{R_e}$ is the resistance due the electrolyte, $\boldsymbol{R_{c,t}}$ is the resistance to charge transfer at the catalyst, $\boldsymbol{\omega}$ is the frequency and C_{dl} is the capacitance of the charged double layer.

As seen from the Eq 2.23, at high frequencies, the value of the second term will tend to zero and thus the real impedance will tend to $\boldsymbol{R_e}$. At low frequencies, however, the value of the denominator of the second term will tend to 1 and, as such the value of the real impedance will equal $\boldsymbol{R_e + R_{c,t}}$. This results in the characteristic semicircle seen on the Nyquist plot (figure 2.13B).At high frequencies, the impedance seen is solely due to the electrolyte and at low

frequencies catalyst impedances will be a result of both the electrolyte and the catalyst. As such, the semicircle plotted on a Nyquist plot will provide a value for charge transfer impedance at the catalyst. The larger the semicircle, the stronger its impedance.

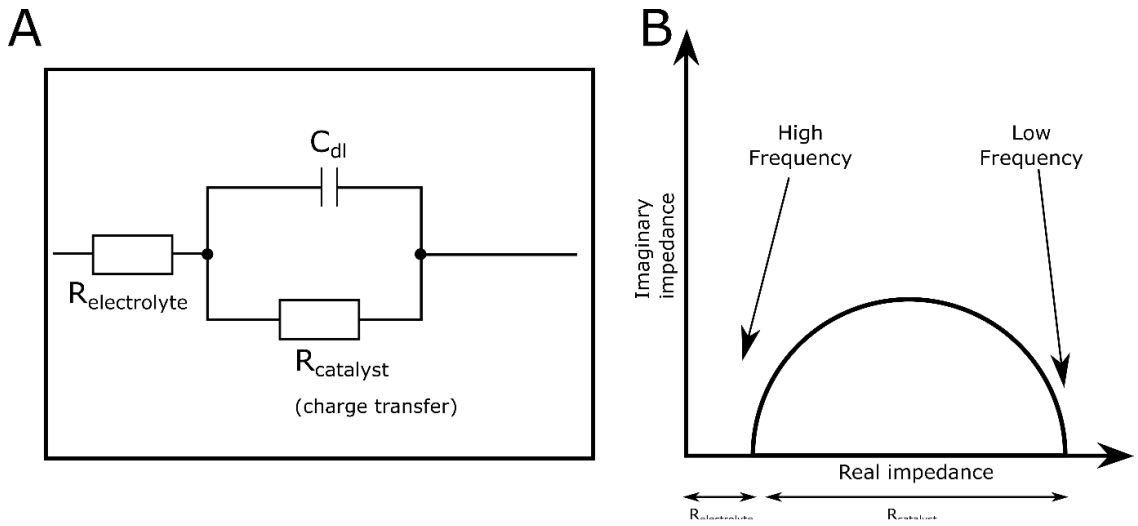

Figure 2.13 (A) Circuit diagram of a simplified Randles cell with the catalyst resistance and electrolyte resistance marked. (B) Nyquist plot of this diagram showing the impedance due to the electrolyte at high frequencies and the combined impedance due the electrolyte and charge transfer at the catalyst at low frequencies.

2.4 Conclusion

These techniques were used to evaluate use of *E. coli*-NPs as PEMFC catalysts in chapter 3 and chapter 4. Those described in section 2.2 were utilised in characterising *E. coli*-Pt, *E. coli*-Pd, *E. coli*-Pt:Pd* and *E. coli*-Pd:Pt* for nanoparticle size, shape, localisation and alloying in chapter 3. The techniques described in section 2.3 were used to evaluate their performance as ORR catalysts for use in PEMFCs in chapter 4.

Chapter 3: Characterisation of bimetallic Platinum and Palladium nanoparticles synthesised by *Escherichia coli* MC4100

3.1 Abstract

E. coli-Pd, *E. coli*-Pt, *E. coli*-Pt:Pd* and *E. coli*-Pd:Pt* were all synthesised and characterised using STEM, SAED, XRD, XPS and ICP-MS. *E. coli*-Pt:Pd* was synthesised by reducing Pt (IV) ions onto *E. coli*-Pd and *E. coli*-Pd:Pt* was synthesised by reducing Pd (II) ions onto *E. coli*-Pt.

STEM analysis showed that *E. coli*-Pd had ubiquitous NP synthesis (intracellular NPs and surface bound clusters) whereas *E. coli*-Pt showed Pt-NPs primarily associated to the surface of the cell. This initial patterning of single metals influenced the synthesis of the bimetallic *E. coli*-NPs. *E. coli*-Pt:Pd* showed similar NP localisation across the cell as *E. coli*-Pd and *E. coli*-Pd:Pt* showed similar NP localisation in surface bound clusters. Unlike *E. coli*-Pt, however, some intracellular NPs were seen.

All *E. coli*-NPs showed promise for ORR activity with the crystal face (111) being detected via XRD and SAED. Furthermore, STEM-EDX showed high co-localisation of Pt and Pd metals in both bimetallic catalysts indicating that they are likely to be alloys of Pt and Pd. This was further evidenced by XPS and XRD data. Finally, *E. coli*-Pt:Pd* showed evidence of a "Pt-rich" skin around clusters whereas this was not seen for *E. coli*-Pd:Pt*.

3.2 Introduction

Previously, the Pd in *E. coli*-Pd was reported to be found ubiquitously across the cell with surface bound clusters (figure 1.11). It showed electrochemical activity, and this was attributed to the highly dispersed Pd-NPs but was not checked for ORR activity.[139] The metal in *E. coli*-Pt synthesised under H_2, however, was previously seen to be clustered primarily at the cell surface (figure 1.13); this causes Pt-NPs in buried areas to be inaccessible for ORR activity.[125] It was hypothesised that *E. coli* synthesised bimetallic Pt/Pd could have potential as a direct-use ORR PEMFC catalyst. As such, this chapter reports two *E. coli*-synthesised bimetallics: *E. coli*-Pt:Pd* and *E. coli*-Pd:Pt*. Here the first metal added to cells is denoted with an asterisk. Hence, *E. coli*-Pt:Pd* refers to cells first allowed to deposit Pd (0) and then challenged with Pt and vice versa.

E. coli-Pt:Pd* (10%:10%) was synthesised by first synthesising *E. coli*-Pd (10%). The Pd-NPs were used as a seed to reduce Pt-NPs autocatalytically under H_2 to 10% Pt (metal wt/ dry cell wt) to a total metal wt% of 20%. Platinum synthesis, usually, requires enzymatic action, but bacteria are inherently dead post-palladium synthesis. This alternate route might divert Pt synthesis onto Pd seeds and result in a more evenly spaced nanoparticle shell as required from an engineered solution. *E. coli*-Pd:Pt* (10%:10%) was synthesised in a similar manner but used *E. coli*-Pt (10%) as seeds for autocatalytic Pd-NP synthesis under H_2 (10 wt % Pd).

This chapter will characterise the synthesised *E. coli*-Pt (20%), *E. coli*-Pd (20%), *E. coli*-Pt:Pd* (10%:10%) and *E. coli*-Pd:Pt* (10%:10%) using STEM, HRTEM,

XRD, SAED and XPS to elucidate nanoparticle sizes, shapes, localisation, alloying and other salient features formed.

3.3 Materials and Methods

3.3.1 Bacterial growth and biosynthesis of nanoparticles

E. coli MC4100 was provided by Dr. D. Linke (University of Oslo). Cells were maintained aerobically at 30 °C on nutrient agar plates. For experiments, cultures were first grown aerobically in nutrient broth number 2 (NB 2, Oxoid) at 37 °C to the mid-exponential phase and a 10% v/v inoculum was used to inoculate 200 mL of anaerobic (under oxygen free N_2 (OFN)) growth medium (NB 2 with 0.5% (vol/vol) glycerol and 0.4% fumarate (wt/vol)) at 37 °C. This was left to grow overnight in sealed anaerobic bottles. At mid-exponential phase, this was used to inoculate 2000 mL of the same anaerobic medium and in sealed bottles (N_2 headspace gas) cells were harvested in mid-exponential phase and then concentrated via centrifugation in air (13,720 g, 15 mins). The pellet was washed three times and re-suspended in 20mM MOPS-NaOH buffer (pH 7) to 25–30 mg mL^{-1} dry weight of cells and stored under OFN at 4 °C until use, usually the next day. The dry wt L^{-1} was estimated by reference to previously determined OD_{600} to dry wt conversion.[125]

For nanoparticle synthesis, 2 mM solutions of K_2PtCl_6 and Na_2PdCl_4 in 0.01 M HNO_3 were used as precursors. For single metal NP synthesis: To a specified volume of metal salt solution, an appropriate amount of *E. coli* suspension was added for a final dry wt ratio of metal:cells of 1:9 (for 10% metal loading, or as otherwise stated). This metal/cell mixture was left to stand at 30 °C for 30 mins

for metal biosorption and then sparged with H_2 for 10 mins to promote reduction of nanoparticles. Metal uptake from solution was monitored using a tin chloride assay as described in Deplanche *et al.*[117] Once nanoparticle synthesis had reached completion (no residual metal by assay[117]), the 'as made' *E. coli*-NP preparation was centrifuged in air (13,720 g, 15 mins), washed three times and re-suspended in ultrapure water.

For bimetallic nanoparticle synthesis, *E. coli*-Pd was first made as above (10wt% Pd) and to this an appropriate volume of Pt solution was added for a final Pt:Pd:cells (w/w/w) ratio of 1:1:8 (for a 10%Pt:10%Pd loading) and sparged with H_2 for a further 20 mins. As with Pd, Pt uptake was monitored using a tin chloride assay. Once nanoparticle synthesis was complete, the 'as made' *E. coli*-Pt:Pd* (10%:10%) was similarly washed and re-suspended in ultrapure water. For the "reverse" NP, the first metal was Pt (IV) to 10wt% followed by Pd (II) solution to make the bimetallic, *E. coli*-Pd:Pt* (10%:10%), under H_2. This was similarly washed and re-suspended in ultrapure water.

3.3.2 STEM analysis

Samples were harvested by centrifugation (13,720g, 15 mins), fixed in 2.5% (w/v) glutaraldehyde, then centrifuged, and resuspended in 1.5 ml 0.1 M sodium cacodylate buffer (pH 7). Cells were dehydrated in a series of ethanol solutions (50, 90, 100, 100 100% dried ethanol, 15 mins each), washed twice in propylene oxide and embedded in epoxy resin and the mixture was left to polymerise (24 h at 60 °C). Resin was sectioned using an ultramicrotome and sections (100–150 nm) were placed onto a copper grid and routinely viewed with a JEOL 1200CX2

TEM with an accelerating voltage of 80 kV. For better visualisation of small bio-NPs, the samples were examined using scanning transmission electron microscopy using a FEI image Cs-corrector configuration Titan™ G2 60–300 STEM microscope, accelerating voltage of 300 kV. The samples were viewed under brightfield and HAADF was used to analyse them as described by Gomez-Bolivar *et al.*[192] Nanoparticle size analysis was conducted primarily using the "analyse particles" function of ImageJ software.[213,214] After an image was chosen, it was uploaded to ImageJ where it was duplicated, and a bandpass filter function was applied to distinguish Pd-NPs. Image thresholding was then done to avoid uneven illumination and the image was cleaned up and used to analyse NP sizes using the "analyse particles" function. In cases where this function could not be used (due to heavily clustered NPs), NPs that could be identified were measured individually on ImageJ. A size distribution histogram was then drawn.[213,214]

Using EDX elemental maps were obtained for all samples. For specific samples, clusters were analysed with an EDX line profile as described by Gomez-Bolivar *et al.*[192] Selected nanoparticle areas were subjected to SAED and diffraction patterns were utilised to identify Miller indices. Finally, specific nanoparticles were selected for high-resolution TEM (HRTEM) to identify lattice spacing within the nanoparticle.

3.3.3 XRD analysis

Catalyst was dried on a filter paper overnight (105 °C), ground to a fine powder using an agate mortar and X-ray powder diffraction patterns were obtained

using a Bruker D8 Advance Diffractometer using a Cu Kα X-ray source. Powder patterns were acquired between 2θ values 20° – 80°.

3.3.4 ICP-MS

Inductively coupled plasma mass spectrometry (ICP-MS) was used to estimate the actual metal loading on the cells (metal weight/total dry weight of catalyst) by analysis of soluble metals in digestate. 0.5 mg of the catalyst powder was dissolved in 10 ml of 25% *aqua regia* (HNO_3/HCl; 6.6%:18.9% vol/vol, with the rest water), sonicated at 90 °C (Ultrawave U300H, 35W; 1 hour) and then mechanically agitated (on a platform shaker; 2 h) to ensure complete dissolution of metal samples. They were diluted to produce a solution of 2% HNO_3 and used for ICP-MS analysis against an appropriate calibration curve using a Perkin Elmer Nexion 300X with plasma wattage of 1500 and a seaspray nebuliser connected to a cyclonic spray chamber used for sample introduction. Sample was pumped through via a peristatic pump (0.3mL/min).

3.3.5 XPS scan

XPS samples were prepared as for XRD, the powders were then drop cast onto a silicon wafer. XPS data were collected at the Harwell XPS facility at Diamond Light Source, Didcot, Oxford. This was conducted using an XPS spectrometer (Thermo Fisher Scientific NEXSA spectrometer, Loughborough, Leictershire, UK) using a micro-fused monochromatic Al Kα source (1486.6eV).

3.4 Results and Discussion

Initially single metal *E. coli*-Pt (20%) and *E. coli*-Pd (20%) (or as otherwise stated) were synthesised and characterised. Results are shown below and discussed.

3.4.1 Single metallics: *E. coli*-Pd (20%) and *E. coli*-Pt (20%)

E. coli-Pd (20%) and *E. coli*-Pt (20%) were synthesised under H_2 as detailed in the Materials and Methods section. *E. coli*-Pd (20%) showed complete metal reduction with all cells reducing metal within less than a minute whereas *E. coli*-Pt (20%) took overnight for complete metal reduction and as noted previously,[125] not all cells showed metal reduction (shown below). The percentage of cells showing metallisation relative to un-metallised cells was not quantified. The catalysts were then dried into powder for XPS and XRD characterisation and prepared (as described above) for observation under a TEM and STEM with EDX.

3.4.1.1 STEM images and localisation

As shown in figure 3.1A all *E. coli*-Pd cells showed Pd reduction with nanoparticles observed ubiquitously across the cell. On comparing with previous result by Courtney *et al.*, (inset), *E. coli*-Pd (20%) (figure 3.1A) showed more surface bound NP clusters. As such, ICP-MS was used to confirm loading for this sample and it was calculated to be 15% (due to experimental error) and is referred to as such wherever appropriate. However, as the features seen for both are similar, it is assumed that true *E. coli*-Pd (20%) will have larger NPs (than *E. coli*-Pd (15%)) with similar crystalline characteristics; future studies

will have to confirm this. figure 3.1B shows a HAADF image of a representative cell with specific features. The HAADF detector was used to image the cell and nanoparticles were observed as bright spots in the cytoplasm, within the periplasm and as clusters located at the surface. To confirm Pd deposition and investigate NP localisation, STEM-EDX maps were obtained for a representative cell for Pd, and P (as shown in figure 3.1C,D and E). The P localisation map shows the boundary of the cell; cell membranes are composed of phospholipids and thus, P atoms are heavily concentrated at the cellular boundary. This can be used in conjunction with the Pd EDX map to show the Pd localisation. Pd nanoparticles are clearly seen ubiquitously across the cytoplasm, periplasm and as surface associated clusters. In contrast to a previous study, with Gram-positive *Bacillus benzeovorans* where Pd was seen co-localised with P, there is no apparent co-localisation of the two elements here.[126]

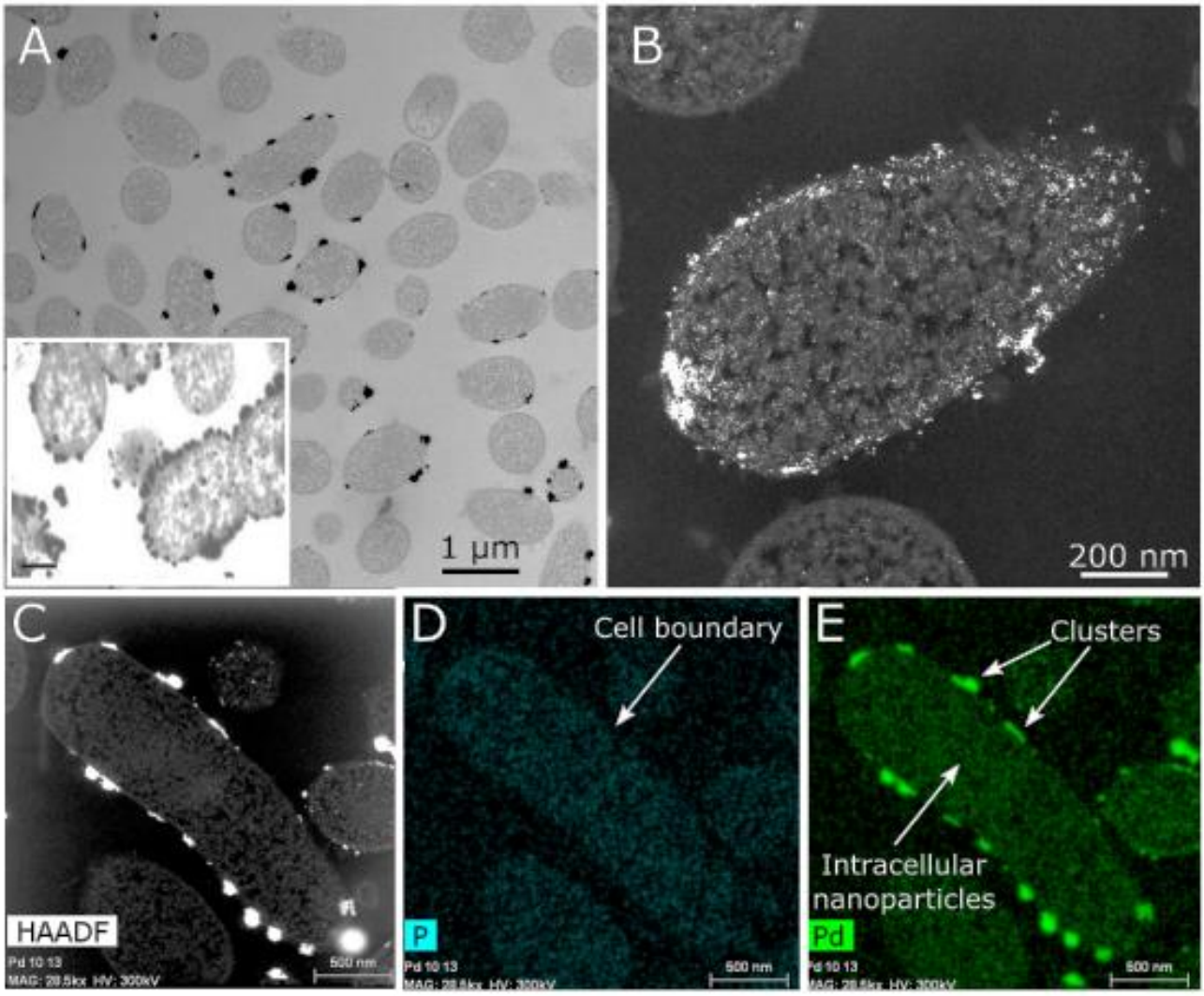

Figure 3.1 (A) STEM image of *E. coli*-Pd (15%). All cells were shown to have reduced nanoparticles. Clusters can be seen on most cells with nanoparticles seen ubiquitously around the cell (inset shows *E. coli*-Pd (20%) adapted with permission from Courtney *et al.*[139] with scale bar of 200 nm) (B) High-resolution STEM-HAADF image of a representative cell. As shown in the figure nanoparticles can be observed intracellularly, in the periplasm and surface located clusters. (C,D,E) STEM-EDX maps of the cell with (C) (via HAADF) showing the cell observed, (D) showing the localisation of the phosphorus (used to identify the cell boundaries) and (E) showing Pd localisation across the cell as surface clusters and numerous small intracellular NPs. Scale bars are shown.

E. coli-Pt (20%) loading was confirmed by ICP-MS. Unlike *E. coli*-Pd (15%), *E. coli*-Pt (20%) did not show consistent metal reduction in all cells. Most cells showed concentrated Pt nanoparticles at the cell surface (with none intracellularly), while some others seemed empty; this effect was previously seen with *E. coli*-Pt (10%) by Williams[125] (figure 3.2A). This was observed experimentally where, on centrifugation, pelleted cells showed a gradient of colour with beige non-metallised cells at the top and grey metallised cells at the bottom. Figure 3.2B shows a STEM-HAADF image of representative *E. coli*-Pt (20%) cells where Pt reduction is heavily clustered. This localisation was further confirmed by STEM-EDX maps obtained. Figure 3.2C shows a STEM-HAADF image of a representative *E. coli*-Pt (20%) cell and figure3.2D and 3.2E shows STEM-EDX maps of P and Pt, respectively. The localisation of P in the cell is used to identify its boundaries and as shown, Pt nanoparticles are clustered together on the surface and for this cell, Pt is absent intracellularly. Interestingly, figure 3.2C show Pt-NPs present within one cell, potentially localised with bacterial DNA (asterix). $[PtCl_4]^{2-}$ is a chemical analogue to cisplatin, commonly known to bind to DNA, and might accumulate here via a similar mechanism.

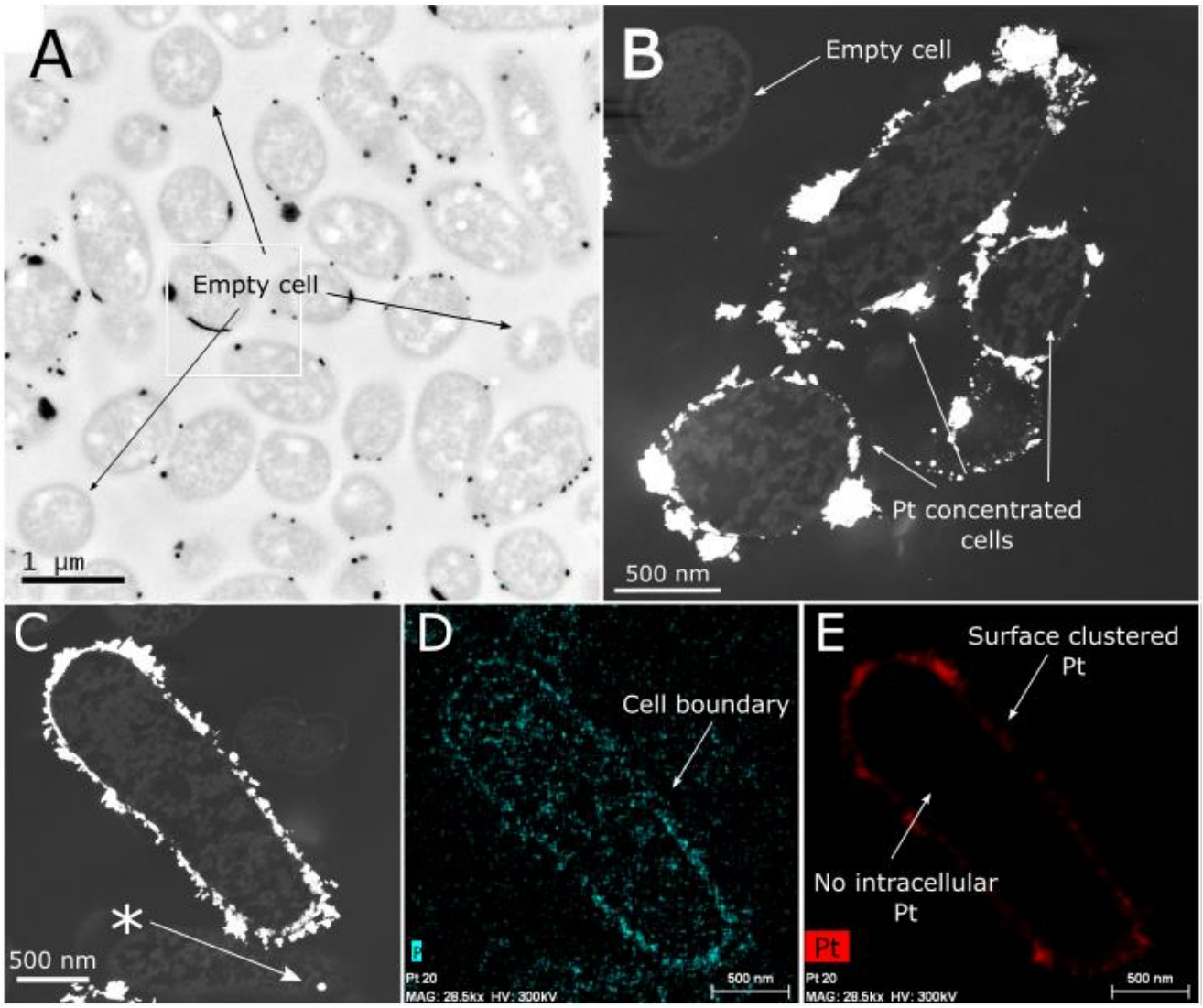

Figure 3.2 (A) TEM image of *E. coli*-Pt (10%) adapted from Williams.[125] Most cells have Pt-NPs while some empty cells are seen. (B) High-resolution STEM HAADF image of Pt concentrated cells where Pt is shown up as bright regions. As shown in the figure, Pt clusters are seen on the cell surface and not intracellularly. Furthermore, an empty cell is observed in the vicinity (arrowed). (C,D and E) STEM-EDX maps of the cell with (C) (via HAADF) showing the cell observed. * shows Pt-NP intracellularly possibly associated with the bacterial DNA, (D) showing the localisation of the phosphorus (used to identify the cell boundaries) and (E) showing Pt localisation on the cell surface. Scale bars are shown.

3.4.1.2 **Size analysis**

The sizes of the *E. coli*-Pd (15%) and *E. coli*-Pt (20%) NPs were characterised using STEM images and ImageJ analysis to create a nanoparticle size distribution. Figure 3.3 and 3.4 shows the investigated *E. coli*-Pd (15%) and *E. coli*-Pt (20%) respectively.

Figure 3.3A shows the Pd-NP size distribution for Pd-NPs present in the (B) cytoplasm, (C) the periplasmic space, and (D) surface located clusters of *E. coli*-Pd (15%) and (figure 3.3B, 3.3C and 3.3D respectively). For (B) and (C), NPs were sized using the "analyse particles" function on ImageJ (Materials and Methods). As seen in figure 3.3B, Pd-NPs are well dispersed with a range of sizes; 224 Pd-NPs were sized, and a median Pd-NP size of 2 nm (with over 50% of NPs sized in the 1.5–2.0nm range) and a mean of 2.4 $\pm$ 1.2 nm was identified.

Figure 3.3C shows the size distribution of Pd-NPs found in the periplasmic space; 30 Pd-NPs were sized and 24 of those sized were in the 1.5–3.5 nm range with a median of 2.5 nm (6 Pd-NPs) and a mean of 2.8 $\pm$ 1.2 nm. This result and error are subjective as membrane boundaries were not clearly defined.

Finally, figure 3.3D shows Pd-NP size distribution in the cluster. The cluster on closer inspection were shown to be agglomerations of individual nanoparticles as described previously elsewhere[139] (high resolution image appendix A2.1.1). The "analyse particles" function could not be used for this image as the nanoparticles were far too clustered for the threshold function. However, 33 individual nanoparticles could be observed, and these were measured. The size distribution for these showed a range of 4 nm to 7.5 nm with a median of 5.5 nm

and a mean of 5.3 ± 0.8 nm. Thus, while Pd-NP sizing is less accurate for Pd-NP clusters (33 clustered Pd-NPs vs 224 Pd-NPs in the cytoplasm), it can be stated with reasonable confidence that clustered Pd-NPs are larger than cytoplasmic and non-clustered periplasmic Pd-NPs. Similar sizes were previously seen with other bio-Pd NPs.[126] The threshold images and the nanoparticles measured are shown in the appendix (A2.1.1).

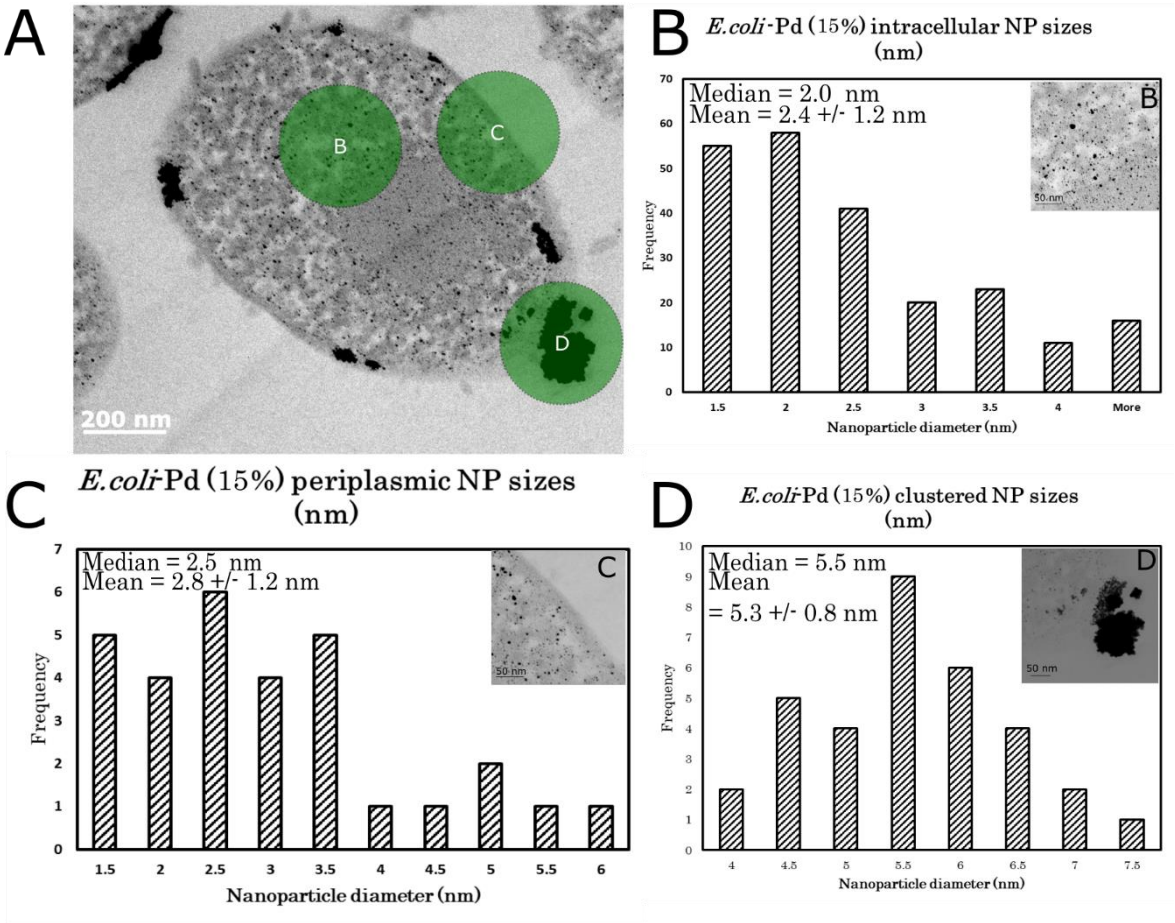

Figure 3.3 (A) shows a representative STEM image of an *E. coli*-Pd (15%) with areas marked in green (B), (C), and (D) to indicate NPs sized in the cytoplasm, periplasm, and surface bound cluster respectively. As seen *E. coli*-Pd shows a median NP of (B) 2 nm in the cytoplasm, (C) 2.5 nm in the periplasm and (D) 5.5 nm in the clusters. Furthermore, a mean of (B) 2.4 nm in the cytoplasm, (C) 2.8 nm in the periplasm and (D) 5.3nm in the clusters were seen. Scale bars are shown.

Figure 3.4A shows Pt-NPs found in surface clusters and these were investigated to size Pt-NPs at locations B and C. Other locations investigated showed were highly clustered and individual NPs could not be identified. Location B was less clustered and thus could be analysed using the analyse particles function on ImageJ and the Pt-NP size distribution is shown (figure 3.4B). 45 Pt-NPs were analysed, and a median Pt-NP range of 2.5–3.5 nm and a mean of 3.7 $\pm$ 1.4 nm is seen. This range was also seen in the more clustered location C. The "analyse particles" function could not be used here and thus, observed nanoparticles were individually measured (figure 3.4C). As seen in figure 3.4D, 8 nanoparticles could be identified and showed a median range of 3.0–3.5 nm and a mean of 3.0 $\pm$ 0.4 nm. The threshold image and individual measurements are shown, alongside a cluster that could not be used to measure individual NPs in appendix A2.1.2. It is important to note that Pt-NP sizing was done with a small sample size and thus, this result is likely less accurate than the sized *E. coli*-Pd NPs.

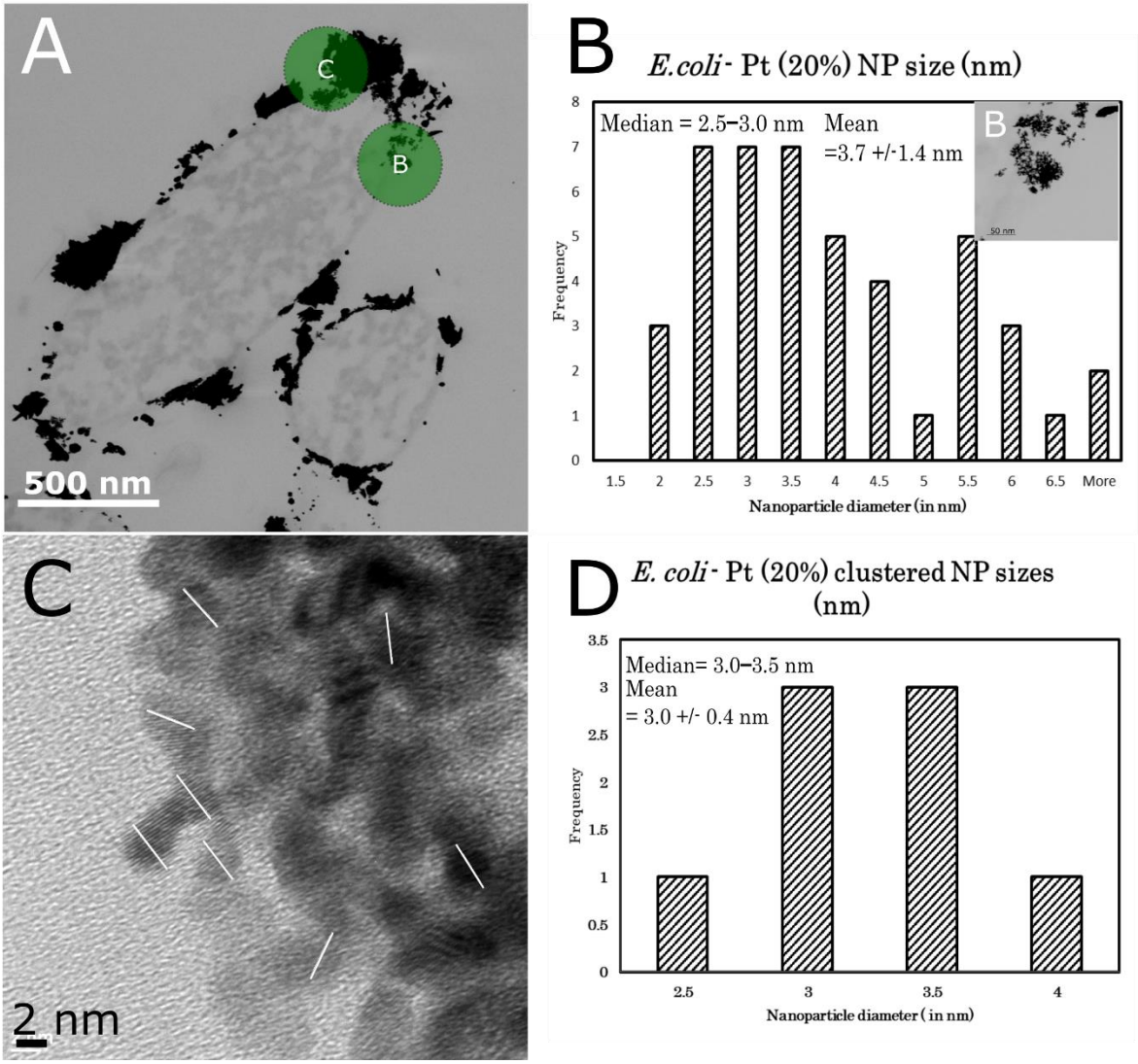

Figure 3.4 (A) shows a representative STEM image of an *E. coli*-Pt (20%) with areas marked in green (B) and (C) to indicate NPs sized in the two separate clusters. As seen, (B) shows the size distribution with a median NP of 2.5 - 3.5 nm for area marked B (shown inset) and (C) and (D) shows the high resolution image of cluster marked C and its size distribution with a median of 3.0 – 3.5 nm respectively. The white bars in C indicate the nanoparticles were sized manually Scale bars are shown

3.4.1.3 **Shape analysis**

XRD, HRTEM and SAED were all used to analyse the shape and crystallinity of the produced *E. coli*-Pd and *E. coli*-Pt NPs. The XRD pattern taken for powdered (*E. coli*-Pd 20%) showed peaks corresponding to (111), (200) and (220) at 2θ values of 40.20°, 46.73° and 68.16° (figure 3.5) indicating an FCC crystal

structure. XRD analysis of *E. coli*-Pt (20%) (figure 3.5) only showed one slightly discernible peak at 2θ values of ~ 40° for the (111) lattice plane which lined up with (111) peak shown by *E. coli*-Pd (20%) (dotted line). This peak can be disregarded for further calculation as it is not clearly defined to elucidate its true value. Furthermore, a novel peak is seen at ~ 30° but as this is not well defined, it is disregarded. This pattern implies low crystallinity which could be attributed to the highly clustered nature of *E. coli*-Pt which would be held as largely non crystalline biomaterial.

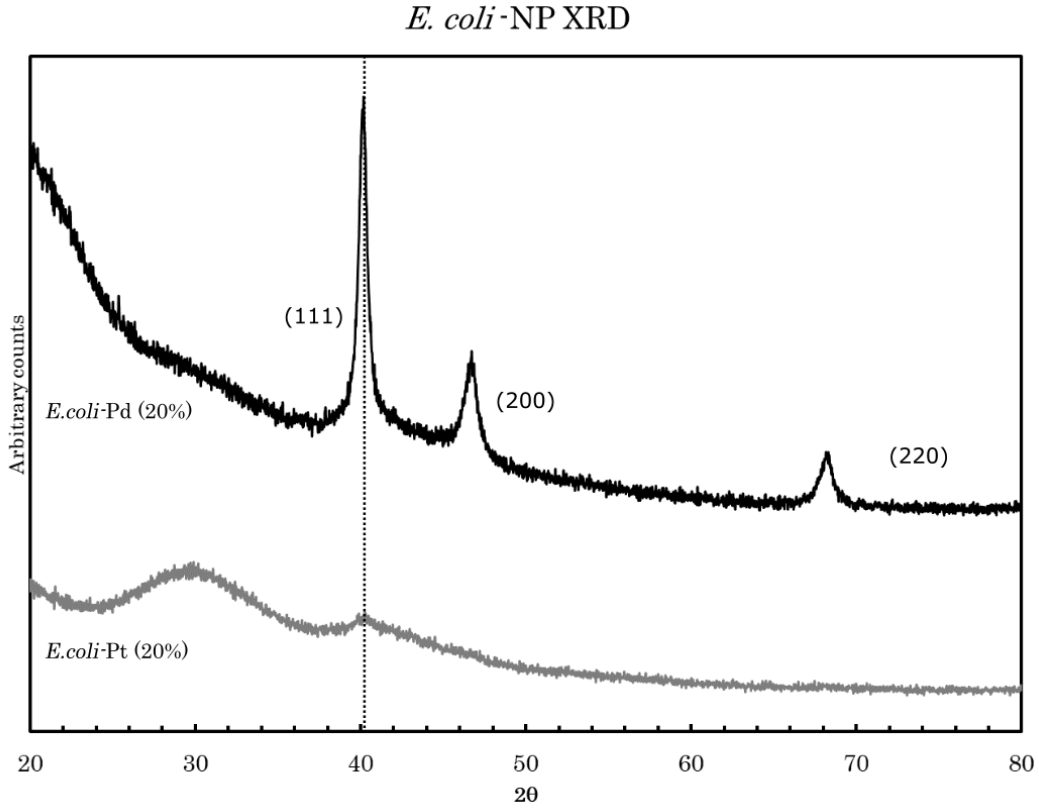

Figure 3.5 shows the XRD pattern for *E. coli*-Pd (15%) (black) and for *E. coli*-Pt (20%) (grey). *E. coli*-Pd (15%) shows peaks at 2θ values of 40.20°, 46.73° and 68.31° corresponding to (111), (200) and (220) respectively. *E. coli*-Pt (20%) shows one discernible peak at 2θ value of corresponding to (111) that lies along the same peak as *E. coli*-Pd (20%) as indicated by the dotted line

These lattice planes were further confirmed by an SAED analysis, figure 3.6A and figure 3.6 C, conducted on a cluster (appendix A2.2) of *E. coli*-Pd (15%) and *E. coli*-Pt (20%) respectively. For *E. coli*-Pd (15%) (figure 3.6A) SAED showed diffraction patterns corresponding to (111), (200) and a pattern for the (220) plane was faintly discernible. These patterns agreed with previous patterns seen for chemically synthesised Pd-NPs.[209] SAED analysis of *E. coli*-Pt (20%) showed a highly crystalline nanostructure within the amorphous bulk. It showed patterns for (111), (200), (220), and higher indexed plane (311) as well. Further patterns were seen, and these were compared to previous SAED images taken for chemically synthesised Pt-NPs.[211] They are expected to be patterns for the (222) and (400) lattice planes but the patterns were too blurry to confirm this. HRTEM images were used to confirm these findings shown in figures 3.6B and 3.6D. For a representative Pd-NP (figure 3.6B), a d spacing of 0.23 nm was seen. This spacing corresponds to the (111) lattice plane for Pd.[210] Furthermore, all of this suggests similar crystallinity between *E. coli*-Pd (15%) and *E. coli*-Pd (20%).

Most HRTEM images taken of *E. coli*-Pt (20%) showed highly clustered NPs, and an example of such an image is showed in appendix figure A2.1.2E. However, for a less clustered HRTEM image, figure 3.5E, a representative Pt-NP is identified. Its d spacing was measured at 0.23 nm which corresponds to the (111) lattice plane.[212] This spacing value differs for *E. coli*-Pt and *E. coli*-Pd in the 0.001 nm range, but this resolution is not achievable here. As such, the lattice spacing value (0.23 nm for both) is thought to correspond to the (111) lattice plane for both and is verified by the presence of this peak in both XRDs.

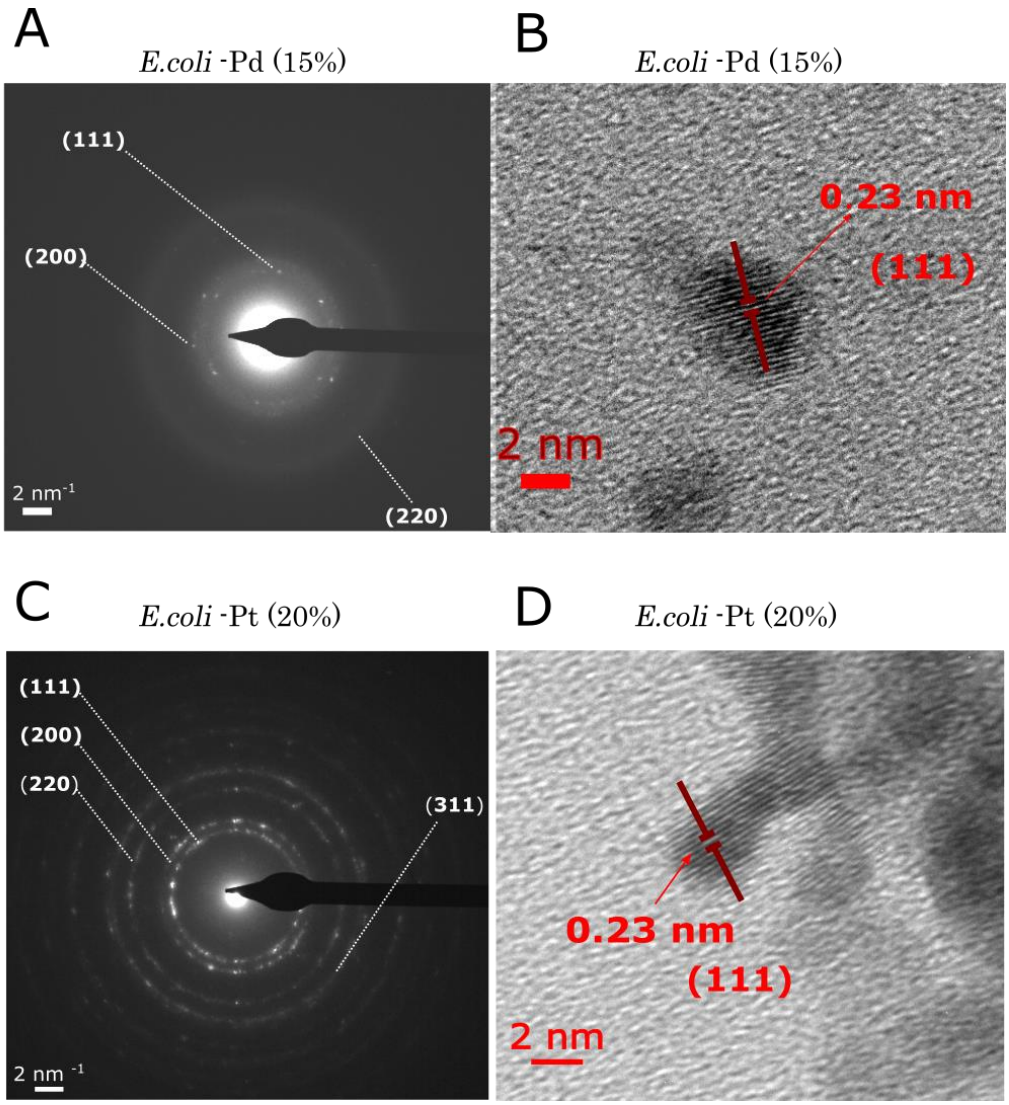

Figure 3.6 (A) and (C) shows the SAED obtained for *E. coli*-Pd (20%) and *E. coli*-Pt (20%) respectively. (A) identifies the SAED diffraction patterns as (111), (200) and (220) and (B) identifies the SAED diffraction patterns as (111), (200), (220) and (311). (B) and (D) shows a representative HRTEM obtained for *E. coli*-Pd (20%) and *E. coli*-Pt (20%) respectively. The lattice fringe spacing for both were identified to be 0.23 nm which correlates to a (111) lattice plane. Scale bars are shown

3.4.1.4 XPS and Oxidation state analysis

XPS analysis was used to analyse the oxidation states of *E. coli*-Pd (20%) and *E. coli*-Pt (20%). The complete XPS survey scans for both *E. coli*-Pd (20%) and *E. coli*-Pt (20%) are shown in appendix (A2.3). Figure 3.7A shows a high-resolution

Pd3d XPS scan of *E. coli*-Pd (20%). The scan is shown in black with the fit to the scan shown as an orange dotted line. The $Pd3d_{3/2}$ and $Pd3d_{5/2}$ binding energy peaks are 340.78 eV and 335.28 eV respectively. Deconvoluting the peaks showed that *E. coli*-Pd is found in both oxidation states Pd (0) (blue) and Pd (II) (green).

A high-resolution Pt 4f scan of *E. coli*-Pt (20%) is shown in figure 3.7B (black) with the curve fit shown as an orange dotted line. These $Pt4f_{5/2}$ and $Pt4f_{7/2}$ peaks were seen at 76.28 eV and 73.08 eV respectively. Deconvoluting the peaks showed Pt in oxidation states Pt (0) (blue), Pt (II) (red) and Pt (IV) (green). Thus, both types of NP were not solely of metallic deposit but contained partially oxidised species as well as metal oxides.

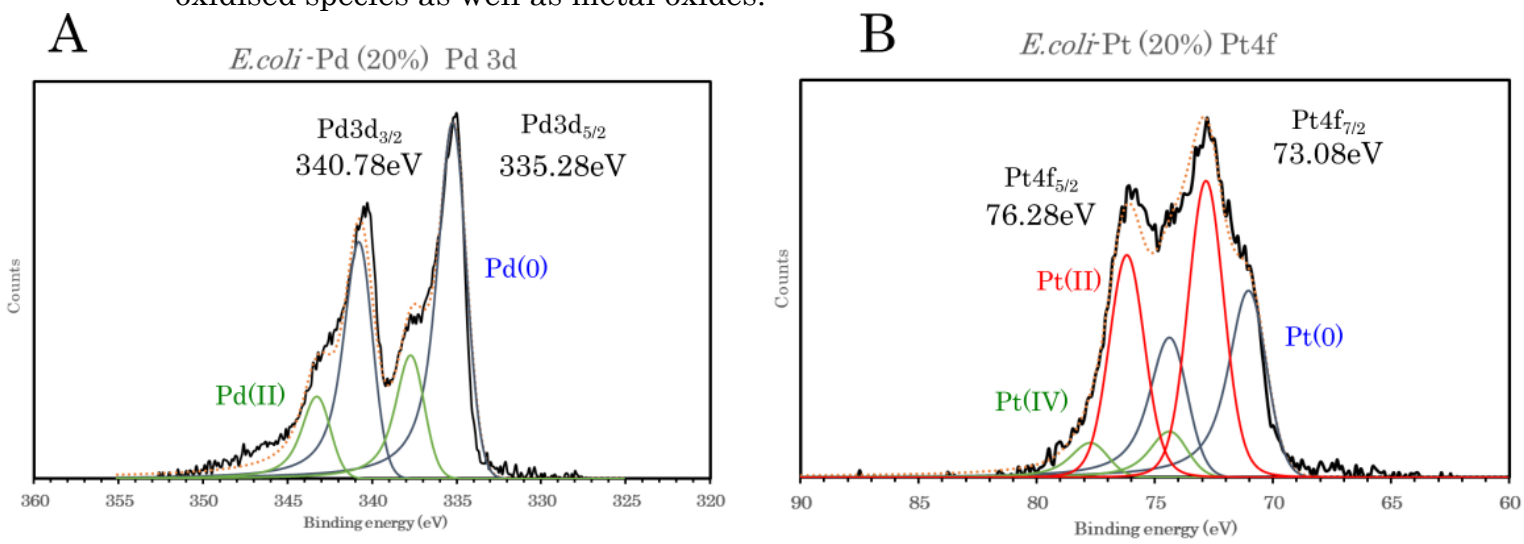

Figure 3.7 (A) High resolution Pd3d XPS scan of *E. coli*-Pd (20%) with the scan shown in black. The curve fit is shown in dotted orange and showed the peaks for $Pd3d_{5/2}$ at 335.28 eV and $Pd3d3_{/2}$ at 340.78 eV. Deconvoluting the peaks showed oxidation states of Pd (0) (in blue) and Pd (II) (in green). (B) High resolution Pt4f XPS scan of *E. coli*-Pd (20%) with the scan shown in black. The curve fit is shown in dotted orange and showed the peaks for $Pt4f_{7/2}$ at 73.08 eV and $Pt4f_{5/2}$ at 76.28 eV. Deconvoluting the peaks showed oxidation states of Pt (0) (in blue), Pt (II) (in red) and Pt (IV) (in green)

3.4.1.5 Summary of *E. coli*-Pd (20%) and *E. coli*-Pt (20%) characterisation

The above results for both *E. coli*-Pt (20%) and *E. coli*-Pd (20%) (and *E. coli*-Pd (15%)) are summarised and discussed here.

E. coli-Pd (15%) shows nanoparticles ubiquitously across the entire cell (in the cytoplasm and periplasmic space) and clusters associated with the surface. The Pd-NPs seen in the cytoplasm had a mean diameter of 2.4 ± 1.2 nm. The clusters were shown to be agglomerations of individual nanoparticles and sized at a range of 4.5nm–7.0 nm with a mean of 5.3 ± 0.8 nm. Regardless of the smaller sample size (33 clustered vs 224 in the cytoplasm), it can be concluded by observation that clustered NPs are bigger in size. Pd-NPs in the periplasm were sized but the boundaries of this space were not well defined and though a mean of 2.8 ± 1.2 nm is obtained; this result is subjective and disregarded.

Taken together, it is clear that the proposed hydrogenase mechanism is not the only mode of Pd-NP reduction as the presence of ubiquitous intracellular Pd-NPs suggest alternative routes to NP synthesis. However, the bigger sizes of Pd-NPs in the surface associated clusters imply a preference for this region of the cell; this is possibly mediated by hydrogenase enzyme activity. Further studies that upregulate hydrogenase enzyme activity may confirm this preference and this effect in *E. coli*-Pd (20%).

E. coli-Pt (20%) however, did not show ubiquitous nanoparticle synthesis. Only a few cells were involved in nanoparticle reduction and this was seen primarily as surface associated clusters. STEM images showed these clusters to be agglomerations of individual nanoparticles. Size analysis conducted on two

clusters showed a mean NP size of around 3.7 ± 1.4 nm. There is an absence of intracellular Pt-NPs and a preference for the surface of cells. This implies that the preferred site of Pt-NP reduction lies within the periplasmic space and/or surface of bacterial cells. A possible involvement of an uptake mechanism for Pd (II) was discussed by Torgeman;[156] it is possible that a cellular recognition mechanism does not exist for Pt (IV) and/or that the latter is highly toxic. It is not conclusive that the hydrogenase mechanism plays a role here as one would expect Pt(II) ions to be detected within the cytoplasm of the cell. More experiments are required to fully dissect this mechanism of reduction.

For *E. coli*-Pd (20%), XRD showed crystallinity in the bulk and SAED analysis of *E. coli*-Pd (15%) confirmed this within the cluster. The lattice planes (111), (200) and (220) were all identified. XRD conducted on bulk *E. coli*-Pt (20%), however, showed only one discernible peak corresponding to the (111) lattice peak; this pattern was attributed to the amorphous biomass and clustered nature of nanoparticles. SAED conducted on a cluster showed highly polycrystalline nanoparticles with similar low index facets (111), (200) and (220) and high index facet (311) as well. Pt faces with a lattice plane of (111) have previously shown good ORR activity[25] and as such, these NPs show potential as ORR electrocatalysts.

Finally, XPS examination showed that *E. coli*-Pd (20%) was present in Pd (0) and Pd (II) oxidation states and *E. coli*-Pt (20%) was present in Pt (0), Pt (II) and Pt (IV) oxidation states. It is likely that reduced NPs were oxidised in ambient

conditions and this range of oxidation states will shift with applied voltage during FC operation.

3.4.2 Bimetallic Pt/Pd synthesis by *E. coli*

Bimetallic Pt and Pd nanoparticles were synthesised using *E. coli* under H_2 as detailed in Materials and Methods. *E. coli*-Pt:Pd* (10%:10%) was synthesised by first synthesising *E. coli*-Pd (10%), then, using these as seeds to subsequently synthesise Pt (to 10wt %) under H_2. Like *E. coli*-Pd (20%), this bimetallic showed metal within all cells (appendix A2.4.1) and ICP-MS confirmed the metal loadings.

E. coli-Pd:Pt* (10%:10%) was synthesised similarly under H_2 using *E. coli*-Pt (10%) as seeds and, similarly to *E. coli*-Pt (20%), only a subsection of the bacterial cells showed nanoparticle reduction (appendix A2.4.1) and ICP-MS confirmed metal loading. The catalyst was then dried into a powder and characterised using XPS and XRD. The catalyst was also dried and sectioned for TEM and observed under a STEM.

3.4.2.1 STEM images and localisation

Figure 3.8A shows a representative cell of *E. coli*-Pt:Pd* (10%:10%) with nanoparticle features similar to *E. coli*-Pd (15%) (figure 3.8B) including surface clusters and nanoparticles observed in the cytoplasm and periplasm. This is expected as the Pt reduction is expected to occur auto-catalytically on previously synthesised Pd nanoparticles. *E. coli*-Pd:Pt* (10%:10%) (figure 3.8C) also showed similar features to *E. coli*-Pt (20%) (figure 3.8D) with primarily surface bound clusters. However, unlike with single metal Pt, this catalyst had small

intracellular nanoparticle clusters seen dispersed throughout the cell (figure 3.8C).

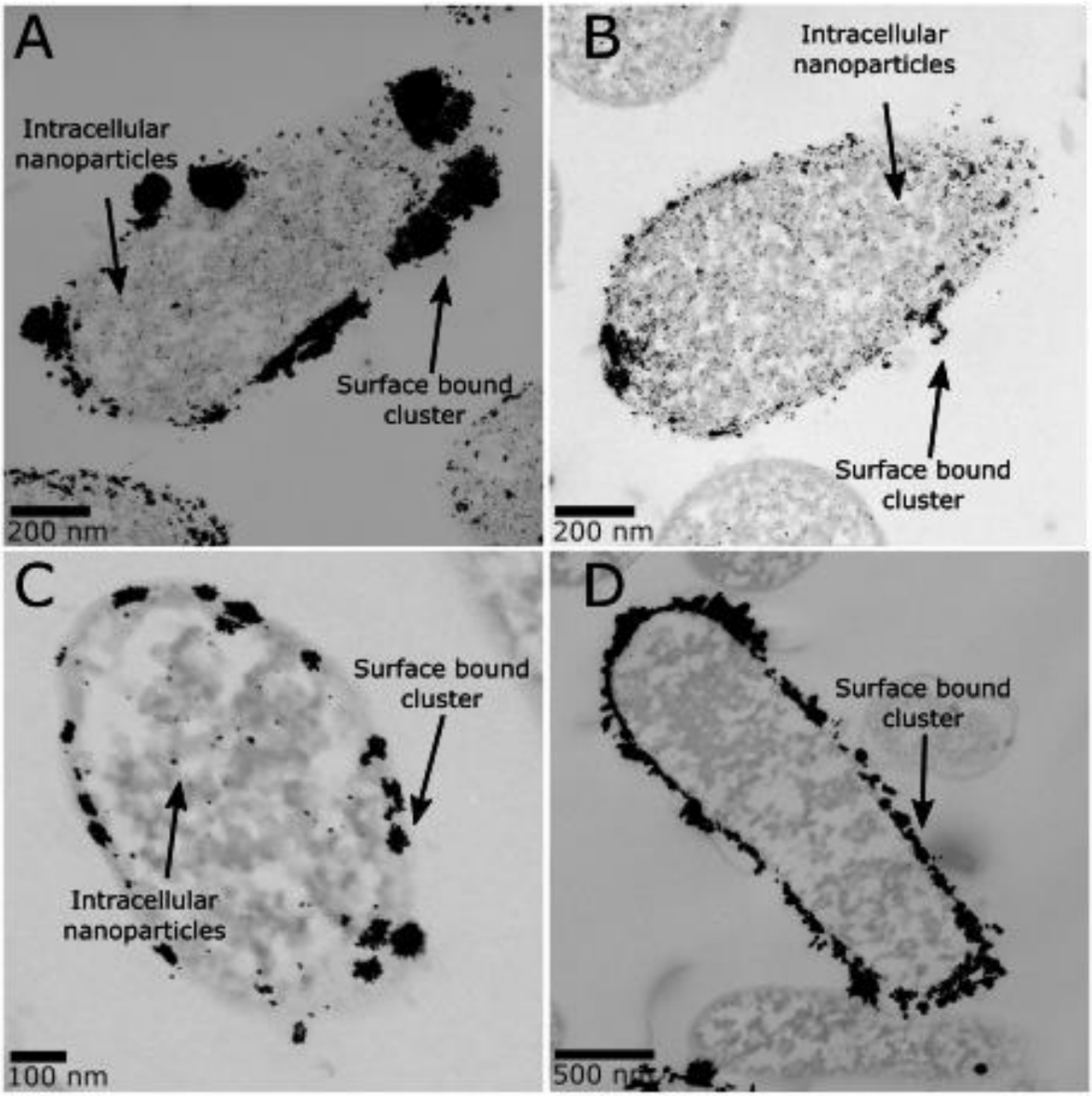

Figure 3.8 (A) and (B) Representative high-resolution STEM images of *E. coli*-Pt:Pd* (10%:10%) and *E. coli*-Pd (15%) respectively. All cells were shown to have reduced nanoparticles. Surface bound clusters and intracellular nanoparticles are seen. (C) and (D) Representative high-resolution STEM images of *E. coli*-Pd:Pt* (10%:10%) and *E. coli*-Pt (20%) respectively. As shown in (C), some nanoparticles can be observed intracellularly, in the periplasm and surface bound clusters. (D) shows no intracellular nanoparticles and only surface clusters. Scale bars are as shown

To further understand localisation of nanoparticles in both, STEM-EDX maps were obtained for a representative cell of each *E. coli*-Pt:Pd* (10%:10%) and *E. coli*-Pd:Pt* (10%:10%) (figure 3.9 and figure 3.11 respectively) showcasing localisation of both Pd, and Pt.

Figure 3.9A shows the HAADF image of representative *E. coli*-Pt:Pd* (10%:10%) cell, with figures 3.9C, D and E showing the EDX localisation of Pt (red), Pd (green) and P (blue) on the cell respectively. The P maps are used to identify cell boundaries. Figure 3.9B shows the overlay image of HAADF Pd and Pt. It is interesting to note that the both Pt and Pd nanoparticles are seen ubiquitously across the cell which disagrees with the above *E. coli*-Pt (20%). Furthermore, there seems to be a greater concentration of Pt in the periplasm relative to the cytoplasm however, this is a qualitative assessment and as such cannot be concluded definitively.

In figure 3.9B, the clusters show up brighter than the rest; this indicates a high-level of co-localisation between the Pt and Pd atoms in the image which in turn implies alloying between the metals. In the representative cluster marked by the arrow in figures 3.9A, B, C and E, both Pt and Pd were shown to be present with Pt seen to be concentrated at the outer edges of the cluster.

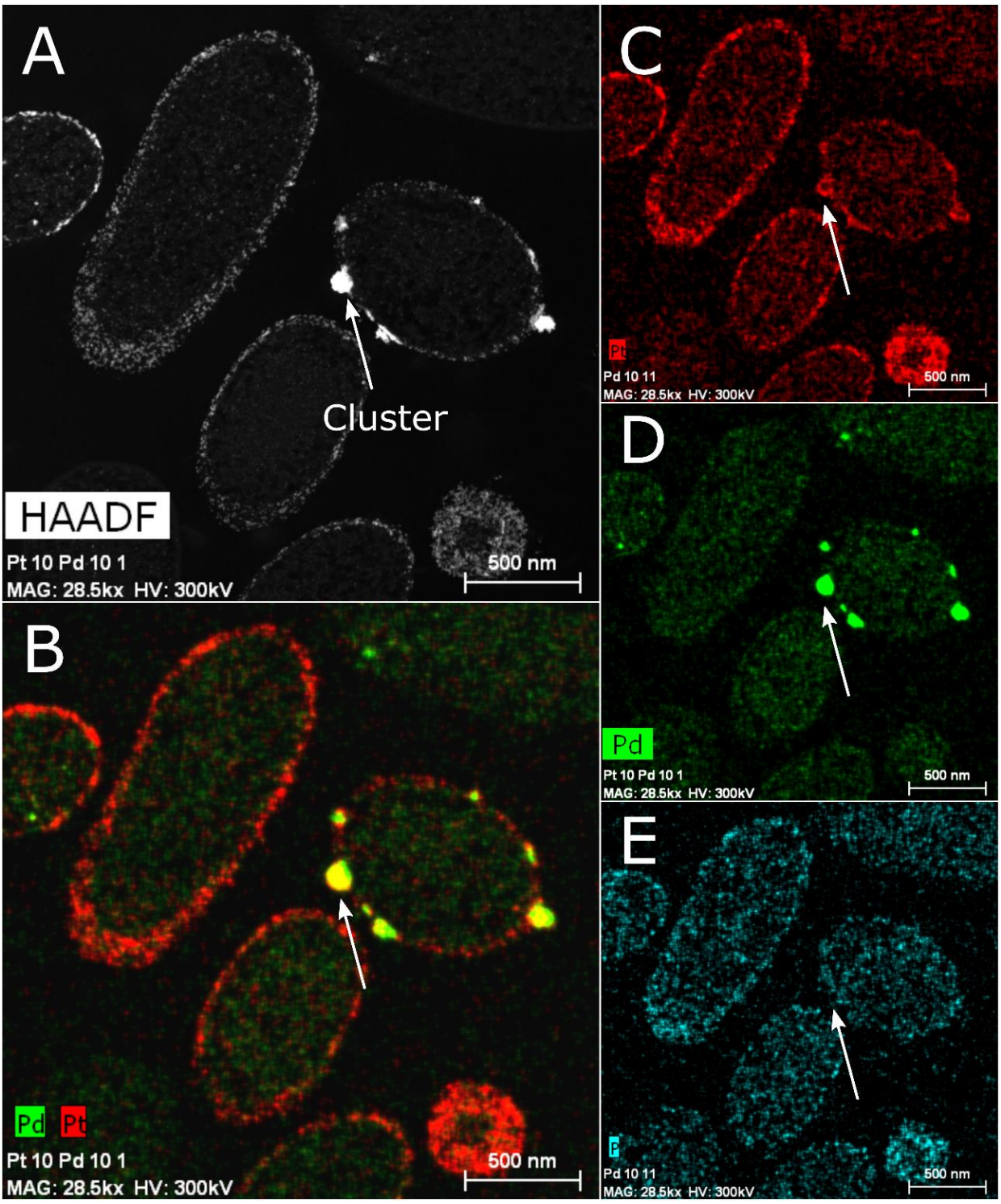

Figure 3.9 (A) STEM image of *E. coli*-Pt:Pd* (10%:10%) with (B) showing an EDX map of the same image showcasing Pt and Pd signals. All cells were shown to have both Pt and Pd reduced nanoparticles. Clusters and intracellular Pt and Pd can be seen on most cells. Figure (C), (D) and (E) show EDX maps of individual elements Pt, Pd and P, respectively. A white arrow is shown in all images identifying a single cluster. Scale bars are as shown.

To further understand the structure of the bimetallic, a line profile was drawn across clusters and elemental composition was mapped across the transect (figure 3.10). As seen, a cluster on a representative *E. coli*-Pt:Pd* (10%:10%) cell (figure 3.10A) was chosen (in green). Two EDX line profiles were drawn across this cluster and their elemental compositions were checked ((B) and (C)). Both NP compositions showed Pt (red) and Pd (green) across the entire cluster with peaks of Pt at the outer edges of the cluster (shown by red arrows). This indicates a Pt-rich skin and was confirmed in further examples as shown in appendix A2.4.2.

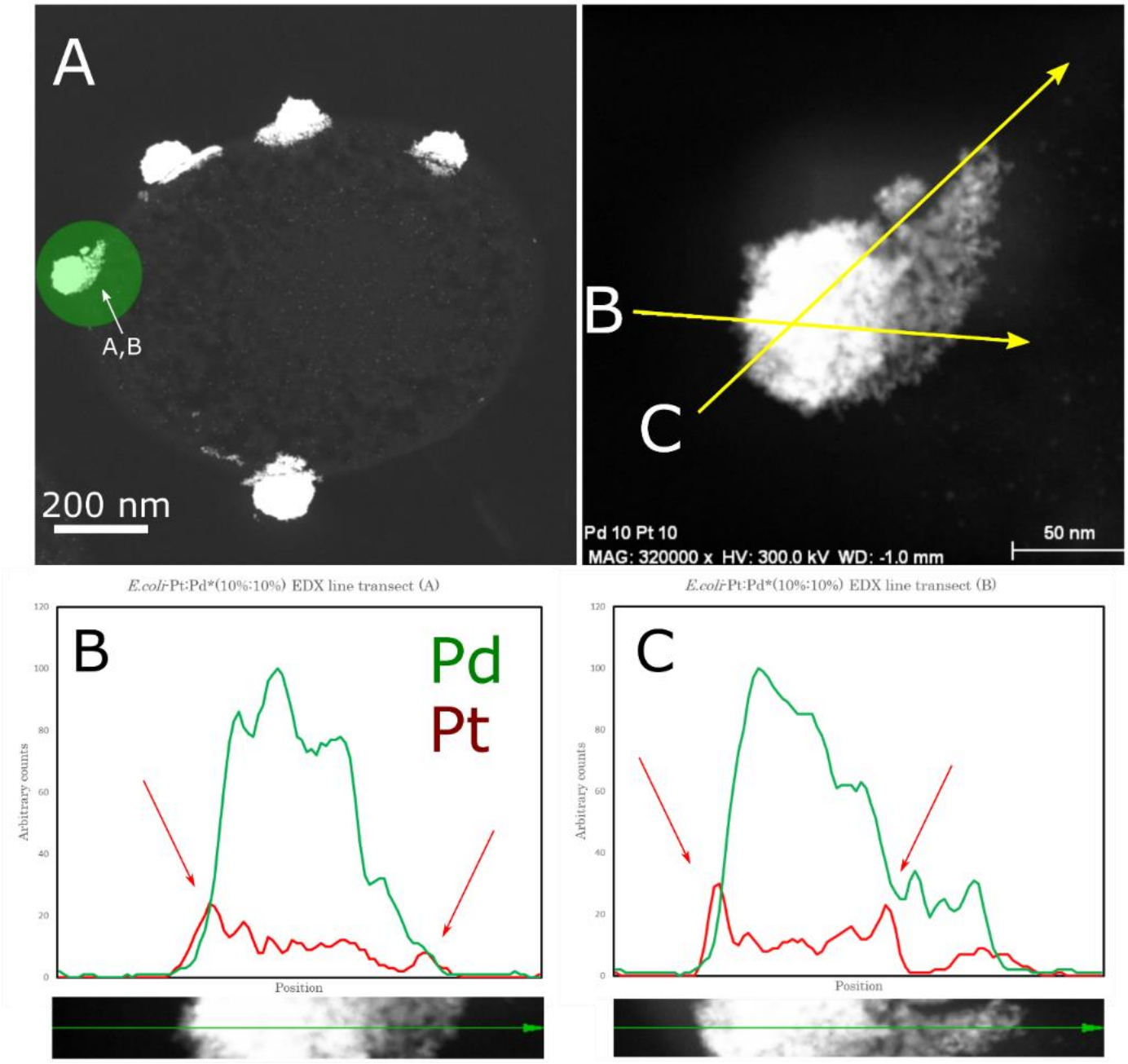

Figure 3.10 (A) High-resolution STEM image of representative *E. coli*-Pt:Pd* (10%:10%) cell with line transects drawn across a representative cluster highlighted in green. (B) and (C) show elemental composition across their respective line transects with Pd and Pt in green and red, respectively. As seen, both elements are seen across the cluster (with Pd to excess) with a peak of Pt on the outer edges of the cluster.

Like *E. coli*-Pt (20%), *E. coli*-Pd:Pt* (10%:10%) did not show metal reduction in all cells (appendix A2.4.1). This was observed experimentally where, on centrifugation, pelleted cells showed a gradient of colour with beige non-metallised cells at the top and grey metallised cells at the bottom. Figure 3.11A shows the HAADF image of a representative *E. coli*-Pd:Pt* (10%:10%) cell, with figures 3.11 C, D and E showing the EDX localisation of Pt (red), Pd (green) and P (blue) on the cell respectively. Figure 3.11B shows the overlay image of HAADF Pd and Pt and like *E. coli*-Pt:Pd* (10%:10%), it shows a good degree of colocalization in the clusters. In the cluster marked by the arrow in figures 3.11 A, B, C, D and E, both Pt and Pd were shown to be present, however, unlike *E. coli*-Pt:Pd* (10%:10%), there seems to be a more equitable distribution of both elements across the cluster. It is interesting to note that unlike *E. coli* - Pt (20%), Pt is seen throughout the cell associated with nanoparticles (bright regions in 3.11A) and biomass in the cytoplasm (dark regions on 3.11A). The cells appear to contain little intracellular Pd (Figure 3.11D) which accords with a toxic effect of Pt (IV), but this was not tested.

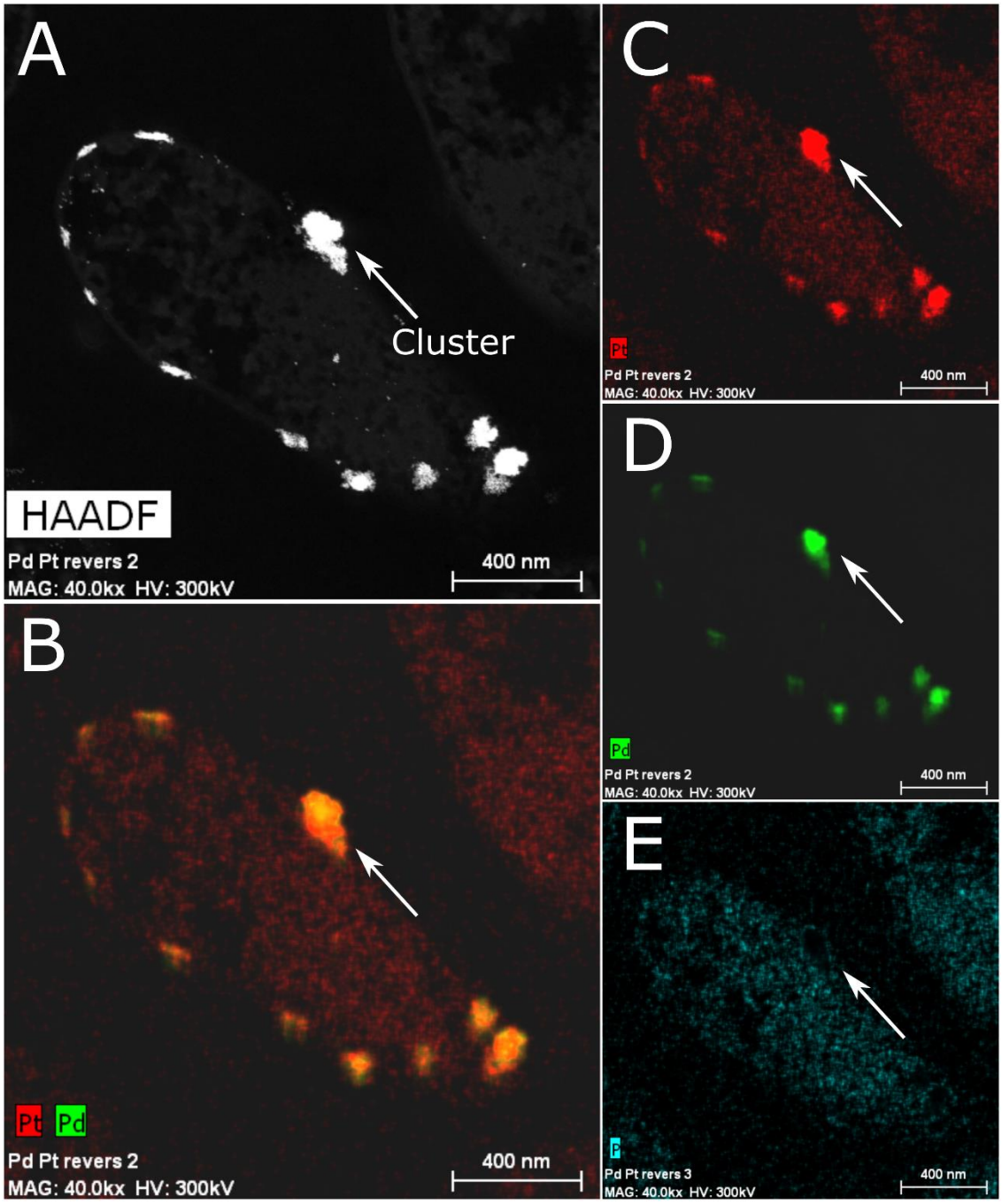

Figure 3.11 (A) STEM image of *E. coli*-Pd:Pt* (10%:10%) with (B) showing an EDX map of the same image showcasing Pt and Pd signals. Clusters and intracellular Pt and Pd can be seen in some cells. Figure (C), (D) and (E) show EDX maps of individual elements Pt, Pd and P, respectively. A white arrow is shown in all images identifying a single cluster. Scale bars are as shown.

To further understand the alloying structure, a line profile was drawn across different clusters and elemental composition was checked, For, a representative *E. coli*-Pd:Pt* (10%:10%) cell (figure 3.12A), two clusters were chosen (in green). EDX line profiles were drawn across both and their elemental compositions were checked ((B) and (C)). This showed Pt and Pd peaks across the cluster in apparently equal proportions with no apparent concentration of Pt at the NP edge in contrast to *E. coli*-Pt:Pd* (10%:10%) (figure 3.10 B,C). Similar line profiles were observed for nanoparticles in clusters, and individual nanoparticles in the periplasm and intracellularly and is shown in the appendix (A2.4.2.2)

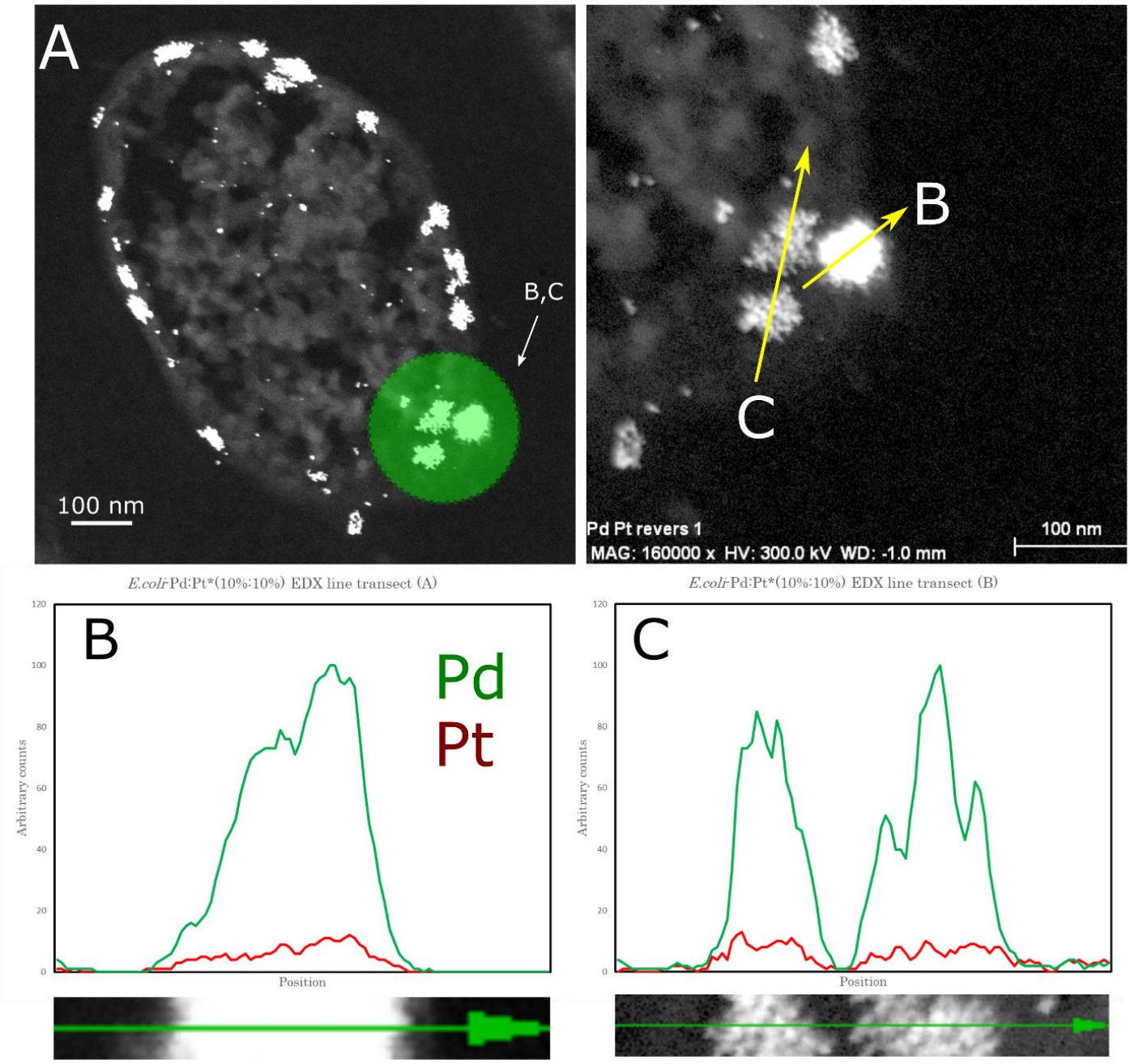

Figure 3.12 (A) High-resolution STEM image of representative *E. coli*-Pd:Pt* (10%:10%) cell with line transects drawn across a representative cluster highlighted in green. (B) and (C) show elemental composition across their respective line transects with Pd and Pt in green and red, respectively. As seen, both elements are seen across the cluster in apparently equal proportions.

3.4.2.2 **Size analysis**

The size distribution of *E. coli*-Pt:Pd* (10%:10%) and *E. coli*-Pd:Pt* (10%:10%) NPs was characterised using STEM images and ImageJ analysis to create a nanoparticle size distribution. Figure 3.13 and 3.14 shows the cells and regions investigated on *E. coli*-Pt:Pd* (10%:10%) and *E. coli*-Pd:Pt* (10%:10%) respectively.

Figure 3.13 shows the Pt:Pd*-NP size distribution for NPs present in the cytoplasm (3.13A), periplasmic space (3.13D), and surface located clusters (3.13G) of *E. coli*-Pt:Pd* (10%:10%). For (A), NPs were sized using the "analyse particles" function on ImageJ as described in Materials and Methods. As seen in figure 3.13B NPs are well dispersed with a range of sizes; 329 NPs were sized, and a median NP size of 2 nm and a mean size of 2.7 $\pm$ 1.3 nm was identified. Over 50% of NPs sized were in the 2.0–3.0 nm range (figure 3.13C). Figure 3.13D shows agglomerations of individual Pt:Pd*-NPs found in the periplasmic space. The "analyse particles" function could not be used for this image as the nanoparticles were far too agglomerated to enable the threshold function. 164 NPs were sized individually, and a median of 4.5 nm and mean of 4.2 $\pm$ 1.2 nm was observed. Over 50% of those sized were in the 3.0–5.0 nm range (figure 3.13E). No clear boundaries could be determined for the periplasm and as such this result is subjective. Finally, figure 3.13H shows Pt:Pd*-NPs in the cluster which, on closer inspection, was shown to be an agglomeration of individual nanoparticles. 27 individual nanoparticles were observed, and these were measured giving a size distribution within a range of 3.0 nm to 6.0 nm with a median of 4.0 nm and mean of 4.1 $\pm$ 0.8 nm (figure 3.13I). Thus, while NP sizing

in the periplasm and cluster is less accurate (fewer NPs measured) and more subjective (observed measurements), it can be stated that periplasmic and clustered NPs are larger than cytoplasmic NPs. The threshold images and the nanoparticles measured are shown in appendix A2.1.3.

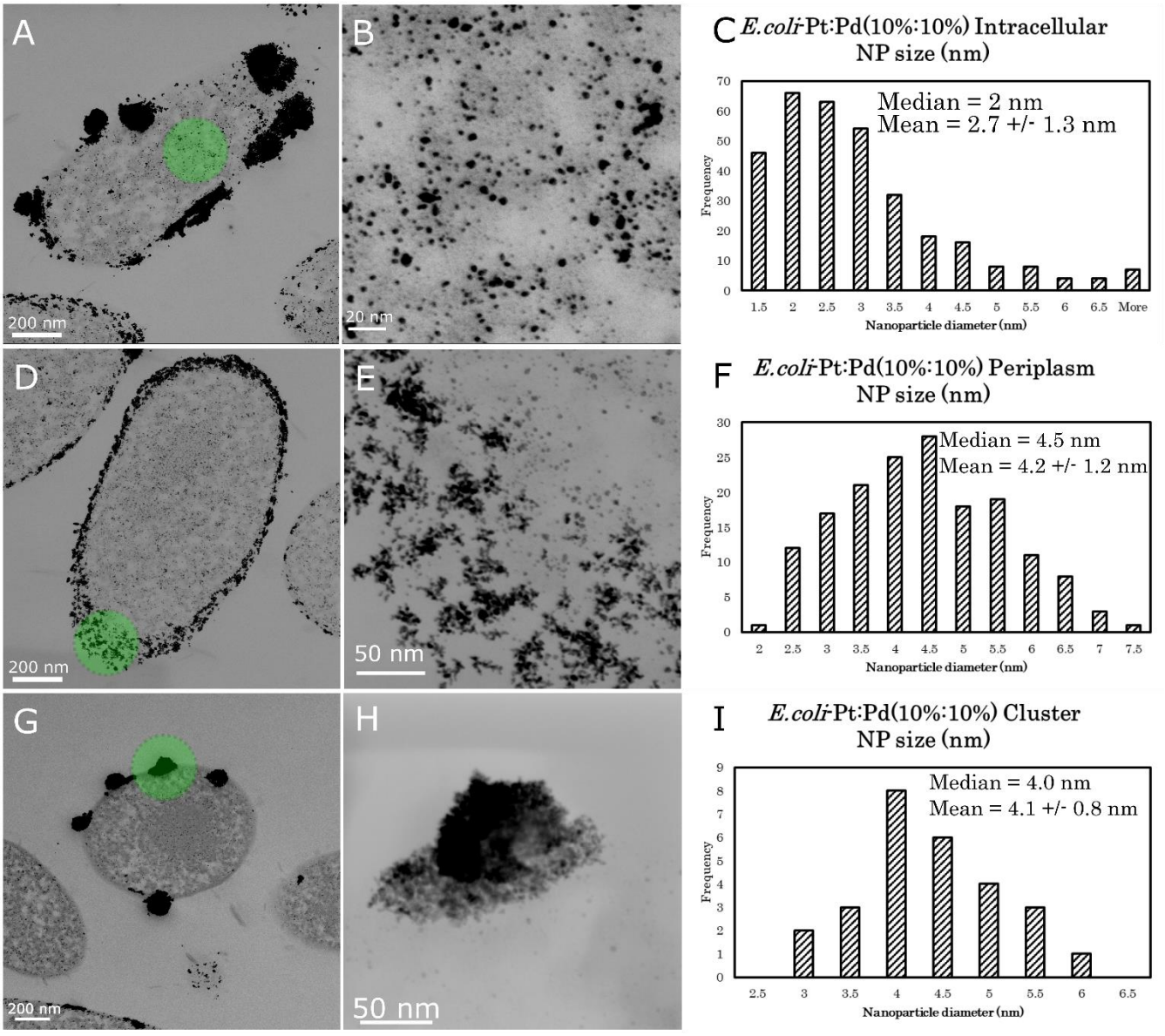

Figure 3.13 A, D and G shows a STEM images of *E. coli*-Pt:Pd* (10%:10%) cells with areas studied marked in green to indicate NPs sized in the cytoplasm, periplasm, and surface bound cluster, respectively. B, E and H shows a high resolution image of the regions highlighted in green for NPs in the cytoplasm, periplasm, and surface bound cluster, respectively. C, F, and I show the size distribution of NPs in the cytoplasm (median = 2 nm, 2.7 ± 1.3 nm), periplasm (median = 4.5nm, 4.2 ± 1.2 nm) and surface associated cluster (median = 4.0 nm, 4.1 ± 0.8 nm) respectively. Scale bars are as shown

Figure 3.14 shows the size distribution of *E. coli*-Pd:Pt* (10%:10%) NPs found in the cytoplasm (figure 3.14A) and in surface associated clusters (figure 3.14D). Intracellular NPs investigated are highlighted in green (figure 3.14A) and, unlike with *E. coli*-Pt:Pd* (above), comprised agglomerations of individual nanoparticles (figure 3.14B). Hence, the "analyse particles" function could not be used here and thus, observed nanoparticles were individually measured. 92 NPs were measured, and the size distribution is shown in figure 3.14C with a range of 2.5–9.0 nm. A median range of 4.0–5.0nm and a mean size of 4.9 $\pm$ 1.5 nm was seen with over 40% of NPs in this range. The individual measurements are shown, in appendix A2.1.4. Figure 3.14D shows a representative cell with a surface associated cluster highlighted in green. Figure 3.14E shows that the cluster is an agglomeration of individual NPs but their boundaries could not be distinguished. Figure 3.14F shows an HRTEM of this cluster and is representative of HRTEM images taken of other clusters (appendix A2.1.4). It is important to note that this sizing was done with a small sample size and thus, this result is less accurate than the sized *E. coli*-Pt:Pd* NPs and this is reflected in the size distribution.

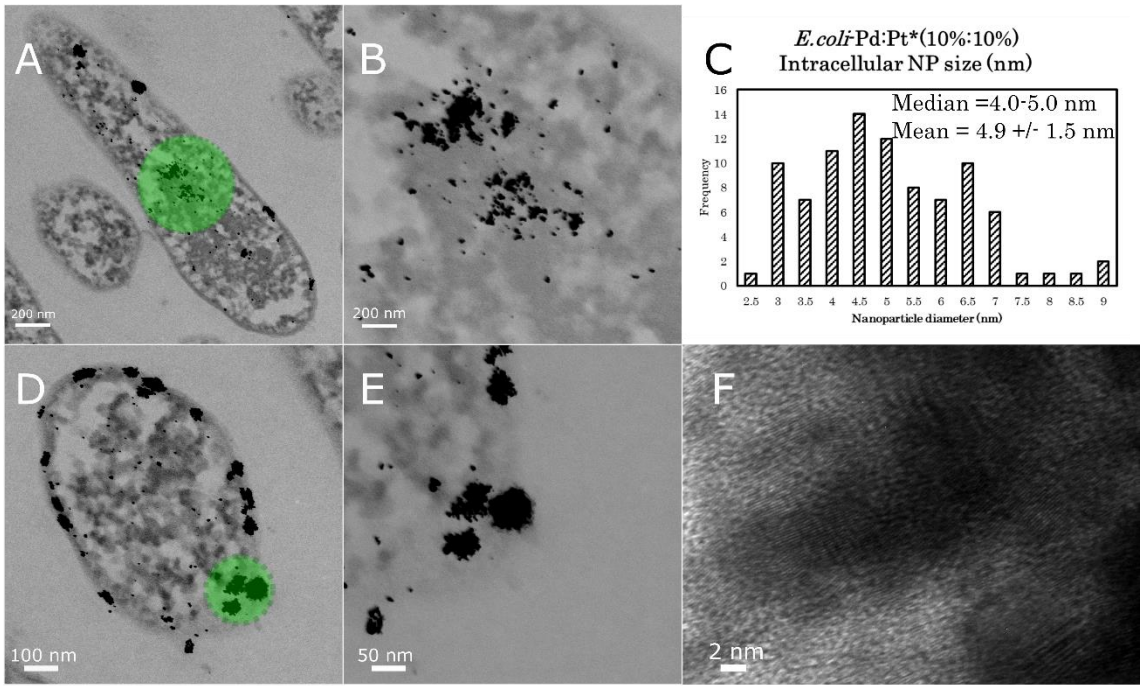

Figure 3.14 A and D show a STEM image of *E. coli*-Pd:Pt* (10%:10%) cell with areas studied marked in green to indicate NPs sized in the cytoplasm, and surface associated cluster, respectively. B and E show high resolution images of the regions highlighted in green for NPs in the cytoplasm, and surface associated cluster, respectively. C shows the size distribution of NPs in the cytoplasm with a median = 4.0–5.0 nm and mean = 4.9 ± 1.5 nm. F shows an HRTEM of the cluster from E where individual nanoparticle boundaries could not be determined. Scale bars are as shown.

3.4.2.3 **Shape analysis**

XRD, HRTEM and SAED were used to analyse the morphology and crystallinity of the produced *E. coli*-Pt:Pd* (10%:10%) and *E. coli*-Pd:Pt* (10%:10%) NPs. XRD patterns taken for both (figure 3.15) powdered catalysts showed peaks corresponding to (111), (200) and (220) lattices indicating an FCC crystal structure. Figure 3.15 shows the XRD powder pattern for *E. coli*-Pd (20%) (in black) with peaks at 2θ values of 40.20, 46.73 and 68.16 (dotted black line). The

peaks of bimetallics were shown at 2θ values of 39.83 (111), 46.36 (200) and 67.81 (220) for *E. coli*-Pt:Pd* and at 39.83 (111), 46.48 (200) and 68.00 (220) for *E. coli*-Pd:Pt* (figure 3.15). Pt/C (40% wt%/wt%) was previously shown to have XRD values of 39.6° (111), 47.4° (200) and 67.1° (220) and (dotted red line).[281] These 2θ values are summarised in table 3.1.

Table 3.1 Summary table showing 2θ values for lattice peaks from XRD powder patterns of catalysts. Pt/C (40%) values were taken from Huy *et al.*[281] As seen bimetallic peaks lie in between *E. coli*-Pd and Pt/C for all 2θ values apart from the 2θ corresponding to the (200) lattice peak (red)

Catalyst examined	(111)	(200)	(220)
***E. coli*-Pd (20%)**	40.20	46.73	68.16
***E. coli*-Pt:Pd* (10%:10%)**	39.83	46.36	67.81
***E. coli*-Pd:Pt* (10%:10%)**	39.83	46.48	68.00
Pt/C	39.60	**47.40**	67.10

As seen in table 3.1 and figure 3.15 there is a progressive shift to lower 2θ values for all peaks relative to E. coli-Pd (20%) (dotted black line) and to higher 2θ values relative to Pt/C (40%) (dotted red line) apart from peak at (200) (shown in red table 3.1). Bimetallic peaks lie in between these peaks for (111) and (220) but not (200).This shift is expected in an alloy, as the heterogeneity of the NP atoms will impose a strain on the crystallite structure. The lattice parameter value changes, which in turn induces a shift in the peaks. The discrepancy for the Pt/C peak at (200) might be attributed to the different supports used (carbon black as opposed to *E. coli*) as this will have an effect on XRD Peaks.

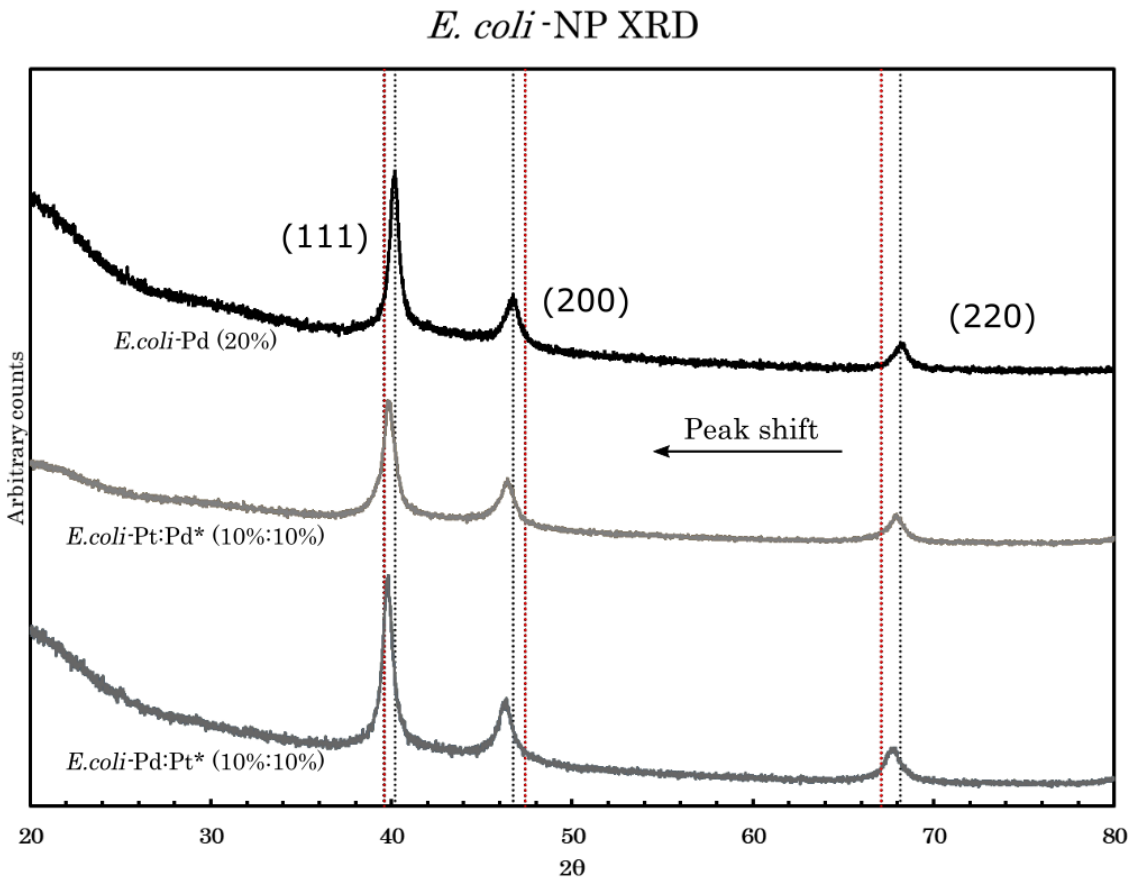

Figure 3.15 shows the XRD pattern obtained for *E. coli*-Pd (20%) (Black), *E. coli*-Pt:Pd* (10%:10%) (light grey) and *E. coli*-Pd:Pt* (10%:10%) (dark grey). *E. coli*-Pt:Pd* has peaks at 2θ values of 39.83 (111), 46.36 (200) and 67.81 (220). *E. coli*-Pd:Pt* shows peaks at 2θ values of 39.83 (111), 46.48 (200) and 68.00 (220). The peaks for bimetallics are shown to have shifted to lower 2θ values from *E. coli*-Pd (20%) (dotted black line) and to higher 2θ from Pt/C (40%) peaks [281] (dotted red line) for all peaks apart from (200).

The identified lattice planes were confirmed for both bimetallics by SAED analysis conducted on their clusters (appendix A2.2). SAED on an *E. coli*-Pt:Pd* (10%:10%) cluster showed distinct diffraction patterns corresponding to (111), (200) lattice planes and an indistinct pattern for the (220) plane (figure 3.16A). The crystallinity of *E. coli*-Pd:Pt* was also confirmed using SAED analysis (figure 3.16C). This showed a highly crystalline nanostructure within the

amorphous bulk. It evidenced distinct patterns for (111), (200), (220), and an indistinct pattern for the (311) plane. These were compared and found to agree with previous SAED images taken for chemically synthesised Pd/Pt-NPs.[215] HRTEM images were used to confirm these findings as seen in figure 3.16B and 3.16D for *E. coli*-Pt:Pd* (10%:10%) and *E. coli*-Pd:Pt* (10%:10%) respectively. In both, a lattice spacing of 0.23 nm was seen. This spacing corresponds to the (111) lattice plane.[215]

In summary, *E. coli*-Pt:Pd* (10%:10%) and *E. coli*-Pd:Pt* (10%:10%) both showed polycrystalline structures with the same lattice planes (111), (200) and (220) observed. *E. coli*-Pt:Pd* (10%:10%) had a wide range of nanoparticle sizes with a mean diameter of around 2.7 $\pm$ 1.3 nm for non-clustered NPs and a mean diameter of 4.1 $\pm$ 0.8 nm for clustered NPs. *E. coli*-Pd:Pt* (10%:10%) on the other hand had very clustered NPs with an estimated mean size of 4.9 $\pm$ 1.5 nm. The HRTEM images and SAED taken together imply that clustered NPs must contain individual crystalline nanoparticles. Furthermore, EDX mapping shows a uniform alloy in *E. coli*-Pd:Pt* but an enrichment of Pt at NP margins in *E. coli*-Pd:Pt*.

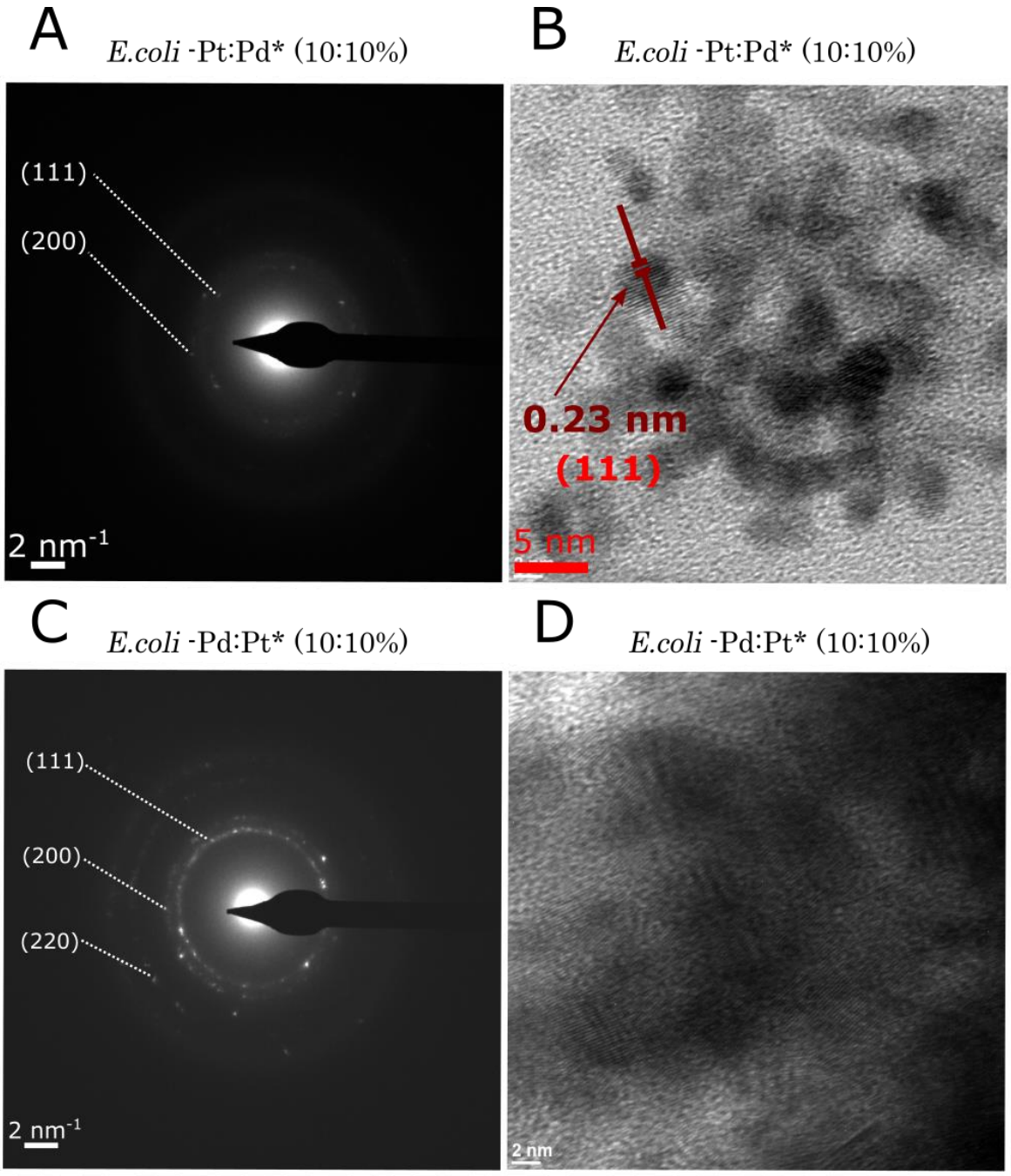

Figure 3.16 (B) and (C) shows the SAED and HRTEM obtained for *E. coli*-Pt:Pd* (10%:10%). (B) identifies the SAED diffraction patterns as (111), (200) and (220) and (C) shows a representative HRTEM image of a representative NP. The lattice fringe spacing was identified to be 0.23 nm which correlates to a (111) lattice plane. (D) and (E) shows the SAED and HRTEM obtained for *E. coli*-Pd:Pt* (10%:10%). (B) identifies the SAED diffraction patterns as (111), (200), (220) and (311). (C) shows a representative HRTEM image of a representative NP. The lattice fringe spacing was identified to be 0.23 nm which correlates to a (111) lattice plane. Scale bars are as shown

3.4.2.4 **Oxidation state and Binding analysis**

XPS analysis was used to analyse the oxidation states of *E. coli*-Pt:Pd* (10%:10%) and *E. coli*-Pd:Pt* (10%:10%). The complete XPS survey scans for both are shown in appendix (A2.3). Figure 3.17A and B show a high-resolution Pd3d and Pt4f XPS scan respectively of *E. coli*-Pt:Pd* (10%:10%). The scans for both are shown in black with the fit to the scan shown as an orange dotted line. As seen in figure 3.17A the $Pd3d_{3/2}$ and $Pd3d_{5/2}$ binding energy peaks are 340.68 eV and 335.18 eV respectively. Deconvoluting the peaks showed that *E. coli*-Pd is found in both oxidation states Pd (0) (blue) and Pd (II) (red). A third peak is also seen at 331.58 eV, which is assigned as the Pt4s peak. Figure 3.17B shows that $Pt4f_{5/2}$ and $Pt4f_{7/2}$ peaks were seen at 74.88 eV and 71.48 eV respectively. Deconvoluting these peaks showed Pt (0) (blue) and Pt (IV) (green) with no evidence of Pt (II) on the surface.

Figure 3.17C and D show a high-resolution Pd3d and Pt4f XPS scan respectively of *E. coli*-Pd:Pt* (10%:10%). The scans for both were less well defined than *E. coli*-Pt:Pd* and this can be attributed to the poor distribution of NPs across the surface. Scans are shown in black and the fit to the scan shown as an orange dotted line. As seen in 3.17C the $Pd3d_{3/2}$ and $Pd3d_{5/2}$ binding energy peaks are 341.08 eV and 335.58 eV respectively. Deconvoluting the peaks showed that *E. coli*-Pd is found in both oxidation states Pd (0) (blue) and Pd (II) (red). A third peak is also seen at 331.88 eV which is assigned as the Pt4s peak. 3.17D shows that $Pt4f_{5/2}$ and $Pt4f_{7/2}$ peaks were seen at 76.08 eV and 72.88 eV respectively. Deconvoluting these peaks only showed a Pt (0) (blue) peak.

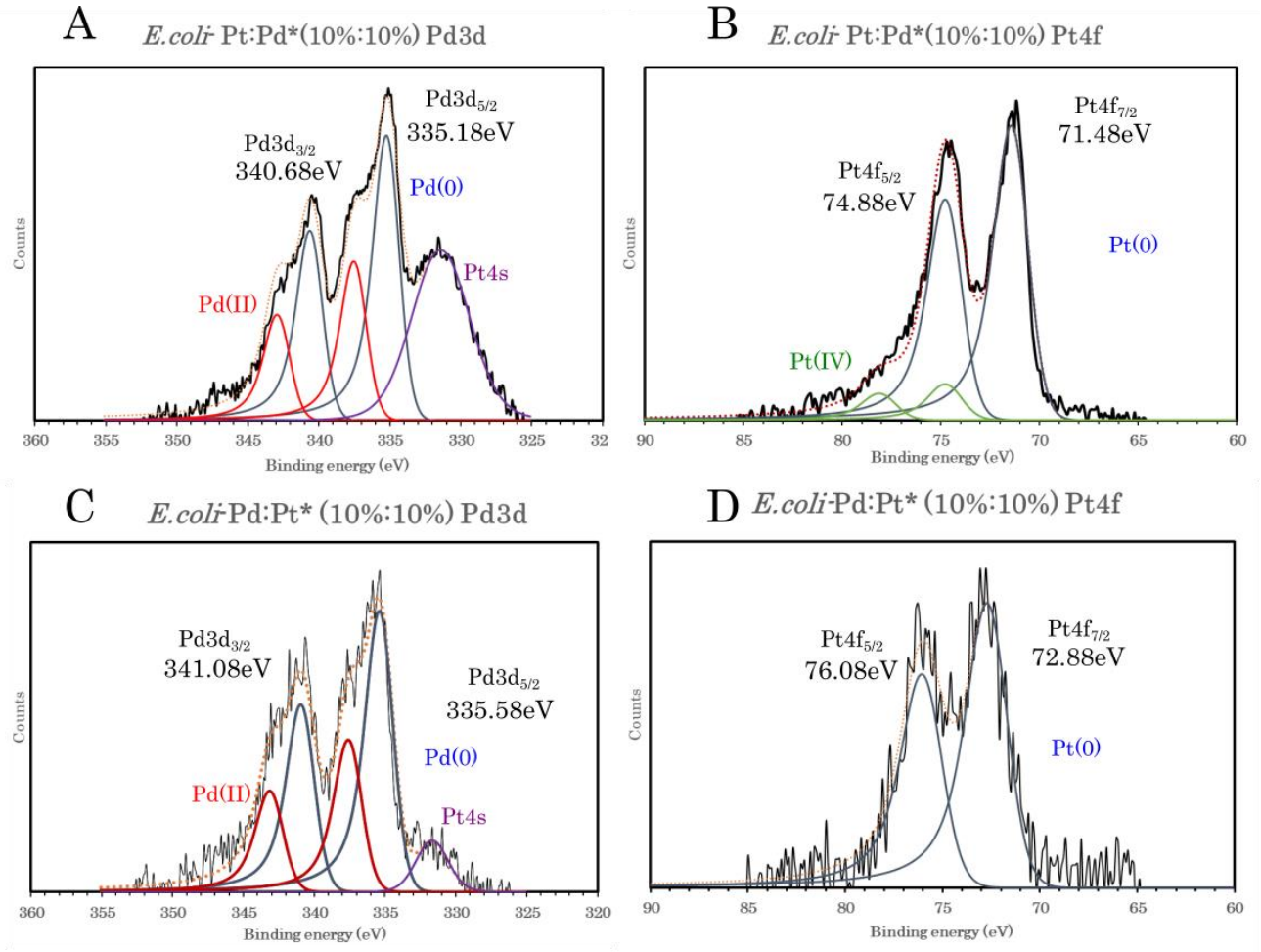

Figure 3.17 (A) and (B) High resolution Pd3d and Pt4f XPS scan of *E. coli*-Pt:Pd* (10%:10%) respectively with the scan shown in black and the curve fit is shown in dotted orange. (A) The peaks for $Pd3d_{5/2}$ at 335.18 eV and $Pd3d_{3/2}$ at 340.68 eV. Deconvoluting the peaks showed oxidation states of Pd (0) (in blue) and Pd (II) (in red). A third peak is also seen at 331.58 eV which is assigned as the Pt4s peak (purple). (B) The peaks for $Pt4f_{7/2}$ at 71.48 eV and $Pt4f_{5/2}$ at 74.88 eV. Deconvoluting the peaks showed oxidation states of Pt (0) (in blue) and Pt (IV) (in green). (C) and (D) High resolution Pd3d and Pt4f XPS scan of *E. coli*-Pd:Pt* (10%:10%) respectively with the scan shown in black and the curve fit is shown in dotted orange. (C) The peaks for $Pd3d_{5/2}$ at 335.58 eV and $Pd3d_{3/2}$ at 341.08 eV. Deconvoluting the peaks showed oxidation states of Pd (0) (in blue) and Pd (II) (in red). A third peak is also seen at 331.88 eV which is assigned as the Pt4s peak (purple). (D) The peaks for $Pt4f_{7/2}$ at 72.88 eV and $Pt4f_{5/2}$ at 76.08 eV. Deconvoluting the peaks showed oxidation states of Pt (0) (in blue).

Like single metal-NPs, both bimetallics were not solely of metallic deposit but contained partially oxidised species as well as metal oxides. Interestingly, while a peak shift was seen in the Pd and Pt fit for both bimetallics (figure 3.18 A and B) it was far more pronounced for Pt4f than for Pd3d (dotted line). This peak shift indicates a change in the local binding environment of both metals and thus the energy of emitted electrons. Thus, this confirms the presence of electron interactions between Pt and Pd for both bimetallics.

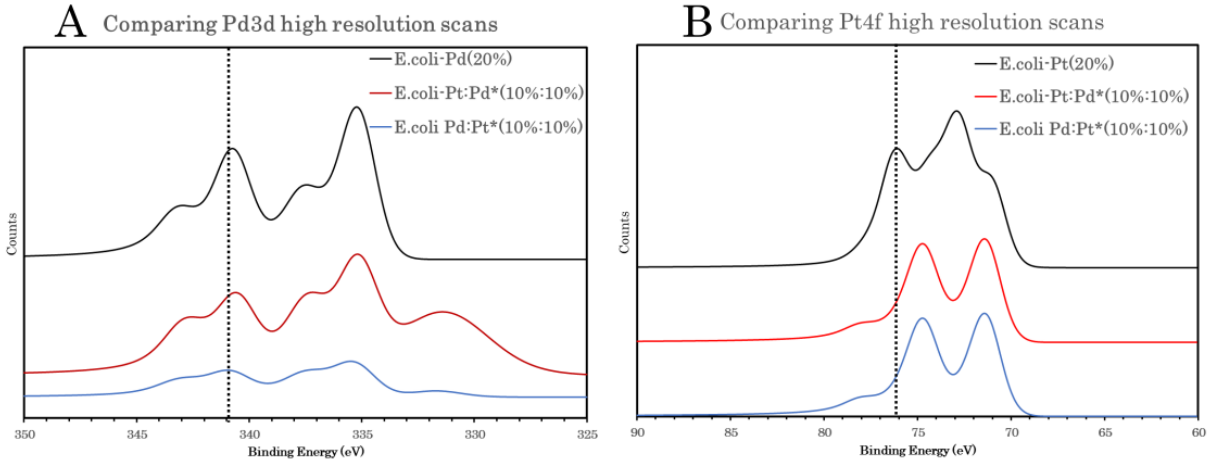

Figure 3.18(A) shows an overlay of Pd3d scans of *E. coli*-Pd (20%) and both bimetallics. A black dotted line is drawn through the $Pd3d_{3/2}$ peak and slight peak shift is observed. (B) shows an overlay of Pt4f scans of *E. coli*-Pt (20%) and both bimetallics. A black dotted line is drawn through the $Pt4f_{5/2}$ peak and a prominent peak shift is observed.

3.4.2.5 Summary of *E. coli*-Pt:Pd* (10%:10%) and *E. coli*-Pd:Pd (10%:10%)

The above results for both *E. coli*-Pt:Pd* (10%:10%) and *E. coli*-Pd:Pt* (10%:10%) are summarised and discussed here.

NP patterning for both bimetallics appears to be dependent on the initial NP synthesised. Like *E. coli*-Pd (15%), E. coli-Pt:Pd (10%10%) shows NPs distributed ubiquitously across the entire cell (in the cytoplasm and periplasmic space) and

clusters associated with the surface. NP sizes were similar in the cytoplasm relative to *E. coli*-Pd (15%) (both around 2.5 nm). Furthermore, the clusters were shown to be agglomerations of individual nanoparticles and sized at a mean of 4.1nm relative to the 5.3 nm of *E. coli*-Pd (15%). Interestingly the bimetallic (but not Pt only) showed Pt localisation throughout the cell. This internalisation of metal mediated by an initial Pd-NP synthesis has been observed before with PdRu. Here, *E. coli*-Ru only synthesises Ru-NPs on surface of cells, but when synthesised on pre-palladised cells, Ru-NPs were seen throughout the cell biomass.[192]

E. coli-Pd:Pt*, on the other hand, primarily concentrated NPs as clusters on cells similar to *E. coli*-Pt (20%). Unlike *E. coli*-Pt (20%), The bimetallic did show some intracellular Pd:Pt*-NPs dispersed throughout the cell. This result is surprising, as the cells are thought to be dead post *E. coli*-Pt (20%) synthesis and it is expected that Pd (II) internalisation requires active transport by cellular machinery. It could be hypothesised, that the permeabilization of cellular membrane during *E. coli*-Pt (10%) synthesis is permanent and allows passage of Pd (II) ions into the cell. Furthermore, EDX maps taken of entire cells indicated the presence of Pt throughout the cell but these could not be identified in HAADF images (figure 3.11).

Both bimetallic-NPs showed crystallinity through XRD scans, SAED and HRTEM images. Lattice planes of (111), (200) and (220) were confirmed using XRD and SAED for both and a lattice fringe spacing of 0.23 nm was identified for both indicating a (111) lattice plane. XRD scans for both bimetallics only

showed one peak corresponding to each lattice plane and a shift in peak 2θ values, thus, indicating alloying in both bimetallics. EDX line profiling of clusters for both bimetallics showed a high degree of colocalization of Pt and Pd. *E. coli*-Pt:Pd* (10%:10%) line profiles showed a Pt peak at the edges of the cluster indicating a Pt-rich skin. *E. coli*-Pd:Pt* (10%:10%) however showed equal proportions of Pt and Pd along its EDX line profiles indicating an evenly arranged nanoalloy. Finally, high resolution XPS Pd and Pt scans were taken for both. Pt and Pd peaks for both bimetallics were shown to have shifted relative to single metal versions of the same further confirming Pt and Pd binding and thus alloying.

Taken together, it is clear that both bimetallics synthesised were similar alloys of Pt and Pd with *E. coli*-Pt:Pd* showing a Pt-Rich skin. The initial metal synthesised is thought to act as a seed site for the secondary metal. The secondary metal is then autocatalytically reduced on these seed sites under H_2 reducing agent and the bimetallic-NP patterning is dependent on the patterning of the initial metal.

3.5 Conclusion

E. coli-Pd (20%), *E. coli*-Pt (20%), *E. coli*-Pt:Pd* (10%:10%), and *E. coli*-Pd:Pt* (10%:10%) were synthesised and characterised. *E.coli*-Pd showed NP synthesis across the entire cell (intracellular NPs and surface bound clusters) whereas *E.coli*-Pt showed Pt-NPs primarily associated to the surface of the cell. This patterning influences the synthesis of bimetallic *E. coli*-NPs. *E. coli*-Pt:Pd* showed similar NP localisation across the cell as *E. coli*-Pd and *E. coli*-Pd:Pt*

showed similar NP localisation to *E. coli*-Pt with surface bound clusters. Unlike *E. coli*-Pt, however, some intracellular NPs were seen. This patterning was previously seen with bimetallic *E. coli*-Pd/Ru[192] and this is further discussed in chapter 6.

The bimetallics are thought to be alloys of Pt and Pd as STEM-EDX showed co-localisation of both metals and XPS and XRD data confirmed this. While *E.coli*-Pt:Pd* showed evidence of a "Pt-rich" skin around clusters, this was not seen for *E.coli*-Pd:Pt*.

Finally, XRD and SAED detected the crystal face (111) in all *E.coli*-NPs, thus, showing promise for ORR activity. Their performance as ORR catalysts is presented in Chapter 4.

Chapter 4: Evaluating the potential of *E. coli*-NPs as PEMFC catalysts using *ex-situ* electrochemical characterisation.

4.1 Abstract

All *E. coli*-NPs were tested ex-situ electrochemically for ORR activity. *E. coli*-Pd:Pt* did not show any discernible electrochemical activity and is not discussed here. *E. coli*-Pt:Pd* (10%:10%), *E. coli*-Pt (20%) and *E. coli*-Pd (20%) all showed ORR activity with *E. coli*-Pt:Pd* outperforming both single metal versions. It had a mass activity (MA) of 2.8 mA mg^{-1}_{PGM} relative to 1.7 mA mg^{-1}_{PGM} for *E. coli*-Pt and 0.3 mA mg^{-1}_{PGM} for *E. coli*-Pd. This increase in performance is credited to the better conductivities afforded by Pt:Pd* NP dispersion, however, these results are significantly lower than MA values for commercial Pt/C catalyst at ~ 250 mA mg^{-1}_{PGM}.

To improve performance by increasing conductivities, multiwalled carbon nanotubes (MWCNTs) were mixed with *E. coli*-Pt:Pd*. This treatment improved conductivities as evidenced by impedance studies performed on the catalyst. Furthermore, it increased mass activities to 8.6 mA mg^{-1}_{PGM} relative to 2.8 mA $mg^{-1}_{PGM}$for untreated *E. coli*-Pt:Pd*. However, this activity still falls significantly short of commercial Pt/C activities (~250 mA mg^{-1}_{PGM}).

4.2 Introduction

The synthesised *E. coli*-Pd (20%), *E. coli*-Pt (20%), *E. coli*-Pt:Pd* (10%:10%) and *E. coli*-Pd;Pt* (10%:10%) were all characterised as described in the previous chapter. This chapter evaluates their potential as ORR catalysts using *ex-situ*

electrochemistry as described below and in chapter 2 (section 2.3). A significant portion of the text and results from this chapter has been published by the author in the following publication:

Stephen AJ, Rees N V, Mikheenko I and Macaskie LE. Platinum and Palladium Bio-Synthesized Nanoparticles as Sustainable Fuel Cell Catalysts. *Front Energy Res*. (2019);**66**.

4.2.1 Evaluating catalysts *ex-situ*

When considering the activity of the catalyst the major metrics to consider are the electrochemically active surface area (ECSA), the specific activity (SA) and the mass activity (MA).[33] Durability of a catalyst can be tested *ex-situ* through a variety of methods.[34] These are described below.

4.2.1.1 Electrochemically Active Surface Area (ECSA)

ECSA is a measure of the total surface available for catalysis and as such increasing the ECSA is an important goal[216] which is often achieved by fine tuning catalyst shape and structure to increase catalytically active sites.[217] ECSA can be calculated by performing cyclic voltammograms (CVs) using a three-electrode half-cell with the catalyst in 0.1M perchloric acid under N_2 as described in section 2.3.1 and in the Materials and Methods. From the CV, the hydrogen oxidation peaks can be used to identify the amount of charges adsorbed onto the catalyst. Then using the following equation, the ECSA[33] can be calculated:

$$\boldsymbol{ECSA_{PGM}\left(m^2 g_{PGM}^{-1}\right) = \left[\frac{Q_{H\ adsoroption}\ (C)}{210\ \mu C\ cm_{PGM}^{-2}\ L_{Pt}(mg_{Pt}cm^{-2})A_g(cm^{-2})}\right] 10^5} \textbf{ (Eq 4.1),}$$

here, $\boldsymbol{Q_H}$ refers to the amount of charges adsorbed (in Coulombs), 210 μC cm^{-2} is the conversion factor, $\boldsymbol{L_{Pt}}$ is the loading of platinum (mg cm^{-2}) on the electrode surface and $\boldsymbol{A_g}$ (cm^{-2}) is the area of the working electrode.

4.2.1.2 Specific Activity (SA)

SA is a measure of the turnover frequency of the catalyst, i.e. the amount of reactions occurring per second. Increasing the SA is thus a priority and done by considering the structural and electronic properties of the catalyst.[218] This is often fine-tuned to maximise the exchange current density for the ORR.[219] The specific activity is measured by conducting Linear Sweep Voltammetries (LSV) using the catalyst in a three-electrode cell in 0.1 M perchloric acid under saturated oxygen.[33] This is performed by rotating the electrode at varying speeds and using these data, and the following Koutecký–Levich equation, the kinetic current can be found:

$$\frac{\mathbf{1}}{\boldsymbol{I_m}} = \frac{\mathbf{1}}{\boldsymbol{I_K}} + \frac{\mathbf{1}}{\boldsymbol{B_L\omega^{0.5}}} \qquad \textbf{(Eq 4.2),}$$

where $\boldsymbol{I_m}$ is the measured current, $\boldsymbol{I_K}$ is the kinetic current $\boldsymbol{B_L}$ is the Levich constant and $\boldsymbol{\omega}$ is the angular speed (in radians). The $\boldsymbol{I_K}$ is then used to identify the specific activity[33] of the catalyst using the following equation:

$$\boldsymbol{Specific\ Activity}\left(\boldsymbol{Ag^{-1}_{PGM}}\right) = \left[\frac{\boldsymbol{I_K\ 210\ \mu C\ cm^{-2}_{PGM}}}{\boldsymbol{Q_{H\ adsoroption}\ (A)}}\right] \qquad \textbf{(Eq 4.3),}$$

where $\boldsymbol{I_K}$ is the kinetic current (A), $\boldsymbol{Q_H}$ refers to the amount of charges adsorbed (C) and 210 μC cm^{-2} is the conversion factor.

4.2.1.3 Mass activity (MA)

While the previous two metrics are important, for the purposes of commercialisation, the mass activity is the most crucial parameter investigated.[220] The mass activity relates to the activity of the catalyst per mass of PGM used. This is measured by performing the same LSVs as previously used to identify the $\boldsymbol{I_K}$. From this the mass activity[33] can be identified using the following equation:

$$\boldsymbol{Mass\ Activity}\left(\boldsymbol{Ag^{-1}_{PGM}}\right) = \left[\frac{\boldsymbol{I_K}}{\boldsymbol{L_{Pt}}(\boldsymbol{mg_{Pt}cm^{-2}})\boldsymbol{A_g}(\boldsymbol{cm^{-2}})}\right] \qquad \textbf{(Eq 4.4)},$$

where, $\boldsymbol{I_K}$ is the kinetic current, $\boldsymbol{L_{Pt}}$ is the loading of platinum ($mg_{Pt}cm^{-2}$) on the electrode surface and $\boldsymbol{A_g}$ (cm^{-2}) is the area of the working electrode.

4.2.1.4 Durability

Most methods for checking durability were primarily developed as *in situ* tests,[221] but *ex-situ* tests have also been developed. Potential cycling is widely used as a method of conducting durability tests *ex-situ*.[222,223,224] When the catalyst is cycled through a potential window between 0.6 V and 1.2 V vs RHE for above 1000 scans, the catalyst degradation can be studied. The stability of Pt/C can be studied in this region. Pt-NP stability decreases at potentials higher than 1.12 V vs RHE as PtO formation occurs. PtO formation is the first step in Pt dissolution and the mechanism alongside the standard potential[225] for each reaction is shown below:

$$\boldsymbol{Pt + H_2O \leftrightarrow PtO + 2H^+ + 2e^-} \qquad \textbf{(Eq 4.5)},$$

$$\boldsymbol{PtO + H_2O \leftrightarrow PtO_2 + 2H^+ + 2e^-} \qquad \textbf{(Eq 4.6)},$$

$$\boldsymbol{PtO_2 + 4H^+ + 4e^- \leftrightarrow\ Pt^{2+} + 2H_2O} \qquad \textbf{(Eq 4.7)},$$

$$Pt^{2+} + 2e^{-} \leftrightarrow Pt \qquad \textbf{(Eq 4.8).}$$

To study catalyst durability, this potential scanning method was used and the percentage decrease in peak current found on the CVs are used as a measure of catalyst durability.

Thus, *E. coli*-Pd (20%), *E. coli*-Pt (20%), *E. coli*-Pt:Pd* (10%:10%) and *E. coli*-Pd;Pt* (10%:10%) were synthesised as described previously and were all tested using *ex-situ* electrochemistry to elucidate their ECSAs, specific activities, mass activities and durabilities as reported below. As these bio-NPs were embedded within a biological matrix, they were expected to perform poorly due to their inherent resistivities. Early work on improving these conductivities included the sintering of bio-NPs[98] but this resulted in highly agglomerated NPs (to around 50nm).[125] Recent attempts to overcome this resistance have used various conductive supports such as graphene[226,100] carbon nanotubes (CNT)[227,228] and conductive polymers such as polypyrrole.[229] Cheng *et al.*, showed that bio-Pd vortex mixed with CNTs showed a 68-fold increase in catalytic activity.[228] Thus, an objective of this study was to report *E. coli*-Pt:Pd* (10%:10%) modified with CNTs and evaluate its ORR activity in comparison to unmodified material. Other attempts to improve conductivities are detailed in appendix A3.1

4.3 Materials and Methods

4.3.1 *E. coli* -NPs and Ink formulation

The catalysts *E. coli*-Pt (20%), *E. coli*-Pd (20%), *E. coli*-Pt:Pd* (10%:10%) and *E. coli*-Pd:Pt* (10%:10%) were produced as described in chapter 3 and suspended in an appropriate volume of diH_2O. An appropriate amount of catalyst was dried

at 105 °C and metal loading was estimated using ICP-MS of hydrolysates. To formulate the catalyst ink, an appropriate volume of the catalyst was mixed with 4 µl of 10% Nafion (Aldrich) (10% w/v in water) and diH_2O to make up 2 ml of ink with a PGM concentration of ~0.2–0.5 mg ml^{-1}. As *E. coli*Pd:Pt* (10%:10%) showed no electrocatalytic activity (Appendix A3.2), further studies were not conducted with this catalyst.

4.3.2 *E. coli*-Pt:Pd* (10%:10%) + CNT synthesis

To make a catalyst with CNTs, multi walled CNTS (MWCNTs) (50–90nm) from Sigma-Aldrich were used. An appropriate volume of catalyst was treated with MWCNTs to ensure a metal:CNT (w/w) ratio of 1:10.[228] This was mixed with 4 µl of 10% Nafion® (Aldrich) (10% w/v in water) and diH_2O to make up 2 ml of ink with a PGM concentration of ~0.2–0.5 mg ml^{-1}.

4.3.3 Characterisation

E. coli-NPs were characterised as described in the previous chapter (chapter 3). *E. coli*-Pt:Pd* (10%:10%) + CNT was further characterised by SEM to check for *E. coli*-NP and CNT interaction. This was done using a tabletop scanning electron microscope (TM3030Plus, accelerating voltage 15 keV, Hitachi, Hitec). SE imaging and BSE imaging modes were both used to examine the *E. coli*-Pt:Pd* and *E. coli*-Pt:Pd* + CNT surface structures.

4.3.4 Electrochemical testing

To evaluate the catalytic activity of the samples they were tested electrochemically *ex-situ* in a three-electrode half-cell consisting of a glassy carbon electrode (GCE; 5 mm in diameter), a reversible hydrogen electrode

(RHE) as the reference electrode (RE) and a platinum mesh counter electrode (CE) (chapter 2, section 2.3.1). The GCE was polished with sequential polishes using 1.0 μm, 0.3 μm and 0.05 μm alumina slurry on polishing pads. 2 mL of the catalyst ink was sonicated for 20 mins (Vibra Cell, 130 W, 40% Amplitude for 10 min with 10 s on and 10 s off). Catalyst sample (10 μL) was drop cast onto the GCE. This was spin dried (under air, 600 RPM) for use as a working electrode. All tests were conducted in 0.1 M $HClO_4$ electrolyte. The electrodes were connected to an Autolab (PGStat302N, Metrohm-Autolab, Utrecht, The Netherlands) potentiotsat /galvanostat through a Pine modulate speed rotator (AFMSRCE Pine research instrumentation, 5 mm).

For cyclic voltammetry (CV) tests, the electrolyte was first purged with N_2 (20 min). Prior to electrochemical analysis, the electrode was cleaned by cycling the applied potential between 0.05 and 1.03 V vs RHE at a scan rate of 0.1 V s^{-1} for 50 scans. CVs were then taken at scan rates of 0.1V s^{-1}. Electrode chemical surface areas (ECSAs) were calculated from the CV data as described by Garsany *et al.*, (2010).[33] While ECSA for palladium nanoparticles are usually calculated from CO stripping experiments, this method was shown to be unusable here as the biomass adsorption of CO results in an overestimated result (A. Stephen, unpublished work) in confirmation of a previous study (J.A. Bennett, unpublished work).

For ORR kinetics tests the electrolyte was saturated with O_2 and linear sweep voltammetries (LSV) were taken in the same potential window at rotation speeds of 0, 400, 800, 1200 and 1600 RPM and scan rate of 0.025 V s^{-1}. From

this specific activities and mass activities were calculated as described by Garsany *et al.*, (2010).[33]

Impedances of the catalysts were measured at a voltage of 0.6 V at a frequency range of 10^{5}–10^{-1} Hz after the electrolyte was saturated with O_2. From this, Nyquist plots were made to show catalyst impedances where the size of the semicircle obtained is related to the impedance (resistance) of the catalyst.[230]

4.4 Results

Initially *E. coli*-Pt (20%), *E. coli*-Pd (20%), *E. coli*-Pt:Pd* (10%:10%) and *E. coli*-Pd:Pt* (10%:10%) were evaluated electrochemically after 50 cleaning scans at a voltage scan rate of 100 mV s^{-1} as detailed above. A CV was taken at this scan rate and used to evaluate the electrochemical surface areas (ECSAs) with activity related to mass of metal via the known electrode loading which was confirmed using ICP-MS of solubilised metal recovered from the electrode (above). *E. coli*-Pd:Pt* (10%:10%) showed poor performances during CV tests (no discernible peaks at high scan rates) and as such was disregarded from any further results. (Appendix A3.2).

4.4.1 CVs to establish ECSAs of catalysts.

As shown in figure 4.1 the CVs acquired for *E. coli*-Pd (20%) (figure 4.1B) and *E. coli*-Pt:Pd* (10%:10%) (figure 4.1C) had more clearly defined peaks for hydrogen adsorption and desorption than *E. coli*-Pt (20%) (figure 4.1A). The ECSA was calculated for each material as described in section 4.3. *E. coli*-Pt/Pd* (10%:10%) had a higher ECSA with a value of 11.27 $m^2g^{-1}_{Metal}$ as compared to 6.74 and 8.77 $m^2g^{-1}_{Metal}$ for *E. coli*-Pt (20%) and *E. coli*-Pd (20%) respectively

(figure 4.1D). The higher ECSA for *E. coli*-Pd (20%) relative to *E. coli*-Pt (20%) could be a result of the more widely dispersed Pd nanoparticles relative to Pt. However, it should be noted that this method of calculating ECSAs often show unrealistic values for Pd as the metal stores H_2.[231] An alternative method would utilise CO stripping to calculate a realistic ECSA however, this could not be employed due to CO adsorption by biomass (unpublished work). The higher ECSA values of *E. coli*-Pt:Pd* (10%:10%), despite having a lower Pt loading, could be attributed to the more dispersed Pt nanoparticles relative to single metal *E. coli*-Pt (20%) (figure 3.8). The smaller and more spaced-out nanoparticles provide more sites for catalysis whilst simultaneously increasing conductivity of the system. *E. coli*-Pt (20%) had a large proportion of native, and thus resistive, cells while *E. coli*-Pd (20%) and Pt:Pd* (10%:10%), showed nearly all cells were metallised (figure 3.8).

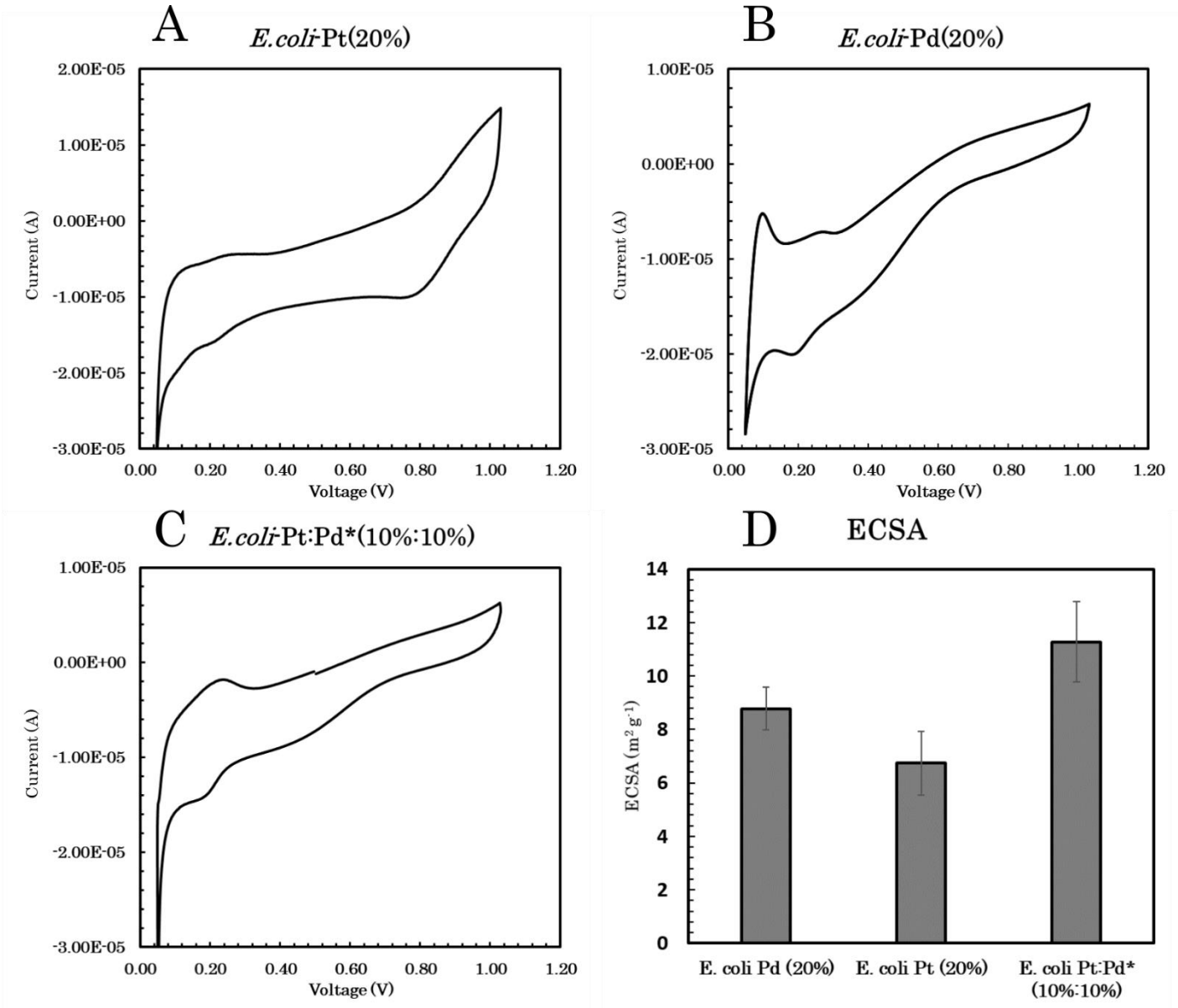

Figure 4.1 Electrochemical tests (cyclic voltammograms) of the (A)*E. coli*-Pd (20%) (B)*E. coli*-Pt (20%) and the bimetallic catalyst (C)*E. coli*-Pt:Pd (10%:10%) in 0.1 M $HClO_4$ at 25°C and in N_2-saturated solutions with a scan rate of 100 mV s^{-1}. Distinct peaks are apparent and used to elucidate their ECSAs shown in (D). *E. coli*-Pt:Pd (10%:10%) shows better ECSAs than single metal catalysts. *E. coli*Pd:Pt* (10%:10%) showed negligible activity (Appendix A3.2).

4.4.2 LSVs to evaluate SA and MA

To evaluate the ORR kinetic performance of the catalysts, linear sweep voltammetries (LSVs) were acquired at varying rotating speeds under O_2-saturated conditions. From this the specific activities and mass activities of the catalysts were evaluated as detailed in section 4.3. Figure 4.2A shows the Koutecky-Levich plots for the three catalysts. From these, the kinetic current $I_{kinetic}$, was deduced (see section 2.3.2) and used to identify specific activity and mass activity (figure 4.2B). The results show that *E. coli*-Pt:Pd* (10%:10%) shows better mass activity (2.8 mA mg^{-1}_{metal}) relative to both *E. coli*-Pd (20%: 0.3 mA mg^{-1}_{metal}) and *E. coli*-Pt (20%: 1.7 mA mg^{-1}_{metal}) i.e., nearly 10 times higher activity for the alloy than by using bio-Pd and 1.6-fold higher than by using bio-Pt. *E. coli*-Pt:Pd* (10%:10%) showed similar specific activities to *E. coli*-Pt (20%) indicating that its activity was primarily due to the action of Pt. The enhancement in mass activity could be attributed to the decreased impedance and as such this was checked as described in the Materials and Methods (section 4.3) (figure 4.2C). However, it is important to note that this mass activity of *E. coli*-Pt:Pd* (10%:10%) (2.8 mA mg^{-1}_{metal}) is still vastly inferior to commercial catalysts (~250 mA mg^{-1}_{metal}).[279]

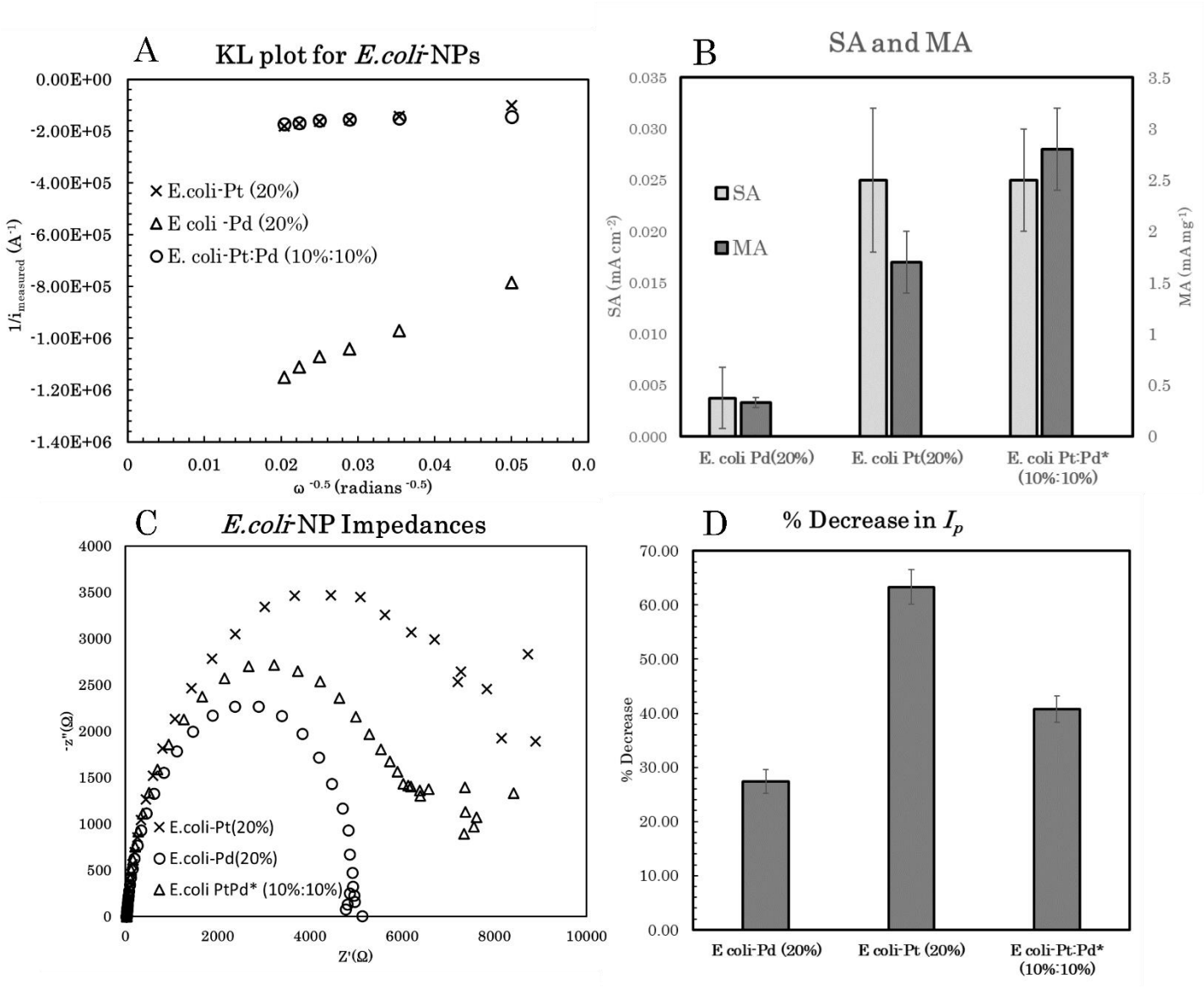

Figure 4.2 (A) KL plots of the *E. coli*-Pd (20%), *E. coli*-Pt (20%) and the bimetallic catalyst *E. coli*-Pt:Pd* (10%:10%) are shown. This was deduced by conducting LSV's in 0.1 M $HClO_4$ at 25°C and in O_2-saturated solutions with a scan rate of 20 mV s^{-1} at varying rotation rates. (B) shows the resultant SA and MA for these catalysts (C) shows the impedance for these catalysts conducted as described in Materials and Methods. (D) Shows the % decrease in peak size for each of these catalysts as a measure of durability.

4.4.3 **Impedance and durabilities**

As shown *E. coli*-Pt (20%) has the highest impedance followed by *E. coli*-Pt:Pd* (10%:10%) and then *E. coli*-Pd (20%) (figure 4.2C). *E. coli*-Pt (20%) has a significant portion of native unmetallised cells resulting in high resistances (figure 3.2). The highly dispersed nanoparticles across all cells in *E. coli*-Pt:Pd* (10%:10%) and *E. coli*-Pd (20%) was likely to have improved conductivities. It was concluded that the alloying of the two metals enhanced the electrochemical activity of the catalyst, attributed to a synergy of the higher catalytic activity of Pt coupled with the better dispersion afforded by the Pd "host" at a mol fraction of Pd:Pt of approx. 2:1.

To further evaluate the potential of these catalysts, their durabilities were checked. An initial CV was conducted on these catalysts and a representative peak was chosen (Appendix A3.3). Then, they were subjected to potential cycling within a window of 0.6–1.2 V for 1000 scans. A final CV was taken across the entire potential window and the decrease in peak current was used as a measure of durability. A representative scan for this is shown in Appendix (A3.3.) and the results are shown in figure 4.2D. As shown, the two metals afford different stabilities to the *E. coli* scaffold. *E. coli*-Pt (20%) has the highest decrease in stability at 64% while *E. coli*-Pd (20%) had the lowest at 28% and *E. coli*-Pt:Pd* (10%:10%) showed a moderate decrease at 41%. This result implies that metallisation, with a Pd component, affords a degree of stability to entire system. The higher dispersion of Pd seems to provide more stability than the highly clustered Pt nanoparticles but this needs to be checked. Furthermore, the permeabilization of the *E. coli* membrane by Pt (IV) during nanoparticle

synthesis might have contributed to a lower durability. This is supported by the bimetallic catalyst showing durabilities between the two. Undoubtedly, further studies will be required to elucidate the effect of metallisation on the bacterial scaffold as the effect of accelerated stress tests on the biomass is unknown. Previously, Pt/C was subjected to a similar durability test by Kim *et al.* A reduction of 33% was seen in its mass activity, however, even at this level of degradation, the mass activity was significantly higher (138 mA mg^{-1} relative to *E. coli*-Pt:Pd* (10%:10%) 2.8 mA mg^{-1}).[278]

4.4.4 Changing the ratios of Pt and Pd.

While *E. coli*:Pt:Pd* (10%:10%) has been shown to be a superior catalyst relative to single metal versions of the same, the effect of the Pt:Pd (w/w) ratios must be evaluated. These was attempted by varying the loading of Pt in the sample whilst keeping Pd loading constant. The electrochemical activities of the new catalysts *E. coli*:Pt:Pd* (5%:10%) and *E. coli*:Pt:Pd* (20%:10%) were then evaluated using CVs and LSVs as described above. The resultant ECSAs, specific activties and mass activities are shown relative to *E. coli*:Pt:Pd* (10%:10%) in figure 4.3 and table 4.1.

As expected, increasing Pt loading with *E. coli*-Pt:Pd* (20%:10%), increased the ECSAs relative to *E. coli*-Pt:Pd* (10%:10%), however, *E. coli*-Pt:Pd* (05%:10%) showed a similar ECSA to *E. coli*-Pt:Pd* (10%:10%) (figure 4.3A). From this, it could be implied that Pt nanoparticle synthesis occurs preferentially at the surface after a certain loading. Checking the specific activities (figure 4.3B) for the three catalysts showed a similar value for all three catalysts. This further

strengthens the previous implication that Pt is the major contributor for ORR activity in this catalyst. i.e., the current output per surface area stays constant regardless of increase in ECSA. These conclusions are further validated by checking the mass activities for all three catalysts. mass activities stayed similar for *E. coli*-Pt:Pd* (05%:10%) relative to *E. coli*-Pt:Pd* (10%:10%) (figure 4.3C) while it increased for *E. coli*-Pt:Pd* (20%:10%). This further implies that the surface of the cell is a preferential site for nanoparticle synthesis once a specific loading has been achieved. However, more detailed and sensitive tests with more experiments need to be conducted before this hypothesis can be justified. The potential benefit of a doubled mass of Pt (i.e., an equivalent atom ratio of the two metals) must be offset against the cost of the metals and this is discussed in chapter 6.

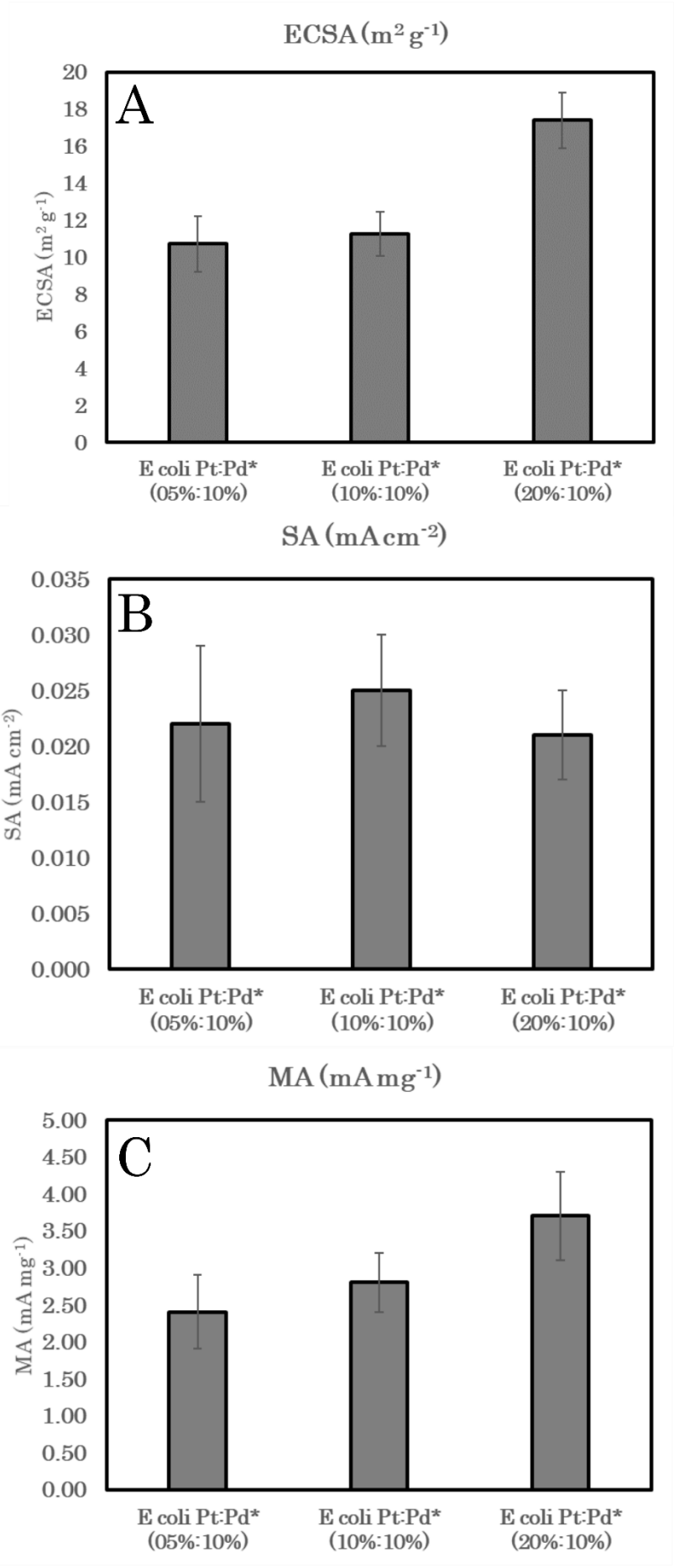

Figure 4.3 (A) ECSAs obtained for *E. coli*-Pt:Pd* (05%:10%), *E. coli*-Pt:Pd* (10%:10%), and *E. coli*-Pt:Pd* (20%:10%). These were obtained by conducting CVs under N_2 at 25 °C in 0.1 M $HClO_4$ at a scan rate of 0.1 V s^{-1}.KL plots of the *E. coli*-Pt:Pd* (05%:10%), *E. coli*-Pt:Pd* (10%:10%), and *E. coli*-Pt:Pd* (20%:10%) were obtained by conducting LSV's in 0.1 M $HClO_4$ at 25 °C and in O_2-saturated solutions with a scan rate of 0.25 mV s^{-1} at varying rotation rates. (B) and (C) shows the resultant SA and MA for these catalysts.

4.4.5 Overcoming Impedances using CNTs

A major barrier to good catalytic activity with bio-NPs have been the inherent impedances of the organic matter. Previous methods to increase conductivity primarily involved biomass carbonisation.[98,100,125] Here, alternative methods that did not require carbonisation have been investigated using *E. coli*-Pt:Pd* (10%:10%) as the representative catalyst. Alternative methods investigated included polymerisation of conductive polymer polypyrrole (PPY) onto cell surface,[229] reducing graphene oxide sheets (rGO)[226] and NPs simultaneously, and utilisation of carbon nanotubes (CNTs) with bacteria.[228] All three methods were attempted but only CNTs proved successful here. Progress with the other methods is detailed in appendix A3.1.

Figure 4. 4 A and B shows an SEM scan using a mix of SE and BSE for *E. coli*-Pt:Pd* (10%:10%) and *E. coli*-Pt:Pd* (10%:10%)+CNT respectively. As seen, the CNT's form a mesh in which the bacteria are embedded. Furthermore, sites of contact between the CNTs and nanoparticles (red arrows) can be seen providing sites for TPBs. CNTs have been previously shown to penetrate the bacterial cell wall by multiple groups[228] but evidence for this is unclear here at the low resolution used. In addition to enhancing conductivity, CNTs penetrating through the cell wall might access internalised nanoparticles thus increasing accessible ECSAs and mass activities. Further tests would be required to confirm this.

The catalyst was then tested in a similar fashion as above and the ECSA and mass activity was calculated (figure 4.4C). As shown, both ECSAs and mass

activities increased (by ~2.5–3 fold) to 28.32 m^2g^{-1} and 8.50 $mAmg^{-1,}$ respectively. These increases could be attributed to the decreased impedance as shown by the Nyquist plot in figure 4.4d. While the CNTs have improved catalyst performances by ~3-fold, it is important to note that the impedance is still significant and that activities are still inferior to commercial catalysts (see chapter 6). This disparity could be attributed to the resistivities of the organic matter, the lack of complete penetration by CNTs and the inaccessibility of a proportion of the nanoparticles.

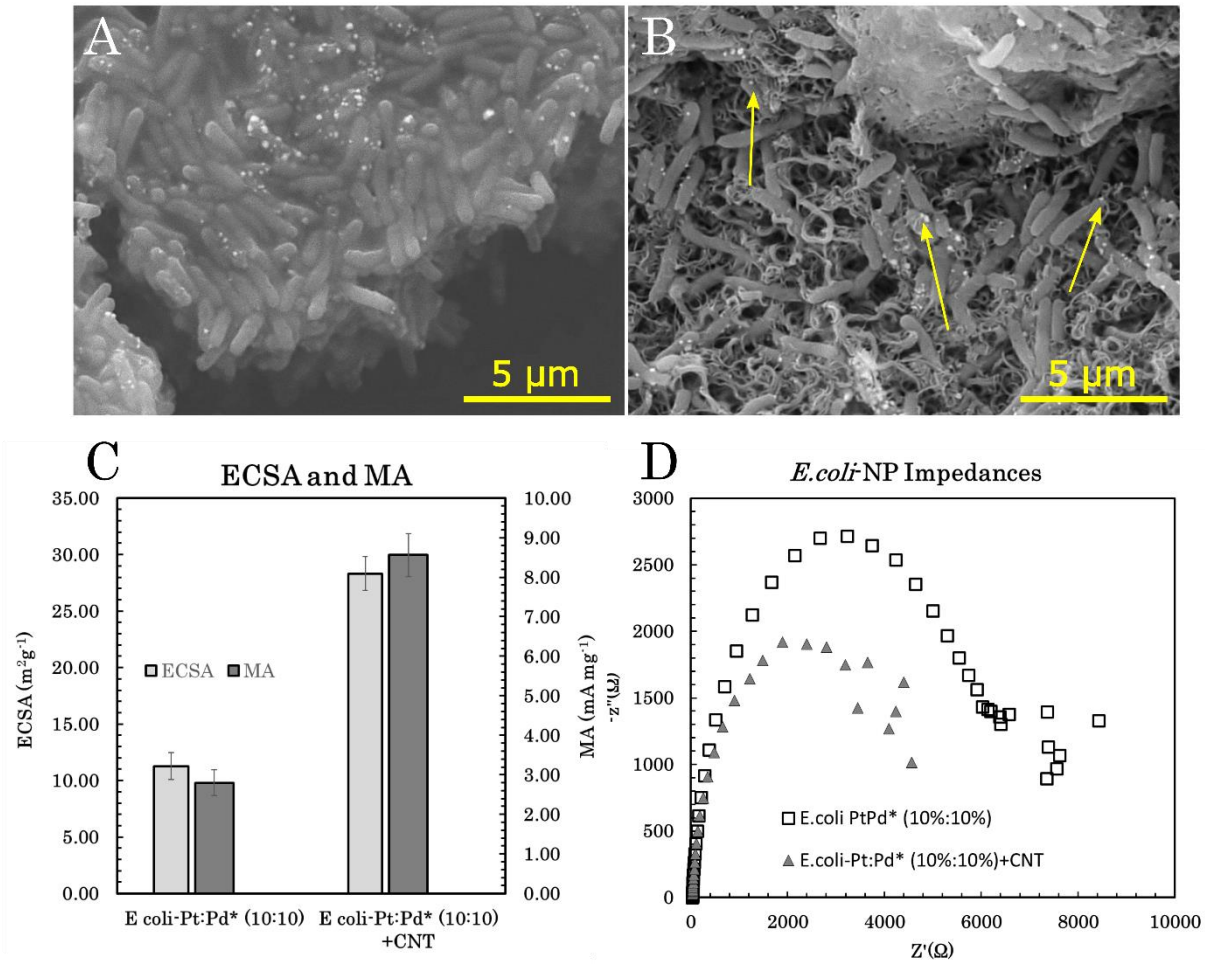

Figure 4.4 (A) and (B) SEM image taken of *E. coli*-Pt:Pd* (10%:10%) and *E. coli*-Pt:Pd* (10%:10%)+CNT respectively, with a mix of BSE and SE signals using a desktop SEM with an electron acceleration of 15 kV and a magnification of 9000x. After a series of similar CVs and LSV's as discussed above, (C) shows the resultant ECSA and MA for these catalysts and (D) shows the impedance for these catalysts conducted (section 4.2)

4.4.6 **Conclusion**

As shown above, *E. coli*-Pt (20%), *E. coli*-Pd (20%) and *E. coli* Pt:Pd* (10%:10%) were evaluated for their ORR catalytic activity using a series of *ex-situ* electrochemical tests. The tests showed the bimetallic outperformed single metal versions of the catalyst with better ECSAs and mass activities. However, the catalyst performed poorly against commercial catalysts due to its high

impedances and Pt utilisation (chapter 6). Furthermore, the effect Pt:Pd w/w ratio was checked, and this showed to influence ORR activity. To overcome impedances, the catalysts were treated by various methods (appendix A3.3). Catalyst without and treated with CNTs was tested for activity. The CNT-treated catalyst showed the highest ECSAs and mass activities at 28.32 $m^2 g^{-1}$ and 8.56 mA mg^{-1} respectively. The data are summarised in the following table.

Table 4.1 Summary table of catalysts evaluated and their evaluated ECSAs, SAs and MAs.

Summary of catalysts and their activity			
Catalyst	**ECSA (m^2g^{-1})**	**SA (mA cm^{-2})**	**MA (mA mg^{-1})**
E. coli-Pd (20%)	8.77	0.004	0.33
E. coli-Pt (20%)	6.74	0.025	1.70
E. coli-Pt:Pd* (10%:10%)	11.27	0.025	2.80
E. coli-Pt:Pd* (05%:10%)	10.73	0.022	2.40
E. coli-Pt:Pd* (20%:10%)	17.39	0.021	3.70
E. coli-Pt:Pd (10%:10%)+CNT	28.32	0.029	8.50
TKK (commercial catalyst)[288]	80.00	0.265	210

Chapter 5: Comparative Life Cycle Assessments of biosynthesised nanoparticles against commercial catalysts

5.1. Abstract

A screening life cycle analysis (LCA) was conducted to establish the environmental benefits in biosynthesis of NPs for PEMFC catalysts. An LCA of a commercial catalyst, with a mass activity of 250 mA mg^{-1}_{PGM}, was compared to an LCA of *E. coli*-Pt:Pd* with a mass activity of 2.80 mA mg^{-1}_{PGM}. The study showed that relative to *E. coli*-NPs, commercial Pt/C only had ~2% of the environmental impacts when used as PEMFC catalysts. This was attributed to the low MA of *E. coli*-NPs relative to Pt/C. An alternative LCA using a hypothetical *E. coli*-Pt:Pd catalyst with an MA of ~250 mA mg^{-1}_{PGM} showed that relative to commercial catalyst (Pt/C) it only had ~50% of the environmental impacts.

5.2. Introduction

With the environmental impacts of the current fossil-fuel based energy system being felt, any sustainable and eco-friendly alternative must be evaluated to prevent further non-obvious impacts.[232,233] A hydrogen-based economy, powered by fuel cells, is poised to be the next great disruptor to the current energy infrastructure.[234] PEMFCs are heavily investigated for mobile automotive applications as they have comparatively low environmental impacts during their use phase.[235] In fact, studies have shown that fuel cell electric vehicles (FCEVs) can offer significant environmental advantages over traditional internal combustion engine vehicles (ICEVs) based on the source of H_2 used (i.e.

renewable H_2 vs fossil fuel based H_2).[236] However, they utilise a significant amount of PGMs as anodic (HOR) and cathodic (ORR) electrocatalysts and catalyst synthesis results in substantial environmental impacts.[237]

Biosynthesis of nanoparticles is often cited as an eco-friendly alternative to chemical synthesis[93,238] but research has shown that this "improvement" is often overstated. For example, when biosynthesised Au nanoparticles, produced by a variety of biosynthetic methods, were compared to commercial chemically synthesised catalysts, the environmental impacts were similar for all.[239] The impacts were primarily due to using gold and not affected by the synthesis method. Thus, even biosynthesis of gold nanoparticles has significant environmental impacts.[239] Similarly, biosynthesis of magnetite nanoparticles was shown to increase environmental impacts, relative to industrial synthesis, when analytical grade raw materials were used. This impact was reversed, and a net environmental saving was seen when the same method used alternative raw materials and metal-containing wastewaters.[240] Thus, any biosynthesised ORR catalyst should be evaluated for its environmental impact and this chapter will conduct a systematic life cycle analysis (LCA) comparing commercial catalysts to biosynthesised nanoparticles for use in PEMFCs.

5.2.1. Investigating environmental impacts using Life Cycle Analysis (LCA)

LCA is an essential analytical tool that determines the environmental impact of a product through its entire lifetime, from extraction and production of raw materials to the final disposal or recycling of end products.[241] It has a variety of applications including identifying areas of improvement for a product, analysis

of the contribution of different life cycle stages and comparisons between different products.[242] Its importance in evaluating the various novel energy systems in development cannot be understated; sources that are suitable for heat production might not be ideal for electricity and transport purposes.[243]

The International Standard Organisation (ISO) defined two leading standards for an LCA; ISO 14040 defined the principles and framework and ISO 14044 defined its requirements and guidelines.[244,245] As shown in figure 5.1, a standard study consists of 4 main phases:[246]

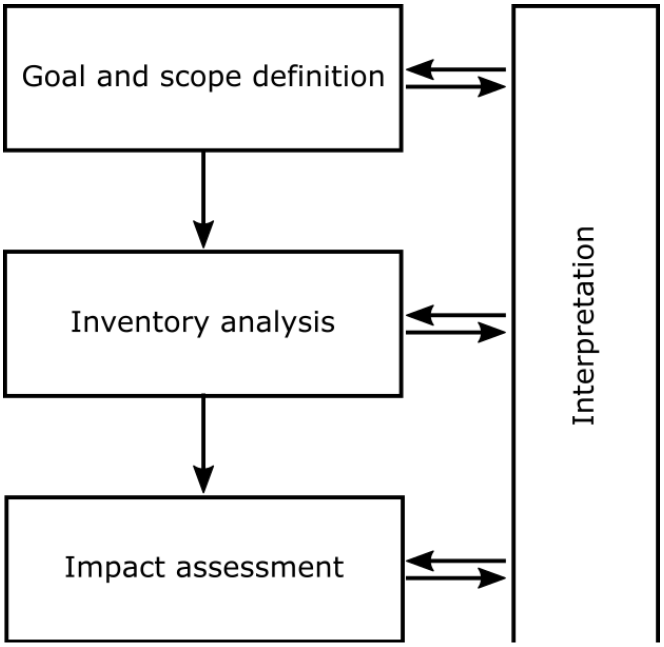

Figure 5.1 A schematic of the methods involved in conducting an LCA for a product. First, a goal and scope of the study needs to be defined. In doing so a functional unit is decided for the study. Then all the inputs and outputs of the entire system is considered in an inventory analysis. Finally, an impact assessment is done on the product using one of the previously described methods. At all points the study is subject to interpretation; and the study is subject to sensitivity and uncertainty analysis.

(1) Defining the goal and scope of the study: As an essential first step, the goal of conducting an LCA, and the product studied, need to be determined. Then a

functional unit is determined for the project; this is a quantified measure of the product and relates to all inputs and outputs of the entire life cycle. For example, an LCA comparing industrial milk production from three different dairies used 1000 litres of milk as a functional unit.[247] Then the scope of the project is determined by defining the system boundaries; for example, the system boundary for milk production at different diaries could be limited to production at the diary or extended to include transport to market.[246]

(2) Inventory analysis: Once the goal, scope and functional unit is defined, an inventory analysis can be done. This is done by collecting data to make a model of the product life cycle with all the environmental inputs and outputs within the defined boundaries.[248] The data collected can be classified into foreground data, which specifies data that are specific to the product and background data, which specifies data that is used for production of generic materials (including industrial plants), energy, water and transport.[246]

(3) Life Cycle Impact Assessment (LCIA): Once an inventory has been established for the various functional units, an LCIA is conducted. This is used to understand the environmental relevance of the inputs and outputs.[246] The impacts of each element are studied and classified into various categories including climate change, human toxicity, eutrophication (enrichment of environment with nutrients) and others.[246] In assessing the impacts, one can develop their own methodology but alternatively, to facilitate comparative studies, several standardised methodologies have been developed. These can be classed into single issue methodologies that only consider a single category (like

climate change) or multiple issue categories (like ReCiPe 2016,[268] CML EU25[252] etc.). Single issue categories often leave out the impacts of various categories for e.g. Skullstead *et al.*, conducted a comparative LCA on the climate change effects of reinforced concrete versus timber for high-rise buildings;[249] however this does not consider impacts on the ecology and human toxicity. As such, multiple issue categories are often preferred. Every LCIA requires the obligatory classification and characterisation of impacts into separate categories. Each characterisation factor (category) must be based on well understood and documented science. Some methods add an extra step that contrast the impact of individual categories against each other. One such step is the normalisation, which as defined by the ISO, calculates the magnitude of each impact category in relation to some reference information.[250] This is shown mathematically as

$$N_i = \frac{S_i}{R_i} \qquad \textbf{(Eq 5.1)},$$

where N_i is the normalised value of the impact category, S_i is the characterised impact of the study, R_i is the characterised impact of a reference study.[251] The reference study can be the impacts of total inputs and outputs over a geographical area for a reference year for e.g. CML EU25 normalises its impact categories over 25 European countries over the reference year of 2006.[252]

A further step used in analysis is the weighting of categories against each other. In this step, a subjective analysis of the relative importance of the categories is done and their values are adjusted to reflect this. This is not recommended by the ISO on studies done for public consumption. Due to its subjective nature, this study will exclude this step.

(4) Interpretation: Once an LCIA is conducted, the results need to be interpreted. For a comparative LCA, the analysis compares the impact for the products in different categories. Further interpretation includes conducting an uncertainty analysis, which checks for the variation in data and this can be done using statistical analysis of the data (i.e., Monte Carlo data analysis etc.). Then the uncertainty in the model is checked for its correctness and incompleteness by evaluating the assumptions of the model. This is done by using a sensitivity analysis that varies the assumptions to check the robustness of the model. For example, a study that researched LCA of wastewater treatment in Denmark then conducted a sensitivity analysis of the study by alternating the end-of-life treatment of the sludge and by applying varying LCIA methods.[253]

5.2.2. LCAs of PEMFC and their catalysts

Multiple studies have been previously conducted on the LCA of PEMFCs.[254,255] These have mainly focused on the entire fuel cell stack and related them to their applications including automotive[235] and power generation.[256] When comparing automotives, these studies have generally shown that fuel cell electric vehicles (FCEVs) have fewer environmental impacts, relative to internal combustion engine vehicles (ICEVs), if they utilised clean (renewable) H_2.[236,257] Furthermore, Simons and Bauer (2015) showed that the MEA of a fuel cell stack is a major contributor to these environmental impacts.[258] When PGM was recycled, Notter *et al.*, (2015) showed that this significantly reduced the environmental impacts of primary extraction[236] thus, implying that the catalyst production is a major contributor. Thus, any catalyst must consider an LCA of its production before commercialisation. Various studies have considered the

LCA of the electrocatalyst within the entire study.[235,236] However, these studies cannot be directly compared as the synthesis methods do not correlate with each other and thus it is important to consider the method used.

5.2.3. Synthesis methods of commercial catalysts

Platinised carbon can be manufactured by either reducing platinum salt directly onto a carbon support or by intially producing Pt nanoparticles prior to supporting them on a scaffold. They all follow a general scheme where Pt (ions) from a precursor are reduced using a reducing agent in an energy intensive process; this promotes nanoparticle synthesis.[38] These NPs have been synthesised using a variety of methods including (1) impregnation reduction methods,[38,39] (2) colloidal method[40] or by (3) physical deposition of metallic platinum directly on the carbon support.[41]

The impregnation reduction method is defined by a deposition step.[259] Pt salt solution is mixed with conductive supports where the liquid precursor is adsorbed onto the pores of the support. The leftover precursors are then separated out before a reducing agent is added, such as H_2 (for a gaseous phase reduction)[260] or liquids like formaldehyde (for a liquid phase reduction).[261] A major drawback of this method is the lack of size control of metal nanoparticles produced but this is often overcome by using a highly ordered scaffold.[259]

The colloidal method is the more commonly used method to synthesise metal nanoparticles.[259] Here, the metal precursor (solution) is mixed with a stabilising agent in an organic medium and then reduced to Pt nanoparticles. The nanoparticles are then mixed with a conductive support and the stabilising

agent is removed.[259] This method is preferred because it can afford good control over nanoparticle sizes.[262]

The physical vapour deposition method involves the physical deposition of Pt metal directly onto the conductive support. For example, Jukk *et al.*, formed Pt nanoparticles on MWCNT, in an inert argon atomsphere, through magnetron sputtering.[263] Here a plasma containing positive ions of the metal is accelerated in an electric field.[264] The support, in the presence of argon, is bombarded with these ions to eject atoms from the support while depositing the metal.[265]

As these techniques vary in their reactive agents and methodology used, this study highlights colloidal Pt/C synthesis as representative approach. Colloidal Pt nanoparticles were synthesised in a glycol solution of NaOH[266] and then supported on carbon to form 30% Pt/C.[266] This synthesis method, reported by Speder *et al.*, was used as it identified the mass activity for this catalyst; the mass activity will be used to describe the functional unit.[266] A screening (preliminary) LCA study will be conducted on this catalyst as reference baseline by combining the chemical plant considerations (for electrocatalyst synthesis) reported by Notter *et al.,* [236] with the Speder electrocatalyst;[266] Notter *et al.,* did not report mass activities. Then, *E. coli*-Pt:Pd* (10%:10%) and a biocatalyst made using a representative industrial microbial consortium (Bangor-Pt:Pd*, see below) will be compared against this standard. It is assumed that the chemical plant used for bio-NPs will be similar to those used by Notter *et al.*[236] The study conducted is a screening study because the industrial production of

all catalysts described here is still hypothetical, with assumed values. As such, a comprehensive analysis cannot be conducted.

5.3. Materials and Methods

A comparative screening LCA was conducted on *E. coli*-Pt:Pd* against commercial Pt/C. The robustness of this study was checked using sensitivity analysis. This is done as shown below.

5.3.1. Goal and Scope Definition

Table 5.1 shows a summary of this section. The goal of this study was to conduct a comparative screening LCA of *E. coli*-Pt:Pd* against a commercial catalyst. The scope of this study was defined from the raw materials to product. In comparing the catalysts, the amount required to perform a specific function must be considered. As such, the functional unit used is defined as the amount of catalyst (in mg) required to produce 0.44 A at 0.9 V (D.O.E. target for mass activity[29]) under standard conditions and this was identified using the following equation:

$$\textbf{\textit{Amount of catalyst}}\ (\boldsymbol{mg}) = \frac{\mathbf{0.44}\ \boldsymbol{A}}{\textbf{\textit{Mass activity}}\ (\boldsymbol{A\ mg^{-1}})} \qquad \textbf{(Eq 5.2)}$$

This correlation assumes that *in-situ* activity of an electrocatalyst can be directly correlated to its *ex-situ* mass activity but this is demonstrably false; Pt/C catalyst TKK showed mass activities of 0.11 A mg^{-1} *in-situ*[33] but values of ~0.25 A mg^{-1} were reported *ex-situ*.[279] Catalysts will be subject to different challenges during *in-situ* operation that can affect further their performance. However, since the *E. coli*- NPs did not perform well enough for *in-situ* tests (section 4.4), this correlation is assumed to be true. The synthesis method for *E.*

coli-Pt:Pd* (10%:10%) (henceforth known as *E. coli*:Pt:Pd* in this chapter) (described in chapter 3, figure 5.2) and Pt/C (figure 5.3)[266] are shown as a flow chart below. Flow charts on the production of H_2PtCl_6, Na_2PdCl_4 and *E. coli* are shown in appendix A4.1.

Things to define:	Definitions:
Goal of the study	Screening LCA comparing environmental impacts of chemically synthesised Pt/C vs biosynthesised *E. coli*-Pt:Pd as PEMFC ORR catalysts.
Scope (System boundaries)	Raw materials to production of 1 kg of electrocatalyst
Intended application of the study	Investigate the potential of biosynthesised nanoparticles as Fuel Cell catalysts
Investigated product A	Electrocatalysts Pt/C
Investigated product B	Biosynthesised *E. coli*-Pt:Pd*
Data Source for A	Published papers[264,266]
Data Source for B	This thesis
Functional unit	Amount of catalyst required to produce 0.44A at 0.9V
Assumptions	Mass activity correlates to *in-situ* operation. Chemical plant considerations are transferrable across

Table 5.1 The goal and scope of the study. This further highlights the functional unit, products studied, and sources used.

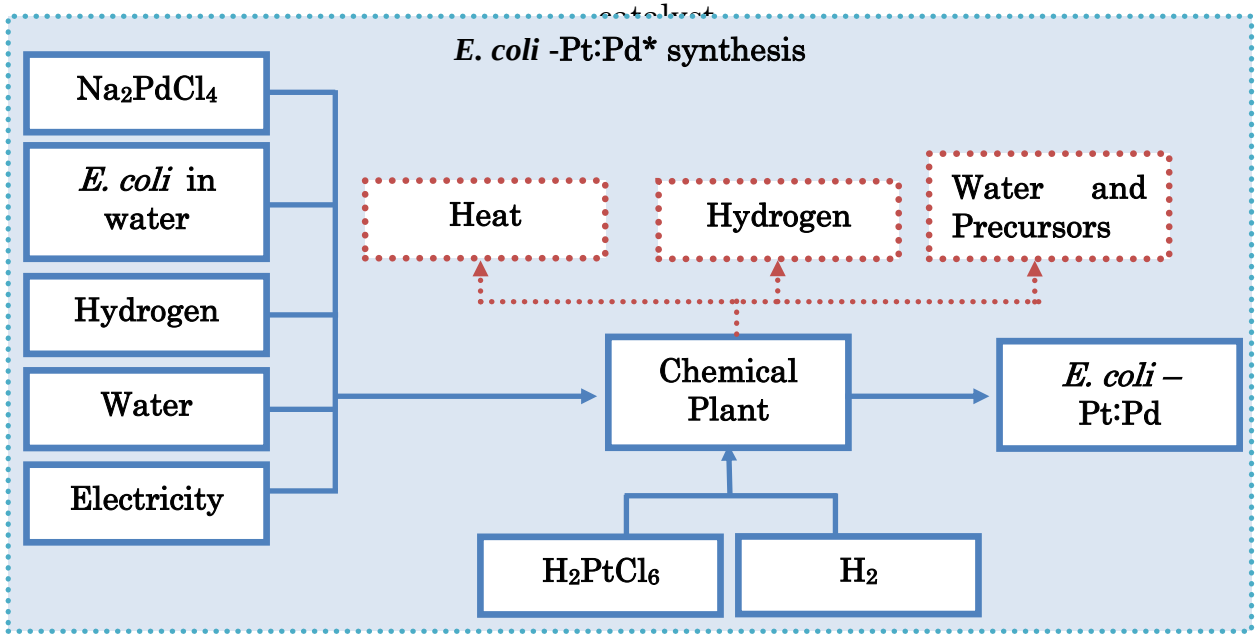

Figure 5.2 A schematic for *E. coli*-Pt:Pd synthesis. The precursor used is Na_2PdCl_4 for palladium and H_2PtCl_6 for platinum. The reducing agent is H_2. The leftover water, H_2 precursors and heat are shown as waste products in red boxes.

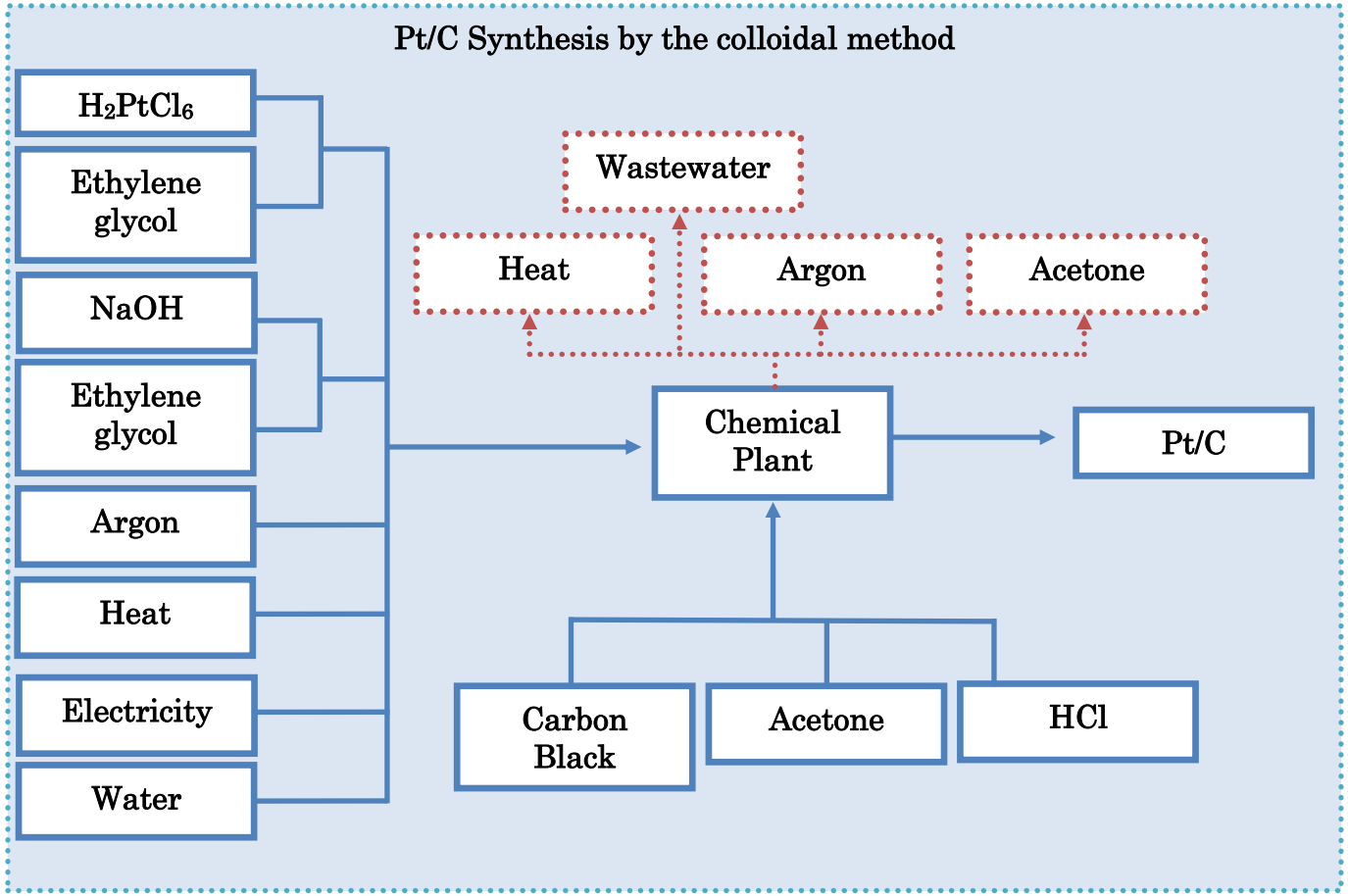

Figure 5.3 A schematic of the Pt/C colloidal synthesis. The precursor used is H_2PtCl_6, the organic medium and reducing agent used is ethylene glycol and the carbon support used is carbon black. The waste emissions are shown in red boxes

5.3.2. LCI

Once the goal and scope of the study was defined, the LCI to produce 1 kg of both products was determined. This was determined using a combination of inhouse studies (for *E. coli*-Pt:Pd*), published papers on Pt/C synthesis[266] and previously conducted LCA studies.[256,236] These are shown below as table 5.2 for Pt/C and table 5.3 for *E. coli*-Pt:Pd*. where unit p refers to one part of the chemical plant (used to indicate the impact in using a chemical plant) and t km is the unit for tonne kilometre which represents the transport of 1 tonne of goods over 1 kilometre.

Table 5.2 LCI detailing the inputs and outputs required to produce 1 kg of commercial catalyst 30% Pt/C. The data used is adapted from Notter *et al.,*[236] and Speder *et al.*[266]

Production of Electrocatalyst powder Pt/C			
Inputs	**Amount**	**Unit**	**Ref**
Carbon black, at plant	7.00×10^{-1}	kg	266
Ethylene glycol, at plant	8.88×10^{1}	kg	266
Hexachloroplatinic acid, at plant	6.29×10^{-1}	kg	266
NaOH, pellets	7.00×10^{-1}	kg	266
Hydrochloric acid, 30% in H20, at plant	1.10×10^{1}	kg	266
Acetone, liquid	1.88×10^{0}	kg	266
Argon, liquid	5.71×10^{-1}	kg	266
Nylon 66, at plant	3.10×10^{-4}	kg	236
Extrusion, plastic film	3.00×10^{-4}	kg	236
Water, ultrapure, at plant	8.64×10^{1}	kg	236
Soap, at plant	1.70×10^{-3}	kg	236
Electricity, low voltage	2.30×10^{0}	k Wh	236
Chemical plant, organics	4.00×10^{-10}	p	236
Transport, freight, rail	8.60×10^{-1}	t km	236
Transport, lorry > 16t, fleet average	1.40×10^{-1}	t km	236
Outputs			
Electrocatalyst powder, Pt/C	1.00×10^{0}	kg	266
Heat, waste	8.40×10^{0}	MJ	236
Argon, gas	5.71×10^{-1}	kg	266
Acetone	1.88×10^{0}	kg	266
Disposal, municipal, solid waste	1.40×10^{-2}	kg	236
Wastewater	1.80×10^{2}	kg	236

Table 5.3 LCI detailing the inputs and outputs required to produce 1 kg of biosynthesised electrocatalyst *E.coil*-Pt:Pd* (10%:10%). The data used is from this thesis and from Notter *et al.*[236]

Production of Electrocatalyst *E. coli* Pt:Pd			
Inputs	**Amount**	**Unit**	**Ref**
E. coli	8.00 x10^{-1}	kg	This study
Hexachloroplatinic acid, at Plant	2.10 x10^{-1}	kg	This study
Sodium tetrachloropalladate	2.76 x10^{-1}	kg	This study
Hydrogen, liquid	2.30 x10^{1}	kg	This study
Nylon 66, at plant	3.10 x10^{-4}	kg	236
Extrusion, plastic film	3.00 x10^{-4}	kg	236
Water, ultrapure, at plant	1.50 x10^{2}	kg	236
Soap, at plant	1.70 x10^{-3}	kg	236
Electricity, low voltage	2.30 x10^{0}	k Wh	236
Chemical plant, organics	4.00 x10^{-10}	p	236
Transport, freight, rail	8.60 x10^{-1}	t km	236
Transport, lorry > 16t, fleet average	1.40 x10^{-1}	t km	236
Outputs			
Electrocatalyst powder, *E. coli*-Pt:Pd, at plant	1.00E x10^{0}	kg	This study
Heat, waste	8.40E x10^{0}	MJ	236
Disposal, municipal, solid waste	1.40E x10^{-2}	kg	236
Hydrogen	2.30E x10^{1}	kg	236
Wastewater	2.00E x10^{2}	kg	236

5.3.3. LCIA

LCIA was conducted using the LCA Software SimaPro 8.5.2.0[246] and the Ecoinvent 3 databases[267] available were used. The methodology chosen was ReCiPe,[268] as this is a damage-oriented LCIA assessment, which provides three endpoint categories i.e., human health, ecosystems and resources. These are further subdivided into 18 midpoint categories. This assessment was conducted on *E. coli*-Pt:Pd*, Pt/C and on catalyst made by an industrial waste consortium (see below) with a microbial composition as detailed in Santos *et al.*[269]

5.3.4. Interpretation

Once the LCIA was conducted on both *E. coli*-Pt:Pd and Pt/C, this methodology was interpreted for its robustness using a sensitivity analysis. To check robustness of this methodology LCIAs were also conducted using the CML,[270] IPCC,[271] Impact 2002+[272] and Eco-indicator 99[273] methods. The assumption was tested by changing the value of mass activity for *E. coli*-Pt:Pd* and the industrial strain (see below) using experimentally determined and hypothetical values.

5.4. Results and Discussion

The functional units for *E. coli*-Pt:Pd* and Pt/C were calculated using Eq 5.2 and it was shown that the amount of *E. coli*-Pt:Pd* with a mass activity of 2.8 mA mg^{-1} (as calculated in chapter 4) would require 157.1 mg of catalyst material (metal and bacteria) while Pt/C with a mass activity[266] of 0.25 A mg^{-1} would require 1.8 mg of catalyst material (metal and carbon). A ReCiPe 2016 Endpoint (H) LCIA was conducted on *E-coli*-Pt:Pd* and Pt/C using the LCI as shown in section 5.3. The results are shown below.

5.4.1. Comparative LCA for Pt/C vs *E. coli*-Pt:Pd*

Figure 5.4 shows the endpoint characterisation of both Pt/C and *E. coli*-Pt:Pd* with categories human health, ecosystems and resources. Figure 5.4A shows their relative impacts with as a percentage of *E. coli*-Pt:Pd* impact (i.e. *E. coli*-Pt:Pd* impact is set to 100% and Pt/C impact is shown as a percentage of this). As seen, Pt/C far outperforms *E. coli*-Pt:Pd* in every category with a relative impact of ~2%.

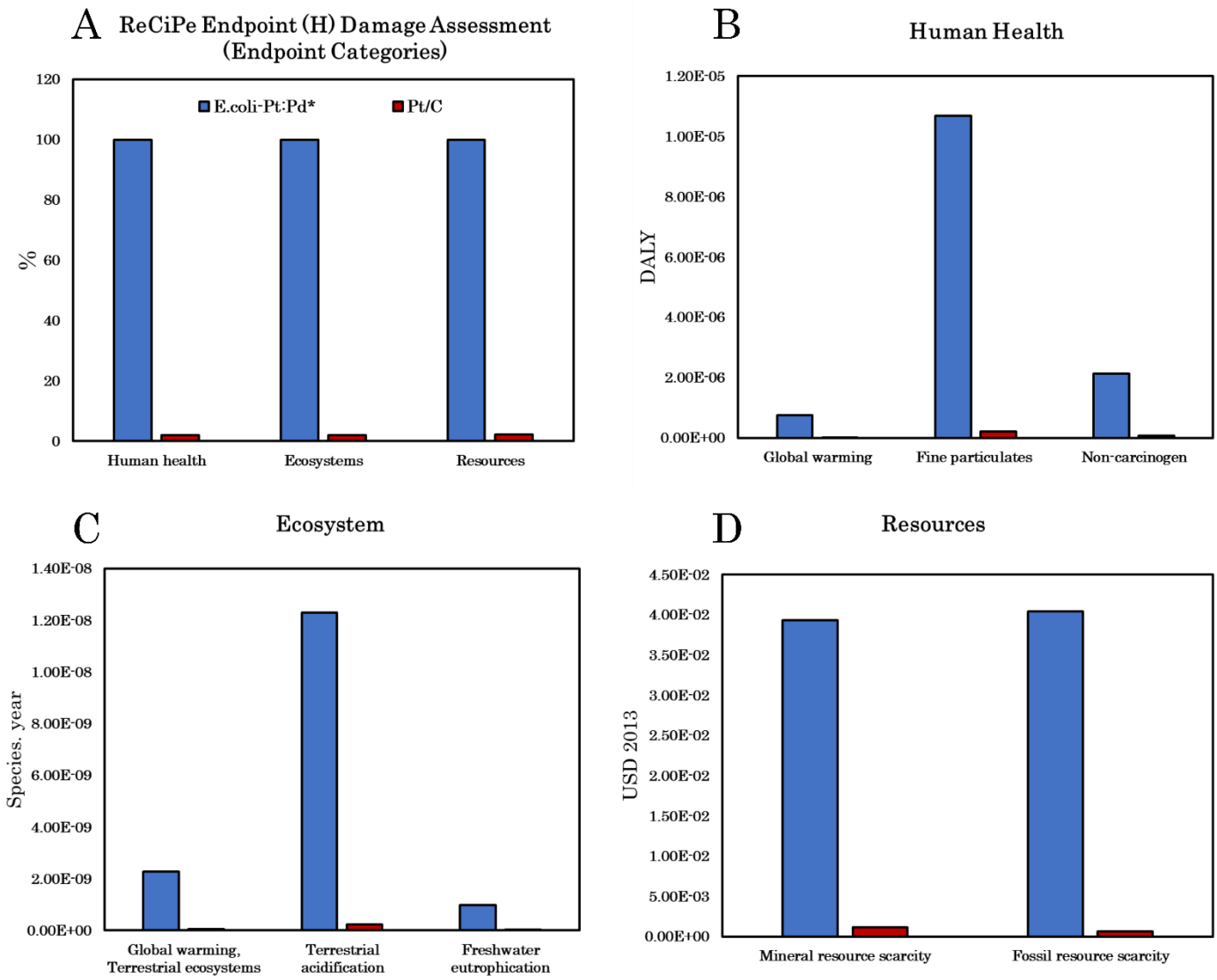

Figure 5.4 A shows the relative impacts of the endpoint categories while conducting an LCIA using the ReCiPe 2016 Endpoint (H) methodology on *E. coli*-Pt:Pd* (blue) and Pt/C (red). As seen Pt/C has a relative impact of around 1% in all categories. Figures 5.4B, C and D expands on the individual endpoint categories (Human health, Ecosystem and Resources respectively) into their individual midpoint categories with the units DALY (measure of overall disease burden expressed as the number of years lost due to ill-health, disease or early death), species.year (measure of the number of species that will become extinct over time) and USD 2013 (measured in cost of resources in US dollars at 2013) respectively. Only the most impactful of these midpoint categories are shown here.

To investigate further, the midpoint categories were investigated, and these are shown in figure 5.4B (Human Health), C (Ecosystems) and D (Resources). Note that only the most impactful midpoint categories are shown here. The human health midpoint categories investigated were global warming, fine particulate matter formation and human non carcinogenic toxicity categories; these were measured in disability adjusted life years (DALY), which is a measure of overall disease burden expressed as the number of years lost due to ill-health, disease or early death. Ecosystems midpoint categories investigated were global warming (terrestrial ecosystems), terrestrial acidification and freshwater eutrophication; these were measured with the background extinction rate units (species.year), which is a measure of the number of species that will become extinct over time. Resource midpoint categories investigated were mineral resource scarcity and fossil resource scarcity; these are measured in cost of resources in US dollars at 2013 (USD 2013).

As seen, *E. coli*-Pt:Pd* has in each case far too high an impact relative to commercial catalyst and this is clearly due to its significantly lower mass activities; its mass activity is a hundred times lower than the commercial equivalent. While these data highlights the relative impact of using *E. coli*-Pt:Pd* at this stage, these histograms also hide the very real environmental impacts of using commercial Pt/C made from primary sources. Thus, the next step was to use a hypothetical *E. coli*-Pt:Pd* catalyst that provides a similar mass activity of 0.25 A mg^{-1} and compare this to Pt/C. This assumes that modifications (e.g. genetic or otherwise) can be made to the bacterial scaffold without making major adjustments to the current life cycle of the catalyst.

5.4.2. Comparative LCA of Pt/C vs *E. coli*-Pt:Pd* (0.25 A mg^{-1})

As seen in figure 5.5 a comparative LCA was conducted on Pt/C and hypothetical catalyst *E. coli*-Pt:Pd* with a mass activity of 0.25A mg^{-1}. Figure 5.5A shows the three end point categories (Human Health, Ecosystem and Resources) for both catalysts as a percentage of Pt/C impact. The Pt/C performed poorly as compared to *E. coli*-Pt:Pd (0.25 A mg^{-1}) in both human health and ecosystem categories. The hypothetical bio-derived catalyst only has around 50% of the impacts relative to Pt/C in these categories. These end point categories were further investigated through their midpoint categories. Figure 5.5B, 5.5C and 5.5D show the midpoint categories of human health, ecosystem and resource categories respectively, with *E. coli*-Pt:Pd* (0.25A mg^{-1}) outperforming commercial catalyst in every midpoint category.

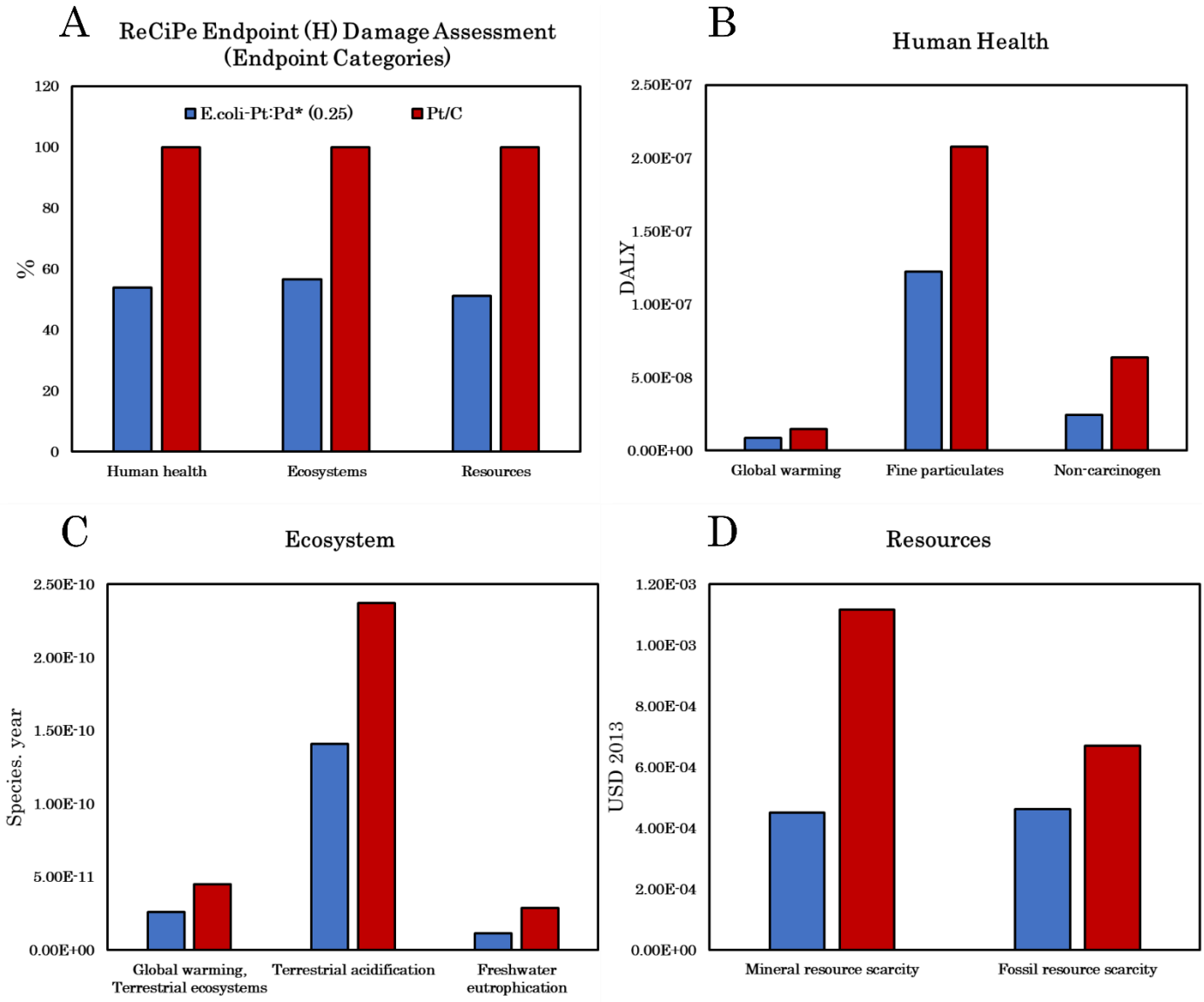

Figure 5.5A shows the relative impacts of the endpoint categories while conducting an LCIA using the ReCiPe 2016 Endpoint (H) methodology on *E. coli*-Pt:Pd* (0.25 A mg^{-1}) (blue) and Pt/C (red). As seen Pt/C has a relative impact higher in human health and ecosystems but is lower in resources. Figures 5.5B, C and D expand on the individual endpoint categories (Human health, Ecosystem and Resources respectively) into their individual midpoint categories with units DALY, species.year and USD2013 respectively. Only the most impactful of these midpoint categories are shown here

5.4.2.1.Robustness of model

The robustness of this model was checked by conducting comparative LCAs of both catalysts using LCIA methodologies CML baseline, IPCC, Eco-indicator 99 and Impact 2002+. From this, similar categories were identified, and the percentage advantage of *E. coli*Pt:Pd* (0.25 A mg^{-1}) against commercial catalyst is compared for all methodologies. This is shown in table 5.4 and as seen, comparing the values show that this model is not very robust. This can be attributed to the screening nature of this model (i.e. not a comprehensive study); true values of emissions can only be ascertained when a supply chain has been established. However, it must be noted that human health and resources agree with two other models (highlighted in yellow) and CML, IPCC and Impact 2002+ show agreement in global warming potential (GWP).

Table 5.4 Comparison of the impact of individual endpoint categories evaluated by different methodologies. The highlighted values in yellow show conformity between different methodologies. A further endpoint category global warming potential (GWP 100a) is also checked. This shows consistency across 3 models. The remainder are consistent between 2 out of 4 models but a different 'pair' in each case.

Evaluating Robustness of the model by comparing endpoint values for 5 models.					
Category	**CML**	**ReCiPe**	**IPCC**	**Eco-indicator**	**Impact 2002+**
Human Health	47.50%	26.60%	N/A	38.70%	24.60%
Ecosystems	50.47%	23.65%	N/A	41.50%	39.50%
Resources	7.50%	6.80%	N/A	28.30%	12.02%
Global warming (GWP 100a)	30.73%	N/A	30.60%	N/A	33.40%

5.4.3. Use of an industrial consortium as a bacterial scaffold

Both *E. coli*-Pt:Pd* and the hypothetical *E. coli*-Pt:Pd* (0.25 A mg^{-1}) used purpose-grown *E. coli* as the bacterial scaffold. An alternative route would be to repurpose leftover bacteria grown industrially for a separate primary use. As stated earlier, Orozco *et al.*, have previously shown that *E. coli* grown for Bio-H_2 production could be used to synthesise nanoparticles as fuel cell catalysts.[131] The advantages of using such second-life bacteria for fuel cell applications must be explored and this is done in this study by using a consortium of bacteria henceforth known as "Bangor". This was obtained with thanks from Professor Barrie Johnson, University of Bangor. The consortium (composition as described in Santos *et al.*[269]) was previously used in a sulfidogenic bioreactor to produce H_2S; the produced H_2S was used "offline" to remove transition metals from synthetic mine water leaving the bacteria as waste.[269] On receipt the cells were used to manufacture bimetallic Pt:Pd* nanoparticles (henceforth called Bangor-Pt:Pd*) as detailed in chapter 3. They were then tested electrochemically *ex-situ* to identify their mass activity as 0.5 mA mg^{-1} (appendix A5) which is five-fold lower than that was seen for *E. coli*-Pt:Pd* (2.8 mA mg^{-1}).

A comparative LCA conducted on *E. coli*-Pt:Pd* vs Bangor-Pt:Pd* and the damage assessment is shown in figure 5.7A. The system boundary for the Bangor cells does not include its growth or previous use; furthermore, it does not account for the environmental advantages gained in its re-use. As shown, *E. coli*-Pt:Pd* outperforms Bangor Pt:Pd* in every category with ~ 20% of the impacts of Bangor-Pt:Pd* impacts. To properly evaluate the catalyst, a hypothetical Bangor-Pt:Pd* is assumed with a mass activity of around 0.25 A mg^{-1} and compared to the

hypothetical *E. coli*-Pt:Pd* (0.25 A mg^{-1}) and this is shown in figure 5.7B. As seen here, the impact of using Bangor cells is lower than using *E. coli*-Pt:Pd* with the biggest difference seen in resources where Bangor-Pt:Pd* (0.25) had ~80% of the impacts seen with *E. coli*-Pt:Pd* (0.25). This difference can be attributed to the impact due to growth of cells; however, as seen, this difference is small (between ~85%–95%) and we can deduce that most of the environmental impact here comes from the synthesis of nanoparticles and not from the growth of cells. It is important to note that, once the recycled nature of the Bangor cells is accounted for, it is expected to provide further environmental savings, but this is not studied here.

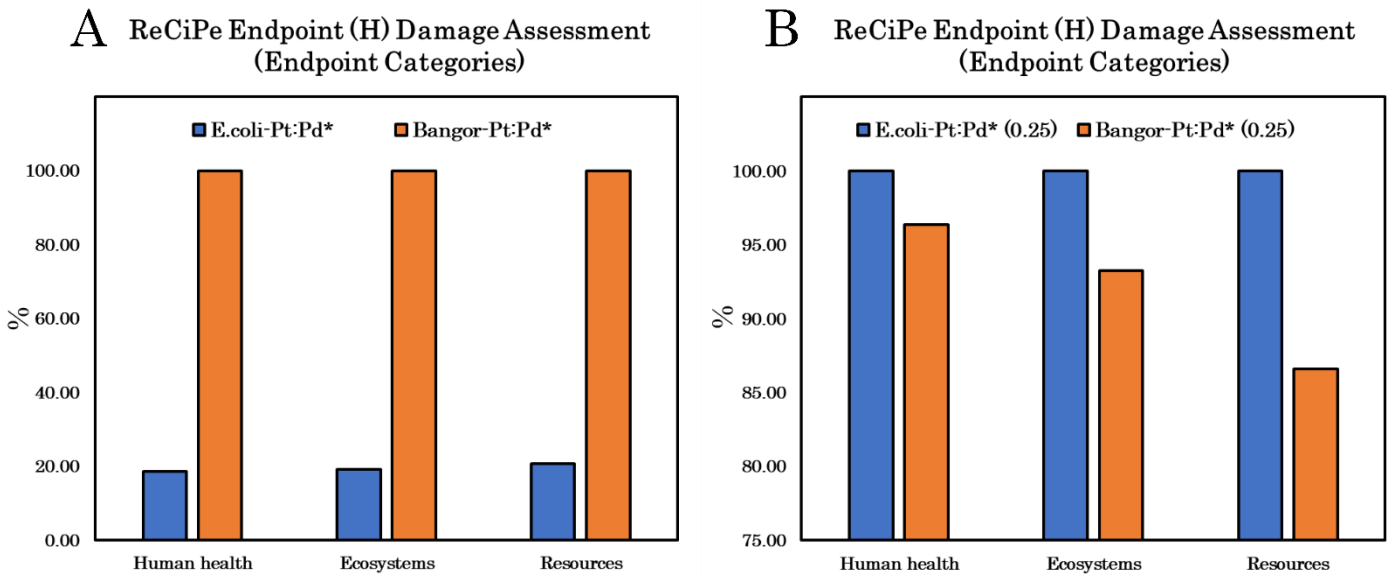

Figure 5.6 (A) The relative impacts of the endpoint categories while conducting an LCIA using the ReCiPe 2016 Endpoint (H) methodology on *E. coli*-Pt:Pd (blue) and Bangor Pt:Pd* (yellow). As seen Bangor-Pt:Pd* has a higher relative impact in all categories. (B) The same study on hypothetical *E. coli*-Pt:Pd (0.25) (blue) and Bangor Pt:Pd (0.25) (yellow). As seen Bangor Pt:Pd has a lower relative impact in all categories.

5.5. Conclusion

A comparative LCA study was conducted on a commercial catalyst 30% Pt/C, *E. coli*-Pt:Pd, a hypothetical *E. coli*-Pt:Pd* (Mass activity of 0.25 A mg^{-1}), Bangor-Pt:Pd and a hypothetical Bangor-Pt:Pd* (Mass activity of 0.25 A mg^{-1}). It was shown that using biosynthesised nanoparticles can provide some environmental advantages only if their electrochemical activities are on par with current commercial catalysts. However, this conclusion assumes that both commercial catalyst and biosynthesised cells will perform similarly in a fuel cell. This assumption is unlikely to stay true and as such, when a better performing biosynthesised catalyst is further proven, a novel LCA study should be conducted. Furthermore, it assumes that the chemical plant considerations for both are the same, however, this is unlikely to be true. When a mature supply chain for bioNPs is established, a comparative LCA will once again be required against FC commercial catalyst. Finally, second life bacteria (Bangor cells) provided small environmental advantages, but this is without considering the advantages of their recycled nature. A more comprehensive study would address this, but, again, this can only be achieved once a proper supply chain has been established.

Chapter 6: Discussion, Conclusion and Future work

This thesis aimed to develop biosynthesised-NPs, as a potential ORR electrocatalyst for use in PEMFCs, in an environmentally friendly synthesis. As stated earlier, it was shown that Pt and Pd are the most efficient bulk metals for ORR activity.[26] A commonly used industrial strain, *E. coli* was previously shown to synthesise Pt-NPs and Pd-NPs with their electrocatalytic activity (ORR[125] and HOR[98]) in PEMFCs confirmed.

Here, *E. coli*-Pt (20%), *E. coli*-Pd (20%) (and *E. coli*-(15%)) and two bimetallics *E. coli*-Pt:Pd* (10%:10%) and *E. coli*-Pd:Pt* (10%:10%) were synthesised and characterised. *E. coli*-Pt:Pd* (10%:10%) was Pt-NPs synthesised on Pd-NP seeds of pre-palladised *E. coli*-Pd (10%) and *E. coli*-Pd:Pt* (10%:10%) was Pd-NPs synthesised on Pt-NP seeds of pre-platinised *E. coli*-Pt (10%) (chapter 3). *E. coli*-Pd showed ubiquitous Pd-NP reduction whereas *E. coli*-Pt showed Pt-NPs primarily associated to the cell surface. This patterning was shown to influence the reduction of the second metal with both bimetallics. *E. coli*-Pt:Pd* showed NPs reduced in a similar pattern to *E. coli*-Pd whereas, *E. coli*Pd:Pt* showed NPs reduced in a similar pattern to *E. coli*-Pt. Unlike *E. coli*-Pt however, *E. coli*-Pd:Pt* also showed few intracellular bimetallic NPs. XPS, XRD and STEM-EDX showed evidence that both bimetallics were alloyed; *E. coli*-Pt:Pd*, however, showed a Pt-rich skin whereas *E. coli*-Pd:Pt* showed a more equal distribution of both metals.

These bimetallics and single metal *E. coli*-NPs were further tested in *ex-situ* electrochemical tests to evaluate their ORR activity. *E. coli*-Pd:Pt* (10%:10%) however showed no electrochemical activity which could be attributed to the NP

dispersion and low Pt loading. Of all *E. coli*-NPs tested, the bimetallic *E. coli*-Pt:Pd* (10%:10%) showed the best activity with a mass activity of 2.8 mA mg^{-1}. This activity could be attributed to the better conductivities and dispersion afforded by patterning of Pt-NPs on Pd seeds of pre-palladised *E. coli*-Pd (10%). The specific activity of the bimetallic was similar to *E. coli*-Pt (20%) at around 0.025 mA cm^{-2} indicating that activity was primarily due to Pt-NPs. While this result is promising, it must be compared to commercially available catalyst. Figure 6.1 compares the ECSA and mass activity of *E. coli*-Pt:Pd* (10%:10%) to commercial Pt/C catalyst TKK. As seen in the figure, the commercial catalyst shows a mass activity[279] of ~ 250 mA mg^{-1}, which is nearly a hundred times better than *E. coli*-Pt:Pd* (10%:10%) (2.80 mA mg^{-1}) (section 4.4.2).

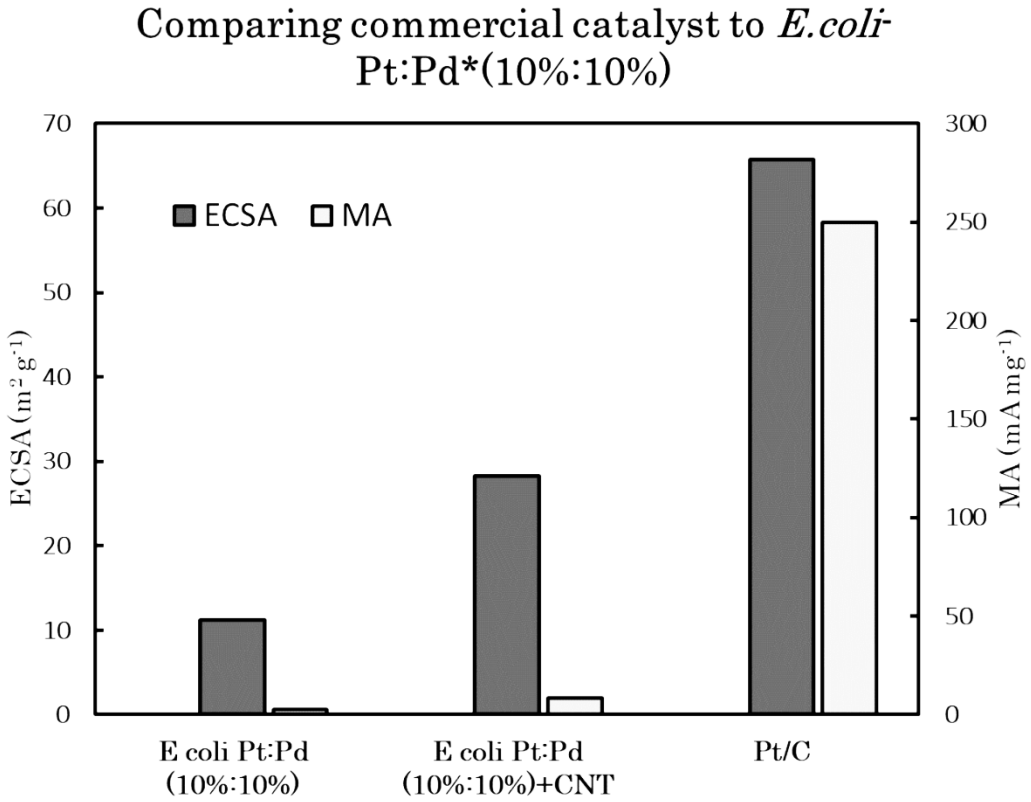

Figure 6.1 Comparing the ECSAs and MAs of commercial catalyst TKK to *E. coli*-Pt:Pd* (10%:10%) and *E. coli*-Pt:Pd* (10%:10%)+CNT.

This discrepancy can be attributed to inherent resistivities of the organic biomass and the inaccessibility of internalised Pt/Pd-NPs within the cell. An attempt to increase conductivities used CNTs with *E. coli*-Pt:Pd* (10%:10%) showed promise. As seen in figure 6.1, this showed an increase in ECSAs from 11.27 to 28.3 $m^2 g^{-1}$ and an increase in mass activity from 2.8 to 8.6 mA mg^{-1}. However, this still falls significantly short of the ECSA and mass activity for commercial Pt/C (section 4.4.5).

If *E. coli*-Pt:Pd* (10%:10%) was used in its current form, a screening LCA conducted showed that commercial Pt/C would only have ~2% of the environmental impacts of using bio-NP catalyst due to vast quantities of bio-NP catalyst required. However, when a hypothetical *E. coli*-NP catalyst that had similar mass activity to commercial catalyst was evaluated, *E. coli*-NP showed significant environmental advantages over commercial catalyst (section 5.4.2) with all characterised endpoints showing ~50% of the environmental impacts relative to Pt/C. These impacts could be further lessened by use of renewable H_2 and recycled PGM. Use of recycled PGM is not without its own environmental impacts, as noted by Archer *et al.*[280] Here the impact of using *Aqua regia* (a mix of concentrated HCl and HNO_3) in the hydrometallurgical recycling of PGM is highlighted, but, recycled PGM is still greatly preferred as compared to freshly extracted PGM.[282] Thus, if a bio-NP catalyst with high mass activities can be engineered, bio-NPs can provide an eco-friendly alternative to current commercial synthesis methods in conjunction with biohydrogen technology (appendix A6).

As noted earlier, *E. coli* can act as a low-cost resource for engineered Pt and Pd-NP synthesis.[97] The *E. coli*-Pt and *E. coli*-Pd NPs synthesised showed appropriate sizes (2.0–4.0 nm) and crystal faces (111) for ORR activity while mixed crystals (alloys) with similar crystal faces were seen for both bimetallics (section 3.4). The mechanism by which *E. coli* synthesises Pt and Pd-NPs is still being elucidated with the hydrogenase enzyme being heavily implicated (section 1.2.3) (but not considered the exclusive mechanism). EM images for *E. coli*-Pd (15%) showed intracellular Pd-NPs that, thus, implied a more complex NP-reduction mechanism than hypothesised (section 3.4.1). EM images for *E. coli*-Pt (20%) showed surface associated clusters which further implies a more complicated mechanism than the hypothesised hydrogenase route. Hydrogenases are periplasmic and *E. coli*-Pt nanoparticles were seen more strongly associated to the surface of the cells. Furthermore, the Pt-NPs were heavily agglomerated and as such, would show low Pt-utilisation for ORR activity (section 3.4.1). Thus, as a primary objective, the mechanisms by which NP reduction occurs must be elucidated. Recent attempts to dissect the genetic and metabolic pathways involved in *E. coli*-NP reduction have been promising.[156] Torgeman demonstrated a high-throughput method of identifying the genes involved in the internalisation and reduction of Pd and Au-NPs in *E. coli*.[156] Further studies will undoubtedly play a vital role in developing a toolkit for engineered *E. coli*-NP synthesis and such studies are underway by D. Linke (University of Oslo) and M. Merroun (University of Grenada) with data withheld pending IP considerations.

Varying chemical parameters can also influence NP synthesis and lead to an engineered solution. Both *E. coli* bimetallics synthesised showed NP patterning

across the cell dependent on the initial metal reduced. *E. coli*-Pt:Pd* showed NP dispersion and structures similar to *E. coli*-Pd and *E. coli*-Pd:Pt* showed a proportion of total cells to be empty like *E. coli*-Pt (section 3.4.1). This dependence has been noted before by Gomez-bolivar *et al.*, when synthesising the bimetallic *E. coli*-Pd/Ru. Like Pt, Ru NP synthesis was primarily confined to the cell surface, but, when synthesised on pre-palladised cells, both Pt (this study) and Ru[192] were internalised. It is possible that both Pt and Ru ions do not require active internalisation by the cells and once internalised, Pd-NPs act as a preferred site for NP reduction. In addition, varying the molar ratios of both metals seems to have an influence on NP activity. As seen in section 4.4.4, the ORR activity of *E. coli* Pt:Pd* increased on doubling the Pt:Pd ratio and thus, this provides another avenue for engineered control. Furthermore, other metals could be utilised for bimetallic core-shell nanoparticle synthesis. Chemically synthesised core-shell nanoparticles often utilise Cu as an intermediary step to Pt/Pd core-shell synthesis to maximise Pt utilisation[143] (section 1.1.3.2), this method could be exploited here.[143] Additionally, pre-treatment of cells before metal reduction can also play a role; Gomez-Bolivar *et al.*, showed that injurious intervention (microwave injury) produced Pd-NPs with an altered dispersion post injury.[285]

Finally, in engineering an *E. coli*-NP electrocatalyst, the inherent resistivities of the organic biomass must be overcome. The challenges posed by this indicate that direct use of bio-NPs is an unrealistic approach, and the catalyst will require a degree of processing. Here, treating *E. coli*-Pt:Pd* with CNTs proved successful with increased specific activities and mass activities (Section 4.4.5). However, neither this nor the attempts with PPy and rGO (Appendix A3.1) were optimised

and must be investigated further. An alternative route might see the synthesis of non-precious metal NPs within the intracellular space, thus, increasing biomass conductivity. This has been investigated in microbial fuel cells, where current drawn from *Shewanella* PV-4 was increased after the cells synthesised iron sulphide NPs on its surface.[283] Carbonisation of the bio-NPs has also proven successful in the past. Yong *et al.*,[98] showed proof of concept for FC activity *in-situ* when they carbonised bio-Pd at high temperatures prior to incorporation into the FC anode. Williams[125] noted that carbonisation of *E. coli*-NPs at high temperatures (700 °C) resulted in significant agglomeration of *E. coli*-NPs thus decreasing NP activity. Xiong *et al.*,[99] and Liu *et al.*,[100] lowered the temperatures of carbonisation of *Shewanella oneidensis* through alkaline activation (to 420 °C) and hydrothermal carbonisation (200 °C), respectively and both developed catalysts showed promise for FC applications. Any of these processing methods used must be evaluated for their environmental impacts.

Taken together, *E. coli*-NP synthesis can provide a green alternative to conventional chemically synthesised ORR catalysts for PEMFCs subject to increasing catalytic activity. To achieve this, however, *E. coli*-NP must be engineered to achieve high mass activities through a combination of genetic and chemical modifications to the synthesis process as well as physiological manipulation of cells (for example by microwave assisted injury[285]). Furthermore, this synthesis will require some level of processing (with low environmental impacts) to improve biomass conductivities. Finally, the synthesis process would ideally use renewable H_2 (through bioH_2 or electrolytically produced H_2 driven by solar PV) as a reducing agent with recycled PGMs. In this manner, a biosynthesis

pathway can provide environmental advantages over conventional methods, but this requires significant further research.

References

1. Mora C, Spirandelli D, Franklin EC, Lynham J, Kantar MB, Miles W, *et al.* Broad threat to humanity from cumulative climate hazards intensified by greenhouse gas emissions. *Nat Clim Chang* (2018); **8**: 1062–71.
2. Hallegatte S. Natural disasters and climate change: An economic perspective. Switzerland: Springer International Publishing. (2014).
3. Nelson GC, Valin H, Sands RD, Havlík P, Ahammad H, Deryng D, *et al.* Climate change effects on agriculture: Economic responses to biophysical shocks. *Proc Natl Acad Sci U S A.* (2014); **111**: 3274–9.
4. Tol RSJ. The economic effects of climate change. *J Econ Perspect.* (2009); **23**:29–51.
5. Abe JO, Popoola API, Ajenifuja E and Popoola OM. Hydrogen energy, economy and storage: Review and recommendation. *Int J Hydrogen Energy.* (2019); **44**: 15072–86.
6. Brandon NP and Kurban Z. Clean energy and the hydrogen economy. *Philos Trans R Soc A Math Phys Eng Sci.* (2017); **375**: 2098.
7. Bak T, Nowotny J, Rekas M and Sorrell CC. Photo-electrochemical hydrogen generation from water using solar energy. Materials-related aspects. *Int J Hydrogen Energy.* (2002); **27**: 991–1022.

8. Genç MS, Çelik M and Karasu I. A review on wind energy and wind-hydrogen production in Turkey: A case study of hydrogen production via electrolysis system supplied by wind energy conversion system in Central Anatolian Turkey. *Renew Sustain Energy Rev.* (2012); **16:** 6631–46.

9. Hallenbeck PC and Liu Y. Recent advances in hydrogen production by photosynthetic bacteria. *Int J Hydrogen Energy*. (2016); **41** :4446–54.

10. Show KY, Yan Y, Ling M, Ye G, Li T and Lee DJ. Hydrogen production from algal biomass – Advances, challenges and prospects. *Bioresour Technol Rep.* (2018); **257**: 290–300.

11. Das V, Padmanaban S, Venkitusamy K, Selvamuthukumaran R, Blaabjerg F and Siano P. Recent advances and challenges of fuel cell based power system architectures and control – A review. *Renew Sustain Energy Rev.* (2017); **73**: 10–8.

12. Suman S. Hybrid nuclear-renewable energy systems: A review. *J Clean Prod.* (2018); **181:** 166–77.

13. Fernández-Galisteo D, Weiss A, Sánchez AL and Williams FA. A one-step reduced mechanism for near-limit hydrogen combustion with general stochiometry. *Combust Flame.* (2019); **208**:1–4.

14. Daud WRW, Rosli RE, Majlan EH, Hamid SAA, Mohamed R and Husaini T. PEM fuel cell system control: A review. *Renew Energy.* (2017); **113**: 620–38.

15. Boudghene Stambouli A and Traversa E. Fuel cells, an alternative to standard sources of energy. *Renew Sustain Energy Rev.* (2002); **6**: 295–304.

16. Choudhury A, Chandra H and Arora A. Application of solid oxide fuel cell technology for power generation - A review. *Renew Sustain Energy Rev.* (2013); **20**: 430–42.

17. Warshay M, Prokopius P, Le M and Voecks G. NASA fuel cell upgrade program for the Space Shuttle Orbiter. *In: Proceedings of the Intersociety Energy Conversion Engineering Conference. IEEE.* (1997); 228–31.

18. Wu B, Matian M and Offer GJ. Hydrogen PEMFC system for automotive applications. *Int J Low-Carbon Technol.* (2012); **7**: 28–37.

19. Zhang J, Zhang H, Wu J and Zhang J Chapter 1 – PEM fuel cell fundamentals. In Zhang J, Zhang H, Wu J and Zhang J (eds). *PEM Fuel Cell Testing and Diagnosis.* Amsterdam, Netherlands: Elsevier. (2013); 1–42.

20. Hao D, Shen J, Hou Y, Zhou Y and Wang H. An improved empirical fuel cell polarization curve modelb on review analysis. *Int J Chem Eng.* (2016); **16.**

21. Carmo M, Paganin VA, Rosolen JM and Gonzalez ER. Alternative supports for the preparation of catalysts for low-temperature fuel cells: The use of carbon nanotubes. *J Power Sources.* (2005);**142**:169–76.

22. Cho EA, Jeon US, Hong SA, Oh IH and Kang SG. Performance of a 1 kW-class PEMFC stack using TiN-coated 316 stainless steel bipolar plates. *J Power Sources.* (2005); **142**:177–83.

23. Talukdar K, Delgado S, Lagarteira T, Gazdzicki P and Friedrich KA. Minimizing mass-transport loss in proton exchange membrane fuel cell by freeze-drying of cathode catalyst layers. *J Power Sources.* (2019); **427**:309–17.

24. Bultel Y, Wiezell K, Jaouen F, Ozil P and Lindbergh G. Investigation of mass transport in gas diffusion layer at the air cathode of a PEMFC. *Electrochim Acta*. (2005); **51**:474–88.

25. Shao M, Chang Q, Dodelet JP and Chenitz R. Recent advances in electrocatalysts for oxygen reduction reaction. *Chem Rev*. (2016); **116:**3594–657.

26. J. K. Nørskov, J. Rossmeisl, A. Logadottir, Lindqvist L, Kitchin JR, Bligaard T, *et al.* Origin of the overpotential for oxygen reduction at a fuel-cell cathode. *J. Phys. Chem. B.* (2004); **108**:17886-17892.

27. Holton OT and Stevenson JW. The role of platinum in proton exchange membrane fuel cells. *Platin Met Rev*. (2013); **57**:259–71.

28. Zhang S, Ding Y, Liu B and Chang C. Supply and demand of some critical metals and present status of their recycling in WEEE. *Waste Manag* (2017); **65**:113–27.

29. U.S.A Department of Energy. *Technical Targets for Polymer Electrolyte Membrane Fuel Cell Components.* Available from:

https://www.energy.gov/eere/fuelcells/doe-technical-targets-polymer-electrolyte-membrane-fuel-cell-components [Accessed: 2020 Feb 27]

30. Gasteiger HA, Kocha SS, Sompalli B and Wagner FT. Activity benchmarks and requirements for Pt, Pt-alloy, and non-Pt oxygen reduction catalysts for PEMFCs. *Appl Catal B.* (2005); **56**: 9–35.

31. Kongkanand A and Mathias MF. The priority and challenge of high-power performance of low-platinum proton-exchange membrane fuel cells. *J Phys Chem Lett.* (2016); **7**:1127–37.

32. Wang X, Li Z, Qu Y, Yuan T, Wang W, Wu Y, *et al.* Review of metal catalysts for oxygen reduction reaction: From nanoscale engineering to atomic design. *Chem.* (2019); **5**:1486–1511.

33. Garsany Y, Baturina OA, Swider-Lyons KE and Kocha SS. Experimental methods for quantifying the activity of platinum electrocatalysts for the oxygen reduction reaction. *Anal Chem.* (2010); **82**:6321–8.

34. Takahashi I and Kocha SS. Examination of the activity and durability of PEMFC catalysts in liquid electrolytes. *J Power Sources.* (2010); **195**:6312–22.

35. Kim M, Park JN, Kim H, Song S and Lee WH. The preparation of Pt/C catalysts using various carbon materials for the cathode of PEMFC. *J Power Sources.* (2006); **163**:93–7.

36. Starz KA, Auer E, Lehmann T and Zuber R. Characteristics of platinum-based electrocatalysts for mobile PEMFC applications. *J Power Sources.* (1999); **84**:167–72.

37. Welch CM and Compton RG. The use of nanoparticles in electroanalysis: A review. *Anal and Bioanal Chem.* (2006); **384**:601–19.

38. Veizaga N, Fernandez J, Bruno M, Scelza O and De Miguel S. Deposition of Pt nanoparticles on different carbonaceous materials by using different preparation methods for PEMFC electrocatalysts. *Int J Hydrogen Energy.* (2012); **37**:17910–20.

39. Liu C, Xue X, Lu T and Xing W. The preparation of high activity DMFC Pt/C electrocatalysts using a pre-precipitation method. *J Power Sources.* (2006); **161**:68–73.

40. Oh HS, Oh JG, Hong YG and Kim H. Investigation of carbon-supported Pt nanocatalyst preparation by the polyol process for fuel cell applications. *Electrochim Acta.* (2007); **52**:7278–85.

41. Fedotov AA, Grigoriev SA, Lyutikova EK, Millet P and Fateev VN. Characterization of carbon-supported platinum nano-particles synthesized using magnetron sputtering for application in PEM electrochemical systems. *Int J Hydrogen Energy*. (2013); **38**:426–30.

42. Shao M, Peles A and Shoemaker K. Electrocatalysis on platinum nanoparticles: Particle size effect on oxygen reduction reaction activity. *Nano Lett*. (2011); **11**:3714–9.

43. Banham D and Ye S. Current status and future development of catalyst materials and catalyst layers for proton exchange membrane fuel cells: An industrial perspective. *ACS Energy Lett* (2017); **2:**629–38.

44. Hafez IH, Berber MR, Fujigaya T and Nakashima N. Enhancement of platinum mass activity on the surface of polymer-wrapped carbon nanotube-based fuel cell electrocatalysts. *Sci Rep.* (2014); **4**:1–8.

45. Wikander K, Ekström H, Palmqvist AEC and Lindbergh G. On the influence of Pt particle size on the PEMFC cathode performance. *Electrochim Acta.* (2007); **52**:6848–55.

46. Xu Z, Zhang H, Zhong H, Lu Q, Wang Y and Su D. Effect of particle size on the activity and durability of the Pt/C electrocatalyst for proton exchange membrane fuel cells. *Appl Catal B Environ.* (2012); **111–112**:264–70.

47. Liu Z, Ma L, Zhang J, Hongsirikarn K and Goodwin JG. Pt alloy electrocatalysts for proton exchange membrane fuel cells: A review. *Catal Rev Sci and Eng.* (2013); **55**:255–88.

48. Walker JS, Rees NV and Mendes PM. Progress towards the ideal core@shell nanoparticle for fuel cell electrocatalysis. *J Exp Nanosci.* (2018); **13**:258–71.

49. Wang Y-J, Long W, Wang L, Yuan R, Ignaszak A, Fang B, *et al.* Unlocking the door to highly active ORR catalysts for PEMFC applications: polyhedron-engineered Pt-based nanocrystals. *Energy Environ Sci.* (2018); **11**:258–75.

50. Papadias DD, Ahluwalia RK, Kariuki N, Myers D, More KL, Cullen DA, *et al.* Durability of Pt-Co alloy polymer electrolyte fuel cell cathode catalysts under accelerated stress tests. *J Electrochem Soc.* (2018); **165**:F3166–77.

51. Cooper J and Beecham J. A study of platinum group metals in three-way autocatalysts. *Platin Met Rev*. (2013); **57**:281–8.

52. Barkholtz H, Chong L, Kaiser Z, Xu T and Liu D-J. Highly active non-PGM catalysts prepared from metal organic frameworks. *Catalysts.* (2015); **5**:955–65.

53. Zhang G, Yang X, Dubois M, Herraiz M, Chenitz R, Lefèvre M, *et al*. Non-PGM electrocatalysts for PEM fuel cells: Effect of fluorination on the activity and stability of a highly active NC-Ar + NH3 catalyst. *Energy Environ Sci.* (2019);**12**:3015–37.

54. Liu J and Xue D. Nano structures via chemistry. *Nanosci Nanotechnol Lett.* (2011); **3**:337–64.

55. Zhuang S, Nunna BB, Mandal D and Lee ES. A review of nitrogen-doped graphene catalysts for proton exchange membrane fuel cells-synthesis, characterization, and improvement. *Nano-Struc Nano-Objects.* (2018); **15:**140–52.

56. Liu Z, Yu C, Rusakova IA, Huang D and Strasser P. Synthesis of Pt3Co alloy nanocatalyst via reverse micelle for oxygen reduction reaction in PEMFCs. *Catalysis.* (2008); **49:**241–50.

57. Jayasayee K, Van Veen JAR, Hensen EJM and De Bruijn FA. Influence of chloride ions on the stability of PtNi alloys for PEMFC cathode. *Electrochim Acta*. (2011); **56**:7235–42.

58. Li W, Zhou W, Li H, Zhou Z, Zhou B, Sun G, *et al*. Nano-stuctured Pt-Fe/C as cathode catalyst in direct methanol fuel cell. *Electrochim Acta.* (2004); **49**:1045–55.

59. Xu Z, Zhang H, Liu S, Zhang B, Zhong H and Su DS. Facile synthesis of supported Pt-Cu nanoparticles with surface enriched Pt as highly active cathode catalyst for proton exchange membrane fuel cells. *Int J Hydrogen Energy*. (2012); **37**:17978–83.

60. Lopes T, Antolini E and Gonzalez ER. Carbon supported Pt-Pd alloy as an ethanol tolerant oxygen reduction electrocatalyst for direct ethanol fuel cells. *Int J Hydrogen Energy*. (2008); **33**:5563–70.

61. Esfandiari A, Kazemeini M and Bastani D. Synthesis, characterization and performance determination of an Ag@Pt/C electrocatalyst for the ORR in a PEM fuel cell. *Int J Hydrogen Energy*. (2016); **41**:20720–30.

62. Colón-Mercado HR and Popov BN. Stability of platinum-based alloy cathode catalysts in PEM fuel cells. *J Power Sources.* (2006); **155**:253–63.

63. Zhao Z, Feng M, Zhou J, Liu Z, Li M, Fan Z, *et al*. Composition tunable ternary Pt-Ni-Co octahedra for optimized oxygen reduction activity. *Chem Commun*. (2016); **52**:11215–8.

64. Ammam M and Easton EB. Oxygen reduction activity of binary PtMn/C, ternary PtMnX/C (X = Fe, Co, Ni, Cu, Mo and, Sn) and quaternary PtMnCuX/C (X = Fe, Co, Ni, and Sn) and PtMnMoX/C (X = Fe, Co, Ni, Cu and Sn) alloy catalysts. *J Power Sources.* (2013); **236**:311–20.

65. Chen X, Si C, Gao Y, Frenzel J, Sun J, Eggeler G, *et al*. Multi-component nanoporous platinum-ruthenium-copper-osmium-iridium alloy with enhanced electrocatalytic activity towards methanol oxidation and oxygen reduction. *J Power Sources*. (2015); **273**:324–32.

66. Escudero-Escribano M, Malacrida P, Hansen MH, Vej-Hansen UG, Velázquez-Palenzuela A, Tripkovic V, *et al.* Tuning the activity of Pt alloy electrocatalysts by means of the lanthanide contraction. *Science*. (2016); **352**:73–6.

67. Zhang L, Lee K and Zhang J. The effect of heat treatment on nanoparticle size and ORR activity for carbon-supported Pd-Co alloy electrocatalysts. *Electrochim Acta.* (2007); **52**:3088–94.

68. Johansson TP, Ulrikkeholm ET, Hernandez-Fernandez P, Malacrida P, Hansen HA, Bandarenka AS, *et al.* Pt skin versus Pt skeleton structures of Pt3Sc as electrocatalysts for oxygen reduction. *Top Catal.* (2014); **57**:245–54.

69. Stephens IEL, Bondarenko AS, Grønbjerg U, Rossmeisl J and Chorkendorff I. Understanding the electrocatalysis of oxygen reduction on platinum and its alloys. *Energy and Environ Sci.* (2012); **5:**6744–62.

70. Xu Y, Ruban AV and Mavrikakis M. Adsorption and dissociation of O2 on Pt-Co and Pt-Fe alloys. *J Am Chem Soc.* (2004); **126**:4717–25.

71. Cui C, Gan L, Heggen M, Rudi S and Strasser P. Compositional segregation in shaped Pt alloy nanoparticles and their structural behaviour during electrocatalysis. *Nat Mater.* (2013); **12**:765–71.

72. Zignani SC, Antolini E and Gonzalez ER. Evaluation of the stability and durability of Pt and Pt-Co/C catalysts for polymer electrolyte membrane fuel cells. *J Power Sources.* (2008); **182**:83–90.

73. Ishiguro N, Kityakarn S, Sekizawa O, Uruga T, Matsui H, Taguchi M, *et al.* Kinetics and mechanism of redox processes of Pt/C and Pt3Co/C

cathode electrocatalysts in a polymer electrolyte fuel cell during an accelerated durability test. *J Phys Chem C*. (2016); **120**:19642–51.

74. Yoshida T and Kojima K. Toyota MIRAI fuel cell vehicle and progress toward a future hydrogen society. *Electrochem Soc Interface*. (2015); **24**:45–9.

75. Ma Y, Zhang H, Zhong H, Xu T, Jin H and Geng X. High active PtAu/C catalyst with core-shell structure for oxygen reduction reaction. *Catal Commun.* (2010); **11**:434–7.

76. Wei ZD, Feng YC, Li L, Liao MJ, Fu Y, Sun CX, *et al.* Electrochemically synthesized Cu/Pt core-shell catalysts on a porous carbon electrode for polymer electrolyte membrane fuel cells. *J Power Sources.* (2008); **180**:84–91.

77. Zhang G, Shao ZG, Lu W, Xie F, Xiao H, Qin X, *et al.* Core-shell Pt modified Pd/C as an active and durable electrocatalyst for the oxygen reduction reaction in PEMFCs. *Appl Catal B Environ.* (2013); **132–133**:183–94.

78. Zhang L, Kim J, Zhang J, Nan F, Gauquelin N, Botton GA, *et al.* Ti4O7 supported Ru@Pt core-shell catalyst for CO-tolerance in PEM fuel cell hydrogen oxidation reaction. *Appl Energy.* (2013); **103**:507–13.

79. Adzic R, Zhang J, Mo Y and Vukmirovic M. Metal-noble metal core-shell electrocatalysts. *United States Patent* (2010) US9005331B2

80. Zhu H, Li X and Wang F. Synthesis and characterization of Cu@Pt/C core-shell structured catalysts for proton exchange membrane fuel cell. *Int J Hydrogen Energy.* (2011); **36**:9151–4.

81. Mani P, Srivastava R and Strasser P. Dealloyed Pt-Cu core-shell nanoparticle electrocatalysts for use in PEM fuel cell cathodes. *J Phys Chem C.* (2008); **112**:2770–8.

82. Rezaei M, Tabaian SH and Haghshenas DF. Electrochemical nucleation and growth of Pd/PdCo core-shell nanoparticles with enhanced activity and durability as fuel cell catalyst. *J Mater Chem A.* (2014); **2**:4588–97.

83. Sasaki K, Naohara H, Cai Y, Choi YM, Liu P, Vukmirovic MB, *et al.* Core-protected platinum monolayer shell high-stability electrocatalysts for fuel-cell cathodes. *Angew Chemie.* (2010); **49**:8602–7.

84. Zhai J, Huang M and Dong S. Electrochemical designing of Au/Pt core shell nanoparticles as nanostructured catalyst with tunable activity for oxygen reduction. *Electroanalysis.* (2007); **19**:506–9.

85. Park J, Wang H, Vara M, Xia Y. Platinum cubic nanoframes with enhanced catalytic activity and durability toward oxygen reduction. *Chem Sus Chem.* (2016); **9**:2855–61.

86. Li M, Zhao Z, Cheng T, Fortunelli A, Chen CY, Yu R, *et al.* Ultrafine jagged platinum nanowires enable ultrahigh mass activity for the oxygen reduction reaction. *Science.* (2016); **354**:1414–9.

87. Yang Z, Li Z, Lu X, He F, Zhu X, Ma Y, *et al.* Controllable biosynthesis and properties of gold nanoplates using yeast extract. *Nano-Micro Lett.* (2017); **9**:1–13.

88. Schröfel A, Kratošová G, Šafařík I, Šafaříková M, Raška I and Shor LM. Applications of biosynthesized metallic nanoparticles – A review. *Acta Biomater.* (2014); **10**:4023–42.

89. Ingale AG and Chaudhari AN. Biogenic synthesis of nanoparticles and potential applications: An eco-friendly approach. *J Nanomed Nanotechol* (2013); **4**:165

90. Iravani S. Green synthesis of metal nanoparticles using plants. *Green Chem.* (2011); **13:**2638–50.

91. Sastry M, Ahmad A, Islam Khan M, Kumar R. Biosynthesis of metal nanoparticles using fungi and actinomycete. *Curr Sci Int.* (2003); **85**:162-170

92. Agnihotri M, Joshi S, Kumar AR, Zinjarde S and Kulkarni S. Biosynthesis of gold nanoparticles by the tropical marine yeast *Yarrowia lipolytica* NCIM 3589. *Mater Lett.* (2009); **63**:1231–4.

93. Hulkoti NI and Taranath TC. Biosynthesis of nanoparticles using microbes–A review. *Colloids Surf B Biointerfaces*. (2014);**121**:474–83.

94. Sardar M and Mazumder JA. Biomolecules assisted synthesis of metal nanoparticles. In: Dasgupta N., Ranjan S., Lichtfouse E. (eds) *Environmental Chemistry for a Sustainable World*. Cham, Swizterland: Springer Ltd. (2019); **21:** 1–23.

95. Órdenes-Aenishanslins N, Anziani-Ostuni G, Quezada CP, Espinoza-González R, Bravo D and Pérez-Donoso JM. Biological synthesis of CdS/CdSe core/shell nanoparticles and its application in quantum dot sensitized solar cells. *Front Microbiol*. (2019); **10**:1587.

96. Castro L, Blázquez ML, Muñoz JA, González F, García-Balboa C and Ballester A. Biosynthesis of gold nanowires using sugar beet pulp. *Process Biochem.* (2011); **46**:1076–82.

97. Macaskie LE, Mikheenko IP, Omajai JB, Stephen AJ and Wood J. Metallic bionanocatalysts: potential applications as green catalysts and energy materials. *Microb Biotechnol*. (2017); **10:**1171-80.

98. Yong P, Paterson-Beedle M, Mikheenko IP and Macaskie LE. From bio-mineralisation to fuel cells: Biomanufacture of Pt and Pd nanocrystals for fuel cell electrode catalyst. *Biotechnol Lett* (2007); **29**:539–44.

99. Xiong L, Chen J-J, Huang Y-X, Li W-W, Xie J-F and Yu H-Q. An oxygen reduction catalyst derived from a robust Pd-reducing bacterium. *Nano Energy*. (2015); **12**:33–42.

100. Liu J, Zheng Y, Hong Z, Cai K, Zhao F and Han H. Microbial synthesis of highly dispersed PdAu alloy for enhanced electrocatalysis. *Sci Adv*. (2016); **2**.

101. Menon S, Shanmugam R and Kumar V. A review on biogenic synthesis of gold nanoparticles, characterization, and its applications. *Resour Technol.* (2017); **3**:516–27.

102. Prasad TNVKV, Kambala V and Naidu R. A critical review on biogenic silver nanoparticles and their antimicrobial activity. *Curr Nanosci.* (2011); **7**:531–44.

103. Singh S, Vidyarthi AS and Dev A. Microbial synthesis of nanoparticles. In: Singh OV (eds) *Bio-Nanoparticles*. Hoboken, NJ: John Wiley & Sons, Inc. (2015); **1**:155–86.

104. Murray AJ, Zhu J, Wood J and Macaskie LE. A novel biorefinery: Biorecovery of precious metals from spent automotive catalyst leachates

into new catalysts effective in metal reduction and in the hydrogenation of 2-pentyne. *Miner Eng*. (2017); **113**:102–8.

105. Gahlawat G and Choudhury AR. A review on the biosynthesis of metal and metal salt nanoparticles by microbes. *RSC Adv.* (2019); **9:**12944–67.

106. Faramarzi MA and Sadighi A. Insights into biogenic and chemical production of inorganic nanomaterials and nanostructures. *Adv Colloid Interface Sci.* (2013); **189-190**:1–20.

107. Merino N, Aronson HS, Bojanova DP, Feyhl-Buska J, Wong ML, Zhang S, *et al*. Living at the extremes: Extremophiles and the limits of life in a planetary context. *Front Microbiol.* (2019);**10**:780.

108. Ahmed M and Malik A. Bioaccumulation of heavy metals by zinc resistant bacteria isolated from agricultural soils irrigated with wastewater. *Bacteriol J*. (2012); **2:**12–21.

109. Nies DH. Heavy metal-resistant bacteria as extremophiles: Molecular physiology and biotechnological use of *Ralstonia sp.* CH34*. Extremophiles.* (2000); **4:**77–82.

110. Silver S. Bacterial heavy metal detoxification and resistance systems. In: Mongkolsuk S, Lovett PS and Trempy JE (eds) *Biotechnology and Environmental Science*. New York, US: Plenum Press. (2007); **1:**109–29.

111. Choudhary S and Sar P. Characterization of a metal resistant *Pseudomonas sp*. isolated from uranium mine for its potential in heavy metal (Ni2+, Co2+, Cu2+, and Cd2+) sequestration. *Bioresour Technol.* (2009); **100**:2482–92.

112. Bridge TAM, White C and Gadd GM. Extracellular metal-binding activity of the sulphate-reducing bacterium Desulfococcus multivorans. *Microbiology*. (1999); **145**:2987–95.

113. Arakaki A, Nakazawa H, Nemoto M, Mori T and Matsunaga T. Formation of magnetite by bacteria and its application. *J R Soc Interface*. (2008); **5:**977–99.

114. Ali J, Ali N, Wang L, Waseem H and Pan G. Revisiting the mechanistic pathways for bacterial mediated synthesis of noble metal nanoparticles. *J Microbiol Methods*. (2019); **159**:18–25.

115. Beveridge TJ and Murray RGE. Sites of metal deposition in the cell wall of *Bacillus subtilis*. *J Bacteriol*. (1980); **141**:876–87.

116. Shivaji S, Madhu S and Singh S. Extracellular synthesis of antibacterial silver nanoparticles using psychrophilic bacteria. *Process Biochem*. (2011); **46**:1800–7.

117. Deplanche K, Caldelari I, Mikheenko IP, Sargent F and Macaskie LE. Involvement of hydrogenases in the formation of highly catalytic Pd (0) nanoparticles by bioreduction of Pd (II) using *Escherichia coli* mutant strains. *Microbiology*. (2010); **156**:2630–40.

118. He S, Guo Z, Zhang Y, Zhang S, Wang J and Gu N. Biosynthesis of gold nanoparticles using the bacteria Rhodopseudomonas capsulata. *Mater Lett*. (2007); **61**:3984–7.

119. Gurunathan S, Kalishwaralal K, Vaidyanathan R, Venkataraman D, Pandian SRK, Muniyandi J, *et al*. Biosynthesis, purification and

characterization of silver nanoparticles using *Escherichia coli*. *Colloids Surf B Biointerfaces*. (2009); **74**:328–35.

120. Shantkriti S and Rani P. Biological synthesis of copper nanoparticles using *Pseudomonas fluorescens* Vol. 3, *Int J Curr Microbiol App Sci.* (2014); **3:**374-383

121. Bharde AA, Parikh RY, Baidakova M, Jouen S, Hannoyer B, Enoki T, *et al*. Bacteria-mediated precursor-dependent biosynthesis of superparamagnetic iron oxide and iron sulfide nanoparticles. *Langmuir.* (2008); **24**:5787–94.

122. Simon-Pascual A, Sierra-Alvarez R andField JA. Platinum(II) reduction to platinum nanoparticles in anaerobic sludge. *J Chem Technol Biotechnol*. (2019); **94**:468–74.

123. Zhou P, Wang H, Yang J, Tang J, Sun D and Tang W. Bacteria cellulose nanofibers supported palladium(0) nanocomposite and its catalysis evaluation in heck reaction. *Ind Eng Chem Res*. (2012); **51**:5743–8.

124. Malhotra A, Dolma K, Kaur N, Rathore YS, Ashish, Mayilraj S, *et al*. Biosynthesis of gold and silver nanoparticles using a novel marine strain of *Stenotrophomonas*. *Bioresour Technol*. (2013); **142**:727–31.

125. Williams A. BioGenic Precious metal-based magnetic nanocatalyst for enhanced oxygen reduction. [PhD Thesis] Birmingham, UK: University of Birmingham. (2015).

126. Omajali JB, Mikheenko IP, Merroun ML, Wood J and Macaskie LE. Characterization of intracellular palladium nanoparticles synthesized

by *Desulfovibrio desulfuricans* and *Bacillus benzeovorans*. *J Nanoparticle Res*. (2015); **17**:264.

127. Yong P, Mikheenko IP, Deplanche K, Redwood MD, Macaskie LE. Biorefining of precious metals from wastes: An answer to manufacturing of cheap nanocatalysts for fuel cells and power generation via an integrated biorefinery? *Biotechnol Lett* (2010); **32**:1821–8.

128. Bennett JA, Mikheenko IP, Deplanche K, Shannon IJ, Wood J and Macaskie LE. Nanoparticles of palladium supported on bacterial biomass: New re-usable heterogeneous catalyst with comparable activity to homogeneous colloidal Pd in the Heck reaction. *Appl Catal B Environ.* (2013); **140–141**:700–7.

129. Dao D Van, Adilbish G, Le TD, Lee IH and Yu YT. Triple phase boundary and power density enhancement in PEMFCs of a Pt/C electrode with double catalyst layers. *RSC Adv*. (2019); **9**:15635–41.

130. Zhu J, Wood J, Deplanche K, Mikheenko I and Macaskie LE. Selective hydrogenation using palladium bioinorganic catalyst. *Appl Catal B Environ*. (2016); **199**:108–22.

131. Orozco RL, Redwood MD, Yong P, Caldelari I, Sargent F and Macaskie LE. Towards an integrated system for bio-energy: hydrogen production by *Escherichia coli* and use of palladium-coated waste cells for electricity generation in a fuel cell. *Biotechnol Lett*. (2010); **32**:1837–45.

132. Baeshen MN, Al-Hejin AM, Bora RS, Ahmed MMM, Ramadan HAI, Saini KS, *et al*. Production of biopharmaceuticals in *E. coli*: current

scenario and future perspectives. *J Microbiol Biotechnol.* (2015); **25**:953–62.

133. Creamer NJ, Baxter-Plant VS, Henderson J, Potter M and Macaskie LE. Palladium and gold removal and recovery from precious metal solutions and electronic scrap leachates by *Desulfovibrio desulfuricans*. *Biotechnol Lett*. (2006); **28**:1475–84.

134. de Vargas I, Macaskie LE and Guibal E. Biosorption of palladium and platinum by sulfate-reducing bacteria. *J Chem Technol Biotechnol*. (2004); **79**:49–56.

135. Mikheenko IP, Rousset M, Dementin S and Macaskie LE. Bioaccumulation of palladium by *Desulfovibrio fructosivorans* wild-type and hydrogenase-deficient strains. *Appl Environ Microbiol*. (2008); **74**:6144–6.

136. Yong P, Rowson NA, Farr JPG, Harris IR, Macaskie LE. Bioreduction and biocrystallization of palladium by *Desulfovibrio desulfuricans* NCIMB 8307. *Biotechnol Bioeng*. (2002); **80**:369–79.

137. Riddin TL, Govender Y, Gericke M and Whiteley CG. Two different hydrogenase enzymes from sulphate-reducing bacteria are responsible for the bioreductive mechanism of platinum into nanoparticles. *Enzyme Microb Technol.* (2009); **45**:267–73.

138. Rashamuse KJ and Whiteley CG. Bioreduction of Pt (IV) from aqueous solution using sulphate-reducing bacteria. *Appl Microbiol Biotechnol*. (2007); **75**:1429–35.

139. Courtney J, Deplanche K, Rees N V. and Macaskie LE. Biomanufacture of nano-Pd (0) by *Escherichia coli* and electrochemical activity of bio-Pd (0) made at the expense of H_2 and formate as electron donors. *Biotechnol Lett*. (2016); **38**:1903–10.

140. Stanca SE, Hänschke F, Ihring A, Zieger G, Dellith J, Kessler E, *et al*. Chemical and electrochemical synthesis of platinum black. *Sci Rep.* (2017); **7**:1–8.

141. Choi S Il, Xie S, Shao M, Odell JH, Lu N, Peng HC, *et al*. Synthesis and characterization of 9 nm Pt-Ni octahedra with a record high activity of 3.3 A/mgPt for the oxygen reduction reaction. *Nano Lett.* (2013); **13**:3420–5.

142. Wang C, Chi M, Li D, Strmcnik D, Van Der Vliet D, Wang G, *et al*. Design and synthesis of bimetallic electrocatalyst with multilayered Pt-skin surfaces. *J Am Chem Soc*. (2011); **133**:14396–403.

143. Taufany F, Pan CJ, Rick J, Chou HL, Tsai MC, Hwang BJ, *et al*. Kinetically controlled autocatalytic chemical process for bulk production of bimetallic core-shell structured nanoparticles. *ACS Nano.* (2011); **5**:9370–81.

144. Chen C, Kang Y, Huo Z, Zhu Z, Huang W, Xin HL, *et al*. Highly crystalline multimetallic nanoframes with three-dimensional electrocatalytic surfaces. *Science*. (2014); **343**:1339–43.

145. Brocklehurst KR and Morby AP. Metal-ion tolerance in *Escherichia coli*: analysis of transcriptional profiles by gene-array technology. *Microbiology.* (2000); **146:**2277-82.

146. Tucker DL, Tucker N and Conway T. Gene expression profiling of the pH response in *Escherichia coli*. *J Bacteriol*. (2002); **184**:6551–8.

147. Deplanche K, Bennett JA, Mikheenko IP, Omajali J, Wells AS, Meadows RE, *et al*. Catalytic activity of biomass-supported Pd nanoparticles: Influence of the biological component in catalytic efficacy and potential application in "green" synthesis of fine chemicals and pharmaceuticals. *Appl Catal B Environ*. (2014); **147**:651–65.

148. Lloyd JR, Yong P and Macaskie LE. Enzymatic recovery of elemental palladium by using sulfate-reducing bacteria. *Appl Environ Microbiol*. (1998); **64**:4607–9.

149. Lubitz W, Ogata H, Rüdiger O, Reijerse E. Hydrogenases. *Chem Rev.* (2014); **114**:081–148.

150. Zeer-Wanklyn CJ and Zamble DB. Microbial nickel: cellular uptake and delivery to enzyme centers. *Curr Opin Chem Biol.* (2017); **37:**80–8.

151. Lacasse MJ, Douglas CD and Zamble DB. Mechanism of selective nickel transfer from HypB to HypA, *Escherichia coli* [NiFe]-Hydrogenase Accessory Proteins. *Biochemistry*. (2016); **55**:6821–31.

152. Herbst RW, Perovic I, Martin-Diaconescu V, O'brien K, Chivers PT, Pochapsky SS, *et al*. Communication between the zinc and nickel sites in dimeric HypA: Metal recognition and pH sensing. *J Am Chem Soc.* (2010); **132**:10338–51.

153. Konishi Y, Ohno K, Saitoh N, Nomura T, Nagamine S, Hishida H, *et al*. Bioreductive deposition of platinum nanoparticles on the bacterium *Shewanella algae*. *J Biotechnol.* (2007); **128**:648–53.

154. Foulkes JM, Deplanche K, Sargent F, Macaskie LE and Lloyd JR. A novel aerobic mechanism for reductive palladium biomineralization and recovery by *Escherichia coli*. *Geomicrobiol J*. (2016); **33**:230–6.

155. Konishi Y, Ohno K, Saitoh N, Nomura T, Nagamine S, Hishida H, *et al*. Bioreductive deposition of platinum nanoparticles on the bacterium Shewanella algae. *J Biotechnol*. (2007); **128**:648–53.

156. Torgeman E. Biosynthesis of gold and palladium nanoparticles via Bacteria. [Masters Thesis] Oslo, Norway: University of Oslo. (2017).

157. Maes S, Props R, Fitts JP, De Smet R, Vilchez-Vargas R, Vital M, *et al*. Platinum recovery from synthetic extreme environments by halophilic bacteria. *Environ Sci Technol.* (2016); **50**:2619–26.

158. Ito R, Kuroda K, Hashimoto H and Ueda M. Recovery of platinum(0) through the reduction of platinum ions by hydrogenase-displaying yeast. *AMB Express*. (2016); **6**:88.

159. Gaidhani S V., Yeshvekar RK, Shedbalkar UU, Bellare JH and Chopade BA. Bio-reduction of hexachloroplatinic acid to platinum nanoparticles employing *Acinetobacter calcoaceticus*. *Process Biochem*. (2014); **49**:2313–9.

160. Elias AM and Saravanakumar MP. A review on the classification, characterisation, synthesis of nanoparticles and their application. *IOP Conf Ser Mater Sci Eng.* (2017); **263**.

161. Brown A and Hondow N. Electron microscopy of nanoparticles in cells. *Front Nanosci*. (2013); **5**:95–120.

162. Antolini E and Cardellini F. Formation of carbon supported PtRu alloys: An XRD analysis. *J Alloys Compd.* (2001); **315**:118–22.

163. Gorzalski AS, Donley C and Coronell O. Elemental composition of membrane foulant layers using EDS, XPS, and RBS. *J Memb Sci.* (2017); **522**:31–44.

164. Olesik JW. Elemental analysis using ICP-OES and ICP/MS. *Anal Chem.* (1991); 63.

165. Dai WL, Qiao MH and Deng JF. XPS studies on a novel amorphous Ni-Co-W-B alloy powder. *Appl Surf Sci*. (1997); **120**:119–24.

166. Inkson BJ. Scanning Electron Microscopy (SEM) and Transmission Electron Microscopy (TEM) for materials characterization. In: Huebschen G, Altpeter I, Tschuncky R and Herrmann HG (eds) *Materials Characterization Using Nondestructive Evaluation (NDE) Methods.* Oxford, UK: Woodhead Publishing. (2016); **1:**17–43.

167. Hauch KD, Ratner BD. Microscopy for biomaterials science. In: Ratner BD, Schoen FJ, Hoffman AS and Lemons JE (eds). *Biomaterials Science: An Introduction to Materials.* Oxford, UK: Elsevier Inc. (2013); **3:**677–92.

168. Heintzmann R and Ficz G. Breaking the resolution limit in light microscopy. *Brief Funct Genomics*. (2006); **5:**289-301.

169. Campbell I D. Microscopy. In: *Biophysical techniques.* Oxford, UK: Oxford University Press. (2012); **1**:258-278.

170. Amelinckx S, van Dyck D, van Landuyt J, van Tendeloo G. Electron microscopy: principles and fundamentals. (2007); **1:** 1-109.

171. Nixon WC. The general principles of scanning electron microscopy. *Philos Trans R Soc London B, Biol Sci*. (1971); **261**:45–50.

172. Akhtar K, Khan SA, Khan SB and Asiri AM. Scanning electron microscopy: Principle and applications in nanomaterials characterization. In: Sharma SK (eds) *Handbook of Materials Characterization.* Spain: Springer International Publishing. (2018); **1**:113–45.

173. Toporov A, Langford RM and Petford-Long AK. Lorentz transmission electron microscopy of focused ion beam patterned magnetic antidot arrays. *Appl Phys Lett*. (2000); **77**:3063–5.

174. Moore KT, Howe JM, Veblen DR, Murray TM and Stach EA. Analysis of electron intensity as a function of aperture size in energy- filtered transmission electron microscope imaging. *Ultramicroscopy*. (1999); **80**:221–36.

175. Vernon-Parry KD. Scanning electron microscopy: An introduction. *III-Vs Rev.* (2000); **13**:40–4.

176. Egerton RF. The Scanning Electron Microscope. In: *Physical Principles of Electron Microscopy.* Boston, MA: Springer US. (2005); **1**:125–53.

177. Goldstein JI. Electron beam-specimen interaction. In: Goldstein JI and Yakowitz H (eds). *Practical Scanning Electron Micrscopy.* New York, NY: Plenum Press. (1975); **1**:49-94

178. Lloyd GE. Atomic number and crystallographic contrast images with the SEM: a review of backscattered electron techniques. *Mineral Mag*. (1987); **51**:3-19.

179. Ratner BD. Surface Properties and surface characterization of biomaterials. . In: Ratner BD, Schoen FJ, Hoffman AS and Lemons JE (eds). *Biomaterials Science: An Introduction to Materials.* Oxford, UK: Elsevier Inc. (2013); **3:**34–55.

180. Tizro P, Choi C and Khanlou N. Sample preparation for transmission electron microscopy. In: Yong WH (eds) *Biobanking*. New York, NY: Humana Press Inc. (2019); **1:**417–24.

181. Bonnamy S and Oberlin A. Transmission Electron Microscopy. In: Inagaki M and Kang F (eds). *Materials Science and Engineering of Carbon.* Oxford, UK: Butterworth-Heinemann. (2016); **1:**45–70.

182. Smallman RE and Ngan AHW. Characterization and analysis. In: Smallman RE and Ngan AHW (eds) *Modern Physical Metallurgy*. Oxford, UK: Elsevier; (2014); **8:**159–250.

183. Kirkland EJ. Improved high resolution image processing of bright field electron micrographs: I. Theory. *Ultramicroscopy.* (1984); **15**:151–72.

184. Tang CY and Yang Z. Transmission Electron Microscopy (TEM). In: Hilal N, Ismail FA, Matsuura T and Oatley-Radcliffe D. (eds) *Membrane Characterization.* Oxford, UK: Elsevier Inc. (2017); **8**:145–59.

185. Mielańczyk Ł, Matysiak N, Klymenko O and Wojnicz R. Transmission Electron Microscopy of biological samples. In: Maaz K (eds) *The Transmission Electron Microscope - Theory and Applications*. Croatia: InTech Open. (2015); **1:**193-240

186. Mourdikoudis S, Pallares RM and Thanh NTK. Characterization techniques for nanoparticles: Comparison and complementarity upon studying nanoparticle properties. *Nanoscale*. (2018); **10**:12871–934.

187. Reimer L. Electron diffraction methods in TEM, STEM and SEM. *Scanning*. (1979); **2**:3–19.

188. Warner JH, Schäffel F, Bachmatiuk A and Rümmeli MH. Characterisation techniques. In: *Graphene*. Waltham, MA: Elsevier Ltd. (2013); **1**:229–332.

189. Maclaren I and Ramasse QM. Aberration-corrected scanning transmission electron microscopy for atomic-resolution studies of functional oxides. *Int. Mat. Rev.* (2014); **58**: 115-31.

190. Singh AK. Experimental methodologies for the characterization of nanoparticles. In: *Engineered Nanoparticles*. Oxford, UK:Elsevier; (2016); **1**:125–70.

191. Reich S, Agarwal S and Greiner A. Electrospun Bacteria-gold nanoparticle/polymer composite mesofiber nonwovens for catalytic application. *Macromol Chem Phys*. (2019); **220**:1900007

192. Gomez-Bolivar J, Mikheenko IP, Orozco RL, Sharma S, Banerjee D, Walker M, *et al*. Synthesis of Pd/Ru bimetallic nanoparticles by *Escherichia coli* and potential as a catalyst for upgrading 5-hydroxymethyl furfural into liquid fuel precursors. *Front Microbiol*. (2019); **10**:1276.

193. Devi L and Joshi S. Ultrastructures of silver nanoparticles biosynthesized using endophytic fungi. *J Microsc Ultrastruct*. (2015); **3**:29.

194. Whitfield P and Mitchell L. X-ray diffraction analysis of nanoparticles: Recent developments, potential problems and some solutions. *Int J Nanosci.* (2004); **3**:757–63.

195. Chatterjee AK. X-ray diffraction. In: Ramachandran VS and Beaudoin JJ (eds). *Handbook of Analytical Techniques in Concrete Science and Technology.* New York, NY: Elsevier Ltd. (2001); **1**:275–332.

196. Misture ST and Snyder RL. X-ray Diffraction. In: Jürgen Buschow KH, Cahn RW, Flemings MC, Ilschner B, Kramer EJ, Mahajan S and Veyssière P (eds). *Encyclopedia of Materials: Science and Technology.* Oxford, UK: Elsevier. (2001); **2**:9799–808.

197. Clegg W. X-ray Diffraction. In: McCleverty JA and Meyer TJ (eds). *Comprehensive Coordination Chemistry II.* Oxford, UK: Elsevier Ltd. (2003); **2**: 57–64.

198. Ingham B. X-ray scattering characterisation of nanoparticles. *Crystallogr Rev*. (2015); **21**:229–303.

199. Butera RA and Waldeck DH. X-ray diffraction investigation of alloys. *J Chem Educ*. (1997); **74**:115–9.

200. Dorofeev GA, Streletskii AN, Povstugar IV, Protasov AV and Elsukov EP. Determination of nanoparticle sizes by X-ray diffraction. *Colloid J.* (2012); **74**:675–85.

201. Lee Y-W, Ko A-R, Han S-B, Kim H-S and Park K-W. Synthesis of octahedral Pt–Pd alloy nanoparticles for improved catalytic activity and stability in methanol electrooxidation. *Phys Chem Chem Phys*. (2011); **13**:5569.

202. Konno H. X-ray Photoelectron Spectroscopy. In: Inagaki M and Kang F (eds). *Materials Science and Engineering of Carbon.* Oxford, UK: Butterworth-Heinemann. (2016); **1**:153–71.

203. Proctor A and Sherwood PMA. Data analysis techniques in X-ray Photoelectron Spectroscopy. *Anal Chem.* (1982); **54**:13–9.

204. Venezia AM. X-ray photoelectron spectroscopy (XPS) for catalysts characterization. *Catalysis Today*. (2003); **77**:359–70.

205. Aricò AS, Shukla AK, Kim H, Park S, Min M and Antonucci V. XPS study on oxidation states of Pt and its alloys with Co and Cr and its relevance to electroreduction of oxygen. *Appl Surf Sci*. (2001); **172**:33–40.

206. de Hoffmann E. Mass Spectrometry. In: Kirk-Othmer (eds) *Kirk-Othmer Encyclopedia of Chemical Technology*. Hoboken, NJ, USA: John Wiley & Sons, Inc.; (2005); **5.**

207. Bard AJ and Faulkner LR. Electrochemical methods: Fundamentals and applications. New York, NY: Wiley. (2002); **2**.

208. Kissinger PT and Heineman WR. Cyclic voltammetry. *Journal of Chem Education.* (1983); **60**:702–6.

209. Mendivil MI, Shaji S, Castillo GA and Krishnan B. Transmission electron microscopic studies on noble metal nanoparticles synthesized

by pulsed laser ablation in liquid. In: Mendez-Vilas (eds). *Microscopy: Advances in Scientific Research and Education*. (2014); **1**:911-20.

210. Zhang D, Jin C, Tian H, Xiong Y, Zhang H, Qiao P, *et al*. An *In-situ* TEM study of the surface oxidation of palladium nanocrystals assisted by electron irradiation. *Nanoscale*. (2017); **9**:6327–33.

211. Nguyen V-L, Ohtaki M, Ngo VN, Cao M-T and Nogami M. Structure and morphology of platinum nanoparticles with critical new issues of low- and high-index facets. *Adv Nat Sci Nanosci Nanotechnol*. (2012); **3**:025005.

212. Xiang X, He W, Xie L and Li F. A mild solution chemistry method to synthesize hydrotalcite-supported platinum nanocrystals for selective hydrogenation of cinnamaldehyde in neat water. *Catal Sci Technol*. (2013); **3**:2819–27.

213. Abramoff MD, Magalhaes PJ and Ram SJ. Image processing with ImageJ. *Biophotonics Int*. (2004); **11**:36–42.

214. Schneider CA, Rasband WS and Eliceiri KW. NIH Image to ImageJ: 25 years of image analysis. *Nat Methods.* (2012); **9**:671-5.

215. Zhang Y, Zhao L, Walton J, Liu Z and Tang Z. Facile fabrication of PtPd alloyed worm-like nanoparticles for electrocatalytic reduction of oxygen. *Int J Hydrogen Energy*. (2017); **42**:17112–21.

216. Li W and Lane AM. Resolving the HUPD and HOPD by DEMS to determine the ECSA of Pt electrodes in PEM fuel cells. *Electrochem Commun.* (2011); **13**:913–6.

217. Hasché F, Oezaslan M and Strasser P. Activity, structure and degradation of dealloyed PtNi 3 nanoparticle electrocatalyst for the Oxygen Reduction Reaction in PEMFC . *J Electrochem Soc.* (2011); **159**:B24–33.

218. Neyerlin KC, Gu W, Jorne J and Gasteiger HA. Determination of catalyst unique parameters for the oxygen reduction reaction in a PEMFC. *J Electrochem Soc*. (2006); **153**:A1955.

219. Oezaslan M, Hasché F and Strasser P. Structure-activity relationship of dealloyed PtCo. *ECS Trans.* (2010); **33:** 333–41.

220. Mani P, Srivastava R, Yu C and Strasser P. In-Situ, In-Layer de-alloying of Pt-M intermetallics for high performance PEMFC electrode layers: MEA activity and durability studies. *ECS Trans.* (2007); **11:** 933–9.

221. Shao Y, Yin G, Gao Y. Understanding and approaches for the durability issues of Pt-based catalysts for PEM fuel cell. *J Power Sources.* (2007); **171**:558–66.

222. Prabhuram J, Krishnan NN, Choi B, Lim TH, Ha HY and Kim SK. Long-term durability test for direct methanol fuel cell made of hydrocarbon membrane. *Int J Hydrogen Energy*. (2010); **35**:6924–33.

223. Pei P, Chang Q and Tang T. A quick evaluating method for automotive fuel cell lifetime. *Int J Hydrogen Energy*. (2008); **33**:3829–36.

224. Shao M, Merzougui B, Shoemaker K, Stolar L, Protsailo L, Mellinger ZJ, *et al*. Tungsten carbide modified high surface area carbon as fuel cell catalyst support. *J Power Sources*. (2011); **196**:7426–34.

225. de Bruijn F. The stability of platinum and carbon in PEMFC electrodes: Insight obtained by applying electrochemical methods. In: *Fuel cells durability & performance : proceedings*. 4th ed. Brookline MA: Knowledge Press; (2009). p. 79–104.

226. Priestley RE, Mansfield A, Bye J, Deplanche K, Jorge AB, Brett D, *et al.* Pd nanoparticles supported on reduced graphene–*E. coli* hybrid with enhanced crystallinity in bacterial biomass. *RSC Adv.* (2015); **5**:84093–103.

227. Qiao Y, Li CM, Bao SJ and Bao QL. Carbon nanotube/polyaniline composite as anode material for microbial fuel cells. *J Power Sources*. (2007); **170**:79–84.

228. Cheng HY, Hou YN, Zhang X, Yang ZN, Xu T and Wang AJ. Activating electrochemical catalytic activity of bio-palladium by hybridizing with carbon nanotube as "e Bridge." *Sci Rep*. (2017); **7**:1–9.

229. Lv Z, Chen Y, Wei H, Li F, Hu Y, Wei C, *et al.* One-step electrosynthesis of polypyrrole/graphene oxide composites for microbial fuel cell application. *Electrochim Acta*. (2013); **111**:366–73.

230. Zhang J, Zhang H, Wu J and Zhang J. Chapter 3 – Techniques for PEM fuel cell testing and diagnosis. In: Zhang J, Zhang H, Wu J and Zhang J (eds). *PEM Fuel Cell Testing and Diagnosis*. (2013); **1**:81–119.

231. Namba K, Ogura S, Ohno S, Di W, Kato K, Wilde M, *et al.* Acceleration of hydrogen absorption by palladium through surface alloying with gold. *Proc Natl Acad Sci U S A*. (2018); **115**:7896–900.

232. Varun, Bhat IK and Prakash R. LCA of renewable energy for electricity generation systems-A review. *Renew Sustain Energy Rev.* (2009); **13:**1067–73.

233. Pehnt M. Dynamic life cycle assessment (LCA) of renewable energy technologies. *Renew Energy*. (2006); **31**:55–71.

234. Staffell I, Scamman D, Velazquez Abad A, Balcombe P, Dodds PE, Ekins P, *et al*. The role of hydrogen and fuel cells in the global energy system. *Energy and Environ Sci*. (2019); **12:**463–91.

235. Evangelisti S, Tagliaferri C, Brett DJL and Lettieri P. Life cycle assessment of a polymer electrolyte membrane fuel cell system for passenger vehicles. *J Clean Prod*. (2017); **142**:4339–55.

236. Notter DA, Kouravelou K, Karachalios T, Daletou MK and Haberland NT. Life cycle assessment of PEM FC applications: Electric mobility and μ-CHP. *Energy Environ Sci*. (2015); **8**:1969–85.

237. Stropnik R, Lotrič A, Bernad Montenegro A, Sekavčnik M and Mori M. Critical materials in PEMFC systems and a LCA analysis for the potential reduction of environmental impacts with EoL strategies. *Energy Sci Eng*. (2019); **7**:2519–39.

238. Agarwal H, Venkat Kumar S and Rajeshkumar S. A review on green synthesis of zinc oxide nanoparticles – An eco-friendly approach. *Resour Technol.* (2017); **3**:406–13.

239. Pati P, McGinnis S and Vikesland PJ. Life Cycle Assessment of "Green" nanoparticle synthesis methods. *Environ Eng Sci*. (2014); **31**:410–20.

240. Sadhukhan J, Joshi N, Shemfe M and Lloyd JR. Life cycle assessment of sustainable raw material acquisition for functional magnetite bionanoparticle production. *J Environ Manage*. (2017); **199**:116–25.

241. Rao SM. Chapter 1 Introduction. In: Rao SM (eds) *Waste Management Series.* Oxford, UK: Elsevier Ltd; (2006). **7:**1–12.

242. Singh A, Olsen SI and Pant D. Importance of life cycle assessment of renewable energy sources. In: Singh A, Pant D and Olsen SI (eds). *Life Cycle Assessment of Renewable Energy Sources.* London, UK: Springer Ltd. (2013); **1:**1–11.

243. Udo de Haes HA. Applications of life cycle assessment: expectations, drawbacks and perspectives. *J Clean Prod*. (1993); **1**:131–7.

244. International Standards organisation. Environmental Management-Life Cycle Assessment – Principles and Framework. (2006). ISO 14040. Available from: https://www.iso.org/standard/37456.html

245. International Standards organisation. Environmental Management-Life Cycle Assessment – Requirements and Guidelines. (2006). ISO 14044. Available from: https://www.iso.org/standard/38498.html

246. Goedkoop M, Oele M, Vieira M, Leijting J, Ponsioen T and Meijer E. SimaPro Tutorial 2: SimaPro Tutorial Written by: PRé. (2016) [Accessed: 2020 Mar 3]. Available from: www.pre-sustainability.com

247. Høgaas-Eide M. Life cycle assessment (LCA) of industrial milk production. *Int J Life Cycle Assess*. (2002); **7**:115–26.

248. Rebitzer G, Ekvall T, Frischknecht R, Hunkeler D, Norris G, Rydberg T, *et al*. Life cycle assessment Part 1: Framework, goal and scope definition, inventory analysis, and applications. *Environ Int.* (2004); **30:**701–20.

249. Skullestad JL, Bohne RA and Lohne J. High-rise timber buildings as a climate change mitigation measure - A comparative LCA of structural system alternatives. *Energy Procedia.* (2016) **96:**112–23.

250. Pizzol M, Laurent A, Sala S, Weidema B, Verones F and Koffler C. Normalisation and weighting in life cycle assessment: quo vadis? *Int J Life Cycle Assess*. (2017); **22**:853–66.

251. Aymard V and Botta-Genoulaz V. Normalisation in life-cycle assessment: consequences of new European factors on decision-making. *Supply Chain Forum*. (2017);**18**:76–83.

252. Prado V, Wender BA and Seager TP. Interpretation of comparative LCAs: external normalization and a method of mutual differences. *Int J Life Cycle Assess.* (2017); **22**:2018–29.

253. Niero M, Pizzol M, Bruun HG and Thomsen M. Comparative life cycle assessment of wastewater treatment in Denmark including sensitivity and uncertainty analysis. *J Clean Prod*. (2014); **68**:25–35.

254. Pehnt M. Life cycle assessment of fuel cell systems. *Erscheint in Fuel Cell Handbook*. (2002); **3.**

255. Hussain MM, Dincer I and Li X. A preliminary life cycle assessment of PEM fuel cell powered automobiles. *Appl Therm Eng*. (2007); **27**:2294–9.

256. Stropnik R, Sekavcnik M, Lorric A and Mori M. Life cycle assessment of 1kW PEMFC system with the focus on critical materials. *IEEE Int Conf Big Knowl*; (2020) 1–7.

257. Ribau JP, Silva CM, Sousa JMC. Efficiency, cost and life cycle CO_2 optimization of fuel cell hybrid and plug-in hybrid urban buses. *Appl Energy*. (2014); **129**:320–35.

258. Simons A and Bauer C. A life-cycle perspective on automotive fuel cells. *Appl Energy.* (2015); **157**:884–96.

259. Islam MA, Anwarul M, Bhuiya K and Islam MS. A review on chemical synthesis process of platinum nanoparticles. *Asia Pacific Journal of Energy and Environment.* (2014); **1**.

260. Cao C, Yang G, Dubau L, Maillard F, Lambert SD, Pirard JP, *et al*. Highly dispersed Pt/C catalysts prepared by the charge enhanced dry impregnation method. *Appl Catal B Environ*. (2014); **150–151**:101–6.

261. Zhou Z, Wang S, Zhou W, Jiang L, Wang G, Sun G, *et al*. Preparation of highly active Pt/C cathode electrocatalysts for DMFCs by an improved aqueous impregnation method. *Phys Chem Chem Phys*. (2003); **5**:5485–8.

262. Coutanceau C, Urchaga P, Brimaud S and Baranton S. Colloidal syntheses of shape- and size-Controlled Pt nanoparticles for electrocatalysis. *Electrocatalysis*. (2012); **3**:75–87.

263. Jukk K, Kozlova J, Ritslaid P, Sammelselg V, Alexeyeva N, Tammeveski K. Sputter-deposited Pt nanoparticle/multi-walled carbon nanotube

composite catalyst for oxygen reduction reaction. *J Electroanal Chem.* (2013); **708**:31–8.

264. Cao Z. Thin film growth for thermally unstable noble-metal nitrides by reactive magnetron sputtering. In: Cao Z (eds) *Thin Film Growth.* Philadelphia:PA, Woodhead Publishing Ltd; (2011) **1:**185–210.

265. Basile A, Tong J and Millet P. Inorganic membrane reactors for hydrogen production: An overview with particular emphasis on dense metallic membrane materials. In: Basile A (ed) Handbook of Membrane Reactors. Philadelphia:PA, Woodhead Publishing Ltd; (2013); **1:**42–148.

266. Speder J, Altmann L, Roefzaad M, Bäumer M, Kirkensgaard JJK, Mortensen K, *et al.* Pt based PEMFC catalysts prepared from colloidal particle suspensions-a toolbox for model studies. *Phys Chem Chem Phys.* (2013); **15**:3602–8.

267. Wernet G, Bauer C, Steubing B, Reinhard J, Moreno-Ruiz E and Weidema B. The ecoinvent database version 3 (part I): overview and methodology. *The International Journal of Life Cycle Assessment.* (2016); **21**:1218–1230.

268. Huijbregts MA, Steinmann ZJ, Elshout PM, Stam G, Verones F, Vieira M, Hollander AK, Zijp MC, and Zelm, RV. ReCiPe 2016. A harmonized life cycle impact assessment method at midpoint and endpoint level. Report 1: Characterization. (2016) Available from: www.rivm.nl/en [Accessed: 01 May 2020]

269. Santos AL and Johnson DB. Design and application of a low pH upflow biofilm sulfidogenic bioreactor for recovering transition metals from

synthetic waste water at a Brazilian copper mine. *Front Microbiol* (2018); **9**:2051.

270. Acero AP, Rodríguez C and Changelog AC. LCIA methods: Impact assessment methods in Life Cycle Assessment and their impact categories. (2016) Available from: https://www.openlca.org/wp-content/uploads/2015/11/LCIA-METHODS-v.1.5.4.pdf [Accessed 01 May 2020]

271. Lin E, Meyer CP and Flugsrud K. Chapter 4 Methodological choice and identification of key categories. In *IPCC Guidelines for National Greenhouse Gas Inventories.* (2006). Available from: https://www.ipcc-nggip.iges.or.jp/public/2006gl/pdf/1_Volume1/V1_4_Ch4_MethodChoice.pdf. [Accessed 01 May 2020]

272. Humbert S, De Schryver A, Bengoa X, Margni M, Jolliet O. IMPACT 2002+: User Guide. (2012). Available from: https://www.quantis-intl.com/pdf/IMPACT2002_UserGuide_for_vQ2.2.pdf. [Accessed 01 May 2020]

273. Eco-indicator 99 Manual for Designers A damage oriented method for Life Cycle Impact Assessment. (2000). Available from: https://www.pre-sustainability.com/download/EI99_Manual.pdf [Accesseed 01 May 2020]

274. Liu J, Zou S, Xiao L and Fan J. Well-dispersed bimetallic nanoparticles confined in mesoporous metal oxides and their optimized catalytic activity for nitrobenzene hydrogenation. *Catal Sci Technol.* (2014); **4**:441–6.

275. Rees N and Horswell S. Introduction to electrochemistry. [Lecture Notes] University of Birmingham, UK. (2017).

276. Lasia A. Electrochemical impedance spectroscopy and its applications. New York, NY: Springer. (2014);1–367.

277. Pine Research. *Koutecky-Levich Analysis (RDE).*Available from: https://pineresearch.com/shop/kb/theory/hydrodynamic-electrochemistry/koutecky-levich-analysis/ [Accessed: 01 May 2020]

278. Kim JH, Cheon JY, Shin TJ, Park JY and Joo SH. Effect of surface oxygen functionalization of carbon support on the activity and durability of Pt/C catalysts for the oxygen reduction reaction. *Carbon*. (2016); **101**:449–57.

279. Song L, Vukmirovic MB, Adzic RR. (Invited) Enhanced oxygen reduction reaction activity on Pt-monolayer-shell PdIr/Ni-core catalysts. *ECS Trans.* (2018); **85**:57–65.

280. Archer SA, Murray AJ, Omajali JB, Paterson-Beedle M, Sharma BK, Wood J and Macaskie LE. Metallic wastes into new process catalysts: Life cycle and environmental benefits within integrated analyses using selected case histories. In: Macaskie LE, Sapsford DJ and Mayes WM (eds) *Resource recovery from wastes: Towards a Circular Economy*. Croydon, UK: RSC Publications. (2019); 315-342.

281. Huy HA, Tran VM, Hunynh TT and Van Hott. Preparation and characterization of high-dispersed pt/c nano-electrocatalysts for fuel cell applications. *Journal of science and technology*. (2016); **53:**472-482.

282. Nuss P and Eckelman MJ. Life cycle assessment of metals: A scientific synthesis. *PLoS One*. (2014); **9**.

283. Lasia A. Electrochemical impedance spectroscopy and its applications. Vol. 9781461489337, Electrochemical Impedance Spectroscopy and its Applications. Springer New York; 2014. 1–367 p.

284. Deplanche K, Merroun ML, Casadesus M, Tran DT, Mikheenko IP, Bennett JA, et al. Microbial synthesis of core/shell gold/palladium nanoparticles for applications in green chemistry. *J R Soc Interface*. (2012); **9**:1705–12.

285. Gomez-Bolivar J, Mikheenko IP, Macaskie LE and Merroun ML. Characterization of palladium nanoparticles produced by healthy and microwave-injured cells of *Desulfovibrio desulfuricans* and *Escherichia coli*. *Nanomaterials*. (2019); **9**.

286. Mai-Prochnow A, Clauson M, Hong J and Murphy AB. Gram positive and Gram negative bacteria differ in their sensitivity to cold plasma. *Sci Rep*. (2016); **6**:38610.

287. Vergalli J, Bodrenko IV, Masi M. et al. Porins and small-molecule translocation across the outer membrane of Gram-negative bacteria. *Nat Rev Microbiol*. (2020); **18**:164–176.

288. Garsany Y, Ge J, St-Pierre J, Rocheleau R and Swider-Lyons K. Analytical Procedure for Accurate Comparison of Rotating Disk Electrode Results for the Oxygen Reduction Activity of Pt/C. *J. Electrochem. Soc*. (2014); **161**: F628-F640.

Appendix

A1: Brief introduction on the fundamentals of electrochemistry

This section covers a basic introduction into electrochemistry and the detail the instrumentation used for analysis and the information relayed is adapted from references Bard and Faulkner [207] and Rees and Horswell [274]. Furthermore, in the following equations, unless stated otherwise, R denotes the molar gas constant, T denotes the temperature and F denotes the Faraday constant and n denotes the number of electrons transferred.

A1.1 Fundamentals of electrochemistry

Electrochemistry is the branch of chemistry that studies chemical reactions that involve the transfer of charges, i.e. redox reactions. The following equation shows a representative redox reaction where a species O gets reduced to species R on gaining n number of electrons.

$$O + ne^- \leftrightharpoons R \qquad \textbf{(Eq A1.1),}$$

The ORR is a redox reaction; for oxygen reduction to occur, it must have gained electrons from the electrode alongside protons from the electrolyte to make water. For an electron transfer to occur from the electrode; the Fermi level of the electrode must be greater than the orbital of the electron acceptor species. Similarly, for an electron transfer to occur to the electrode, the Fermi level of the electrode must be lower than the electron of the donor species. The Fermi level of the electrode can be adjusted by altering the potential across the electrode. The thermodynamics and kinetics of this interaction is described below.

A1.1.1 Electrochemistry thermodynamics

The maximum non-expansion work that can be extracted from a thermodynamically closed system is given by the following equation.

$$\Delta G = \Delta G^{\theta} + RT ln Q \qquad \textbf{(Eq A1.2)},$$

where ΔG is the Gibbs free energy of the reaction, ΔG^{θ} is the Gibbs free energy of the reaction under standard conditions, and Q is the reaction quotient. When the work done is electrochemical (i.e. involves transfer of charges), the Gibbs free energy is also given by the following equation

$$\Delta G = -nFE \qquad \textbf{(Eq A1.3)},$$

where E is the potential difference of the redox reaction. From this we can derive the Nernst equation that correlates potential difference of the reaction, concentration of reactions and products and potential difference at standard conditions (standard cell potential). This is shown below

$$E = E^{\theta} + \frac{RT}{nF} ln \frac{a_O}{a_R} \qquad \textbf{(Eq A1.4)},$$

where E is the potential difference, E^{θ} is the standard cell potential and a_O and a_R are the activities of the oxidised and reduced species respectively. However, this equation is not entirely accurate when considering electron transfer via electrodes. The concentration of reduced and oxidised species at the electrode will be not equal the bulk concentration. As such the following equation is utilised instead.

$$E = E^{\theta'} + \frac{RT}{nF} ln \frac{C_O^*}{C_R^*} \qquad \textbf{(Eq A1.5)},$$

where C_O^* and C_R^* are the concentrations of the oxidised and reduced species on the electrode surface and $E^{\theta\prime}$ is the conditional cell potential given by the following equation

$$E^{\theta\prime} = E^{\theta} + \frac{RT}{nF} ln \frac{\gamma_O}{\gamma_r} \qquad \textbf{(Eq A1.6),}$$

where γ_O and γ_r are the activity coefficient of the oxidised and reduced species. This equation provides a proportional relationship between the concentration of species on the electrode and its activity. When concentrations are low, the activity coefficient tends to 1 thus resulting in $E^{\theta\prime}$being equal to E^{θ}.

A1.1.2 Electrochemistry Kinetics

The kinetics of a reaction is related to the activation energy of a reaction. Figure A1.1, shows the progress of reaction (Eq A1.1) from oxidised species to reduced species. As seen, the reactant must overcome an energy barrier to reach an intermediate state before which it can be converted into the product. With a catalyst, the activation energy is lowered. The reaction rate is related to the activation free energy by the Arrhenius equation

$$k = A\, e^{-\left(\frac{E_A}{RT}\right)} \qquad \textbf{(Eq A1.7),}$$

where k is the reaction rate, A is a constant and E_A is the activation energy. Thus, with a catalyst (and a lower E_A), the reaction rate will be increased.

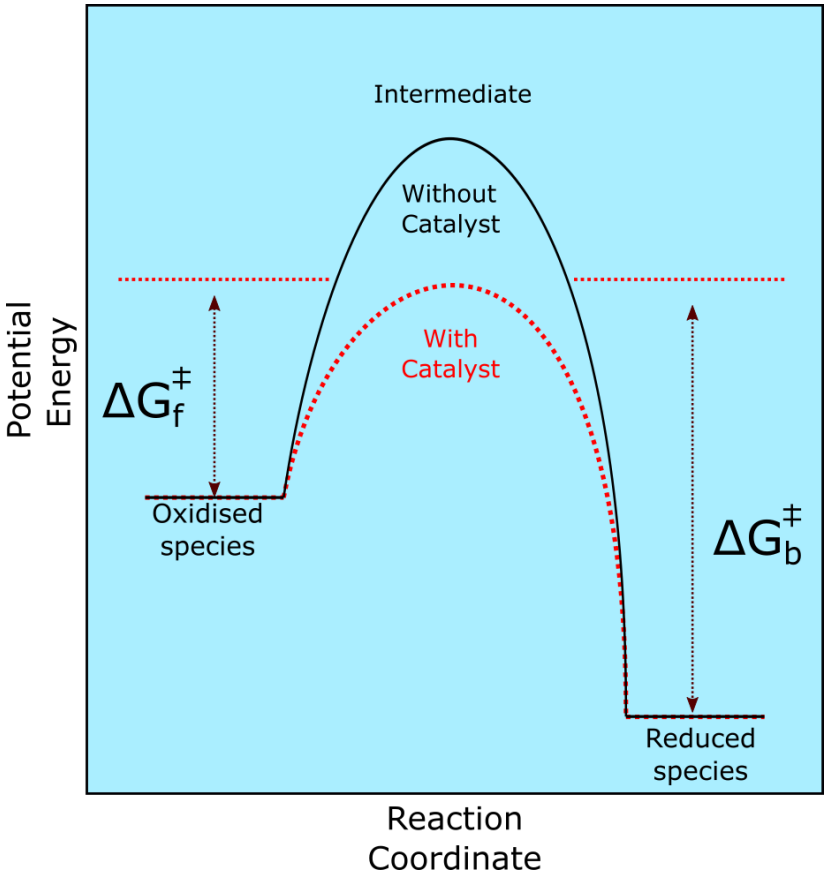

Figure A1.1 Schematic diagram of changes in potential energy of a reaction. The oxidised species must overcome the activation barrier with free energy ($\boldsymbol{E_A}$). For the forward reaction this is $\boldsymbol{\Delta G_f^{\ddagger}}$ and for the backward it is $\boldsymbol{\Delta G_b^{\ddagger}}$. This energy barrier is decreased with a catalyst. This is adapted from Bad and Faulkner [207]

Using equations eq A1.7 and A1.3, we can identify the reaction rates of the individual reduction and oxidation reactions in eq A1.1. As seen in the figure A1.1 there is a free energy requirement associated with the forward ($\boldsymbol{\Delta G_f^{\ddagger}}$) and backward ($\boldsymbol{\Delta G_b^{\ddagger}}$) reactions; here it will be ($\boldsymbol{\Delta G_{Red}^{\ddagger}}$) and ($\boldsymbol{\Delta G_{Ox}^{\ddagger}}$) respectively. Using eq A1.3 we can get the value for $\boldsymbol{E_A}$ in terms of potential $\boldsymbol{E}$ and thus derive the following equations for the rate of reactions for reduction and oxidation of a species

$$k_{red} = k_o \, exp^{\left(\frac{\beta n F \eta}{RT}\right)} \quad \textbf{(Eq A1.8)},$$

$$k_{ox} = k_o \, exp^{\left(\frac{-\alpha n F \eta}{RT}\right)} \quad \textbf{(Eq A1.9)},$$

where k_{red} and k_{ox} is the reaction rates of reduction and oxidation respectively, k_o is the reaction rate at equilibrium and η is the overpotential where $\eta = E - E^{\theta}$, n is the number of electrons transferred and α and β are the transfer coefficients. The transfer coefficients are a measure of how similar the transition state is to the reactants and products where $\alpha + \beta = 1$. If $\alpha = \beta = 0.5$, then the transition state lies between the oxidised and reduced species. The current drawn from an electrochemical reaction (i.e. the ORR in a fuel cell) is given by the equation

$$I = nFAj \quad \textbf{(Eq A1.10)},$$

where I is the current (amps), A is the area of the electrode and j is the flux of the reactant. Since net current is given by

$$I = nFA(-j_{red} + j_{ox}) \quad \textbf{(Eq A1.11)},$$

and flux of oxidised species and reduced species is given by

$$j_{red} = k_{red} C_o^* \quad \textbf{(Eq A1.12)},$$

$$j_{ox} = k_{ox} C_R^* \quad \textbf{(Eq A1.13)},$$

Putting equations A1.8, A1.9, A1.11, A1.12 and A1.13 together we get the Butler-Volmer equation given as the following.

$$I = \ nFAk_o \left(C_o^* e^{\left(\frac{\beta nF\eta}{RT}\right)} - \ C_R^* e^{\left(\frac{(-\alpha)nF\eta}{RT}\right)} \right) \qquad \textbf{(Eq A1.14),}$$

which can be rewritten as

$$I = \ I_o \left(\frac{C_o^*}{C_o^B} e^{\left(\frac{\beta nF\eta}{RT}\right)} - \frac{C_R^*}{C_R^B} e^{\left(\frac{(-\alpha)nF\eta}{RT}\right)} \right) \qquad \textbf{(Eq A1.15),}$$

where I_0 is the exchange current given by $I_o = nFAk_o \frac{(C_R^B)^\beta}{(C_O^B))^{\beta-1}}$, C_O^B and C_R^B are the bulk concentrations of the reduced and oxidised species respectively. This can be rewritten as in terms of current density, j, where $j = \frac{I}{Electrode\ Area}$, as the following

$$j = j_o \left(\frac{C_o^*}{C_o^B} e^{\left(\frac{\beta nF\eta}{RT}\right)} - \frac{C_R^*}{C_R^B} e^{\left(\frac{(-\alpha)nF\eta}{RT}\right)} \right) \qquad \textbf{(Eq A1.16),}$$

Where j is the net current density and j_o is the exchange current density. This is an essential equation that correlates the overpotential of the system to the net current drawn from it.

j_o can be regarded as the background current occurring to which the net current density is normalised. i.e., at equilibrium when net current is zero, there is an equal and opposite current density at both the cathode and anode. It is a measure of electron transfer between the reactant and the electrode. The higher the value of j_o, the more readily the reaction will occur and the better kinetics it will have.

As seen, j will also be affected by the surface and bulk concentration of the electroactive species. The means by which they approach the electrode is described in the following section.

A1.1.3 Mass transport of reactants

Mass transport is the means by which electroactive species can reach the electrode surface from bulk solution and this influences the overall net current density, $\boldsymbol{j}$. This has three major components: diffusion, migration, and convection.

A1.1.1.3.1 Diffusion

Diffusion is the movement of species through a chemical potential gradient and is governed by Fick's Laws. Fick's first law describes the net flux to the electrode from bulk solution and is given by the equation

$$\boldsymbol{j} = -\boldsymbol{D}\frac{\boldsymbol{\delta[A]}}{\boldsymbol{\delta x}} \qquad \textbf{(Eq A1.17),}$$

where, $\boldsymbol{j}$ is the flux of electroactive species A to the surface of the electrode, $\boldsymbol{x}$ is the displacement of $\boldsymbol{A}$ from the electrode and $\boldsymbol{D}$ is a constant, called the diffusion coefficient. Fick's second law describes the change in bulk concentration over time

$$\frac{\boldsymbol{\delta[A]}}{\boldsymbol{\delta t}} = \boldsymbol{D}\frac{\boldsymbol{\delta^2[A]}}{\boldsymbol{\delta x^2}} \qquad \textbf{(Eq A1.18),}$$

A1.1.1.3.2 Migration

Migration is the movement of charged molecules through an electric gradient in a local electric field. This arises when a potential gradient is established between the electrode and the bulk solution. While this could be viewed as an ideal mode of mass transfer, its dependence on small variations in localised electric fields makes it difficult to model. In order to eliminate migration, an excess of supporting electrolyte, which is chemically and electrochemically inert, is usually added to the reaction solution. This creates an abundance of ions near the interface region which maintains electroneutrality.

A1.1.1.3.3 Convection

There are two forms of convection possible in mass transfer: natural and forced convection. Natural convection occurs as a result of density gradients in the solution or caused by localised thermal variations. These are irreproducible and cannot be controlled. As such, in quantitative experiments, they are undesirable and can influence results. However, thermal variations are easily avoided by lowering the voltage scan rate used in current-potential experiments.

Forced convection is the intentional agitation or stirring of the electrolyte by mechanical means. In doing so, this deliberate form of mass transfer can be modelled. As seen in figure A1.2, rotating the WE at a set rotation speed results in a controlled mass transfer of reactants. Furthermore, this rotation rate can be related to current using the Levich equation as seen below (see section 2.3.2.2)

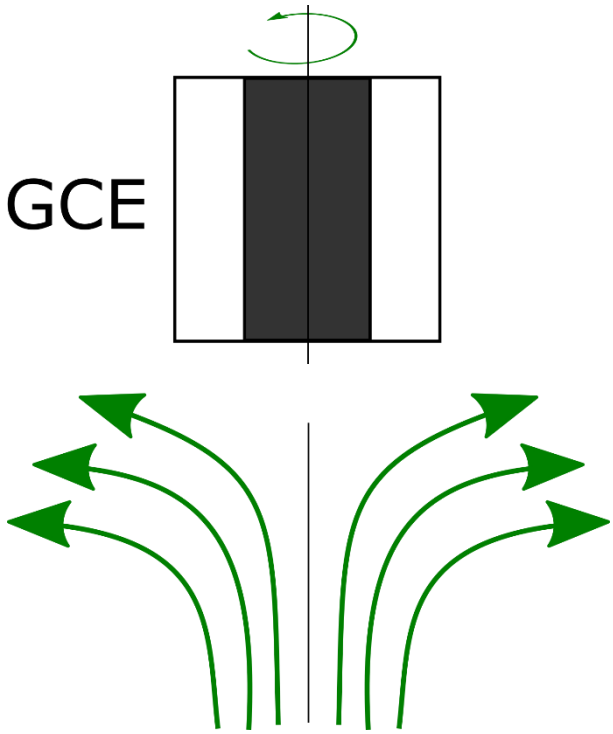

$$I_l = 0.62nFAD_0^{\frac{2}{3}}\omega^{\frac{1}{2}}v^{-\frac{1}{6}}C_0^*$$

Figure A1.2 Rotation of GCE working electrode induces a laminar flow (in green) of reactants to the surface of the WE.

A2: *E. coli*-NP characterisation

This section covers the supplementary material from chapter 3 that details NP characterisation. This includes NP sizing, XPS full survey scans and SAED measurements made.

A.2.1 STEM images and Nanoparticle sizing

This section details all the threshold images and the measured images used to size NPs for *E. coli*-Pd (20%), *E. coli*-Pt (20%) *E. coli*-Pt:Pd* (10%:10%) and *E. coli*-Pd:Pt* (10%:10%).

A.2.1.1 *E. coliI*-Pd (20%)

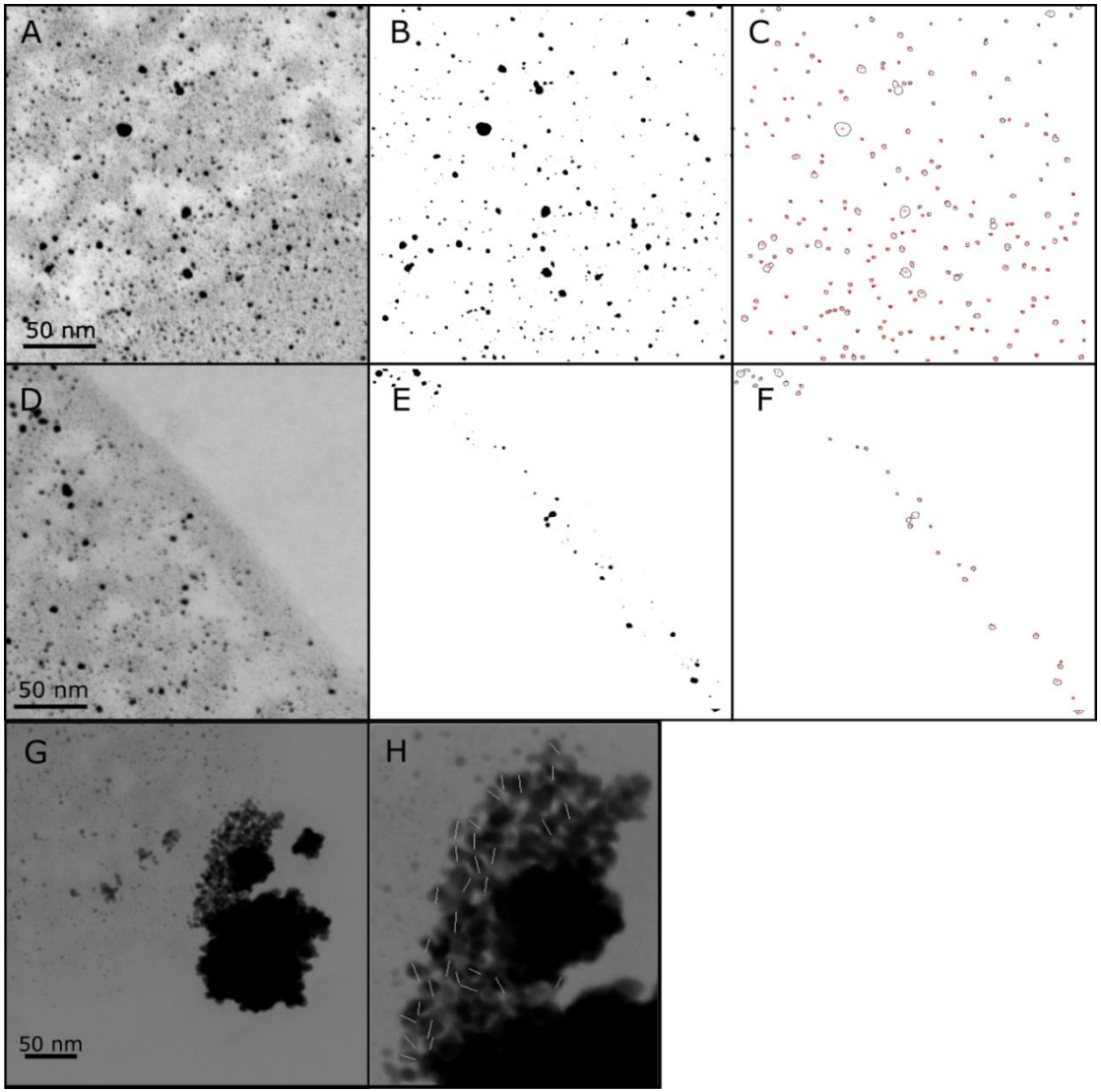

Figure A2.1.1 shows Pd-NPs sized with *E. coli*-Pd (15%) (figure 3.3). Location 3.3B is shown in (A), with its threshold image and NPs sized shown in (B) and (C) respectively. Similarly, Location 3.3C is shown in (D) with its threshold image and NPs sized shown (E) and (F) respectively. (C) and (F) show the outlines of the nanoparticles sized. Location 3.3C is shown in (G) and as seen, "analyse particles" cannot be used on the clustered NPs. As such, they are individually measured, and this is shown in (H) with white lines

A2.1.2 *E. coli*-Pt (20%)

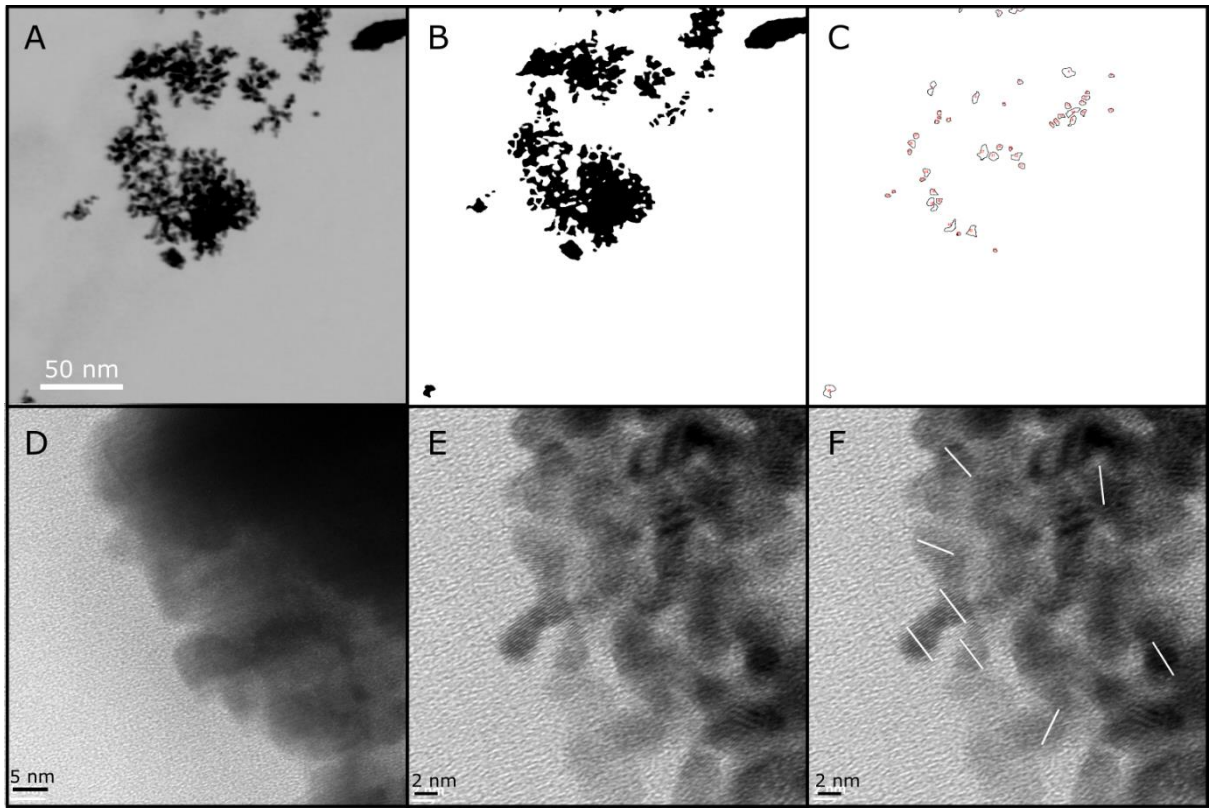

Figure A2.1.2 shows Pt-NPs sized with *E. coli*-Pt (20%) (figure 3.4). Location 3.4B is shown in (A), with its threshold image and NPs sized shown in (B) and (C) respectively. (D) shows a clustered region where individual NPs could not be easily observed. Location 3.4C is shown in (E) and as seen, "analyse particles" cannot be used on the clustered NPs. As such, they are individually measured, and this is shown in (F) as white lines.

A2.1.3 *E. coli*-Pt:Pd* (10%:10%)

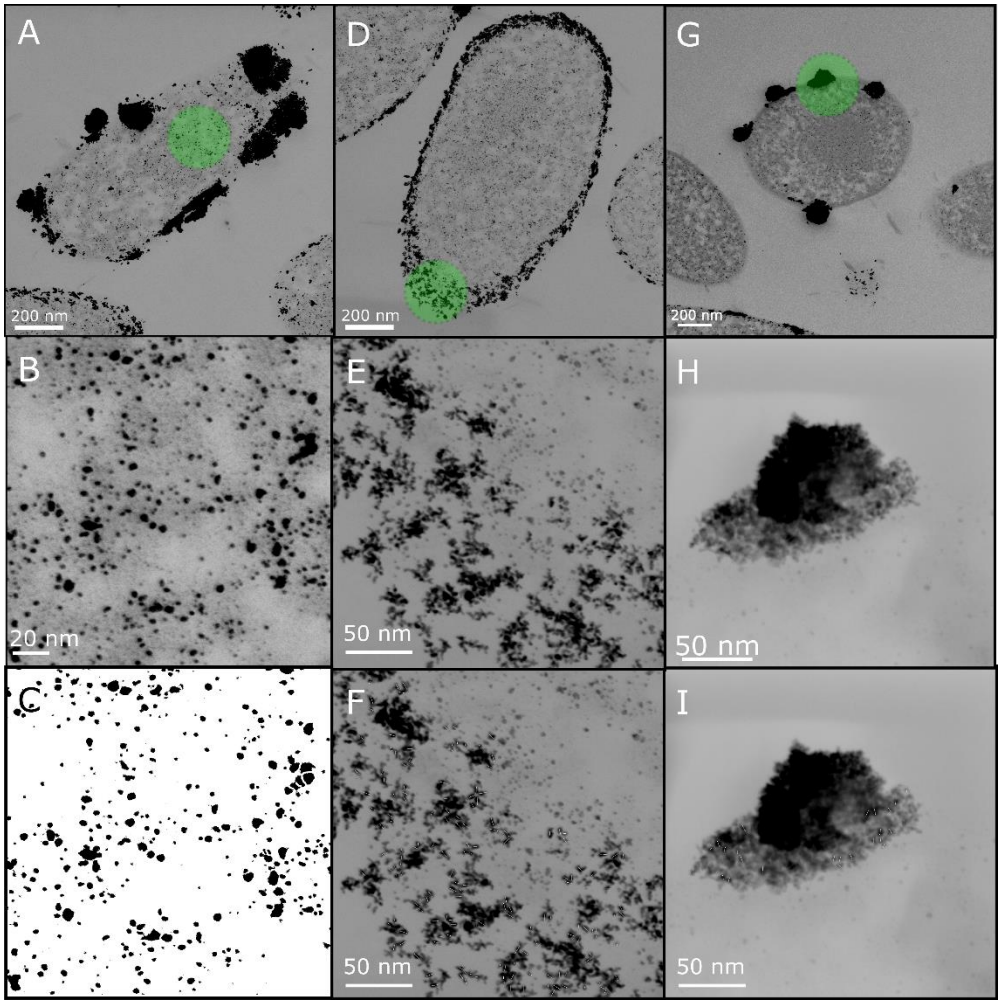

Figure A2.1.3 shows Pt:Pd*-NPs sized with *E. coli*-Pt:Pd (10%:10%) (figure 3.13). (A) shows the cell studied and the area highlighted in green. (B) shows the intracellular NPs sized, its threshold image in (C). (D) shows a different cell with NPs in the periplasmic space studied highlighted in green. (E) shows the periplasmic NPs sized, the individual NPs measured in (F). (G) shows a different cell with clustered NPs in studied highlighted in green. (H) shows the clustered NPs sized and the individual NPs measured in (I) shown as white lines.

A2.1.4 *E. coli*-Pd:Pt* (10%:10%)

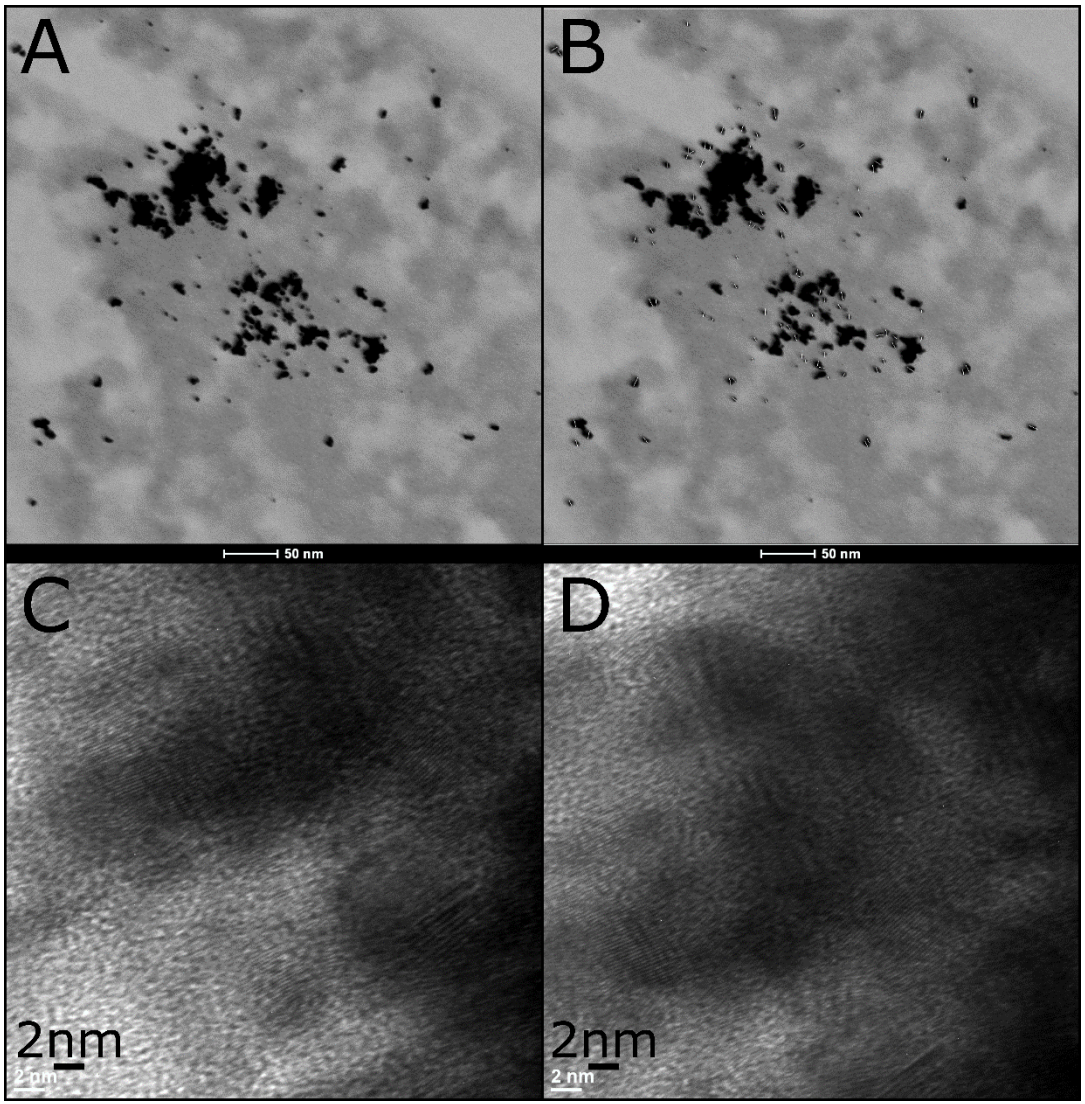

Figure A2.1.4 shows Pd-NPs sized with *E. coli*-Pd:Pt* (10%:10%) (figure 3.14). (A) shows the agglomerated intracellular NPs sized and the individual NPs measured in (B). (C) and (D) shows HRTEM images of clusters where individual NP boundaries can not be determined.

A2.2 SAED clusters

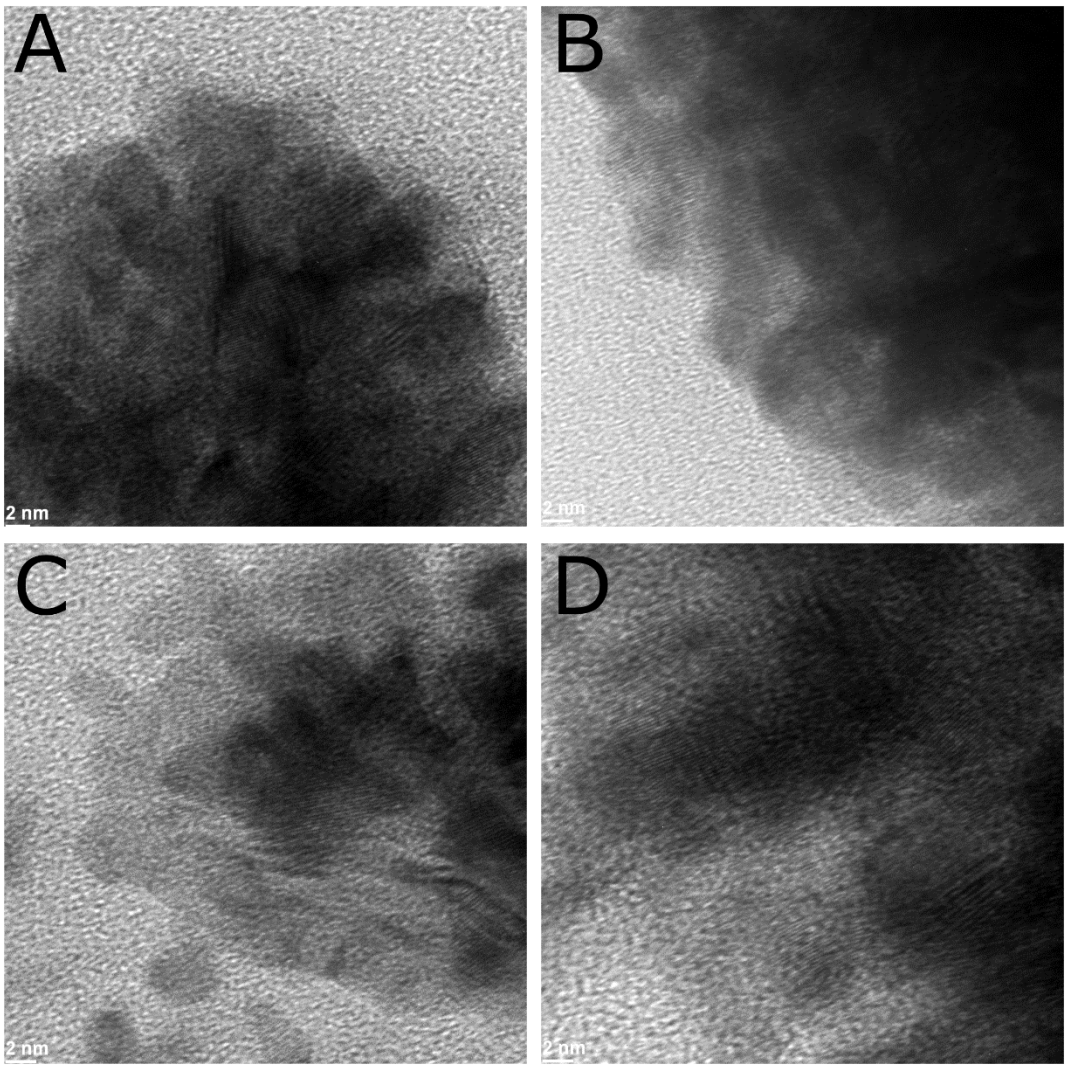

Figure A2.2 Clusters used for SAED analysis in Chapter 3 for (A) *E. coli*- Pd (15%), (B) *E. coli*-Pt (20%) (C) *E. coli*-Pt:Pd* (10%:10%) and (D) *E. coli*-Pd:Pt* (10%:10%).

A2.3 XPS Survey scans

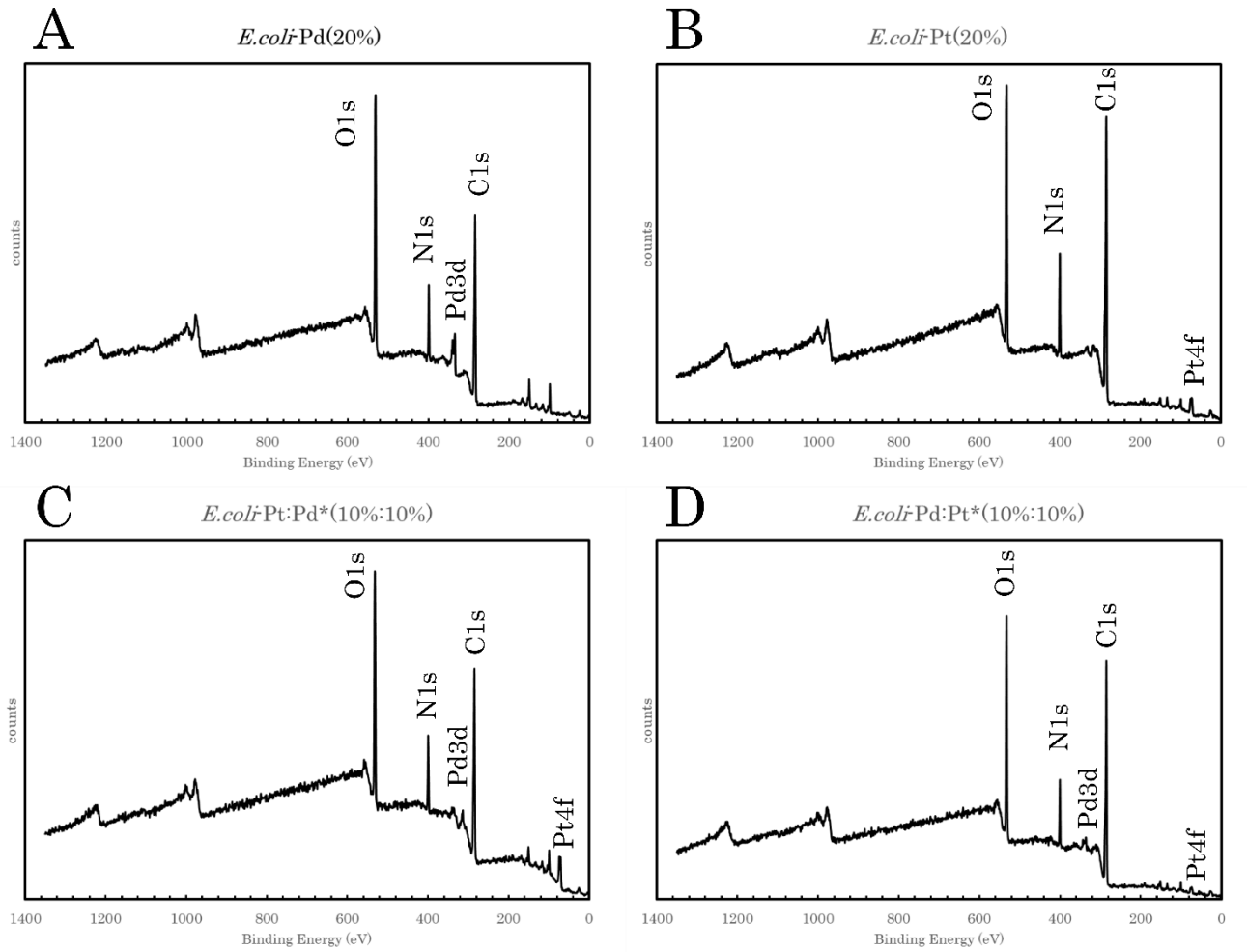

Figure A2.3.2.2 XPS survey scans shown for (A) *E. coli*-Pd (20%), (B) *E. coli*-Pt (20%), (C) *E. coli*-Pd:Pt* (10%:10%), and (D) *E. coli*-Pd:Pt* (10%:10%).

A2.4 STEM images of bimetallics

Supplementary material relevant to the STEM characterisation of the bimetallics are shown here (i.e., localisation and EDX line transects)

A2.4.1 Metal reduction in *E. coli*-Pt:Pd* (10%:10%) and *E. coli*-Pd:Pt* (10%:10%)

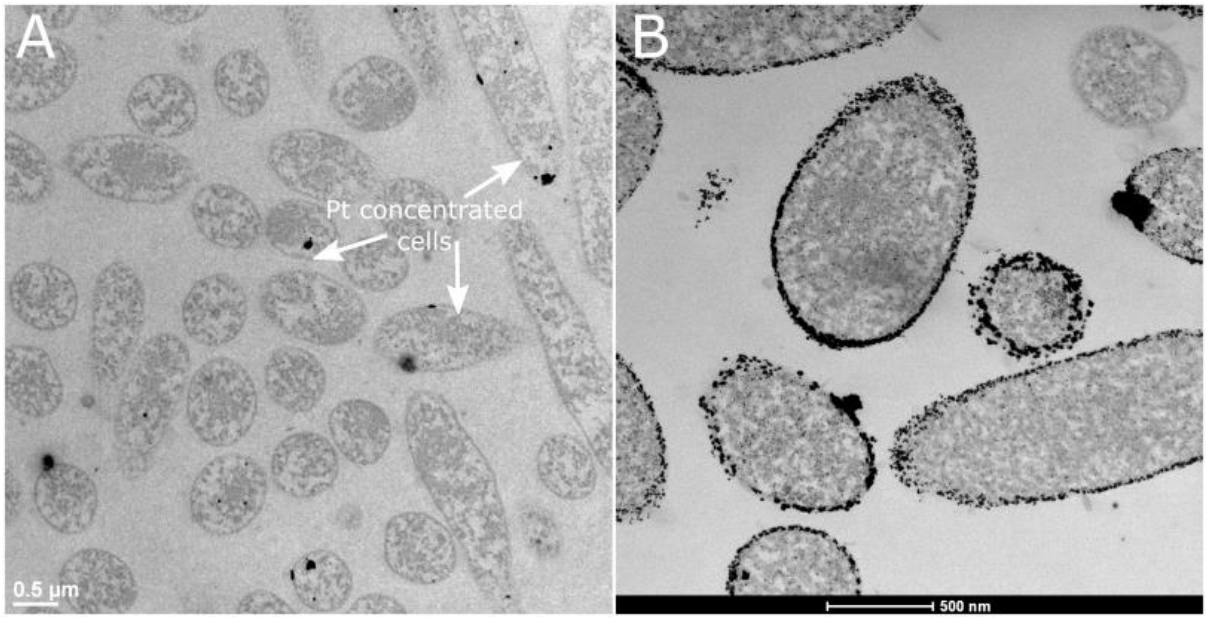

Figure A2.4.1 (A) shows *E. coli*-Pd:Pt* (10%:10%) with metal reduction in only a few cells. (B) shows *E. coli*-Pt:Pd (10%:10%) with metal reduction in all cells

A2.4.2 EDX line transects for *E. coli*-Pt:Pd* (10%:10%) and *E. coli*-Pd:Pt* (10%:10%)

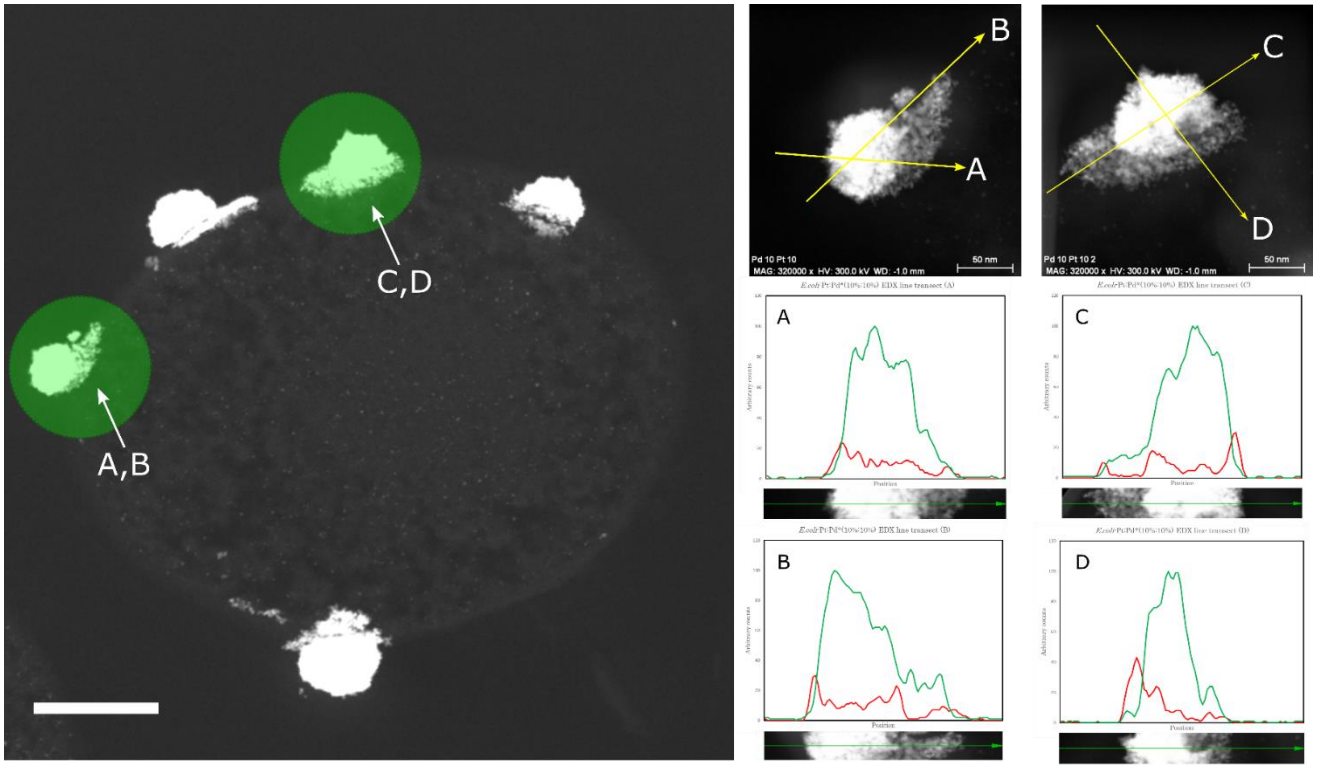

Figure A2.4.2.1 shows line transects taken across two clusters of *E. coli*-Pt:Pd* (10%:10%). (A) and (B) are line transects across one cluster (highlighted in green) and (C) and (D) are line transects across a secondary cluster (highlighted in green). As seen all line transects showed Pt (red) and Pd (green) across the entire cell with a Pt-rich skin at the outer edges of the cluster.

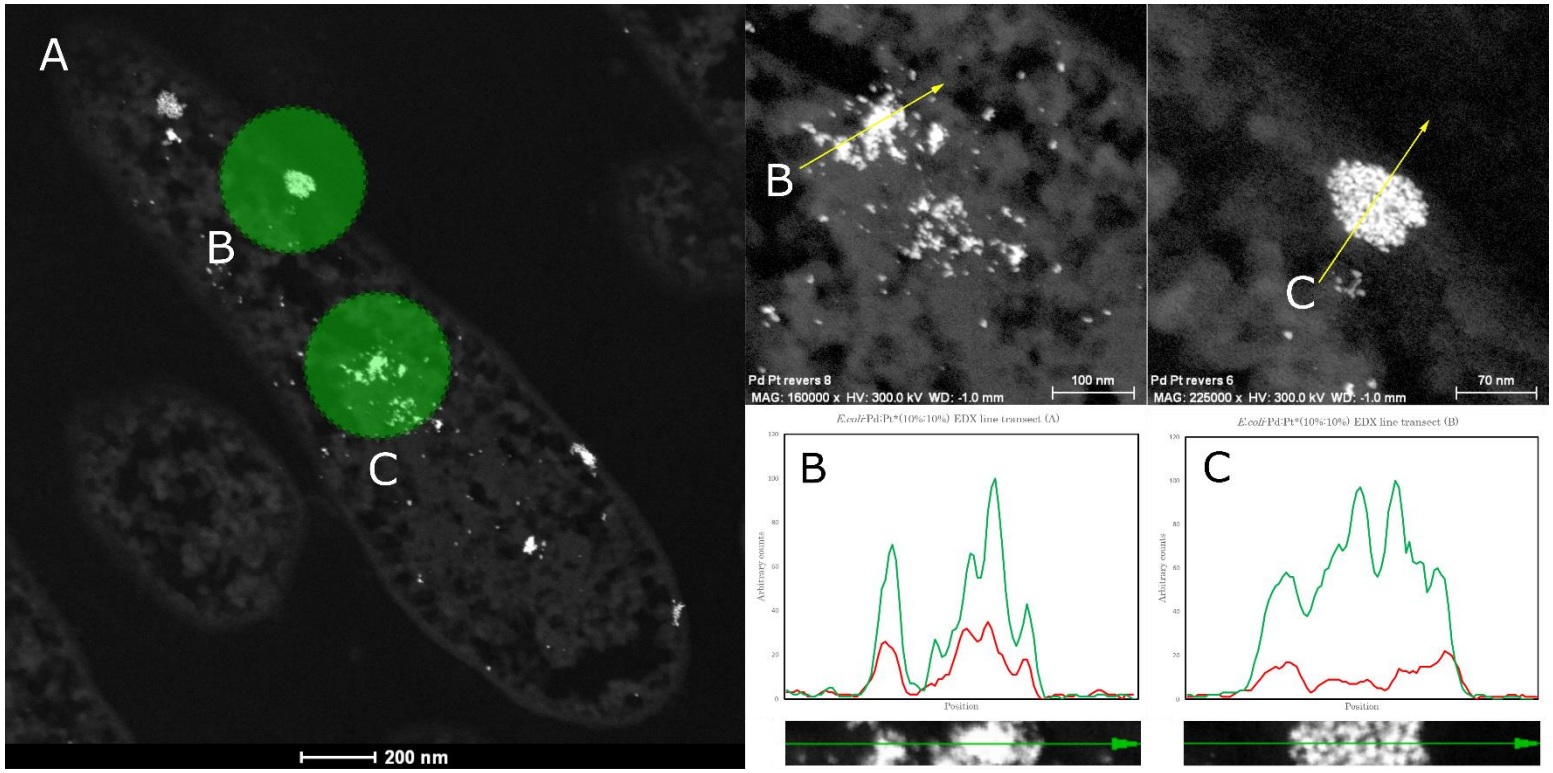

Figure A2.4.2.2 shows line transects taken across two clusters of *E. coli*-Pd:Pt* (10%:10%). (B) and (C) are line transects across clusters (highlighted in green) As seen all line transects showed Pt (red) and Pd (green) across the entire cluster with an apparent equal proportion of both.

A3 *Ex-situ* electrochemistry of *E. coli*-NPs

This section details additional information relating to *ex-situ* electrochemical characterisation of *E. coli*-NPs.

A3.1 Attempts to improve conductivities

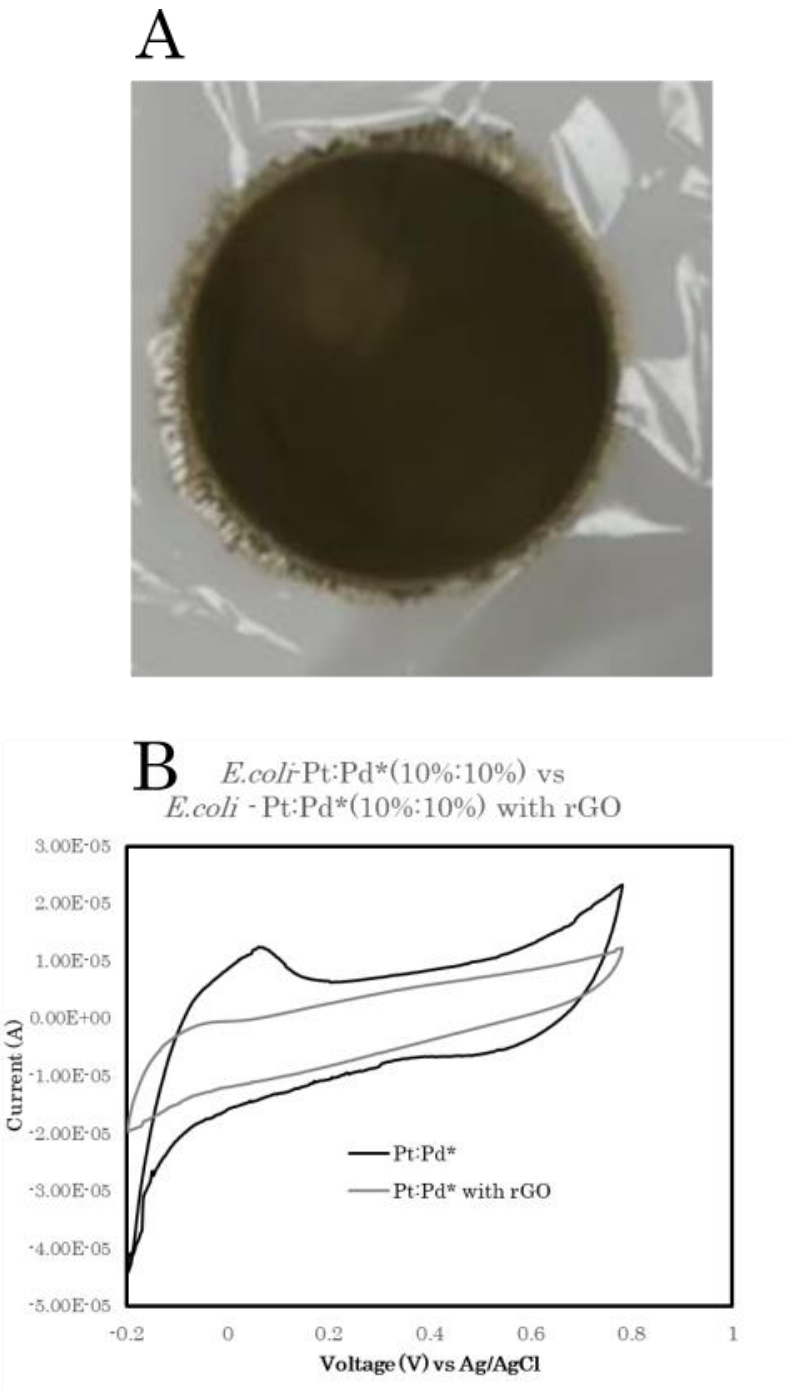

Figure A3.1 Alternative attempts to improve conductivities of *E. coli*-Pt:Pd* (10%:10%). (A) *E. coli* MC4100 with conductive polymer polypyrrole (PPY) polymerised onto cell surface following methods described by Lv et al.[229] Green surface shows polymerisation of pyrrole onto bacterial cell surface but this could not be confirmed by spectroscopy methods. Furthermore, this was not tested with *E. coli*-NPs. As such, this warrants further research.

(B) Priestley et al., showed simultaneous reduction of graphene oxide (GO) to rGO alongside Pd synthesis by *E. coli* [(226)]. This method [(226)] was used to synthesise *E. coli*-Pt:Pd*-rGO. CVs of the catalyst with and without rGO are shown here. As seen, there is a reduction in peak current. However, this method was not optimised and warrants further research

A3.2 CV of *E. coli*-Pd:Pt* (10%:10%)

As seen in the representative CV below, CVs of *E. coli*-Pd:Pt* (10%:10%) on multiple attempts did not show any peaks and as such was disregarded from future experiments.

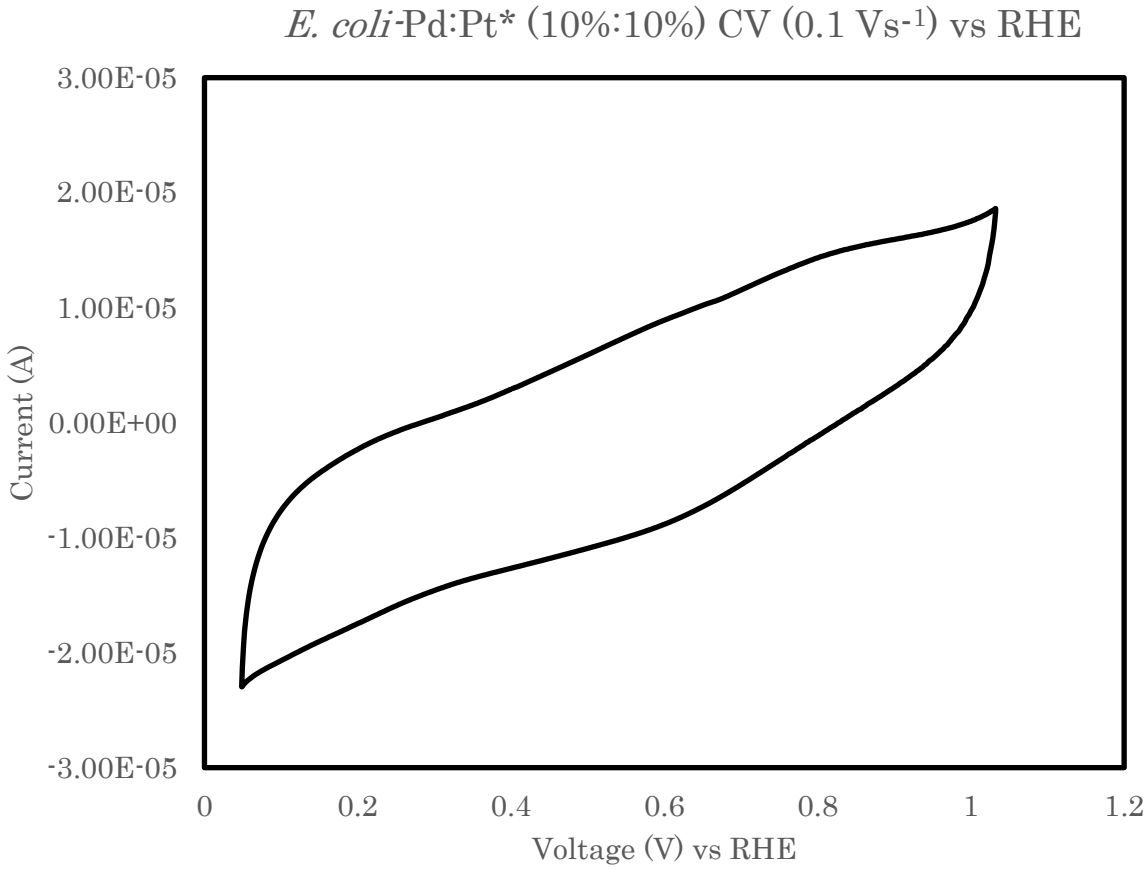

A3.3 Durability examples

A representative durability experiment out of 3 separate experiments is shown below for *E. coli*-Pd (20%). Black line shows the representative peak for *E. coli*-Pd (20%) taken after cleaning and before stress test. Grey line shows the representative peak after 1000 scans with the black arrow showing the decrease in peak size after stress test. Interestingly a peak shift is also noted.

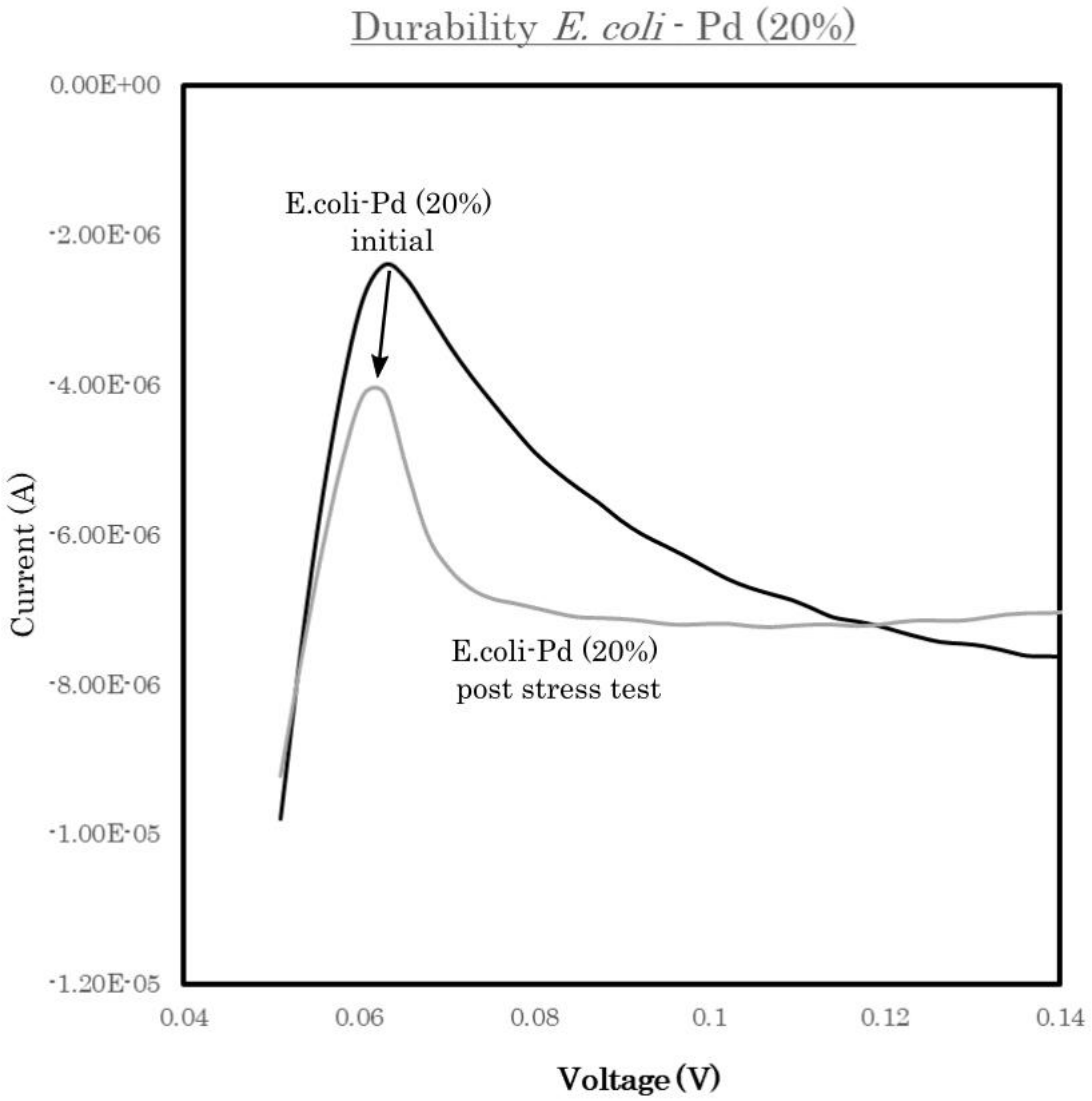

A4 LCA Flow charts

The flow charts for synthesis of H_2PtCl_6, Na_2PdCl_4 growth of *E. coli* is shown here. The boxes in red show the emissions and wastes for each process. All chemicals used were found in the LCA Software SimaPro 8.5.2.0 [246] and the Ecoinvent 3 databases [267] . The green arrow shown for *E. coli* growth relates to the inoculum required for *E. coli*-growth. It is assumed that there are no environmental impacts for initial *E. coli* growth. Finally, Bangor cells are assumed to be obtained concentrated and suspended in MOPS and without requiring any further processing.

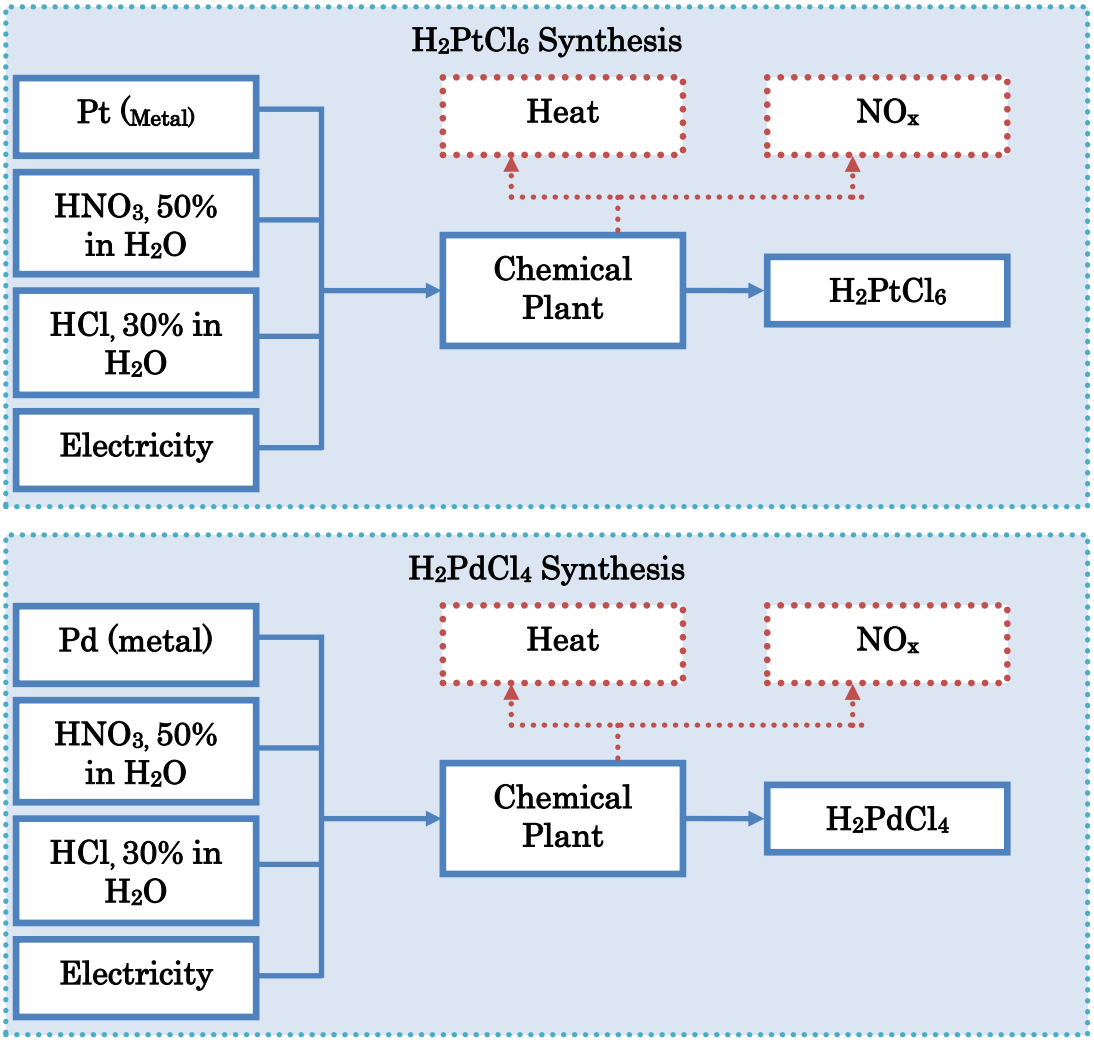

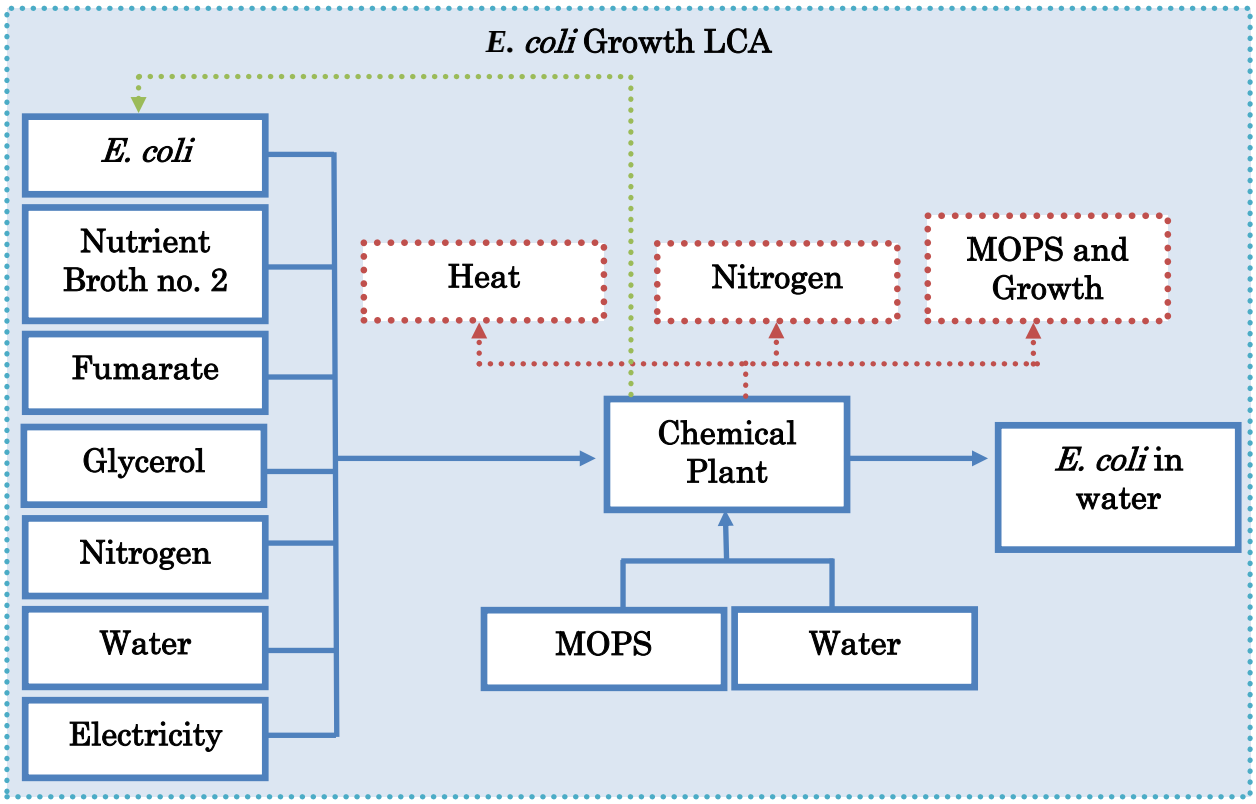
E. coli Growth LCA
E. coli
Nutrient Broth no. 2
Fumarate
Glycerol
Nitrogen
Water
Electricity
Heat
Nitrogen
MOPS and Growth
Chemical Plant
E. coli in water
MOPS
Water

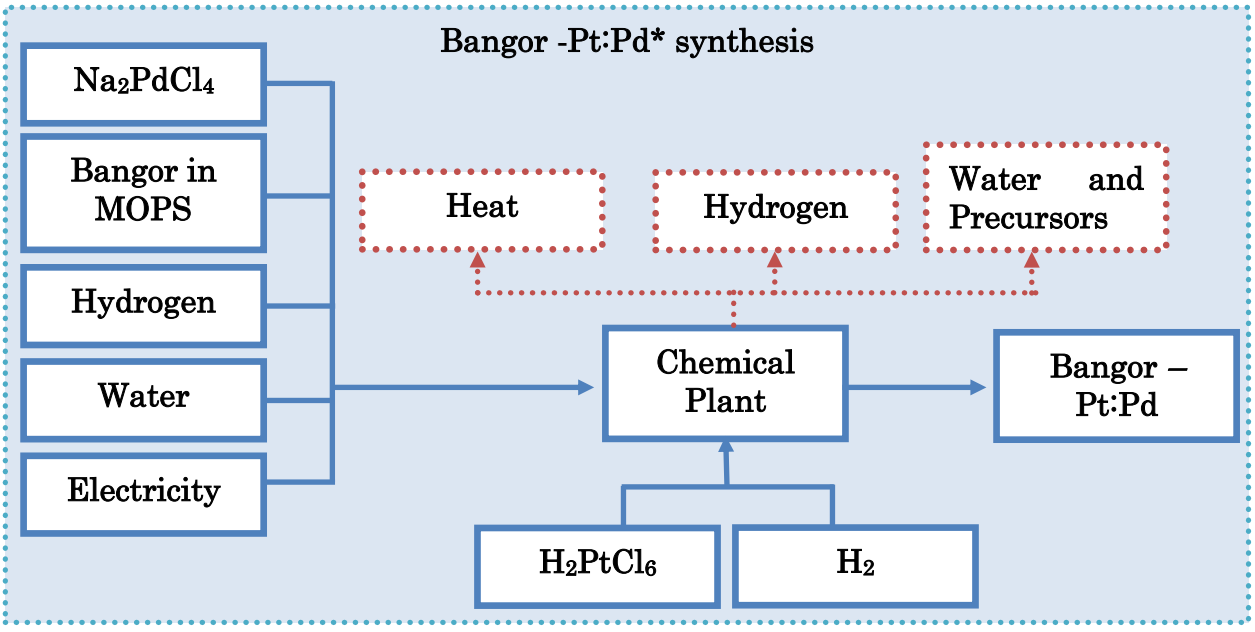
Bangor -Pt:Pd* synthesis
Na2PdCl4
Bangor in MOPS
Hydrogen
Water
Electricity
Heat
Hydrogen
Water and Precursors
Chemical Plant
Bangor – Pt:Pd
H2PtCl6
H2

A5 *Ex-situ* electrochemistry results for Bangor-Pt:Pd* (10%:10%)

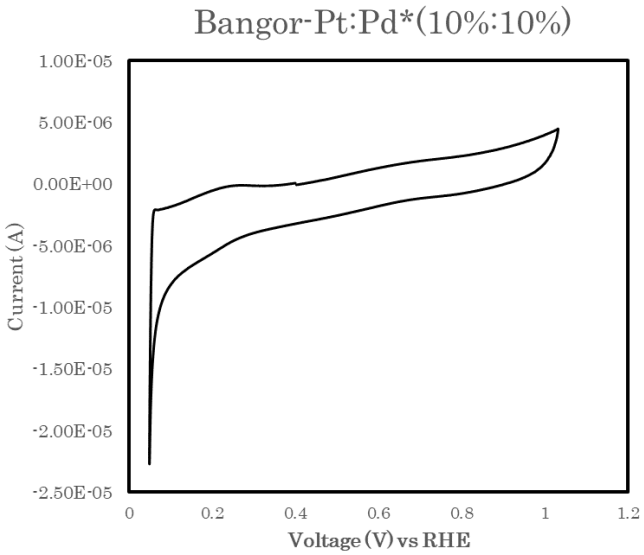

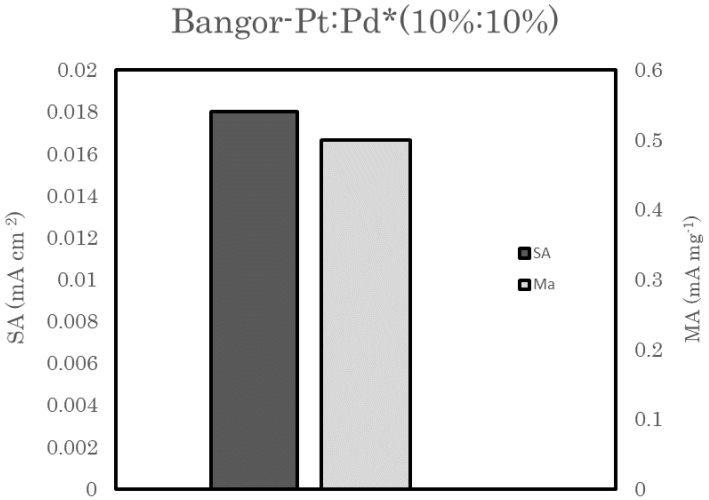

Ex-situ electrochemistry tests were conducted on as made Bangor-Pt:Pd* (10%:10%) as described in section 4.3. The results show ECSAs of 2.4 $m^2 g^{-1}$, SA of 0.021 mA cm^{-2} and MA of 0.50 mA mg^{-1}.

A6 BioH_2 production through linked photo and dark fermentation.

Bio-Hydrogen Production Through Linked Photo and Dark Fermentation

Alan. J. Stephen*[1], Rafael. L. Orozco and Lynne. E. Macaskie[1]

[1]Centre for Hydrogen and Fuel Cell Research, School of Chemical Engineering, University of Birmingham, Edgbaston, B15 2TT, U.K.

*Email: AJS578@bham.ac.uk, www.fuelcells.bham.ac.uk

Introduction

Bio-hydrogen can be produced from sugars through dark fermentation (DF) and photo fermentation (PF). DF is thermodynamically limited (Thauer limit)[1] to 4 mols of H_2 per molecule of glucose (from a maximum possible of 12 mols H2/glucose)[1]. An *E. coli* parental strain, MC4100 and its previously reported modified strains (FTD67, FTD89, IC007 and RL009)[2] produced between 1.1-1.7 mols H_2 /mol glucose whilst diverting reducing power into organic acid (OA) mixtures. A downstream PF step can utilize these OA mixtures to produce additional bio-hydrogen anaerobically under light. Thus this project aimed to compare PF H2 yields against theoretical projections and identify which organic acids fail to realise their potentials as bio-H2 feed-stocks in PF by *Rhodobacter Spp.*

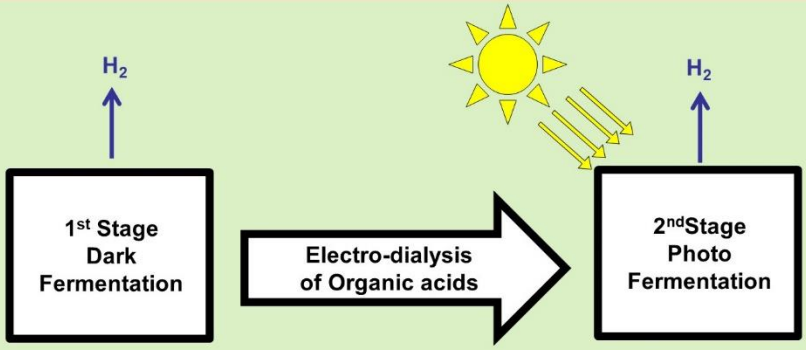

EXPERIMENTAL STUDY

Two purple non-sulphur bacteria (*R. capsulatus* and *R. sphaeroides*) were compared for their ability to produce hydrogen, from the OA mixtures (produced by the various *E. coli* strains) in this PF step. OA mixtures (40 mM) were made according to published values[2]. The bacteria were grown anaerobically in nitrogen limited media under light (3 days) with the OA mixtures (triplicates). H_2 production was measured by water displacement and initial and residual OAs was determined via HPLC analysis to determine hydrogen production potential (HPP)[3] of OA mixture and acid consumption.

RESULTS AND DISCUSSION

H_2 production by both strains realised approximately 50% of the maximum HPP for all OA mixtures (Figure 1). While both PNS strains delivered near-complete consumption of all acids, succinate and butyrate often showed incomplete consumption. This was confirmed by feeding with succinate or butyrate only controls (40 mM each, not shown) which confirmed low utilization of both OA's. Finally increased hydrogen yield from combining both DF and PF steps was confirmed with E. coli strain RL009 and *R. capsulatus*, the dual fermentation producing ~ 6.0 mols H2 /glucose, i.e. a> three-fold enhancement over the dark fermentation alone. However this was still with less than 50% photo-conversion of OAs showing clear scope for onward development.

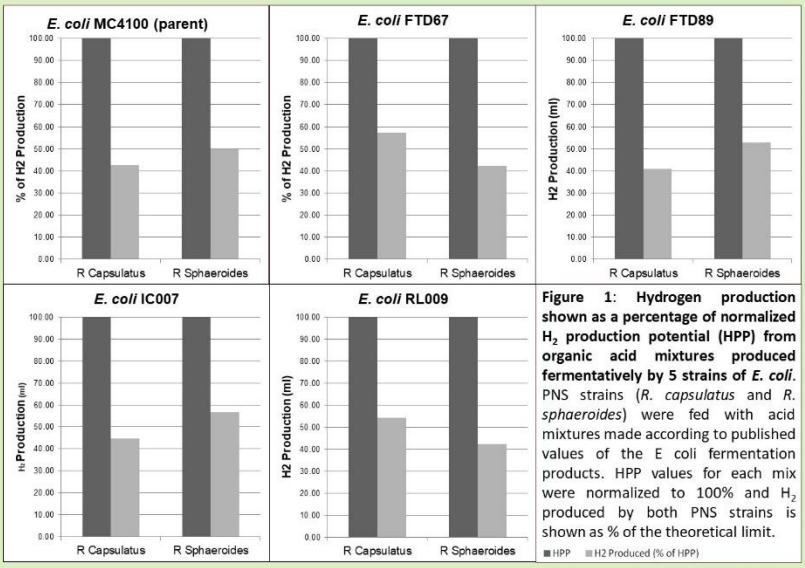

Figure 1: Hydrogen production shown as a percentage of normalized H_2 production potential (HPP) from organic acid mixtures produced fermentatively by 5 strains of *E. coli*. PNS strains (*R. capsulatus* and *R. sphaeroides*) were fed with acid mixtures made according to published values of the E coli fermentation products. HPP values for each mix were normalized to 100% and H_2 produced by both PNS strains is shown as % of the theoretical limit.

CONCLUSION

Downstream photofermentative H_2 production is restricted by inefficient photo-conversion of supplied OA's and limited utilization of succinate and butyrate. Specific variations in the OA mix composition do not affect downstream photo-fermentation. Future studies will aim to address the inefficient photo-conversion via metabolic engineering and also determine the level at which light availability becomes limiting.

References

1. Thauer R. Microbial Energy Conversion. Oxford, Pergamon: 201-204 (1977).
2. Orozco RL Bio-hydrogen and biomass supported palladium catalyst for energy production and waste minimisation. PhD University of Birmingham UK,(2011)
3. Eroğlu E et al. Photobiological hydrogen production by using olive mill wastewater as a sole substrate source. Int J Hyd Energy 29:163-171 (2004)

BLUESKYBIO
UNIVERSITY OF BIRMINGHAM
EPSRC Engineering and Physical Sciences Research Council